Optical interferometric multi-parameter flow sensing of particle suspensions with complex refractive index models

Speets, P.N.A.

DOI
10.4233/uuid:f200afd0-b618-4fde-9a17-a0a5de8c654e

Publication date
2025

Document Version
Final published version

Citation (APA)
Speets, P. N. A. (2025). *Optical interferometric multi-parameter flow sensing of particle suspensions with complex refractive index models*. [Dissertation (TU Delft), Delft University of Technology]. https://doi.org/10.4233/uuid:f200afd0-b618-4fde-9a17-a0a5de8c654e

Important note
To cite this publication, please use the final published version (if applicable).
Please check the document version above.

Optical interferometric multi-parameter flow sensing of particle suspensions with complex refractive index models

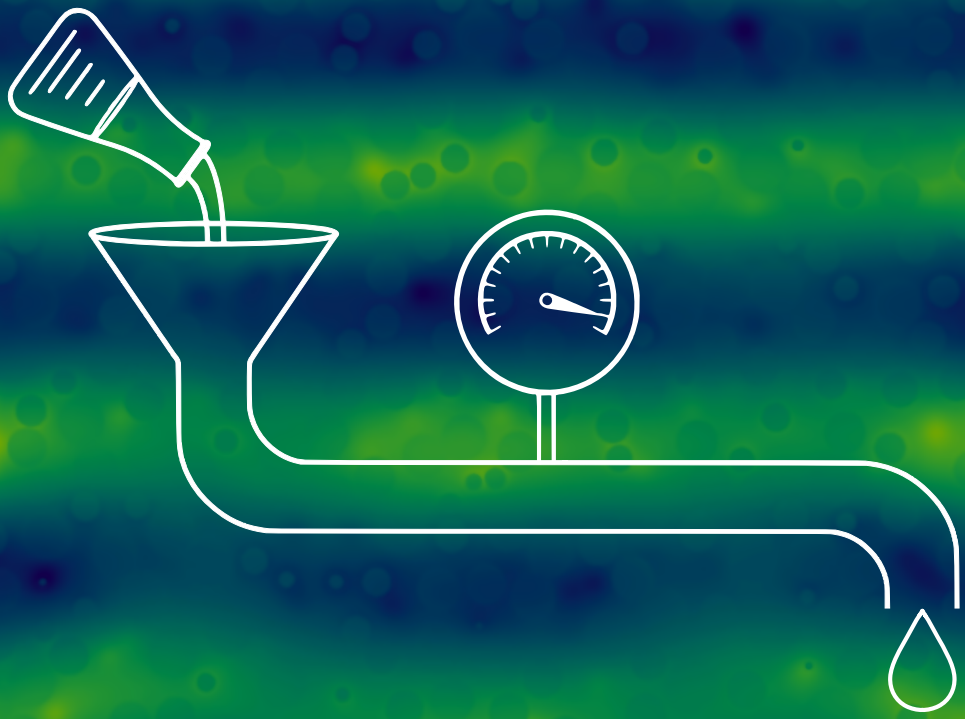

Peter Speets

OPTICAL INTERFEROMETRIC MULTI-PARAMETER FLOW SENSING OF PARTICLE SUSPENSIONS WITH COMPLEX REFRACTIVE INDEX MODELS

OPTICAL INTERFEROMETRIC MULTI-PARAMETER FLOW SENSING OF PARTICLE SUSPENSIONS WITH COMPLEX REFRACTIVE INDEX MODELS

Dissertation

for the purpose of obtaining the degree of doctor
at Delft University of Technology,
by the authority of the Rector Magnificus prof. dr. ir. T.H.J.J. van der Hagen,
chair of the Board for Doctorates,
to be defended publicly on Tuesday 2, September 2025 at 15:00 o'clock

by

Peter Nicolaas Adriaan SPEETS

Master of Science in Physics and Climate Science,
Utrecht University, Utrecht, the Netherlands
born in Amsterdam, the Netherlands.

This dissertation has been approved by the promotors.

Composition of the doctoral committee:

Rector Magnificus,	chairperson
Dr. J. Kalkman	Delft University of Technology, *promotor*
Prof. dr. B. Rieger	Delft University of Technology, *promotor*
Independent members:	
Prof. dr. W.L. Vos	University of Twente
Prof. dr. A.P. Mosk	Utrecht University
Prof. dr. V. Garbin	Delft University of Technology
Dr. R. Besseling	Inprocess LSP
Prof. dr. S.M. Witte	Delft University of Technology, *reserve member*

This work is part of the research programme Synoptics with project number P17-24 project 6, which is (partly) financed by the Dutch Research Council (NWO).

Keywords:	interferometry, scattering, spectroscopy, sensing, flowmetry, dynamic light scattering
Printed by:	Ipskamp Printing
Front & Back:	Front: electric field in a disordered medium with a cartoon of an on-line sensor. Back: electric field in an ordered medium.

ISBN 978-94-6473-888-9

An electronic version of this dissertation is available at
`http://repository.tudelft.nl/`.

CONTENTS

SUMMARY

One of the challenges in the process industry, such as the food and pharmaceutical industry, is the quantitative measurement of various quantities in fluid flows. Examples are the relative volume fractions of the different components of mixtures, the particle size of suspended or emulsified particles and the flow speed. The use of optical sensors to measure these quantities has many advantages: it is fast, non-invasive, and the application is generally straightforward. This thesis describes how (spectral) interferometry and heterodyne dynamic light scattering (DLS) can be used to measure the aforementioned quantities. Special attention is paid to the combination of the two techniques, and the combination of the multiple physical quantities that can be measured.

In Chapter 2, a transmission spectral Mach-Zehnder interferometer is described. From the interference spectrum, both the transmission spectrum and the path length difference due to the sample can be measured. These can be measured simultaneously, due to the application of Fourier filtering techniques on the interference spectrum. The measured path length difference depends on the refractive properties of the material of interest. These are the group index n_g and the group velocity dispersion (GVD). With these two parameters, the volume fraction of the mixture can be determined. This is applied to water and glycerol mixtures, water and ethanol mixtures, and turbid samples of water and Intralipid. Broadband interferometric sensing allows for a more precise measurement of the GVD than traditional wavelength swept Abbe refractometry. In addition, the single shot measurement of the transmission spectrum and the interference spectrum allows this method to be used for in-line optical sensing.

Chapter 3 explores in more depth the nonlinear volume fraction dependence of both the transmission and the refractive index of colloidal suspensions. The transmission and the refractive index can be described by a complex refractive index: the real part is related to the phase delay of the light wave, and the imaginary part to the attenuation of the light due to scattering. The complex refractive index is determined for samples of various volume fractions of 100 nm sodium silicate particles with the same interferometer as described in Chapter 2. The measured attenuation is well described with far field interference, and the group index has a linear relationship with the volume fraction as expected for independent scattering. However, an interesting new non-linear effect was found in the GVD showing that the increase of the GVD with the volume fraction is lower than what is expected from independent scattering. We believe that this work is the first experimental demonstration of concentration-dependent scattering in the real part of the effective refractive index of colloidal media. With a dipole model very similar to the Lorentz-Lorenz model, the particle size and polydispersity of the sample are determined. This method is particularly useful for determining the refractive index of porous particles, as a conventional index matching experiment cannot be used reliably.

For industrial applications, real-time sensing is often necessary. Chapter 4 describes how a transmission interferometer is augmented with the addition of dynamic light scat-

tering (DLS). By means of DLS the speed and size of nano and micro particles can be measured from the time correlations in the scattered light. In heterodyne DLS this back-scattered light is amplified with a strong reference signal. With the combined optical transmission and DLS measurements, various process relevant parameters were simultaneously measured such as the volume fraction, mean particle size, size polydispersity, and flow speed. This is not possible with conventional DLS and spectral interferometry separately. This method is applied to sodium silicate particles to test the method. Furthermore, the applicability for industrial sensing is shown with a real-time measurement of the dissolution and aggregation of an Intralipid emulsion mixed with hydrochloric acid.

SAMENVATTING

Eén van de uitdagingen in de procesindustrie, zoals de voedsel- of the farmaceutische industrie, is het kwantitatief meten van verscheidende grootheden in vloeistofstromen. Voorbeelden zijn de relatieve volumefracties van verschillende componenten van mengsels, de deeltjesgrootte van gesuspendeerde of gemulgeerde deeltjes en de stroomsnelheid. Het gebruik van optische sensoren om deze grootheden te meten heeft vele voordelen: het is snel, niet-indringend, en over het algemeen eenvoudig toe te passen. Dit proefschrift beschrijft hoe (spectrale) interferometrie en heterodyne dynamische lichtverstrooiing (DLS) gebruikt kunnen worden voor de hierboven genoemde grootheden. Hiermee gaat speciale aandacht uit naar de samenvoeging van de twee technieken en de verschillende fysische grootheden die hiermee gemeten kunnen worden.

In Hoofdstuk 2 wordt een spectrale transmissieinterferometer beschreven. Met behulp van het interferentiespectrum kunnen zowel het transmissiespectrum als het padlengteverschil door het monster worden gemeten. Deze kunnen gelijktijdig worden gemeten door de toepassing van Fourierfilteringstechnieken op het interferentiespectrum. Het gemeten padlengteverschil hangt af van de lichtbrekingseigenschappen van de te meten stof. Deze zijn de groepsindex n_g, en de dispersie in de groepssnelheid (GVD). Met deze twee parameters kan de volumefractie van een mengsel worden bepaald. Dit is toegepast op water- en glycerolmengsels en ethanol- en watermengsels, en troebele monsters van water en Intralipid. Breedband interferometrische detectie maakt het mogelijk voor een meer nauwkeurigere meting van de GVD dan een traditionele Abbe refractometrische meting per golflengte. Daarbij maakt het in één keer meten van zowel het transmissiespectrum als interferentiespectrum het mogelijk om deze methode toe te passen voor optische detectie in een vloeistofstroom.

In Hoofdstuk 3 wordt dieper ingegaan op de niet-lineaire volumefractieafhankelijkheid van zowel de transmissie, als de brekingsindex van colloïdale suspensies. De transmissie en de brekingsindex kunnen worden samengevat als een complexe brekingsindex: het reële deel is gerelateerd aan de fasevertraging van de lichtgolf, en het imaginaire deel aan de extinctie van het licht door verstrooiing. De complexe brekingsindex is voor monsters van verschillende volumefracties van 100 nm natriumsilicaat nanodeeltjes met dezelfde interferometer als in beschreven in Hoofdstuk 2 gemeten. De extinctie wordt goed beschreven door verreveldinterferentie en de groepsindex heeft een lineair verband met de volumefractie, zoals verwacht bij onafhankelijke verstrooiing. Een interessant nieuw niet-lineair effect is gevonden voor de GVD waarbij de toename van de GVD met de volumefractie is lager dan zoals verwacht voor onafhankelijke verstrooiing. Wij geloven dat dit werk is de eerste experimentele demonstratie van concentratieafhankelijke verstrooiing in het reële deel van de complexe brekingsindex van colloïdale media. Met een dipoolmodel dat sterk lijkt op het Lorentz-Lorenz model konden de deeltjesgrootte en polydispersiteit van het monster worden bepaald. Deze methode is in het bijzonder nuttig om de brekingsindex van poreuze deeltjes te bepalen, daar een

conventioneel index-matching experiment niet betrouwbaar genoeg is.

Voor industriële toepassingen is realtime monitoring vaak noodzakelijk. In Hoofdstuk 4 wordt beschreven hoe de transmissie-interferometer is uitgebreid met dynamische lichtverstrooiing (DLS). Met DLS kan de snelheid en grootte van nano- en microdeeltjes worden gemeten door middel van de tijdscorrelaties in het verstrooide licht. In heterodyne DLS wordt dit teruggestrooide licht versterkt met een sterk referentiesignaal. Met de gecombineerde optische transmissie- en DLS-metingen, kunnen verscheidende parameters die van belang zijn voor de procesindustrie worden gemeten zoals: volumefractie, gemiddelde deeltjesgrootte, polydispersiteit en stroomsnelheid. Dit is niet mogelijk met conventionele DLS. Deze methode is toegepast op deeltjes van natriumsilicaat om de methode te testen. Verder is de toepasbaarheid voor industriële sensoren aangetoond met een realtime meting van de oplossing en aggregatie van een Intralipidemulsie gemengd met zoutzuur.

1

INTRODUCTION

1

Process manufacturing is the systematic and large-scale production of substances in various states of matter, such as in the chemical industry. Besides bulk chemicals, process industry products include dairy products, beverages, plastics, and medicines. The common denominator in the production of these materials is the presence of fluid flow. These flows are often multiphase, meaning that they are composed of components with different thermodynamic phases, such as in emulsions, suspensions, and slurries.

1.1. SENSING IN THE PROCESS INDUSTRY

In the process industry, the production can be divided into batch processes and continuous processes. In a batch process, all ingredients or precursor materials are added together in a mixer or reactor vessel, and a batch of product is finished after a fixed time, as schematically shown in Fig. 1.1(a). Batch processing is typically used for smaller amounts of produced materials. The quality of the product or intermediates is often only tested after it went through the whole process.

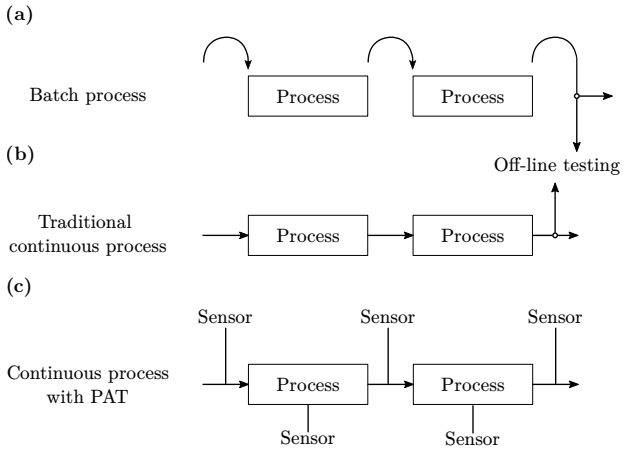

Figure 1.1: **(a)** Flow chart of a batch process. **(b)** Continuous production process with off-line sampling, or with **(c)** process analytical technology (PAT).

In a continuous process, as shown in Fig. 1.1(b), ingredients are continuously pumped into the system, and the product is continuously produced. Continuous processing is most often used for larger volume production, such as in the (petro)chemical industry. The flow chart in Fig. 1.1(b) depicts a conventional process pipeline, where after a few production steps, the manufactured product is tested off-line after all processing steps have taken place. When a processing step fails, it will only be noticed after the off-line quality assurance (QA) check. With this method of testing, the failed product not only undergoes many unnecessary processing steps, but it is also not known which processing step has caused the defect. In addition, the entire end product needs to be rejected.

Hence ideally, for continuous processes and larger than lab-scale batch processes, all gas and fluid streams at every processing step need to be monitored and controlled in real-time. Here, the time scale of what can be considered real-time, depends on the

process that is monitored, and can vary from milliseconds to several minutes[1, 2]. Figure 1.1(c) shows the same flow chart, but now with a sensor at each processing step, which is an implementation of process analytical technology (PAT). These sensors can be used to monitor the process itself and be added to the reactor vessel, mixer, or distillation column. Sensors can also be placed in-line on the pipes or tubing between each processing step. When there is a defect in one of the processing steps, it will be detected immediately by the sensors. The production then can be immediately halted and the defect can be resolved. Moreover, the sensors can be used to provide real-time information on the processes, thereby allowing for feedback control to keep the process quality constant. For process quality monitoring, the parameter that contains the most information on whether the process is operating under nominal conditions is the critical quality attribute (CQA)[3]. If a sensor detects that the CQA is out of the nominal operating range, operator attention is required to troubleshoot the problem.

1.1.1. PROCESS ANALYTICAL TECHNOLOGY

The application of sensors to monitor the production process is called process analytical technology. This term is most commonly used in the context of the pharmaceutical industry, and the regulatory framework to replace off line batch testing with in-line sensing [4, 5] technology. However, this term is also used in a broader sense for all kinds of process industries [6–8]. In this thesis, PAT refers to the latter, broader, interpretation.

Besides process control, PAT can be applied to other factors in the process industry. A breakout of the applications of PAT is shown in Fig. 1.2. PAT is used in the research and development phase for both data collection for understanding and modeling of the process, and the design and optimization of the process itself. After this phase, it can be used for the scale-up of the process. The main aim of data gathering in the research and development (R&D) phase is to correlate the sensor output to the desired outcome of a processing step. This can be the quality of the product, but also the speed or efficiency of the production process. Thereby, PAT information can be used for improved reactor design, or to achieve a faster scale-up from a pilot reactor [7, 9]. However, a larger production version of the pilot plant is not always comparable in performance. Therefore, during scale-up the production parameters need to be adapted for the new plant.

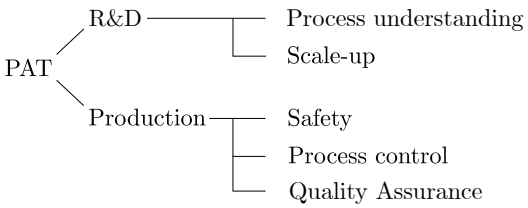

Figure 1.2: Overview of the applications for process analytical technology (PAT) in research and development (R&D) and production.

PAT can be used for product and plant safety, process control and feedback, the aforementioned QA, or a combination thereof. In-flow sensing for plant safety is an obvious application for PAT, which can be applied with something as simple as a temperature sensor to prevent overheating. However, in a broader sense, this applies to product safety

as well. For example, in the food industry, PAT is used to detect spoilage or chemical contamination [10, 11]. Most notably for the pharmaceutical industry, the American Food and Drug Administration considers that the control and monitoring of each production step is a necessary condition for drug safety [12].

PAT can also be used to regulate the production process where it is used in a feedback loop to regulate the input parameters or input streams. This is important to ensure a consistent quality of the final product, particularly for complicated or unstable reactions. Examples include the fabrication of nano and microparticles [13–15], bioreactors [16–18], or for unstable reactions [19].

Nowadays, PAT is a relevant topic for any process industry [7, 20], whether it is the chemical industry [21], food industry [8, 11, 22–24], or pharmaceutical industry [7, 25–27]. Three concrete examples of the parameters of interest that are relevant in the oil industry, pharmaceutical industry, and food industry are given below.

One of the oldest applications for PAT is on large scale processes in the petrochemical industry. As early as the 1950s, in-line infrared spectrometry was used in the oil industry for QA in the production of high octane fuel [28, 29]. Also, refractive index sensing was used for feedback systems in distillation columns, since the refractive index is sensitive to the relative fractions in the column [30, 31] as the longer carbon chains have a higher refractive index than the shorter chains.

An example from the pharmaceutical industry is the synthesis of paracetamol. Traditionally, paracetamol is fabricated in a batch process. However, PAT enables the fabrication of paracetamol in a continuous process [32]. Like many other active pharmaceutical ingredients (API), the production requires crystallization [32–35]. This can be a complicated process that is dependent on the shape and size of the reactor. In addition, the size distribution of some crystallized APIs can influence the efficiency of product removal and the chemistry in subsequent processing steps. Most importantly, it can influence the effectiveness of the medicine [9, 33]. Therefore, the size distribution of the crystallized product, and the total throughput of all ingredients must be constantly measured.

In the dairy industry, the quality of cow's milk is often determined by the protein and fat content [22, 36, 37]. The fat in the milk is often dispersed in globules with a very wide size distribution. The fat globule size is related to fat content and the health of the cow. In addition, the per cow variability of the milk can affect the quality and consistency of dairy products, such as cheese [8, 24, 38].

For all the five PAT applications shown in Fig. 1.2 and in the examples given above, it is important that the sensor does not influence the product itself, i.e., it is non-destructive and non-invasive. Also, it should be fast to give real-time feedback. Finally, it should work in-line with the process flow when the process components flow past the sensor.

An important consideration is that any parameter of interest, e.g., composition, is only measured indirectly, for example through the refractive index. Next, this physical parameter, here the refractive index, is converted either through modeling or calibration to the quantity of interest, e.g., volume fraction. However, in real processes there can be confounding factors that influence the result, e.g., through the presence of contaminants or the interrelation of physical parameters. Hence, it is often beneficial to combine sensors to reduce ambiguity. For example, the refractive index measurement can be combined with a measurement of the transmission spectrum. In that case, a contami-

nation by particles or other absorbing compounds can be detected, on top of the relative volume fractions.

1.2. SENSING OF THE MAIN PARAMETERS OF INTEREST

As the examples described in the previous section show, there is a need for non-invasive in-line sensing of multi-component flows of molecular mixtures and particle suspensions. A cartoon of such a sensor is shown in Fig. 1.3. Common flow parameters are the partial volume fraction, particle size and flow speed. These fluid properties can be measured optically or non-optically. In the following three sections, techniques will be described for sensing these parameters, with a focus on optical methods.

1.2.1. PARTIAL VOLUME FRACTION

Most commonly, the composition, or partial volume fraction, of a mixture is measured with a transmission spectrum using quantification of the optical attenuation. Next to the examples given above, this has been used to measure the fat content in bovine milk [22] and human milk [39, 40], the characterization of blood [41] or the monitoring of water quality [42]. A measurement of the transmission spectrum can be used for the measurement of the volume fractions of absorbing or scattering media. Furthermore, for turbid media, the transmission spectrum strongly depends on the particle size distribution.

Since the transmission spectrum contains a lot of information other than the volume fraction, for example, due to absorption and scattering, it can be challenging to obtain the volume fraction without a secondary sensing method. This is not the case for the refractive index, which is almost exclusively dependent on the mixing ratio between two components. Therefore, the refractive index can provide valuable information on the partial volume fraction of the sensed components. Moreover, the refractive index can be spectrally resolved, and the dispersion can be used for more detailed analysis. Refractive index composition analysis has been used for the measurement of salinity [43, 44] or glucose content [43, 45, 46]. Although refractive index sensing provides a clear benefit for transparent media, it can also be used in scattering media. Examples include the differentiation between blood groups [47], the measurement of the amount of

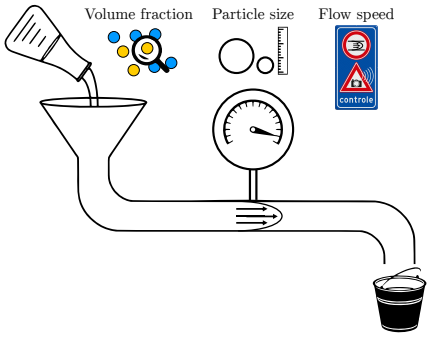

Figure 1.3: Cartoon of in-line flow sensing showing various physical properties that can be measured in-line.

hemoglobin [48], and particle sizing [49]. However, multiple scattering of the suspended particles can make a refractive index measurement ambiguous, since the multiple scattered light has an optical path length longer than the ballistic light.

The refractive index and the refractive index dispersion can be measured with various techniques. Traditionally, the refractive index is measured with an Abbe refractometer [50], which measures the refractive index by means of the critical angle. This can also be used for turbid media[51–53]. However, it cannot simultaneously measure the transmittance. Furthermore, care must be taken to accurately take the scattering of suspended particles into account [54–56].

The refractive index can also be measured with optical coherence tomography, but only for specific use cases [57]. Other methods for refractive index sensing are by means of tapered optical fibers [58], plasmonics [59, 60], or microresonators [61, 62]. An advantage of these methods is that these can be applied in biosensors. These are sensors with a functionalized surface to increase sensitivity and specificity [58, 59, 63].

Refractometry and transmission spectroscopy can be combined with spectral interferometry. Here, both the attenuation spectrum and the refractive index can be measured simultaneously [45, 64]. In that case, the transmitted intensity is retrieved from the envelope of the interference spectrum. The refraction and dispersion are then related to the spectral frequency of the interference, and the chirp, respectively. This method can potentially be applied to reduce the effects of multiple scattering in a highly turbid medium, by filtering out the longer optical path lengths [45, 65, 66]. It is this method that is applied in this thesis. A more in depth description of the theory and experiment is given in Chapter 2.

1.2.2. PARTICLE SIZE

A second important flow parameter is the particle size in a suspension. Particularly, for in-line sensing, current commercial in-flow particle sizers are often unwieldy and expensive [67]. The particle size is seldom a single size, but rather is described by a size distribution. The particle size distribution is characterized by the polydispersity, which is a measure of the spread of particle size. The size distribution can be measured with various techniques, but often the outcome is dependent on the used technique [68], and it may be poorly defined for multimodal size distributions. The polydispersity can be defined in multiple ways, for example, mass [69], volume [70] and, for spherical particles, diameter. In this thesis the polydispersity is defined by the standard deviation of the number particle size distribution, often given as a percentage of the diameter.

Non-optically, the particle size distribution can be measured, for example with ultrasound [71], or with the electrical resistance [72], or impedance [73]. Here, we focus on optical particle sizing techniques.

In industry, a common optical sizing method is focused beam reflection measurements (FBRM) [14]. With FBRM, laser light is focused just in front of a probe. This focal point is rapidly rotated, making circles in the bulk medium, and the fluctuations of the reflected beam over time are detected. The larger a particle, the longer time the moving focus spot spends on a particle. FBRM measures a chord length distribution, instead of a particle size distribution, because each nonspherical particle will be measured with a random angle, and the focus spot does not necessarily go through the center of mass of

each particle [74, 75]. A main drawback is that it is not always possible to convert a chord length distribution to a particle size distribution. A second disadvantage of FBRM is that it is only sensitive to relatively large particles (> 100 nm) [76].

Another rather common method for particle sizing is laser diffraction analysis (LDA) or static light scattering (SLS). With LDA, the diffraction pattern of the light scattered from a particle or a group of particles is measured on a detector array or camera [67, 77]. With SLS the angle dependence is measured, either by scanning a detector over a range of incidence angles, or with a detector array [78].

With these methods, the angle dependence of the scattering, or the phase function, can be determined. The angle dependence can be related to the particle size by, for example, comparing it to the phase function calculated with Mie theory. Most importantly, laser diffraction analysis techniques have the potential to be used for in-line sensing [67, 79]. For example, in many flow cytometers the cell size is estimated through measurement of the scattered power at different angles, which is related to the phase function of the cell. In a flow cytometer a fluid flow is funneled into a small tube such that the particles, or more often cells, flow sequentially past the sensor. Cytometers often consist of waveguides placed such that they make different angles with respect to the axial direction. When a cell passes the detector, the scattered light is measured with on multiple detectors [80]. This is similar to SLS, but with the use of only a limited number of angles. Flow cytometers can also measure the size and refractive index of the cells simultaneously [81].

The particle size can also be measured by imaging the particles over time in a video and track their displacements from frame to frame. This is called particle tracking analysis (PTA), also known as nanoparticle tracking analysis (NTA). Due to Brownian motion the particles make a random walk with a mean displacement that is proportional to the diffusion constant and the time. The particle size can be determined from the diffusion constant and the Stokes-Einstein equation. The collective particle movement is directly related to the local flow speed. Although in 2020 Gross-Rother *et al.* [82] considered PTA as an emerging technique, PTA is widely applied and commercially available [83–85]. A disadvantage of PTA is that it is difficult to implement in flow and can only be applied to dilute samples. Furthermore, the particle size needs to be large enough, and a flow rate slow enough, that the particle motion is visible in enough consecutive frames. With hollow optical fibers it is possible to measure diameters lower than 20 nm [86, 87], however, it is not possible to implement this for industrial sensing applications. For freely diffusing nanoparticles the smallest measurable particle size is much larger, with a typical minimum of 100 nm under no flow conditions [88]. Often, the illumination and the camera frame rate is a limiting factor to measure small particles.

A second well-established technique that measures the Brownian motion for particle sizing is dynamic light scattering (DLS) [89, 90]. With DLS, the time correlations in the detected scattered light are detected. Light scattering from particles in Brownian motion results in a fluctuating interference pattern. Small particles have fast Brownian motion and induce high-frequency fluctuations in the detected signal, whereas large particles cause low-frequency fluctuations. The DLS signal can be detected with a low-coherence spectral interferometer. With this technique, DLS optical coherence tomography (DLS-OCT), or spatially resolved DLS (SR-DLS), both the diffusion and flow can be spatially

resolved [91, 92]. Furthermore, DLS-OCT can be applied to very turbid samples, and the multiple scattering can be filtered out [91]. DLS-OCT sensors are already commercially available.

Finally, the particle size distribution can be measured in transmission with optical spectroscopy [93]. When the particles are of the same order as the wavelength, the scattering causes Mie resonances in the detected signal that can be used to fit a particle size [94]. However, with complex particle size distributions, or small particles, there is ambiguity between the size polydispersity and mean particle size. Also, the Mie resonances are washed out for strongly polydisperse particle size distributions. Furthermore, there are no Mie resonances present in the spectrum in the Rayleigh scattering regime. In the absence of Mie resonances, the volume fraction of the particles needs to be known in order to retrieve the mean particle size from the attenuation spectrum.

1.2.3. FLOW SPEED

Whereas optical methods are important for composition and particle sensing due to their noninvasive nature, the flow speed is often measured non-optically. In fact, for transparent media the flow speed is hardly measurable with optical methods at all, and if so, only indirectly by using optical sensing in the detection method for fiber or microelectromechanical systems (MEMS) sensors [95, 96].

Instead, non-optical methods are readily available for flow sensing. An advantage of many flow rate sensors is that they can be readily miniaturized as MEMS. There are many mechanisms and measurement strategies for flow sensing with MEMS [97]. For example, flow speed can be measured by differential pressure sensing [98]. Other sensors locally heat the fluid and measure the temperature difference between two positions, one upstream and one downstream [99, 100]. A third mechanism with which the flow rate can be measured, is by the drag force on an object. For example, this can be a rod or fiber placed into the flow. The flow is then measured by the displacement of the object [95, 101]. A fourth technique utilizes the Coriolis effect to measure the mass flow. The flow itself is guided in a narrow loop. This loop is brought to vibrate by an actuator and the Coriolis force from the flowing mass brings a twist mode in the vibration of the loop. This twist mode is detected by two sensors, placed at the position where the vibrations have the largest amplitude [102, 103].

Optical measurements of the flow speed are possible in turbid media. In that case, the flow speed is measured by light that is reflected or scattered from suspended particles. A straightforward approach is particle image velocimetry (PIV). With this technique, particle displacements are imaged and tracked across multiple frames [104]. This can only be done if the particle suspension is sufficiently dilute such that the images of the particles do not overlap. Also, the particles need to be large enough to individually visualize them or they need to be fluorescently labeled.

A method to measure flow speed that is more suitable for industrial sensing, and often applied in biomedical research, is laser Doppler velocimetry (LDV) [105]. Here, the light is split into a reference and a sample beam. A Doppler shift in the sample arm is detected from the interference with the field of the reference beam. The Doppler shift is proportional to the flow speed in the direction of the beam.

The flow speed can be measured by means of DLS from the time decorrelation of the

detected intensity of light scattered from a sample. This method is used in Chapter 4, not only to measure the mean particle size, but also the flow speed. When a reference field is used to increase the sensitivity, i.e., in a heterodyne detection scheme, DLS is very similar to LDV.

A related technology is optical coherence tomography (OCT). This technique is also similar to LDV, however it uses a broad spectrum and spectral interference, instead of monochrome light. With Doppler OCT the frequency shift can be measured as a phase shift in the spectral interference fringes [106, 107]. The Doppler shift can be converted to the flow velocity in the direction of the optical beam.

OCT can also be used in combination with DLS, which makes it possible to measure the spatially resolved total flow speed [92, 107]. This can even be done in the sub-diffusive regime with the use of number fluctuation DLS-OCT [107]. In addition, a measurement of the spatially resolved velocity, and the flow direction, can be made, but this requires adapted scanning and processing strategies [108, 109]. This is also possible with the use of DLS OCT in combination with Doppler OCT [108, 110, 111]. Here, the Doppler part of the signal is sensitive to the speed in the axial direction, and the DLS part of the signal is sensitive to the total flow speed.

OCT has an advantage over LDV in that it is possible to measure the local flow speed in arbitrary channels, whereas the LDV signal is an average of all flow speeds in the sample. This can be accounted for with prior knowledge of the laminar flow profile and the optical properties of the medium. Furthermore, DLS OCT requires a spectrometer, which is usually slower, hence it cannot measure very high flow speeds. Moreover, it is more expensive than the photodiodes that are used in LDV and conventional DLS.

1.2.4. MULTIPARAMETER SENSING

The aforementioned methods are meant for direct detection of relevant sample parameters. However, sometimes these parameters cannot be measured directly and a related parameter can be used as a proxy. For example, the chord length distribution as obtained with FBRM is strongly related to the particle size distribution. With proper calibration, FBRM alone is often sufficient for in-line monitoring of particle-size changes [7]. Although strategies exist to obtain the particle size distribution from the FBRM chord length distribution, the reconstruction of the particle size distribution remains an ill-posed problem [112]. Therefore, the addition of a second sensing method can be used to overcome this ambiguity. FBRM can be combined with a second sensor based on in-line microscopy [113], or laser diffraction analysis [114] to obtain a particle size distribution from the FBRM chord length distribution.

Alternatively, multiple parameters can affect the same measured parameter. For example, if the particle size is not close to the used wavelength for sensing nor is it monodisperse, the transmission spectrum is smoothened out and particle sizing becomes ambiguous because the spectral shape is dependent on the volume fraction of the particles and on the polydispersity of the size distribution. This ambiguity can be broken by measuring additional parameters, for example the volume fraction, or the diffusion coefficient (DLS autocorrelation). Both are used in this work, and used for particle sizing in Chapters 3 and 4.

1

1.3. MEASURING OPTICAL PROPERTIES WITH INTERFEROMETRY AND DLS

1.3.1. ATTENUATION OF LIGHT IN TRANSMISSION

In one dimension, light can be described as an electromagnetic plane wave with wavelength λ and wavenumber $k = 2\pi/\lambda$, and field amplitude $E_0(k)$, and intensity amplitude $I_0(k) = |E_0(k)|^2$. Generally, any medium has two effects on the transmittance of an optical wave. First, the amplitude of the wave can decrease due to absorption or scattering, and second, the phase can be retarded due to the refractive index of the medium. Both effects are sketched in Fig. 1.4 for a sample with size L. The top light wave E_{sam} goes through the sample, whereas the bottom reference wave E_{ref} does not. After passing through the sample, the top wave has a lower amplitude and has a phase retardation compared to the reference wave. In a scattering medium, the scattering decreases the

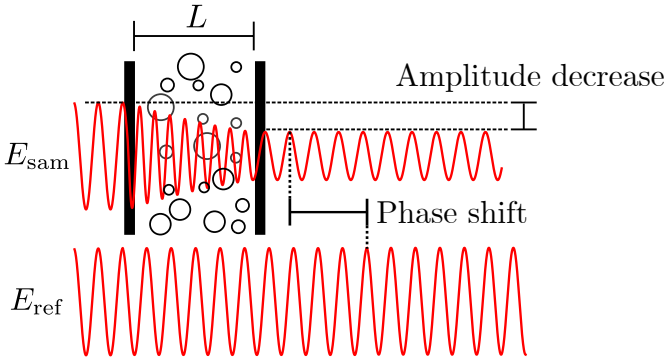

Figure 1.4: Sketch of an optical wave in a transmission experiment. The electromagnetic wave E_{sam} is attenuated and delayed compared to E_{ref}.

intensity of the light in the forward direction as illustrated by the decay in amplitude in the sample. This decrease in amplitude can be measured, and, when L is known, related to the attenuation spectrum $\mu(\lambda)$. This follows a Lambert-Beer-like expression[115, 116]

$$E(\lambda) = E_0(\lambda)e^{-\frac{1}{2}\mu(\lambda)L}, \qquad I(\lambda) = E^2(\lambda) = I_0(\lambda)e^{-\mu(\lambda)L}. \tag{1.1}$$

The intensity spectrum of the light after propagating through the sample is shown in Fig. 1.5(a). Here, the transmission spectrum of the light that goes through a sample is shown in red, and the reference transmittance that does not pass through the sample is shown in blue.

In this work, the attenuation $\mu(\lambda)$ is a parameter used for particle sizing. When the embedding medium is transparent, i.e., there is no molecular absorption, the attenuation $\mu(\lambda)$ is determined only by the scattering attenuation: $\mu(\lambda) = \mu_{\text{sca}}(\lambda)$. The scattering attenuation is dependent on the volume fraction of particles, the particle size and the correlation of the positions of the particles.

The scattering attenuation can be calculated from the particle size and refractive index with Mie scattering theory. An example is shown in Fig. 1.5(b). Here, the scattering

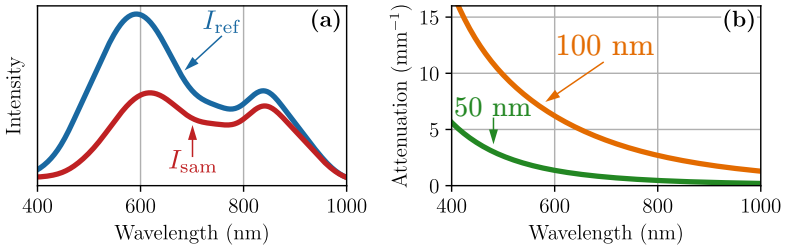

Figure 1.5: **(a)** Transmission spectrum showing the intensity reduction due to scattering. **(b)** Example of an attenuation spectrum for $a = 100$ nm (orange) and $a = 50$ nm (green) silica particles in water with a volume fraction of 0.1.

attenuation is shown for silica particles with a volume fraction of $f_v = 0.1$ suspended in water. When the size parameter, $x = 2\pi n_m a/\lambda$, with n_m the refractive index of the embedding medium and a the particle radius, is larger than, or around, unity, the Mie spectrum has resonances that can be used for particle sizing. For dilute media, dependent scattering effects, which arise from interference effects due to scattering from dense particle ensembles, can often be neglected. However, the dependent scattering effect is stronger for high particle volume fractions. This is further discussed in Chapter 3.

The second effect that media have on light waves is phase retardation. In Fig. 1.4 this is sketched as a decrease of the wavelength inside the medium. The effect of the refractive index $n(k)$ of a medium with length L can be seen in the phase of the complex electric field $E(k)$. The phase of the wave is not observable in the intensity, only in the field. The phase shift between the wave through the sample E_{sam} and the reference wave E_{ref} is $\Delta\phi = (n(k)-1)kL$. Together with Eq. 1.1, the electric field E_{sam} compared to E_{ref} is given by

$$E_{\text{sam}} = E_0 e^{-\frac{1}{2}\mu(\lambda)L} e^{i(n(k)-1)kL}. \tag{1.2}$$

Although the phase of the wave cannot be measured directly, the relative phase with a reference wave can be measured. The phase shift, as shown in Fig. 1.4, can be measured with spectral interferometry. With spectral interferometry, a reference field with a differ-

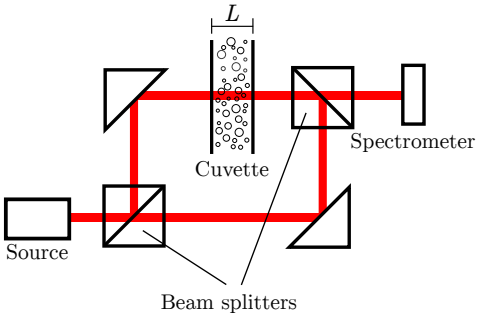

Figure 1.6: Sketch of a Mach-Zehnder interferometer with measurement cuvette.

ent path length δ, and therefore a different phase $k\delta$, is added to the phase of the sample field. This can be done with, for example, a Mach-Zehnder interferometer [45], as shown in Fig. 1.6. Here, light with a broad spectrum is split into two arms, where one of them goes through the sample. The fringe pattern caused by interference of the two beams is detected on a spectrometer. An example of such a spectrum is shown in Fig. 1.7(a). The spacing of the fringes is related to the refractive index, with increasing spectral frequency being the signature of increasing sample refractive index, shown in Fig. 1.7(b).

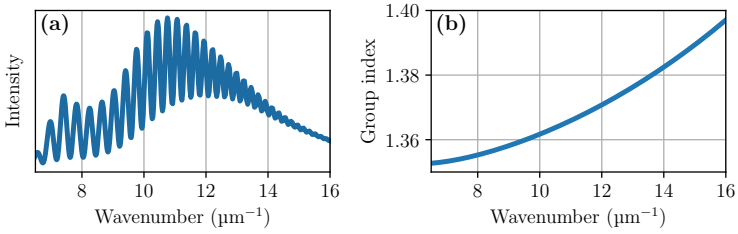

Figure 1.7: **(a)** Interference spectrum. **(b)** Group index spectrum of $a = 100$ nm silica particles in water with a volume fraction of 0.1 determined from the interference spectrum.

The refractive properties are often specified by the group index n_g and the group velocity dispersion (GVD). The advantage of parametrization of the refractive properties with n_g compared to, for example, polynomial coefficients, is that they directly relate to the refractive properties of the material over a spectral range. Both the group index and the GVD are tabulated for many materials. Further discussion on the spectral interferometer, the group index and the GVD can be found in Chapter 2.

1.3.2. SIGNAL FLUCTUATIONS WITH DYNAMIC LIGHT SCATTERING

As indicated in the previous section, the particle size determined solely from the transmission spectrum can be ambiguous. This ambiguity can be circumvented with an independent measurement of the particle size with DLS. In addition to size, DLS can also be used to measure the flow speed of the particles.

A DLS measurement can be made by a simple detection of the backscattered inten-

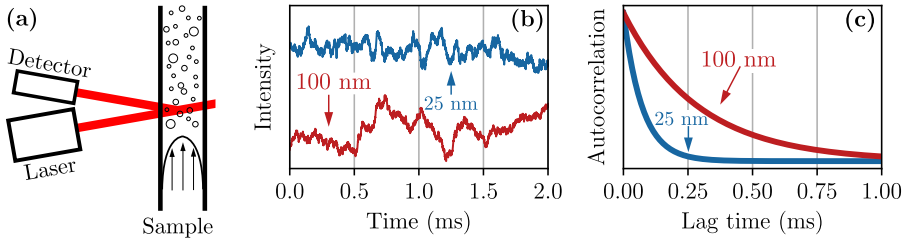

Figure 1.8: **(a)** Sketch of homodyne dynamic light scattering setup. **(b)** Intensity fluctuations over time due to particle diffusion for $a = 25$ nm particles (blue), and $a = 100$ nm particles (red), and **(c)** the autocorrelations of the intensities of the signal in **(b)**.

sity over time. An example of a DLS setup is shown in Fig. 1.8(a). The intensity of the backscattered light is the coherent summation of all backreflected waves. Because the particle positions change over time due to the flow and Brownian motion, the phase of the reflected fields varies in time leading to changes in the interference that gives rise to intensity fluctuations. An example of these fluctuations is shown in Fig. 1.8(b) for particles with a radius of 25 nm (blue) and 100 nm (red). The signal of the smaller particles shown in blue fluctuates at a much shorter time scale than the signal of the larger particles shown in red. The rate at which a fluctuating random signal varies in time can be quantified by its autocorrelation function. For the intensity of the backscattered light, the intensity time correlation $g_2(\tau)$ for a particle suspension under flow and illuminated with a Gaussian beam is given by [117]

$$g_2(\tau) = \frac{\langle I_{\text{det}}(t) I_{\text{det}}(t+\tau)\rangle_\tau}{I_{\text{det}}^2} = A e^{-2Dq^2\tau} e^{-2v^2\tau^2/w_0^2}. \tag{1.3}$$

Here, the intensity detected with a detector at time t is given by $I_{\text{det}}(t)$, τ a time delay after time t, where A depends on the signal-to-noise ratio of the data, q is the length of the scattering vector given by $q = 2n_m k$ for backreflected light, and v is the speed of the particles. The constant w_0 is the Gaussian beam waist at the focal point. The parameter D is the diffusion coefficient that relates the Brownian motion to the particle size through the Stokes Einstein equation [118–120]

$$D = \frac{k_B T}{6\pi\eta a}, \tag{1.4}$$

where k_B is the Boltzmann constant, T is the temperature and η is the viscosity. The particle size can be obtained from the diffusion constant D which is obtained from a fit of the autocorrelation function to Eq. 1.3.

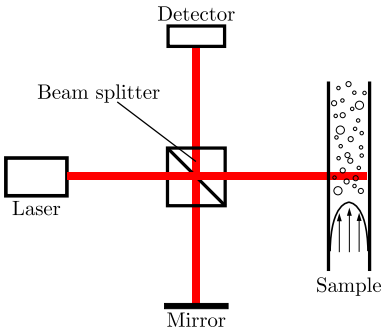

Figure 1.9: Sketch of a heterodyne dynamic light scattering setup

In a homodyne DLS experiment, as shown in Fig. 1.8(a), the light is directly detected after scattering from the particles in the medium. However, the DLS sensitivity can be increased with the addition of a reference signal. An example can be seen in Fig. 1.9, where the reference is created from the light source by splitting off some light and mixing it with the field reflected from the sample.

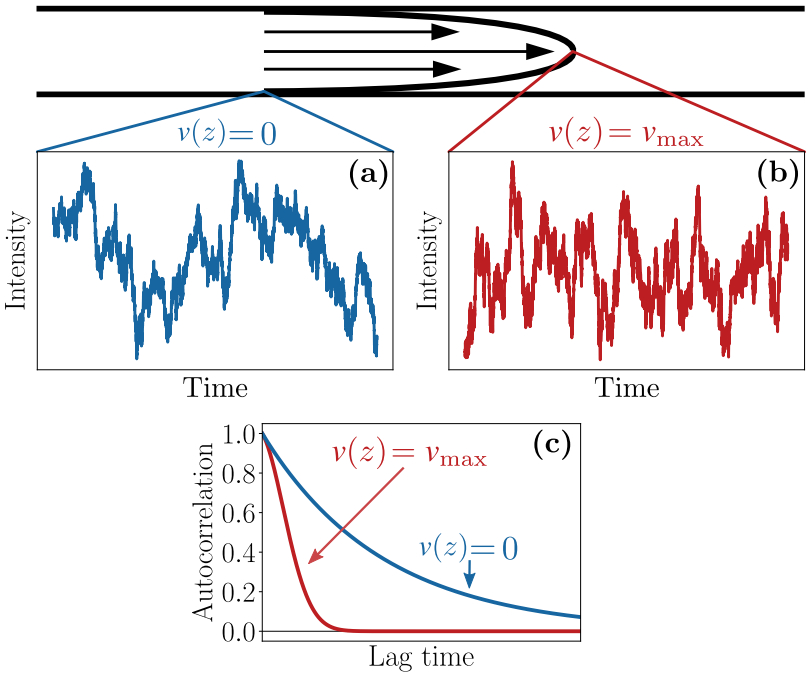

Figure 1.10: The effect of flow on the autocorrelation. **(a)** The DLS signal from the sides of the flow profile with flow speed $v(z) = v_{\max}$. **(b)** The DLS signal from the center of the flow with flow speed $v(z) = v_{\max}$. **(c)** The autocorrelations for $v(z) = 0$ and $v(z) = v_{\max}$ as given by Eq. 1.5.

This configuration of DLS detection is called heterodyne DLS. Heterodyne detection has two main advantages over homodyne detection. First, a low sample signal can be amplified with the addition of the reference beam. Second, in heterodyne detection, the field time correlation is the square root of the intensity correlation. It therefore decorrelates more slowly, hence smaller particles with faster dynamics can be detected easier. The field autocorrelation of a particle suspension under flow illuminated with a Gaussian beam is given by[117]

$$g_1(\tau) = Ae^{-Dq^2\tau} e^{-v^2\tau^2/w_0^2} e^{iqv_z\tau}. \tag{1.5}$$

The complex-valued component is caused by the Doppler shift when the particle moves in the direction of the beam. Therefore, it depends on the speed in the axial direction v_z. The latter two exponents in Eq. 1.5 need to be determined or compensated for the flow in order to determine the diffusion from the remaining part. Alternatively, when the diffusion is known it can also be used for measurement of the flow speed, when properly calibrated.

The effect of flow on the DLS signal is shown in Fig. 1.10. For sufficiently low flow speeds compared to the channel cross section, the fluid flow can be considered laminar. In a wide rectangular channel spanning a depth range from 0 to L, the flow speed of a

laminar flow is given by a parabolic flow speed profile [121],

$$v(z) = \frac{6Q}{L^3 W} z(z-L)\,. \tag{1.6}$$

Here, L is again the width of the channel in the axial direction, and W the size of the channel in the lateral direction with $W \gg L$.

Examples of two autocorrelation functions for flowing particles illuminated by a Gaussian beam are given in Fig. 1.10(a) and (b). The signal in Fig. 1.10(a) is the intensity at the detector that is scattered from particles near the edge of the flow cell where the speed is zero. Therefore, only the diffusive term is present in the signal. In Fig. 1.10(b), the fluctuations in the signal are stronger, and less correlated, due to the effect of the high flow speed in the center of the channel.

In Fig. 1.10(c), the real-valued autocorrelation functions g_1 for the two signals are shown. The autocorrelation shown in blue decays with a single exponential, whereas the autocorrelation shown in red is also multiplied with the Gaussian flow term. Close to $\tau = 0$, the decay rates are equal, but for larger τ, the Gaussian term becomes much stronger than the single exponential diffusive term.

In reality, the DLS signals for different depths cannot be measured separately, unless by means of DLS-OCT. Eq. 1.5 only applies to a single flow speed, therefore the resulting autocorrelation is averaged over the flow velocity that varies over the channel width. When the dimensions of the channel are known in advance and the flow is laminar, a DLS measurement can be used simultaneously for a flow speed measurement and for particle sizing. This method is further described in Chapter 4.

1.4. THE CONCENTRATION DEPENDENT SCATTERING EFFECT

The optical properties of a scattering medium depend on the volume fraction of the scatterers. For low concentration, the attenuation increases linearly with concentration. The nonlinear dependence of the optical properties on the concentration of scatterers is called 'dependent scattering', or sometimes the 'dependent scattering effect'. Usually, this term only refers to the attenuation, or the imaginary part of the complex refractive index. However, the term 'dependent scattering' is somewhat vague. Particularly, if it is left implicit what the scattering depends on. Consequently, the use of terminology and even the cause of the dependent scattering effects has attracted some controversy [122–126].

The propagation of light through a scattering medium may depend on the density of scatterers in three mechanisms: multiple scattering, far-field interference and near-field effects. These three mechanisms are sketched in Fig. 1.11.

Multiple scattering in a dense medium is an N body problem. The electric field at position $\boldsymbol{r}$ in a group of discrete scatterers $\boldsymbol{E}(\boldsymbol{r})$ is sketched in Fig. 1.11(a) and is given by the Foldy-Lax equation,

$$\boldsymbol{E}(\boldsymbol{r}) = \boldsymbol{E}_0(\boldsymbol{r}) + \sum_i^N \overleftrightarrow{G}(\boldsymbol{r}_i - \boldsymbol{r})\boldsymbol{E}(\boldsymbol{r}_i)\,. \tag{1.7}$$

The local field at a scatterer $\boldsymbol{E}(\boldsymbol{r}_i)$, in turn, depends on the field radiated by all other scatterers. How the local field $\boldsymbol{E}(\boldsymbol{r})$ depends on the field at a scatterer $\boldsymbol{E}(\boldsymbol{r}_i)$ is described by

the, for now arbitrary, scattering operator $\overleftrightarrow{G}$. Note the vectorial nature of the equation, where the operator $\overleftrightarrow{G}$ may couple the polarization directions of the electric field. One method to solve Eq. 1.7 is to start with the Born approximation. This means that the local field is approximated with the driving field: $\boldsymbol{E}(\boldsymbol{r}) = \boldsymbol{E}_0(\boldsymbol{r})$. Subsequently, the resulting scattered field is then used to correct the local field $\boldsymbol{E}(\boldsymbol{r}_i)$ at each scatterer, resulting in the Born series. This process can be iterated to obtain a final solution.

The coupling $\overleftrightarrow{G}(\boldsymbol{r})$ depends on the properties of the particles themselves. When the scattering cross section of the particles is small, the local electric field can be approximated as the incoming field $\boldsymbol{E}_0$ (the Born approximation). This greatly simplifies Eq. 1.7 and means that multiple scattering events are ignored. The optical properties of the medium may still depend on the particle volume fraction due to interference of the scattered wave, as sketched in Fig. 1.11(b). Both particles are radiating a wave with the same frequency, but with a phase difference since the waves are received and emitted from different positions $\boldsymbol{r}_0$ and $\boldsymbol{r}_1$, since they are both driven by the same field $\boldsymbol{E}_0(\boldsymbol{r})$. These fields interfere at a large distance R from the particles with waves that have a phase difference $\Delta\phi$, which depends only on the relative distance between the two particles. A derivation of the effect of far-field interference on the scattering attenuation is given in Chapter 3.

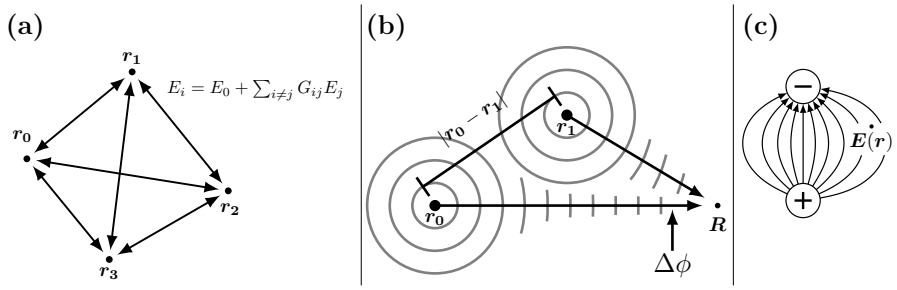

Figure 1.11: Example of **(a)** multiple scattering. The field at $\boldsymbol{r}_i$ is given by the sum of all contributions from all other particles at positions $\boldsymbol{r}_{i\neq j}$, as given by Eq. 1.7. **(b)** far-field interference. The field at position $\boldsymbol{R}$ is the sum of the fields emitted by the particles at $\boldsymbol{r_0}$ and $\boldsymbol{r}_j$. **(c)** near-field effects due to a dipole field $\boldsymbol{E}(\boldsymbol{r})$.

Near-field effects, as depicted with a dipole in Fig. 1.11(c), may be argued to alter the single particle scattering [127]. However, it is the local field $\boldsymbol{E}(\mathbf{r}_i)$ that is influenced by the presence of other particles, not the scattering operator $\overleftrightarrow{G}$. Therefore, in a strict sense, it can only play a role in combination with multiple scattering. For the imaginary part of the refractive index, the local field effects only play a role when the average distance between the particles is very small. Near-field effects only become relevant from volume fractions larger than 0.3 [128].

The near-field effects are described in the Green's function $\overleftrightarrow{G}(\boldsymbol{r})$ in Eq. 1.7, which, for dipole scattering, is given by

$$\overleftrightarrow{G}(\boldsymbol{r}) = \left[\left(3\hat{\boldsymbol{r}} \otimes \hat{\boldsymbol{r}} - \overleftrightarrow{I}\right)\left(\frac{1}{k^3 r^3} - \frac{i}{k^2 r^2}\right) \times \frac{1}{kr}(\hat{\boldsymbol{r}} \otimes \hat{\boldsymbol{r}} - \overleftrightarrow{I})\right] \exp(ikr). \tag{1.8}$$

Here, k is the wavenumber of the wave, $\otimes$ the dyadic outer product, and $\overleftrightarrow{I}$ the unit

dyadic. The terms that decay with $1/r$, are the same spherical waves that cause the far-field interference. The $1/r^2$ and $1/r^3$ terms correspond to the intermediate and near-field zones. Because the latter two decay much faster with distance, near-field effects are often small. Since the Mie solution for spherical particles can be expanded in a series of multipoles [129, 130], a similar reasoning for the near-field effects of Mie scatterers can be made.

In this thesis, *dependent scattering* is considered to be any nonlinear relation of the bulk optical properties of a scattering material with the volume fraction of scatterers, a definition also used by other authors [131]. This means that it includes multiple scattering, far-field interference, and near-field effects, i.e., all three mechanisms depicted in Fig. 1.11.

Another definition of dependent scattering is that the scattered power of a particle depends on the presence of near particles, which is distinct from multiple scattering [127]. This would only include near-field effects, as sketched in Fig. 1.11(c). This view has drawn some negative attention [123, 126], because the scattering of the particle itself does not change, only the local field that it scattered on the particle.

A third definition of dependent scattering is the dependence of optical properties on the correlations in particle positions [132]. This is virtually the same as the definition used in this thesis, because it is precisely these correlations that cause the nonlinear volume fraction dependence of the scattering. This definition leaves some ambiguity for strongly forward-scattering particles [133] or higher harmonic generation in disordered media [134, 135], but this is outside the scope of this thesis.

Multiple scattering of a coherent wave is present when higher-order terms of the Born series are needed to model the light propagation in a medium [126]. Whereas some authors consider dependent scattering as distinct from multiple scattering [127, 136], the consensus seems to be that multiple scattering is one of the causes of dependent scattering [123, 126]. Admittedly, this question is mostly semantic.

This leads to the question what 'independent scattering' is. According to Eq. 1.7, there is always some interaction if the number of particles in a system is larger than 1. Therefore, there is no such thing as fully independent scattering for coherent waves [126]. It depends on the level of accuracy that is needed whether a scattering process can be considered independent, and any volume fraction cutoff will be arbitrary.

1.5. THIS THESIS

Chapter 2 describes the experimental setup with which the optical parameters of transparent and turbid media were measured. The setup is a spectral Mach-Zehnder interferometer with a supercontinuum laser source. With this interferometer the group refractive index and group velocity dispersion (GVD) of water dilutions of ethanol and glycerol were measured in the wavelength range between 400 nm and 930 nm. In addition to these parameters, the scattering attenuation of water dilutions of Intralipid were measured. It was shown that the volume fraction of binary mixtures of both turbid and transparent media can be quantified.

In Chapter 3, the interferometer as described in Chapter 2 was used to measure the scattering attenuation, the group index and the GVD for various dilutions of 100 nm silica nanoparticles in water. It was found that, on top of the well known dependent scat-

tering effects in the scattering attenuation, there is a small and subtle volume fraction effect on the real part of the effective index of the medium as well. This effect can be properly described with a refractive index model that takes into account the spatial correlations of suspended particles.

In Chapter 4, a multi-parameter approach was used for the real-time in-line and in-flow measurement of the flow speed and particle size distribution for dilutions of monodisperse sodium silicate particles in water, and an Intralipid dilution with a particle size distribution that was gradually altered over time with an incremental addition of HCl. For this, the interferometer was changed such that a heterodyne DLS measurement could be made together with the transmission measurements as described in Chapters 2 and 3. Heterodyne DLS was used to measure the mean particle size, which was combined with the transmission spectrum and a model for the dependent Mie scattering to reconstruct the particle size distribution. These calculations required the volume fraction of the particles, which was obtained from the measured group index. The work in this Chapter demonstrates the feasibility of real-time multi-parameter sensing of flow speed, particle size, and volume fraction of flowing particle suspensions.

This thesis concludes with suggestions for future research on the bulk optical properties of scattering media, and the applicability of the effective medium theories used in this thesis for larger particles. In addition, ideas are proposed for signal and data processing techniques for multi-parameter flow sensing in both laboratory and industrial settings. Furthermore, considerations are given for the applicability and feasibility of the methods used in this thesis for both industrial applications and miniaturization.

REFERENCES

[1] M. Rössler, P. U. Huth, and M. A. Liauw, Process analytical technology (PAT) as a versatile tool for real-time monitoring and kinetic evaluation of photocatalytic reactions, *Reaction Chemistry & Engineering*, 5(10):1992–2002, 2020.

[2] D. J. Goodwin, S. Van Den Ban, M. Denham, and I. Barylski, Real time release testing of tablet content and content uniformity, *International Journal of Pharmaceutics*, 537(1-2): 183–192, 2018.

[3] L. X. Yu, G. Amidon, M. A. Khan, S. W. Hoag, J. Polli, G. Raju, and J. Woodcock, Understanding pharmaceutical quality by design, *The AAPS Journal*, 16:771–783, 2014.

[4] FDA, Guidance for industry, pat-a framework for innovative pharmaceutical development, manufacturing and quality assurance, *U.S. Department of Health and Human Services*, 2004.

[5] H. Wu, Z. Dong, H. Li, and M. Khan, An integrated process analytical technology (PAT) approach for pharmaceutical crystallization process understanding to ensure product quality and safety: FDA scientist's perspective, *Organic Process Research & Development*, 19(1):89–101, 2015.

[6] A. L. Pomerantsev and O. Y. Rodionova, Process analytical technology: a critical view of the chemometricians, *Journal of Chemometrics*, 26(6):299–310, 2012.

[7] L. L. Simon, H. Pataki, G. Marosi, F. Meemken, K. Hungerbühler, A. Baiker, S. Tummala, B. Glennon, M. Kuentz, G. Steele, *et al.*, Assessment of recent process analytical technology (PAT) trends: A multiauthor review, *Organic Process Research & Development*, 19(1):3–62, 2015.

[8] R. R. Panthi, A. L. Kelly, D. J. O'Callaghan, and J. J. Sheehan, Measurement of syneretic properties of rennet-induced curds and impact of factors such as concentration of milk: A review, *Trends in Food Science & Technology*, 91:530–540, 2019.

[9] C. D. Papageorgiou, C. Mitchell, J. L. Quon, M. Langston, S. Borg, F. Hicks, D. am Ende, and M. Breault, Development of a novel screening methodology for the assessment of the risk of particle size attrition during agitated drying, *Organic Process Research & Development*, 24 (2):242–254, 2020.

[10] C. B. Singh and D. S. Jayas, Optical sensors and online spectroscopy for automated quality and safety inspection of food products, In *Robotics and Automation in the Food Industry*, pages 111–129. Elsevier, 2013.

[11] M. I. Veríssimo, J. A. Gamelas, A. J. Fernandes, D. V. Evtuguin, and M. T. S. Gomes, A new formaldehyde optical sensor: Detecting milk adulteration, *Food Chemistry*, 318:126461, 2020.

[12] FDA, Guidance for industry, process validation: General principles and practices, *U.S. Department of Health and Human Services*, 2011.

[13] M. T. Dokucu, M.-J. Park, and F. J. Doyle, Reduced-order methodologies for feedback control of particle size distribution in semi-batch emulsion copolymerization, *Chemical Engineering Science*, 63(5):1230–1245, 2008, Control of Particulate Processes.

[14] R. Xalter and R. Mülhaupt, Online monitoring of polyolefin particle growth in catalytic olefin slurry polymerization by means of lasentec focused beam reflectance measurement (FBRM) and video microscopy (PVM) probes, *Macromolecular Reaction Engineering*, 4(1): 25–39, 2010.

[15] B. Freeland, R. McCann, P. O'Neill, S. Sreenilayam, M. Tiefenthaler, M. Dabros, M. Juillerat, G. Foley, and D. Brabazon, Real-time monitoring and control for high-efficiency autonomous laser fabrication of silicon nanoparticle colloids, *The International Journal of Advanced Manufacturing Technology*, 114:291–304, 2021.

[16] K. S. Y. Yeung, M. Hoare, N. F. Thornhill, T. Williams, and J. D. Vaghjiani, Near-infrared spectroscopy for bioprocess monitoring and control, *Biotechnology and Bioengineering*, 63(6): 684–693, 1999.

[17] Y. Xu, A. S. Jeevarajan, J. M. Fay, T. D. Taylor, and M. M. Anderson, On-line measurement of glucose in a rotating wall perfused vessel bioreactor using an amperometric glucose sensor, *Journal of The Electrochemical Society*, 149(4):H103, 2002.

[18] N. D. Lourenço, J. Lopes, C. Almeida, M. C. Sarraguça, and H. M. Pinheiro, Bioreactor monitoring with spectroscopy and chemometrics: a review, *Analytical and Bioanalytical Chemistry*, 404:1211–1237, 2012.

[19] J. Wiss, M. Länzlinger, and M. Wermuth, Safety improvement of a grignard reaction using on-line NIR monitoring, *Organic Process Research & Development*, 9(3):365–371, 2005.

[20] W. Chew and P. Sharratt, Trends in process analytical technology, *Analytical Methods*, 2(10): 1412–1438, 2010.

[21] J. Emmerich, Q. Tang, Y. Wang, P. Neubauer, S. Junne, and S. Maaß, Optical inline analysis and monitoring of particle size and shape distributions for multiple applications: Scientific and industrial relevance, *Chinese Journal of Chemical Engineering*, 27(2):257–277, 2019.

[22] B. Aernouts, E. Polshin, J. Lammertyn, and W. Saeys, Visible and near-infrared spectroscopic analysis of raw milk for cow health monitoring: reflectance or transmittance?, *Journal of Dairy Science*, 94(11):5315–5329, 2011.

[23] M. Tajammal Munir, W. Yu, B. R. Young, and D. I. Wilson, The current status of process analytical technologies in the dairy industry, *Trends in Food Science & Technology*, 43(2): 205–218, 2015.

[24] G. Rocchetti, S. Galimberti, M. L. Callegari, and L. Lucini, Metabolomics and proteomics approaches provide a better understanding of non-enzymatic browning and pink discoloration in dairy products: A mini review, *Food Bioscience*, 56:103328, 2023.

[25] B. Y. Shekunov, P. Chattopadhyay, H. H. Y. Tong, and A. H. L. Chow, Particle size analysis in pharmaceutics: principles, methods and applications, *Pharmaceutical Research*, 24:203–227, 2007.

[26] A. F. T. Silva, A. Burggraeve, Q. Denon, P. Van der Meeren, N. Sandler, T. Van Den Kerkhof, M. Hellings, C. Vervaet, J. P. Remon, J. A. Lopes, *et al.*, Particle sizing measurements in pharmaceutical applications: Comparison of in-process methods versus off-line methods, *European Journal of Pharmaceutics and Biopharmaceutics*, 85(3):1006–1018, 2013.

[27] H. Hsieh, D. J. Griffin, A. M. K. Nambiar, N. Sarkar, H. Youssef Ismail, K. Saigal, D. E. Shen, N. Goudas-Salomon, R. Wimalasinghe, A. Zeng, *et al.*, PAT-enabled automated feedforward control: An application to the continuous manufacture of apremilast, *Organic Process Research & Development*, 2024.

[28] P. D. Foote, Optics in the oil industry, *Journal of the Optical Society of America*, 42(12):886–897, 1952.

[29] B. W. Thomas, Process instrumentation, symposium introduction, *Industrial & Engineering Chemistry*, 46(7):1371–1373, 1954.

[30] R. F. Wall, Process control by refractive index, *Industrial & Engineering Chemistry*, 51(11): 69A–70A, 1959.

[31] G. Wilson, *Distillation column dynamics and control*, University of Canterbury. Chemical Engineering, 1979.

[32] L. R. Agnew, T. McGlone, H. P. Wheatcroft, A. Robertson, A. R. Parsons, and C. C. Wilson, Continuous crystallization of paracetamol (acetaminophen) form II: selective access to a metastable solid form, *Crystal Growth & Design*, 17(5):2418–2427, 2017.

[33] A. J. Alvarez and A. S. Myerson, Continuous plug flow crystallization of pharmaceutical compounds, *Crystal Growth & Design*, 10(5):2219–2228, 2010.

[34] S. S. Kadam, J. A. Vissers, M. Forgione, R. M. Geertman, P. J. Daudey, A. I. Stankiewicz, and H. J. Kramer, Rapid crystallization process development strategy from lab to industrial scale with PAT tools in skid configuration, *Organic Process Research & Development*, 16(5):769–780, 2012.

[35] A. Adamo, R. L. Beingessner, M. Behnam, J. Chen, T. F. Jamison, K. F. Jensen, J.-C. M. Monbaliu, A. S. Myerson, E. M. Revalor, D. R. Snead, *et al.*, On-demand continuous-flow production of pharmaceuticals in a compact, reconfigurable system, *Science*, 352(6281):61–67, 2016.

[36] N. C. Friggens, C. Ridder, and P. Løvendahl, On the use of milk composition measures to predict the energy balance of dairy cows, *Journal of Dairy Science*, 90(12):5453–5467, 2007.

[37] A. Gastélum-Barrios, G. M. Soto-Zarazúa, A. Escamilla-García, M. Toledano-Ayala, G. Macías-Bobadilla, and D. Jauregui-Vazquez, Optical methods based on ultraviolet, visible, and near-infrared spectra to estimate fat and protein in raw milk: A review, *Sensors*, 20 (12), 2020.

[38] L. Wiking, J. Stagsted, L. Björck, and J. H. Nielsen, Milk fat globule size is affected by fat production in dairy cows, *International Dairy Journal*, 14(10):909–913, 2004.

[39] C. Veenstra, A. Lenferink, W. Petersen, W. Steenbergen, and N. Bosschaart, Optical properties of human milk, *Biomedical Optics Express*, 10(8):4059–4074, 2019.

[40] P. C. Pericas, A. Sundararajan, R. Wiegerink, and J. C. Lötters, Towards in-flow monitoring of fat content and fluid composition of dairy milk using microfluidic confocal Raman spectroscopy, In *Microfluidics, BioMEMS, and Medical Microsystems XX*, volume 11955, pages 56–59. SPIE, 2022.

[41] N. Bosschaart, G. J. Edelman, and M. C. G. Aalders, A literature review and novel theoretical approach on the optical properties of whole blood, *Lasers in Medical Science*, 29:453–479, 2014.

[42] J. Trevathan, W. Read, and S. Schmidtke, Towards the development of an affordable and practical light attenuation turbidity sensor for remote near real-time aquatic monitoring, *Sensors*, 20(7), 2020.

[43] S. M. Bagherzadeh, B. Grajciar, C. K. Hitzenberger, M. Pircher, and A. F. Fercher, Dispersion-based optical coherence tomography OCT measurement of mixture concentrations, *Optics Letters*, 32(20):2924–2926, 2007.

[44] J. Chen, W. Guo, M. Xia, W. Li, and K. Yang, In situ measurement of seawater salinity with an optical refractometer based on total internal reflection method, *Optics Express*, 26(20): 25510–25523, 2018.

[45] A. K. Trull, J. van der Horst, J. G. Bijster, and J. Kalkman, Transmission optical coherence tomography based measurement of optical material properties, *Optics Express*, 23(26):33550–33563, 2015.

[46] S. K. Chamoli, S. C. Singh, and C. Guo, Design of extremely sensitive refractive index sensors in infrared for blood glucose detection, *IEEE Sensors Journal*, 20(9):4628–4634, 2020.

[47] R. H. Sagor, M. F. Hassan, A. A. Yaseer, E. Surid, and M. I. Ahmed, Highly sensitive refractive index sensor optimized for blood group sensing utilizing the Fano resonance, *Applied Nanoscience*, 11(2):521–534, 2021.

[48] Y. Park, T. Yamauchi, W. Choi, R. Dasari, and M. S. Feld, Spectroscopic phase microscopy for quantifying hemoglobin concentrations in intact red blood cells, *Optics Letters*, 34(23): 3668–3670, 2009.

[49] M. Mohammadi, Colloidal refractometry: meaning and measurement of refractive index for dispersions; the science that time forgot, *Advances in Colloid and Interface Science*, 62(1): 17–29, 1995.

[50] E. Abbe, *Neue Apparate zur Bestimmung des Brechungs-und Zerstreuungsvermögens fester und flüssiger Körper*, Mauke's Verlag, 1874.

[51] W. R. Calhoun, H. Maeta, S. Roy, L. M. Bali, and S. Bali, Sensitive real-time measurement of the refractive index and attenuation coefficient of milk and milk-cream mixtures, *Journal of Dairy Science*, 93(8):3497–3504, 2010.

[52] M. K. Dong, K. G. Goyal, B. Worth, S. Makkar, W. R. Calhoun III, L. M. Bali, and S. Bali, Accurate in situ measurement of complex refractive index and particle size in Intralipid emulsions, *Journal of Biomedical Optics*, 18(8):087003, 2013.

[53] H. Contreras-Tello and A. García-Valenzuela, Refractive index measurement of turbid media by transmission of backscattered light near the critical angle, *Applied Optics*, 53(21):4768–4778, 2014.

[54] E. Gutiérrez-Reyes, A. García-Valenzuela, and R. G. Barrera, Extension of Fresnel's formulas for turbid colloidal suspensions: A rigorous treatment, *Journal of Physical Chemistry B*, 118 (22):6015–6031, 2014.

[55] G. H. Meeten, Refractive index errors in the critical-angle and the brewster-angle methods applied to absorbing and heterogeneous materials, *Measurement Science and Technology*, 8 (7):728–733, 1997.

[56] H. Liu, J. Ye, K. Yang, M. Xia, W. Guo, and W. Li, Real part of refractive index measurement approach for absorbing liquid, *Applied Optics*, 54(19):6046–6052, 2015.

[57] C. Photiou and C. Pitris, Comparison of tissue dispersion measurement techniques based on optical coherence tomography, *Journal of Biomedical Optics*, 24(4):046003, 2019.

[58] S. Korposh, S. W. James, S.-W. Lee, and R. P. Tatam, Tapered optical fibre sensors: Current trends and future perspectives, *Sensors*, 19(10):2294, 2019.

[59] E. Wijaya, C. Lenaerts, S. Maricot, J. Hastanin, S. Habraken, J.-P. Vilcot, R. Boukherroub, and S. Szunerits, Surface plasmon resonance-based biosensors: From the development of

different spr structures to novel surface functionalization strategies, *Current Opinion in Solid State and Materials Science*, 15(5):208–224, 2011.

[60] Y. Xu, P. Bai, X. Zhou, Y. Akimov, C. E. Png, L.-K. Ang, W. Knoll, and L. Wu, Optical refractive index sensors with plasmonic and photonic structures: promising and inconvenient truth, *Advanced Optical Materials*, 7(9):1801433, 2019.

[61] I. Brice, K. Grundsteins, K. Draguns, A. Atvars, and J. Alnis, Whispering gallery mode resonator temperature compensation and refractive index sensing in glucose droplets, *Sensors*, 21(21):7184, 2021.

[62] A. Ksendzov and Y. Lin, Integrated optics ring-resonator sensors for protein detection, *Optics Letters*, 30(24):3344–3346, 2005.

[63] H.-Y. Lin, C.-H. Huang, G.-L. Cheng, N.-K. Chen, and H.-C. Chui, Tapered optical fiber sensor based on localized surface plasmon resonance, *Optics Express*, 20(19):21693–21701, 2012.

[64] C. Zhou, M. K. Hedayati, and A. Kristensen, Multifunctional waveguide interferometer sensor: simultaneous detection of refraction and absorption with size-exclusion function, *Optics Express*, 26(19):24372–24383, 2018.

[65] V. D. Nguyen, D. J. Faber, E. van der Pol, T. G. van Leeuwen, and J. Kalkman, Dependent and multiple scattering in transmission and backscattering optical coherence tomography, *Optics Express*, 21(24):29145–29156, 2013.

[66] J. van der Horst, A. K. Trull, and J. Kalkman, Deep-tissue label-free quantitative optical tomography, *Optica*, 7(12):1682–1689, 2020.

[67] R. Hussain, M. Alican Noyan, G. Woyessa, R. R. Retamal Marín, P. Antonio Martinez, F. M. Mahdi, V. Finazzi, T. A. Hazlehurst, T. N. Hunter, T. Coll, *et al.*, An ultra-compact particle size analyser using a cmos image sensor and machine learning, *Light: Science & Applications*, 9 (1):21, 2020.

[68] W. C. K. Poon, E. R. Weeks, and C. P. Royall, On measuring colloidal volume fractions, *Soft Matter*, 8(1):21–30, 2012.

[69] M. Rogošić, H. J. Mencer, and Z. Gomzi, Polydispersity index and molecular weight distributions of polymers, *European Polymer Journal*, 32(11):1337–1344, 1996.

[70] L. Arleth and J. S. Pedersen, Droplet polydispersity and shape fluctuations in AOT [bis (2-ethylhexyl) sulfosuccinate sodium salt] microemulsions studied by contrast variation small-angle neutron scattering, *Physical Review E*, 63(6):061406, 2001.

[71] M. J. W. Povey, Ultrasound particle sizing: A review, *Particuology*, 11(2):135–147, 2013.

[72] W. Zhang, Y. Hu, G. Choi, S. Liang, M. Liu, and W. Guan, Microfluidic multiple cross-correlated Coulter counter for improved particle size analysis, *Sensors and Actuators B: Chemical*, 296:126615, 2019.

[73] S. Mishra and R. Molinaro, Physics informed neural networks for simulating radiative transfer, *Journal of Quantitative Spectroscopy and Radiative Transfer*, 270:107705, 2021.

[74] A. R. Heath, P. D. Fawell, P. A. Bahri, and J. D. Swift, Estimating average particle size by focused beam reflectance measurement (FBRM), *Particle & Particle Systems Characterization: Measurement and Description of Particle Properties and Behavior in Powders and Other Disperse Systems*, 19(2):84–95, 2002.

[75] A. Cameirão, H. Le Ba, M. Darbouret, J.-M. Herri, J.-L. Peytavy, and P. Glénat, Chord length distributions interpretation using a polydispersed population: Modeling and experiments, *Journal of Crystal Growth*, 342(1):65–71, 2012.

[76] M. Muhaimin, A. Y. Chaerunisaa, and R. Bodmeier, Real-time particle size analysis using focused beam reflectance measurement as a process analytical technology tool for continuous microencapsulation process, *Scientific Reports*, 11(1):19390, 2021.

[77] S. J. Blott, D. J. Croft, K. Pye, S. E. Saye, and H. E. Wilson, Particle size analysis by laser diffraction, *Geological Society, London, Special Publications*, 232(1):63–73, 2004.

[78] D. J. Slotboom, R. H. Duurkens, K. Olieman, and G. B. Erkens, Static light scattering to characterize membrane proteins in detergent solution, *Methods*, 46(2):73–82, 2008.

[79] A. Wilms, R. Meier, and P. Kleinebudde, Development and evaluation of an in-line and on-line monitoring system for granule size distributions in continuous roll compaction/dry granulation based on laser diffraction, *Journal of Pharmaceutical Innovation*, 16:247–257, 2021.

[80] J. T. Butement, P. M. Holloway, J. A. Welsh, J. A. Holloway, N. A. Englyst, P. Horak, J. West, and J. S. Wilkinson, Monolithically-integrated cytometer for measuring particle diameter in the extracellular vesicle size range using multi-angle scattering, *Lab on a Chip*, 20:1267–1280, 2020.

[81] J. Agagliate, I. Lefering, and D. McKee, Forward modeling of inherent optical properties from flow cytometry estimates of particle size and refractive index, *Applied Optics*, 57(8): 1777–1788, 2018.

[82] J. Gross-Rother, M. Blech, E. Preis, U. Bakowsky, and P. Garidel, Particle detection and characterization for biopharmaceutical applications: Current principles of established and alternative techniques, *Pharmaceutics*, 12(11):1112, 2020.

[83] E. Meijering, O. Dzyubachyk, and I. Smal, Chapter nine - methods for cell and particle tracking, In P. Michael, editor, *Imaging and Spectroscopic Analysis of Living Cells*, volume 504 of *Methods in Enzymology*, pages 183–200. Academic Press, 2012.

[84] K. P. McComiskey and L. Tajber, Comparison of particle size methodology and assessment of nanoparticle tracking analysis (NTA) as a tool for live monitoring of crystallisation pathways, *European Journal of Pharmaceutics and Biopharmaceutics*, 130:314–326, 2018.

[85] M. A. Al-Khafaji, A. Gaál, A. Wacha, A. Bóta, and Z. Varga, Particle size distribution of bimodal silica nanoparticles: A comparison of different measurement techniques, *Materials*, 13(14):3101, 2020.

[86] S. Faez, Y. Lahini, S. Weidlich, R. F. Garmann, K. Wondraczek, M. Zeisberger, M. A. Schmidt, M. Orrit, and V. N. Manoharan, Fast, label-free tracking of single viruses and weakly scattering nanoparticles in a nanofluidic optical fiber, *ACS Nano*, 9(12):12349–12357, 2015.

[87] M. Nissen, R. Förster, T. Wieduwilt, A. Lorenz, S. Jiang, W. Hauswald, and M. A. Schmidt, Nanoparticle tracking in single-antiresonant-element fiber for high-precision size distribution analysis of mono-and polydisperse samples, *Small*, 18(38):2202024, 2022.

[88] C. Finder, M. Wohlgemuth, and C. Mayer, Analysis of particle size distribution by particle tracking, *Particle & Particle Systems Characterization: Measurement and Description of Particle Properties and Behavior in Powders and Other Disperse Systems*, 21(5):372–378, 2004.

[89] R. Pecora, Doppler shifts in light scattering from pure liquids and polymer solutions, *The Journal of Chemical Physics*, 40(6):1604–1614, 1964.

[90] R. Foord, E. Jakeman, C. Oliver, E. R. Pike, R. J. Blagrove, E. Wood, and A. R. Peacocke, Determination of diffusion coefficients of haemocyanin at low concentration by intensity fluctuation spectroscopy of scattered laser light, *Nature*, 227(5255):242–245, 1970.

[91] R. Besseling, M. Damen, J. Wijgergangs, M. Hermes, G. Wynia, and A. Gerich, New unique PAT method and instrument for real-time inline size characterization of concentrated, flowing nanosuspensions, *European Journal of Pharmaceutical Sciences*, 133:205–213, 2019.

[92] K. Cheishvili, R. Besseling, M. Hermes, and J. Kalkman, Wavenumber-dependent dynamic light scattering optical coherence tomography measurements of collective and self-diffusion, *Optics Express*, 32(11):19963–19983, 2024.

[93] F. R. A. Onofri, I. Rodriguez-Ruiz, and F. Lamadie, Microfluidic lab-on-a-chip characteriza-

tion of nano-to microparticles suspensions by light extinction spectrometry, *Optics Express*, 30(2):2981–2990, 2022.

[94] F. Ferri, A. Bassini, and E. Paganini, Modified version of the chahine algorithm to invert spectral extinction data for particle sizing, *Applied Optics*, 34(25):5829–5839, 1995.

[95] R. Philip-Chandy, P. J. Scully, and R. Morgan, The design, development and performance characteristics of a fibre optic drag-force flow sensor, *Measurement Science and Technology*, 11(3):N31, 2000.

[96] G. Gervinskas, D. J. Day, and S. Juodkazis, Optofluidic Fabry-Pérot sensor for water solutions at high flow rates, *Optical Materials Express*, 2(3):279–286, 2012.

[97] F. Ejeian, S. Azadi, A. Razmjou, Y. Orooji, A. Kottapalli, M. Ebrahimi Warkiani, and M. Asadnia, Design and applications of MEMS flow sensors: A review, *Sensors and Actuators A: Physical*, 295:483–502, 2019.

[98] R. E. Oosterbroek, T. S. J. Lammerink, J. W. Berenschot, G. J. M. Krijnen, M. C. Elwenspoek, and A. van den Berg, A micromachined pressure/flow-sensor, *Sensors and Actuators A: Physical*, 77(3):167–177, 1999.

[99] T. S. J. Lammerink, N. R. Tas, M. Elwenspoek, and J. H. J. Fluitman, Micro-liquid flow sensor, *Sensors and Actuators A: Physical*, 37-38:45–50, 1993, Proceedings of Eurosensors VI.

[100] S. Kim, T. Nam, and S. Park, Measurement of flow direction and velocity using a micromachined flow sensor, *Sensors and Actuators A: Physical*, 114(2):312–318, 2004, Selected papers from Transducers 03.

[101] M. Dijkstra, J. J. Van Baar, R. J. Wiegerink, T. S. J. Lammerink, J. H. De Boer, and G. J. M. Krijnen, Artificial sensory hairs based on the flow sensitive receptor hairs of crickets, *Journal of Micromechanics and Microengineering*, 15(7):S132, 2005.

[102] D. Alveringh, R. J. Wiegerink, and J. C. Lötters, Integrated pressure sensing using capacitive Coriolis mass flow sensors, *Journal of Microelectromechanical Systems*, 26(3):653–661, 2017.

[103] A. C. De Oliveira, T. V. P. Schut, J. Groenesteijn, Q. Fan, R. J. Wiegerink, and K. A. A. Makinwa, A MEMS Coriolis mass flow sensing system with combined drive and sense interface, In *2019 IEEE SENSORS*, pages 1–4. IEEE, 2019.

[104] C. E. Willert and M. Gharib, Digital particle image velocimetry, *Experiments in Fluids*, 10(4): 181–193, 1991.

[105] V. Rajan, B. Varghese, T. G. van Leeuwen, and W. Steenbergen, Review of methodological developments in laser Doppler flowmetry, *Lasers in Medical Science*, 24:269–283, 2009.

[106] J. Kalkman, A. V. Bykov, D. J. Faber, and T. G. van Leeuwen, Multiple and dependent scattering effects in Doppler optical coherence tomography, *Optics Express*, 18(4):3883–3892, 2010.

[107] K. Cheishvili and J. Kalkman, Sub-diffusion flow velocimetry with number fluctuation optical coherence tomography, *Optics Express*, 31(3):3755–3773, 2023.

[108] K. Cheishvili and J. Kalkman, Scanning dynamic light scattering optical coherence tomography for measurement of high omnidirectional flow velocities, *Optics Express*, 30(13):23382–23397, 2022.

[109] L. Han, B. Tan, L. Schmetterer, and K. Bizheva, Localized transverse flow measurement with dynamic light scattering line-scan OCT, *Biomedical Optics Express*, 14(2):883–905, 2023.

[110] B. K. Huang and M. A. Choma, Resolving directional ambiguity in dynamic light scattering-based transverse motion velocimetry in optical coherence tomography, *Optics Letters*, 39 (3):521–524, 2014.

[111] N. Uribe-Patarroyo and B. E. Bouma, Velocity gradients in spatially resolved laser Doppler flowmetry and dynamic light scattering with confocal and coherence gating, *Physical Review E*, 94(2):022604, 2016.

[112] O. S. Agimelen, P. Hamilton, I. Haley, A. Nordon, M. Vasile, J. Sefcik, and A. J. Mulholland, Estimation of particle size distribution and aspect ratio of non-spherical particles from chord length distribution, *Chemical Engineering Science*, 123:629–640, 2015.

[113] M. Kempkes, J. Eggers, and M. Mazzotti, Measurement of particle size and shape by FBRM and in situ microscopy, *Chemical Engineering Science*, 63(19):4656–4675, 2008.

[114] C. Ferreira, J. Cardona, O. Agimelen, C. Tachtatzis, I. Andonovic, J. Sefcik, and Y.-C. Chen, Quantification of particle size and concentration using in-line techniques and multivariate analysis, *Powder Technology*, 376:1–11, 2020.

[115] J. Lambert, *Photometria sive de mensura et gradibus luminis, colorum et umbrae*, Sumptibus viduae Eberhardi Klett, typis Christophori Petri Detleffsen, 1760.

[116] A. Beer, Bestimmung der Absorption des rothen Lichts in farbigen Flüssigkeiten, *Annalen der Physik*, 162(5):78–88, 1852.

[117] N. Weiss, T. G. van Leeuwen, and J. Kalkman, Localized measurement of longitudinal and transverse flow velocities in colloidal suspensions using optical coherence tomography, *Physical Review E*, 88:042312, 2013.

[118] G. G. Stokes, On the effect of the internal friction of fluids on the motion of pendulums, *Transactions of the Cambridge Philosophical Society*, 9:8, 1851.

[119] W. Sutherland, A dynamical theory of diffusion for non-electrolytes and the molecular mass of albumin, *The London, Edinburgh, and Dublin Philosophical Magazine and Journal of Science*, 9(54):781–785, 1905.

[120] A. Einstein, Über die von der molekularkinetischen Theorie der Wärme geforderte Bewegung von in ruhenden Flüssigkeiten suspendierten Teilchen, *Annalen der Physik*, 4:549–560, 1905.

[121] J. V. Boussinesq, Mémoire sur l'influence desfrottements dans les mouvements réguliers des fluides, *Journal de Mathématiques pures et Appliquées*, 13(2):377–424, 1868.

[122] M. I. Mishchenko, Multiple scattering, radiative transfer, and weak localization in discrete random media: unified microphysical approach, *Reviews of Geophysics*, 46(2), 2008.

[123] J. Auger and B. Stout, Dependent light scattering in white paint films: clarification and application of the theoretical concepts, *Journal of Coatings Technology and Research*, 9: 287–295, 2012.

[124] S. Fitzwater and J. W. Hook III, Response to "Dependent light scattering in white paint films: clarification and application of the theoretical concepts"[Auger, JC., Stout, B., J. Coat. Technol. Res., DOI 10.1007/s11998-011-9731-9], *Journal of Coatings Technology and Research*, 10 (6):923–927, 2013.

[125] J. Auger and B. Stout, Discussion on dependent light scattering phenomenon in white paint films, *Journal of Coatings Technology and Research*, 10:929–931, 2013.

[126] M. I. Mishchenko, Independent and dependent scattering by particles in a multi-particle group, *OSA Continuum*, 1(1):243–260, 2018.

[127] S. Fitzwater and J. W. Hook III, Dependent scattering theory: a new approach to predicting scattering in paints, *JCT, Journal of Coatings Technology*, 57(721):39–47, 1985.

[128] V. P. Tishkovets, E. V. Petrova, and M. I. Mishchenko, Scattering of electromagnetic waves by ensembles of particles and discrete random media, *Journal of Quantitative Spectroscopy and Radiative Transfer*, 112(13):2095–2127, 2011.

[129] W. T. Doyle, The Clausius-Mossotti problem for cubic arrays of spheres, *Journal of Applied Physics*, 49(2):795–797, 1978.

[130] T. Liu, R. Xu, P. Yu, Z. Wang, and J. Takahara, Multipole and multimode engineering in Mie resonance-based metastructures, *Nanophotonics*, 9(5):1115–1137, 2020.

[131] A. García-Valenzuela, A. Acevedo-Barrera, O. Vázquez-Estrada, A. Nahmad-Rohen, and R. G. Barrera, Full dynamic corrections to the Maxwell Garnett mixing formula and correspond-

ing extensions beyond the dipolar approximation, *Journal of Quantitative Spectroscopy and Radiative Transfer*, 302:108578, 2023.

[132] H. C. van de Hulst, *Light Scattering by Small Particles*, Dover Books on Physics. Dover Publications, 1981, ISBN 9780486642284.

[133] A. Nahmad-Rohen and A. García-Valenzuela, Multiple-scattering model for the effective refractive index of dense suspensions of forward-scattering particles, *Journal of the Optical Society of America A*, 40(8):1552–1562, 2023.

[134] E. V. Makeev and S. E. Skipetrov, Second harmonic generation in suspensions of spherical particles, *Optics Communications*, 224(1-3):139–147, 2003.

[135] S. Faez, P. M. Johnson, D. A. Mazurenko, and A. Lagendijk, Experimental observation of second-harmonic generation and diffusion inside random media, *Journal of the Optical Society of America B*, 26(2):235–243, 2009.

[136] B. L. Drolen and C. L. Tien, Independent and dependent scattering in packed-sphere systems, *Journal of Thermophysics and Heat Transfer*, 1(1):63–68, 1987.

2

MEASURING OPTICAL PROPERTIES OF CLEAR AND TURBID MEDIA WITH BROADBAND SPECTRAL INTERFEROMETRY

The group index (n_g), group velocity dispersion (GVD), and the scattering attenuation coefficient μ_{sca} were measured for dilutions of glycerol, ethanol and Intralipid 20% with water. The experiments were performed with a supercontinuum laser based Mach-Zehnder spectroscopic interferometric setup for wavelengths between 400 *nm and* 930 *nm. All optical properties could be retrieved from a single calibrated measurement of the interference spectrum. The scattering attenuation was determined from the envelope of the interference. The group index and the GVD were retrieved from the unwrapped spectral phase. It was found that the group indices of glycerol and ethanol dilutions are in accordance with the Lorentz-Lorenz mixing formula. The scattering attenuation matches well to a semi-empirical model based on the Twerksy effective packing fraction.*

2.1. INTRODUCTION

Optical characterization of liquids has been done for centuries [2] and is used for studying both fluid dynamic processes and fluid composition. The non-invasive nature of light makes it particularly suitable for sensing fluid optical properties such as the attenuation, caused by both absorption and scattering, and the refractive index. Measurement of the attenuation coefficient is, among others, used for characterization of human milk [3], blood [4], or quality control of water [5] or dairy products [6]. Likewise, refractive index sensing can provide valuable information about a sample, for example

Parts of this chapter have been published in P.N.A. Speets and J. Kalkman, *Measuring optical properties of clear and turbid media with broadband spectral interferometry*, Applied Optics, 62, 4349-4358 (2023).[1]

to distinguish blood groups [7], or to measure glucose content [8] or water salinity [9]. The dispersion of the refractive index can be considered as valuable additional information. Similar to the refractive index itself, it was used to determine the concentration of glucose [10, 11], salinity [10], or the amount of hemoglobin in red blood cells [12].

An established technique to measure the attenuation coefficient of a sample is by means of double integrating spheres [6, 13]. Although this can be used for spectral attenuation measurements, measurement of the refractive index of the sample is not possible since all path length information is lost with this technique. In turn, very sensitive techniques to measure the refractive index are by means of tapered optical fibers [14] or microresonators [15, 16]. An advantage of these sensors is that they can be functionalized for high specificity [14, 17]. However, these techniques are not compatible with a simultaneous measurement of the attenuation coefficient.

An old, but widely used, technique to measure the refractive index is by measurement of the critical or the Brewster angle. With this method, it is possible to simultaneously determine the refractive index and the attenuation coefficient [18–20]. For these methods, the scattering needs to be taken into account in the Fresnel equations [21]. However, the critical angle can be difficult to accurately determine for absorbing or strongly scattering media [22, 23]. In addition, the maximum refractive index that can be measured is limited by the refractive index of the prism or half cylinder that is used in the measurement. Moreover, multiple wavelengths cannot be measured simultaneously and need to be measured consecutively.

The attenuation coefficient and refractive index can also be measured with optical coherence tomography (OCT). In the case of reflection OCT, the signal attenuation coefficient of the sample can be fitted to the exponential decay of the intensity with respect to the optical path length [4, 24–27]. The dispersion of the refractive index can be obtained with reflection OCT by fitting the phase to the PSF of a strong reflector or speckle [28]. A second method to measure the refractive properties with reflection OCT is with the spatial displacement between the Fourier transform of different parts of the measured spectrum [29]. Obviously, the need for backscattering requires a turbid medium and is not applicable to transparent samples.

With transmission OCT the attenuation coefficient, group index, and GVD can be measured simultaneously. If the intensity of both arms of the interferometer is measured separately, the attenuation coefficient can be measured straightforwardly from the transmission. The transmittance of a sample can also be measured from the height of the optical path length (OPL) peak [11] or with a low pass filter on the interference signal [30]. The group index and the GVD are obtained from the phase of the interference signal [11, 31]. The combined measurement of attenuation and group index can even be spatially mapped in 3D [32].

In this work, we applied broadband transmission OCT to simultaneously measure the wavelength dependence of the group index n_g, GVD, and the optical attenuation of clear fluids and turbid media in a single shot. The large bandwidth allows for a highly accurate determination of n_g and GVD. This setup was used to measure the group index and GVD of glycerol, ethanol, and Intralipid at different concentrations. In addition, the scattering coefficient of suspensions of Intralipid 20% dilutions was measured. The refractive index and attenuation coefficient were compared to models based on literature

values of the fluid components.

2.2. THEORY

2.2.1. THE INTERFEROMETRIC SIGNAL

To obtain both amplitude and phase information we use spectral interferometry, as schematically shown in Fig. 2.1. The light from the source, with wavenumber $k = 2\pi/\lambda$ and spectral density $S(k)$, passes a beam splitter with intensity splitting ratio α. We assume ballistic light interaction with the sample. Hence, the intensity in the sample is exponentially attenuated by absorption, characterized by $\mu_a(k)$, and scattering, characterized by $\mu_s(k)$ over a length L. The phase of the signal is determined by the refractive index $n(k)$ of the sample. The intensity as measured with the spectrometer $I_{\text{tot}}(k)$ can be considered as the sum of the intensity of the sample arm $I_{\text{sam}}(k)$, the reference arm $I_{\text{ref}}(k)$ and the interference $I_{\text{int}}(k)$

$$I_{\text{tot}}(k) = I_{\text{sam}}(k) + I_{\text{ref}}(k) + I_{\text{int}}(k)\,. \tag{2.1}$$

The light through the sample is recombined with the reference by a second beam splitter with intensity splitting ratio α. Assuming negligible absorption, the detected field from the sample arm is

$$E_{\text{sam}}(k) = \sqrt{S(k)}\sqrt{\alpha(1-\alpha)}\,\mathrm{e}^{-\frac{1}{2}\mu_s(k)L}\mathrm{e}^{in(k)kL}\,. \tag{2.2}$$

With the reference field propagating in air, i.e., $n = 1$, the detected field from the reference arm is

$$E_{\text{ref}}(k) = \sqrt{S(k)}\sqrt{(1-\alpha)\alpha}\,\mathrm{e}^{ik\delta}\,. \tag{2.3}$$

Here δ is the difference in path length in air between the sample arm and the reference arm. Combining Equation 2.2 and 2.3 and removing the constant intensities results in the interference intensity

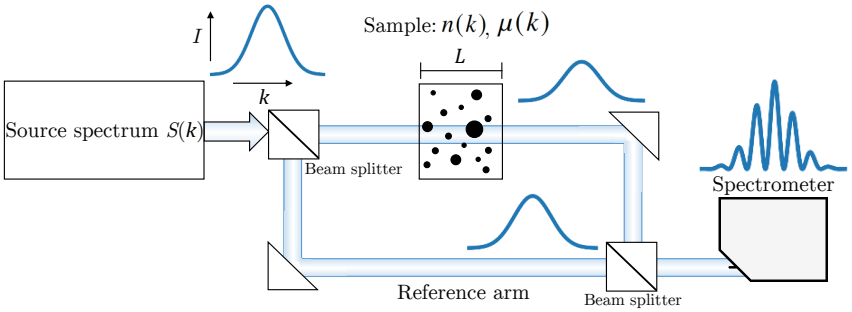

Figure 2.1: Schematic overview of the spectral interferometric setup. Light from a broadband source is split into a reference arm and a sample arm. The amplitude through the sample arm is attenuated by the sample. The phase of the light through the sample arm is delayed by the refractive index of the sample.

$$I_{\text{int}}(k) = 2S(k)\alpha(1-\alpha)\,\mathrm{e}^{-\frac{1}{2}\mu_s(k)L}\cos\left(k\delta - n(k)kL\right). \tag{2.4}$$

The cosine part of the interference term of Eq. (2.4) consists of a phase delay due to the refractive index of the sample and a constant phase offset given by the path length difference δ. The optical path length distribution of the transmitted light is given by the inverse Fourier transform of the interference intensity.

The phase of the cosine term $\phi = (k\delta - n(k)kL)$ varies with k and can be obtained from the interference intensity using a Hilbert transform, denoted by $\mathscr{H}$. The Hilbert transform rotates the Fourier transform of the signal with $-\frac{1}{2}\pi$ in the complex plane and inverts the sign of the negative frequencies. This transforms the cosine term in a sine term. The complex-valued interference spectrum $\tilde{I}_{\text{int}}(k)$ can then be obtained by combining Eq. 2.4 with the Hilbert transform as

$$\tilde{I}_{\text{int}}(k) = I_{\text{int}}(k) + i\mathscr{H}\{I_{\text{int}}(k)\}. \tag{2.5}$$

The phase $\phi(k)$ of the interference is then obtained from the Eq. 2.5 in the conventional way as

$$\phi(k) = \arctan\left(\frac{\mathrm{Im}\{\tilde{I}_{\text{int}}(k)\}}{\mathrm{Re}\{\tilde{I}_{\text{int}}(k)\}}\right). \tag{2.6}$$

Similarly, the envelope of the interference spectrum can be calculated with the absolute value of Eq. 2.5. The intensity transmittance with respect to a calibration sample can be obtained by taking the ratio of the envelopes of the interference signal. This is given by

$$T(k) = \frac{\left|\tilde{I}^{\text{sam}}_{\text{int}}(k)\right|^2}{\left|\tilde{I}^{\text{cal}}_{\text{int}}(k)\right|^2}. \tag{2.7}$$

Here $T(k)$ is the transmittance of the sample, $\tilde{I}^{\text{sam}}_{\text{int}}(k)$ and $\tilde{I}^{\text{cal}}_{\text{int}}(k)$ the complex interference spectrum of the sample of interest and the spectrum of a calibration sample. The attenuation follows from $T(k) = \exp(-\mu(k)L)$.

2.2.2. PARAMETRIZATION OF THE REFRACTIVE INDEX

In the visible and near infrared regions that are far from molecular absorption peaks, the refractive index $n(k)$ is well described by the Cauchy equation[33]. This is a polynomial parametrization that is monotonically decreasing with wavelength. With the Cauchy equation the interferometric phase is given by

$$\phi(k) = n(k)Lk + 2\pi N = \sum_m \phi_m k^m, \tag{2.8}$$

with N the number of full wavelengths λ that fit into the distance L and ϕ_m a set of empirical parameters. The phase $\phi(k)$ is used to calculate the group index n_g by

$$n_g = n + k\frac{dn}{dk} = L^{-1}\frac{d\phi}{dk} \tag{2.9}$$

and the GVD

$$GVD = \frac{2}{c^2}\frac{d\,n(k)}{dk} + \frac{k}{c^2}\frac{d^2 n(k)}{dk^2} = \frac{1}{Lc^2}\frac{d^2\phi(k)}{dk^2}\,, \tag{2.10}$$

with c the speed of light in vacuum. Therefore, when the phase $\phi(k)$ is determined from the complex-valued interference signal of Eq. 2.4, the group refractive index and GVD of the sample can be determined.

2.2.3. THE REFRACTIVE INDEX OF MOLECULAR MIXTURES

The refractive index of a mixture of molecular components is, for many mixtures, well approximated by the Arago-Biot equation [34]. For a two-component mixture the Arago-Biot approximation for the refractive index of the mixture is

$$n_{\text{mix}}(k) = f_v\, n_1(k) + (1 - f_v)\, n_2(k)\,, \tag{2.11}$$

with f_v the volume fraction of the solute and $n_1(k)$ and $n_2(k)$ the refractive indices of component 1 and 2, respectively. The Arago-Biot equation holds well for mixtures where the mass density of the mixture is the volume-weighted average of the two components. For mixtures where the mass density ρ_{mix} depends non-linearly on the volume fraction f_v, e.g., due to strong inter-molecular interactions, an improved model is the Lorentz-Lorenz mixing formula [35, 36]. The Lorentz-Lorenz model for the refractive index can be derived by considering the medium as a collection of coupled dipole oscillators.

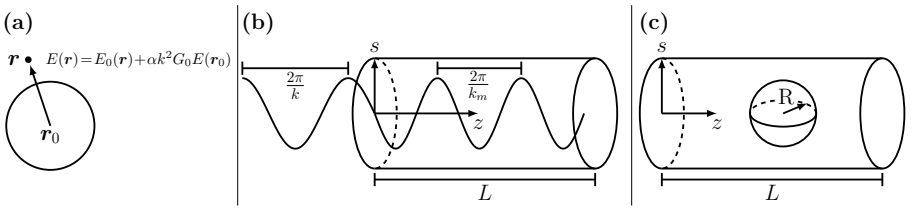

Figure 2.2: (**a**) A sketch of a dipole and the field at position $\boldsymbol{r}$ given by Eq. 2.12. (**b**) Sketch of a wave inside a cylinder. Outside the cylinder the wavenumber is given by k, and inside the wavenumber is $k_m = nk$. (**c**) A sphere with radius R inside a cylinder for the substitution in Eq. 2.17.

When a dipole at position $\boldsymbol{r}_0$ with polarizability α is driven by an oscillating external field $\boldsymbol{E}_0(\boldsymbol{r})$, the dipole radiates a wave with the same frequency. Dropping the polarization and time dependence, the resulting field $E(\boldsymbol{r})$ is given by [37]

$$E(\boldsymbol{r}) = E_0(\boldsymbol{r}) + \alpha k^2 G_0 E(\boldsymbol{r}_0)\,, \tag{2.12}$$

where G_0 is the Green's function. For large distances from the dipole, the wave scattered from the dipole can be considered as a spherical wave. In this case, the Green's function is

$$G_0(\boldsymbol{r} - \boldsymbol{r}_0) = \frac{e^{ik|\boldsymbol{r}-\boldsymbol{r}_0|}}{|\boldsymbol{r} - \boldsymbol{r}_0|}\,. \tag{2.13}$$

Equations 2.12 and 2.13 are schematically illustrated in Fig. 2.2(a). To describe a medium with a constant dipole density ρ, Eq. 2.12 is averaged over the medium and the total field is the integral over the volume V

$$E(\boldsymbol{r}) = E_0(\boldsymbol{r}) + \alpha\rho k^2 \int_V G_0(\boldsymbol{r}-\boldsymbol{r}')E(\boldsymbol{r}')\,\mathrm{d}\boldsymbol{r}'. \tag{2.14}$$

Here, the field inside the medium E appears on both sides of the integral and hence Eq. 2.14 is difficult to solve. Since we consider the solutions to be plane waves inside the dielectric material, we consider an infinitely wide cylindrical slab of dielectric material of length L. This is sketched in Fig. 2.2(b). The external driving field E_0 is a plane wave given by $A_0 e^{ikz}$. We can write the field inside the medium as a superposition of two counterpropagating waves in the axial direction z [38]:

$$E(z) = A^+ e^{ik_m z} + A^- e^{-ik_m z}. \tag{2.15}$$

Here $A^\pm$ are the amplitudes of the forward and backward traveling waves and the wavenumber $k_m = nk$ is the resultant wavenumber in the medium given by the superposition of all the scattered waves in the medium. The resulting integral equation in cylindrical coordinates is given by

$$A^+ e^{ik_m z} + A^- e^{-ik_m z} = A_0 e^{ikz} + \alpha\rho k^2 \int_0^L \int_0^\infty \int_0^{2\pi} \left(A^+ e^{ik_m z'} + A^- e^{-ik_m z'}\right) \frac{e^{ikR}}{R}\, s\,\mathrm{d}\theta\,\mathrm{d}s\,\mathrm{d}z'. \tag{2.16}$$

Here s the radial coordinate, R is the distance between a point z on the z-axis and a point in the medium given by $R = \sqrt{s^2 + (z'-z)^2}$, as shown in Fig. 2.2(c). The integral equation Eq. 2.16 has no valid solution. However, since $R > |z'-z|$, the fraction s/R can be expanded as

$$\frac{s}{R} = \sqrt{1 - \frac{(z-z')^2}{R^2}} = 1 - \frac{1}{2}\frac{(z'-z)^2}{R^2} + O\left(\frac{(z'-z)^4}{R^4}\right) \approx 1. \tag{2.17}$$

By keeping only the first term, which is unity, this approximation fully eliminates the dependence on s and R outside the exponent. Changing the integral limits of the integral over z with $L \to \infty$ will not change the calculated refractive index at the end of the calculation, but it simplifies the calculation. After substituting $\mathrm{d}s \to \mathrm{d}R$ and changing corresponding integral bounds, the integral on the right hand side of Eq. 2.16 is then given by

$$\alpha\rho k^2 \int_0^\infty \int_{|z'-z|}^\infty \int_0^{2\pi} \left(A^+ e^{ik_m z'} + A^- e^{-ik_m z'}\right) e^{ikR}\,\mathrm{d}\theta\,\mathrm{d}R\,\mathrm{d}z'. \tag{2.18}$$

After evaluation of this integral, Eq. 2.16 can be written as

$$\frac{2\pi\alpha\rho k^2}{(k_m-k)(k_m+k)} \left(2kA^+ e^{ik_m z} + 2kA^- e^{-ik_m z} - \left(A^-(k-k_m) + A^+(k+k_m)\right) e^{ikz}\right) = A^+ e^{ik_m z} + A^- e^{-ik_m z} - A_0 e^{ikz}. \tag{2.19}$$

Since Eq. 2.19 must be valid for all z, the amplitudes of the same exponents can be equated which relates the amplitudes $A^\pm$ to the amplitude of the driving field A_0. The amplitude of the exponent e^{ikz} on the left-hand side must be equal to the amplitude of

the exponent e^{ikz} on the right-hand side of Eq. 2.19. This means that the driving field $A_0 e^{ikz}$ is fully dampened with the field

$$A_0 e^{ikz} = \frac{2\pi\alpha\rho k^2 e^{ikz}}{(k_m - k)(k_m - k)} \left(A^+(k + k_m) - A^-(k - k_m)\right) e^{ikz}. \tag{2.20}$$

The driving field with frequency k is fully attenuated in the medium, as described by the Ewald-Oseen extinction theorem. This theorem was already tacitly assumed in the ansatz given by Eq. 2.15. Here, it was assumed that there exists a meaningful refractive index, and the wavenumber of the wave traveling through the medium is given by k_m. Therefore, there is no ballistic light with speed c, but the speed of the resultant wave of the superposition of all scattered light waves $A^{\pm} e^{\pm ik_m z}$ is given by c/n.

Reaping the amplitudes of the exponents $e^{ik_m z}$ together gives the fraction of the amplitudes of the forward and backward propagating waves A^+/A^-. Equating all amplitudes by setting $z = 0$, and using the relations obtained above for the terms with e^{ikz} and $e^{\pm ik_m z}$, the polarizability α can be expressed as

$$4\pi\alpha\rho = n^2 - 1. \tag{2.21}$$

Interestingly, this relation leads to the Sellmeier-Drude mixing formula [39, 40], also known as the Newton mixing formula [41–43].

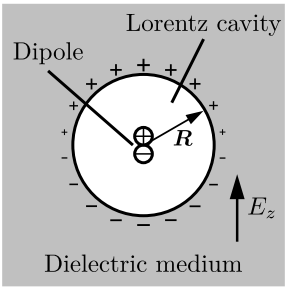

Figure 2.3: Example of a Lorentz cavity. The surface charge is induced by the driving field E_z.

In order to obtain the Lorentz-Lorenz equation, the finite size of the molecules must be considered [44–46]. An example of a finite dipole is shown in Fig. 2.3. The molecule is modeled as a single dipole in an empty sphere, called the Lorentz cavity. When this cavity is placed into an electric field, such as the field of a light wave, the dipoles in the medium align with the applied field. This creases a small surface charge σ_p on the inside of the cavity. When the size of the dipole is small compared to the wavelength, the driving field is assumed to be constant over the diameter of the cavity, and this surface charge is given by $\sigma_p = \alpha\rho \boldsymbol{E}\cdot\hat{\boldsymbol{n}}$ with $\hat{\boldsymbol{n}}$ the unit normal vector to the surface of the cavity. The field of this surface charge at the center of the cavity E_{LC} is given by [45]

$$\begin{aligned} E_{LC}(z) &= \int_S \frac{\sigma_p(\boldsymbol{R})}{|\boldsymbol{R}|^4}\,\mathrm{d}S = 2\pi\alpha\rho E(z)\int_0^{\pi}\cos^2(\theta)\sin(\theta)\,\mathrm{d}\theta \\ &= \frac{4\pi}{3}\alpha\rho E(z) = \frac{4\pi}{3}\alpha\rho\left(A^+ e^{ik_m z} + A^- e^{-ik_m z}\right). \end{aligned} \tag{2.22}$$

Here, $\boldsymbol{R}$ is a position on the surface of the sphere, and S the surface of the sphere. We can add the effect of this local field $E_{\mathrm{LC}}(z)$ to Eq. 2.16 as

$$E(z) = E_0(z) + \alpha\rho k^2 \int_V G_0 E(\boldsymbol{r})\,\mathrm{d}\boldsymbol{r} + E_{\mathrm{LC}}(z)\,, \tag{2.23}$$

where the first three terms are the same as Eq. 2.16, and reaping the amplitudes together in a similar procedure as described above, the polarizability is given by the Lorentz-Lorenz equation:

$$\alpha\rho = \frac{3(n^2-1)}{4\pi(n^2+2)}\,. \tag{2.24}$$

The Lorentz-Lorenz mixing formula can be calculated by solving Eq. 2.24 for a binary mixture. This results in

$$\frac{n^2_{\mathrm{mix}}(k)-1}{n^2_{\mathrm{mix}}(k)+2}\,\frac{f_v\rho_1+(1-f_v)\rho_2}{\rho_{\mathrm{mix}}(f_v)} = f_v\,\frac{n_1^2(k)-1}{n_1^2(k)+2} + (1-f_v)\,\frac{n_2^2(k)-1}{n_2^2(k)+2}\,. \tag{2.25}$$

Here, $n_{\mathrm{mix}}(k)$ is the refractive index of the mixture, ρ_1 and ρ_2 are the mass densities of components 1 and 2, respectively. The Lorentz-Lorenz mixing formula explicitly incorporates the mass density of the mixture $\rho_{\mathrm{mix}}(f_v)$, which may non-linearly depend on the volume fraction f_v.

2.2.4. THE ATTENUATION COEFFICIENT OF A SCATTERING MEDIUM

For suspensions with a wide particle size distribution, e.g., Intralipid, the wavelength dependence of the scattering coefficient of Intralipid can be described with a power law [47]

$$\mu_s = A\lambda^{-\alpha}\,, \tag{2.26}$$

with A a proportionality constant, λ the wavelength and α an empirical parameter. For particles in the Rayleigh regime, $\alpha = 4$.

Dependent scattering effects on the attenuation coefficient can be modelled with the Twersky effective packing fraction W [48, 49], which is defined as

$$W = f_v\left(\frac{(1-f_v)^{p+1}}{1+f_v(p-1)^{p-1}}\right), \tag{2.27}$$

with p the packing dimension, which is exactly 3 for monodisperse hard sphere particles. The packing dimension decreases for particles that can be packed more efficiently than hard spheres. Therefore, it is expected that $p < 3$ for anisotropic particles or polydisperse particle size distributions. The dependent scattering coefficient can be modeled with the effective packing fraction as

$$\mu_s(\lambda) = A\lambda^{-\alpha}W = A\lambda^{-\alpha}f_v\left(\frac{(1-f_v)^{p+1}}{1+f_v(p-1)^{p-1}}\right). \tag{2.28}$$

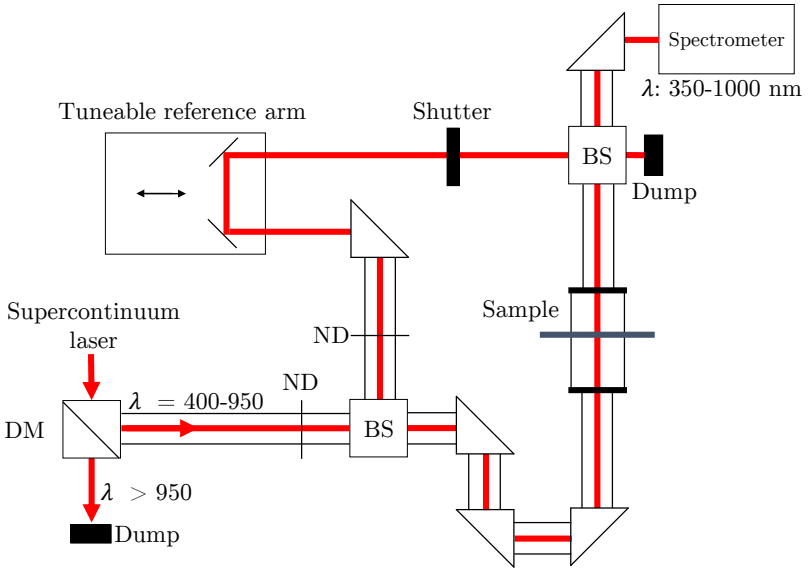

Figure 2.4: Overview of the broadband spectral interferometry setup. DM, BS, ND indicate the dichroic mirror, the beam splitter and the neutral density filter, respectively.

2.3. METHODS AND MATERIALS

2.3.1. EXPERIMENTAL SETUP

A schematic of the experimental setup is shown in Fig. 2.4. The light source is a supercontinuum laser (EVO EUL-10, NKT) that has a collimator at the end of its fiber. The laser is operated at maximum power to emit the light with optimal stability and to obtain the maximum spectral bandwidth. The infrared part of the light is filtered from the spectrum by a dichroic mirror (DMLP950, Thorlabs) that reflects wavelengths between 400 nm and 950 nm. The light within the visible wavelength band is attenuated by two neutral density filters (ND4A and ND10A, Thorlabs). Subsequently, the light is split into the reference arm and the sample arm by a 50-50 beam splitter (BS013, Thorlabs) for the glycerol and ethanol measurements and a 10-90 beamsplitter (BS025, Thorlabs) for the Intralipid measurements, directing more power to the sample to compensate for the lower transmittance. The collimated beam passes through the sample without any focusing.

In the reference arm, a neutral density filter (NDC-100C-4M, Thorlabs) is placed, but set to the transparent area for the glycerol and ethanol measurements. For the Intralipid measurements, the filter wheel was set such that the intensity of the reference arm was close to the intensity of the light transmitted through the sample. The light is recombined with a 50-50 beam splitter (BS013, Thorlabs). The recombined beam passes through an iris (SM05D5D, Thorlabs) set at the smallest diameter of 0.7 mm. The spectrum is measured with a 2046 pixel spectrometer (FX VIS-NIR, Ocean Optics). When feasible, the optical components were connected with a cage system. The system was

enclosed in a shielded environment to avoid air current variations and ensure safe operation.

2.3.2. SAMPLE PREPARATION AND METHODS

A cuvette with an inner width of 500 µm (106-0.50-40, Hellma) was used for the measurements with the glycerol dilutions. The lower viscosity of ethanol allowed for the use of a larger flow cell of 1000 µm (45/Q/1, Starna). Due to the high scattering of the undiluted Intralipid, a thinner 200 µm flow cell (45/Q/0.2, Starna) was used that still transmits for these concentrations.

The glycerol (M152-1L, Amresco), ethanol (99.8% 1L, Riedel-de Haën) and Intralipid (I141-100ML, Sigma-Aldrich) were diluted with demineralized water (Milli-Q 15 MΩcm). For the glycerol measurement the cuvette was cleaned with isopropanol between each measurement. Before each measurement on ethanol or Intralipid dilutions, the previous sample was flushed out by air and demineralized water. The mixture was introduced to the flow cell by a BD10 Luer-Lock syringe while the flow cell was maintained at the exact same location. The setup was calibrated with phase and attenuation measurements of demineralized water.

The optical path length difference between the reference arm and the sample arm was set between 50 µm and 100 µm, well below the maximum optical path length difference of 340 µm for this setup. The exposure time of the spectrometer was varied between each measurement such that each measurement could use a large portion of the dynamic range of the spectrometer. This was 100 µs for both the glycerol and ethanol measurements, and their calibration measurements. For Intralipid this was 1 ms for the lowest volume fraction to 5 ms for the highest volume fraction. For the calibration of the Intralipid measurements, the exposure time of the spectrometer was set to 200 µs. The number of spectra ranged from 2000 to 20 000 such that the noise in the light source, the shot noise, and the electronic noise was properly averaged out. The background spectrum was measured by blocking both arms and was subtracted from each measured spectrum for each different integration time.

2.3.3. DATA ANALYSIS

The analysis of the spectrum of a measurement is summarized in the flow chart shown in Fig. 2.5 with as the first step the measured spectrum $I_{\text{measured}}(\lambda)$. As an example, the analysis steps of the spectrum of a measurement of an Intralipid dilution of 2.27 vol.% in water is shown in Fig. 2.6.

In the first step, a wavelength range is selected in which there is sufficient signal; determined by the spectrum of the light source, dichroic mirror, the response of the grating and sensor in the spectrometer, and the attenuation of the sample. The resulting spectrum is $I_{\text{tot}}(\lambda)$. For the glycerol and ethanol dilutions, wavelengths between 400 and 930 nm were used. For low wavelengths, the measurements of the Intralipid dilutions were strongly attenuated. Therefore, the lower wavelength bound was increased for higher volume fractions of Intralipid. For the volume fractions between 2.27 vol.% and 13.62 vol.% the lower bound was set to 460 nm, for the volume fractions 15.59 vol.% and 18.16 vol.% this was 480 nm and for the volume fraction of 20.43 vol.% soy oil in water and undiluted Intralipid (22.7 vol.%) this was 500 nm.

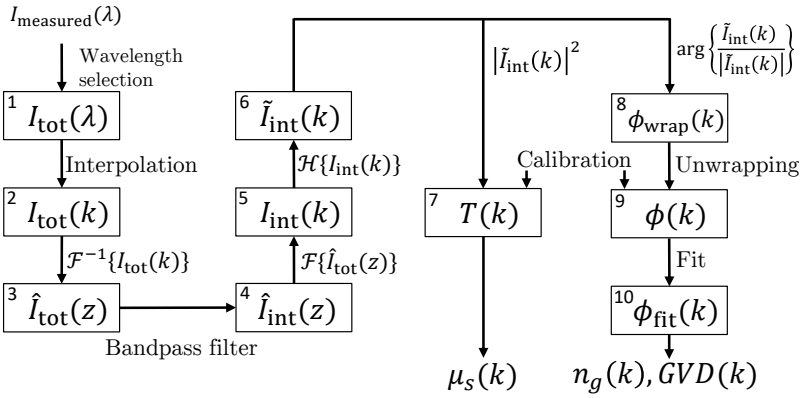

Figure 2.5: Flow chart of the analysis steps.

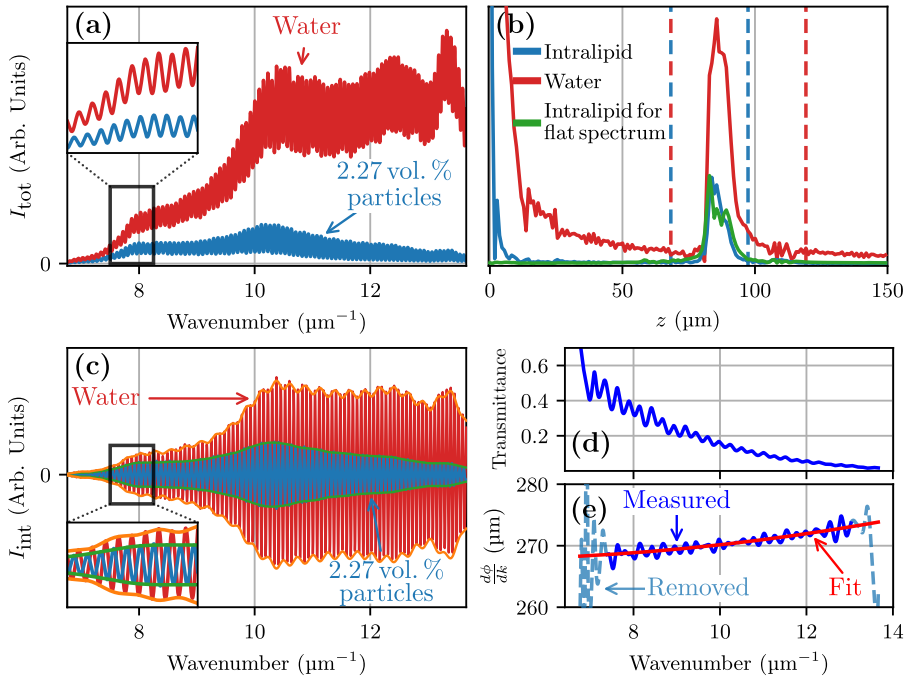

Figure 2.6: Measured spectra of water and an Intralipid dilution with 2.27 vol.% oil particles in water (a). Fourier transform of aforementioned spectra (b). The dashed vertical lines indicate the bandpass filter. The filtered interference (c). Transmittance of the Intralipid (d) and derivative of the phase $\phi(k)$ of Intralipid (e).

In the second step, the measured spectrum is interpolated from the wavelength domain to linear wavenumbers with the Scipy [50] `interp1d` function. The interpolated interference spectra of the Intralipid dilution and its reference water measurement are shown in Fig. 2.6(a).

In the third step, the spectral data is inverse Fourier transformed to the spatial domain. The absolute value of the inverse Fourier transform is shown in Fig. 2.6(b). The peaks around 85 µm correspond to the optical path length difference between the reference arm and the sample arm. The shape of these peaks is determined by the envelope of the interference spectrum and the dispersion caused by the sample and the optical elements.

In the fourth step, the Fourier transform of the pure interference term, as shown in Eq. (2.4), was obtained by applying a bandpass filter to the signal. The boundaries of the bandpass filter are indicated with dashed lines in Fig. 2.6(b), with the colors indicating the edge for the different substances. Because the Fourier peak is not symmetric, the bounds of the bandpass filter are separately calculated for the left and the right side. The bounds are taken to be eight times the distance between the position of the maximum value and the position at half the maximum value of the envelope corrected peak. For the measurements shown in Fig. 2.6(b), the lower bound is set at 68 µm. The upper bound was set for the Intralipid measurement to 97 µm, indicated by the blue line. For the water calibration this it was set at 119 µm, as indicated with the red line.

In step 5, the signal is Fourier transformed back to the spectral domain. The filtered spectral signal is shown in Fig. 2.6(c). In step 6, the complex interference $\tilde{I}(k)$ is determined with the Hilbert transform according to Equation 2.5. In step 7, the envelope of the interference is calculated with the absolute value of the complex interference of the filtered signal $|\tilde{I}_{int}(k)|$. The envelopes of the interference of the Intralipid dilution and water are indicated with green and orange, respectively, in Fig. 2.6(c). The transmittance is calculated from the envelope according to Eq. 2.7 and a calibration measurement of water.

The phase and amplitude of the Hilbert transform can have a fringe pattern near the edges. This can be seen in Fig. 2.6(c) for wavenumbers smaller than 7 µm^{-1}. Therefore, the envelope of the interference spectrum is only calculated for a spectral region 100 nm smaller than the full wavelength range. The transmittance is calculated according to Eq.(2.7) and is shown for 2.27 vol.% soy oil in Fig. 2.6(d).

In step 8, the phase $\phi(k)$ is obtained from the complex interference $\tilde{I}_{int}(k)$. First, the interference spectrum is divided by the envelope of the interference. The Fourier transform of this reshaped interference is shown in green in Fig. 2.6(b). Without the envelope, the Fourier spectrum has the typical shape of an up-chirped signal. The phase is calculated by taking the angle of the complex-valued interference spectrum of Eq. (2.6). It is possible to obtain the phase from a Hilbert transform of the interference of step 3. However, isolating the interference frequencies and normalizing the signal greatly reduces the fringe patters that can be seen in Fig. 2.6(e).

In step 9, this phase is unwrapped. After unwrapping, the spectral phase needs to be compensated for the system dispersion. This is done with a calibration measurement with demineralized water. The phase of the sample ϕ_{sample} is

$$\phi_{\text{sample}}(k) = \phi_m(k) - \phi_c(k) + n_{\text{water}}(k)\,kL, \tag{2.29}$$

with $\phi_m(k)$ the measured phase of the medium, $\phi_c(k)$ the phase of the water calibration measurement, and $n_{\text{water}}(k)\,kL$ the phase of the water. The refractive index of water $n_{\text{water}}(k)$ is taken from Daimon *et al.*[51] for 20 °C. The unwrapped phase of the same

measurement with diluted Intralipid is shown in Fig. 2.6(e).

The group index and the GVD are proportional to, respectively, the first and second derivative of the phase with respect to the wavenumber k. To obtain these derivatives, the phase is fitted in step 10 with the polynomial of Eq. (2.8). For the glycerol and ethanol measurements a fourth-order polynomial was fitted to the phase with the first and last 200 elements removed from the total of 8192. For Intralipid, the phase is fitted with a third-order polynomial and the first and last 750 elements were removed from the measured spectrum. The elements that were retained are shown in dark blue in Fig. 2.6(e). The reduction of the spectral range was done to avoid edge effects on the phase estimation, as shown in light blue in Fig. 2.6(e). The lower order polynomial for Intralipid means that the measured GVD was assumed to be at most linearly dependent on wavenumber. The wavenumber dependent group index and GVD are calculated using Equations 2.9 and 2.10 from the polynomial fit of the sample phase.

The dependence of the group index and the GVD on the mixture ratio of glycerol and ethanol was parameterized with a parabola and with a linear dependence for Intralipid. The confidence interval was given by the standard error of the fit parameters. The confidence interval of the scattering attenuation measurements was determined from the standard deviation of the fit parameters A, α and p of Eq. (2.28).

2.3.4. OPTICAL REFERENCE DATA

The group index and GVD of glycerol and ethanol are compared with literature data and the Lorentz-Lorenz mixing formula. The refractive indices of water, glycerol and ethanol were taken from Daimon *et al.* [51] Gupta *et al.* [52] and Kedenburg *et al.* [53], respectively. However, Gupta *et al.* measured the refractive index of glycerol only for wavelengths lower than 710 nm. Therefore the dispersion formula, as reported by Gupta *et al.*, was extrapolated to higher wavelengths.

The refractive index of water glycerol and water ethanol mixtures is dependent on the mixing ratio and the mass density. The mass density as a function of volume fraction of glycerol in water is taken from Volk *et al.* [54] and for ethanol in water from Danahy *et al.* [55]. With this data, the phase index for the mixture was calculated with the Lorentz-Lorenz equation, Eq. (2.25). The expected group index and the GVD were calculated with Eq. 2.9 and 2.10.

2.4. RESULTS

2.4.1. REFRACTIVE PROPERTIES OF UNDILUTED SAMPLES

In Fig. 2.7 the measured group index and GVD of pure glycerol, ethanol, and Intralipid are shown. The measured group index of ethanol follows the expected Cauchy relationship with wavenumber k. The measured group index of glycerol is slightly higher than reported by Gupta *et al.* [56]. For pure Intralipid the scattering attenuation for wavenumbers higher than 11.5 μm^{-1} (550 nm) was too high to reliably measure the phase of the interference spectrum. For Intralipid, no reliable literature data is available. For the GVD, the data of the ethanol measurements agree well with the literature values by Kedenburg *et al.* [53]. For glycerol, the GVD at the center wavenumber matches the literature values reasonably well. However, the measured wavenumber dependence is much stronger

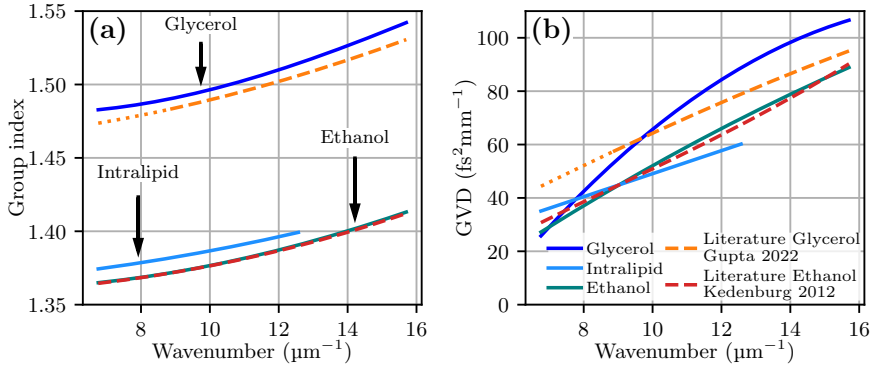

Figure 2.7: Wavenumber dependence of the measured group index (a) and GVD (b) compared to literature. Interpolated literature values are indicated with a dashed line, extrapolated values with a dotted line.

than reported by Gupta *et al.*

The dependence of the group index and GVD of glycerol and ethanol on the mixing ratio at various wavelengths is shown in Fig. 2.8. In Fig. 2.8(a) the measured group index of the glycerol dilutions matches the prediction by Eq. (2.25). In Fig. 2.8(b) the mixing ratio dependence of the GVD is linear for all glycerol-water mixtures. This is expected as the mass density of glycerol-water mixtures is an almost linear function of the mixing ratio [54] and hence gives a GVD that depends almost linearly on the mixing ratio according to Eq. (2.25). The results are in good agreement with the literature values, especially at the center of the spectrum where the phase estimation is most accurate.

The group index of ethanol is shown in Fig. 2.8(c). For ethanol, the dependence of the group index on the mixing ratio is nonlinear. In fact, the group index of ethanol reaches a maximum at a volume fraction of 75 vol.%. The nonlinear behavior of the group index is due to the nonlinear relationship of the mass density with the mixing ratio. This is caused by the strong hydrogen bond interactions in the mixture. Not only between ethanol and water molecules, but also among molecules of the same species [57].

In contrast to the glycerol-water mixtures, the mixing ratio dependence of the GVD of ethanol-water mixtures is nonlinear. This follows from the prediction of Eq. (2.25) and the mixing ratio dependence of the mass density of ethanol-water mixtures [55]. Fig. 2.8(d) shows that the GVD at 800 nm monotonically increases with volume fraction. For the wavelengths 500 nm and 600 nm the GVD obtains a maximum at high ethanol concentrations.

The absorption of glycerol (< 0.25 mm^{-1} at 589 nm [58]) and ethanol (~ 0.1 m^{-1} at 589 nm [53]) was too small to reliably measure with the path length of the flow cell used in this experiment.

2.4.2. OPTICAL PROPERTIES OF PARTICLE SUSPENSIONS

The concentration dependence of the group index and GVD of Intralipid is shown in Fig. 2.9. The group index of the Intralipid mixtures increases monotonically with volume

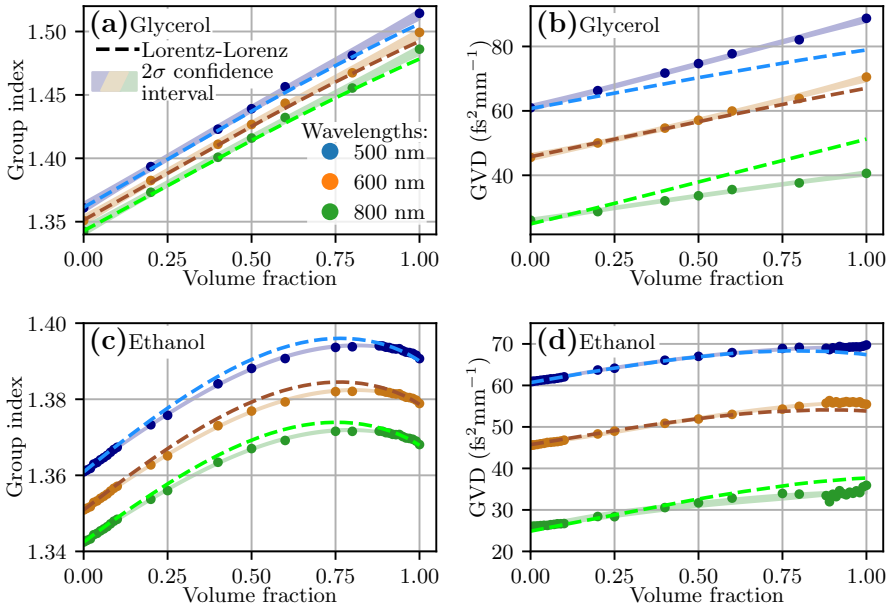

Figure 2.8: Group index and GVD of glycerol and ethanol mixtures as function of volume fraction at various wavelengths.

fraction. The nonpolar soy oil droplets in an Intralipid emulsion are hydrophobic. It is expected that these droplets have very small interactions with the solvent at the molecular level. Therefore the mass density, and hence the group index and GVD, are a linear function of the mixing ratio.

The low transmittance and smaller channel sizes of the Intralipid samples significantly increased the confidence interval of both the group index and the GVD, particularly for wavelengths at the edge of the spectral range.

In Fig. 2.10(a) the scattering attenuation coefficient of Intralipid is shown as a function of wavelength for various volume fractions. Overall, the attenuation coefficient shows a monotonous decay with increasing wavelength. In this wavelength range, water absorption is negligible and the attenuation is solely caused by scattering. Also, Mie resonances are not visible in the spectra as the sample is very polydisperse and the typical particle size 50-300 nm for Intralipid [25, 47, 61] is relatively small compared to the wavelength.

In Fig. 2.10(b) the volume fraction dependence of the attenuation coefficient is shown for various wavelengths. The effect of dependent scattering is clearly visible by a nonlinear increase in the attenuation coefficient. The volume fraction of maximum attenuation is 0.265 as obtained from the fit of Eq. (2.28). This is larger than the volume fraction of soy oil in undiluted Intralipid 20%. The data matches well to literature values at the wavelengths of 635 nm and 750 nm (Aernouts et al [59]) and 800 nm (Kodach et al [60]).

The attenuation data is fitted with Eq. (2.28). The proportionality constant is found

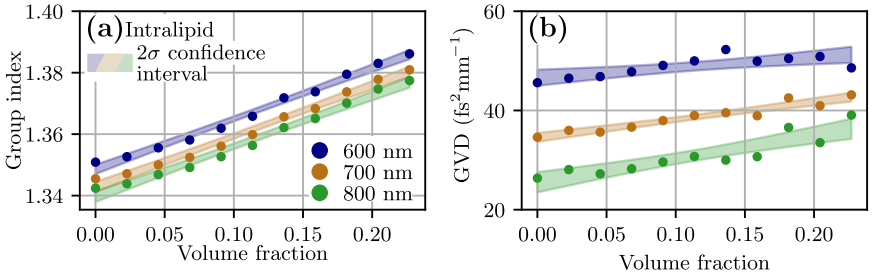

Figure 2.9: (a) Group index of dilutions of Intralipid 20% as function of volume fraction for various wavelengths. (b) GVD of dilutions of Intralipid 20% as a function of volume fraction for various wavelengths. The expected value is calculated by using the average refractive index weighted by volume fraction.

to be $A = 1.57 \pm 0.01$, the wavelength dependence is given by the parameter $\alpha = 2.587 \pm 0.001$, and the packing dimension $p = 1.04 \pm 0.01$.

2.5. DISCUSSION

2.5.1. REFRACTIVE INDEX

This work not only provides the optical properties for separate wavelengths, the broad range also results in a more accurate determination of the dispersive refractive properties with the quantification of the group index and the GVD.

The measured group index for pure and dilutions of glycerol is slightly higher than reported in literature, *red* which is possibly due to the measurement taking place at a lower temperature compared to the temperature at which the literature values were obtained [52, 56]. The GVD has a good match at the center wavelength, for other wavelengths there is a deviation that we attribute to the occurrence of the fringes near the edges in the phase of the Hilbert transform.

The group index of pure ethanol is very close to the value determined by Kedenburg *et al.* [53]. For the ethanol dilutions, the effect of the volume contraction is slightly less prominent than predicted with Eq. (2.25) and the mass density dependence as determined by Danahy *et al.* [55]. Similarly, the GVD is well predicted by the literature values.

Many authors [51–53, 62] measure the refractive index for each wavelength separately and obtain the dispersion through a fit. Since the GVD is a sum of the first and second derivative to the wavenumber of the refractive index, any choice of the dispersion equation or the presence of noise in the measured data points has a disproportional effect on the GVD. Therefore, literature values of the GVD vary wildly. The reported values of the GVD of glycerol at the wavelength of 589 nm range from 45.5 $\mathrm{fs^2\,mm^{-1}}$ [52] to 68.1 $\mathrm{fs^2\,mm^{-1}}$ [56]. We determined it at 72.4 ± 0.5 $\mathrm{fs^2\,mm^{-1}}$. For ethanol reported value range from 55.1 $\mathrm{fs^2\,mm^{-1}}$ [53] to 65.3 $\mathrm{fs^2\,mm^{-1}}$ [63]. We determined it at 56.8 ± 0.3 $\mathrm{fs^2\,mm^{-1}}$. Both are close to, or well within, the range of values provided in literature.

Because the spectral phase is obtained from what is close to a continuum of wavelengths, the dispersive properties could be obtained more accurately, than when the refractive index is only measured for a limited number of wavelengths. Therefore, the

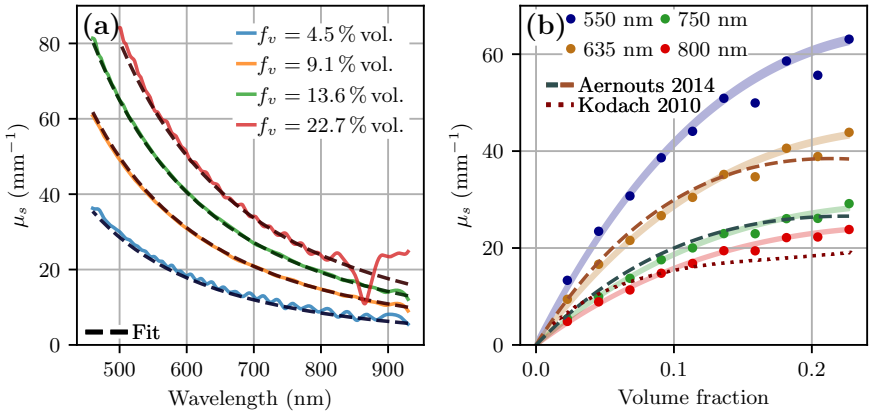

Figure 2.10: (a) Attenuation coefficient of Intralipid as function of wavelength for various volume fractions. Fits are with Eq. (2.28). (b) Scattering coefficients for various wavelengths. The effect of dependent scattering is clearly visible as a flattening of the scattering coefficient. Literature data from Aernouts [59] and Kodach [60] are shown at the same wavelength as the measurements.

method presented in this work would provide a method to accurately determine the GVD of a medium. To provide an accurate measurement of the GVD with other methods, for example an Abbe refractometer, individual measurements at many wavelengths would be required.

The spread in the datapoints of the group index and GVD of Intralipid as shown in Fig. 2.9 is much higher than the spread observed in the data of the transparent media. This is due to the lower transmittance and the necessity to use a smaller flow channel size. For wider flow channels the GVD can be more accurately determined as the increased path length leads to more accumulated phase change. However, this would lead to very small signals at very high volume fractions.

2.5.2. OPTICAL ATTENUATION

The wavelength-dependent scattering attenuation shown in Fig.2.10(a) generally matches the expected dependent scattering for Mie scatterers. The anomaly between 800 nm and 900 nm for undiluted Intralipid is caused by the lower response of the spectrometer for longer wavelengths, as can be seen from the water calibration measurement in Fig. 2.6(a). Here, the measured intensity for wavenumbers lower than 7.5 μm^{-1} (840 nm) is very low for both the measurement and the calibration.

The measured dependent scattering attenuation coefficient of Intralipid is similar to that reported in literature [13, 47, 59–61, 64] for all wavelengths. The value of the wavelength dependence parameter in Eq. (2.28) $\alpha = 2.587 \pm 0.001$ compares well to values reported in literature. Reported values for α range from $\alpha = 2.40$ [64] to $\alpha = 2.59$ [59].

Although the attenuation spectra are similar, the obtained fitted packing dimension $p = 1.04 \pm 0.01$ is much lower. Since p parameterizes the volume fraction of minimum transmittance, deviations at high volume fractions have a disproportional effect on the

fit parameter p. Since the spread in the scattering attenuation data is higher at high volume fractions, the standard error in the estimate of p from the fit is probably not representative of the uncertainty. This value also differs significantly from the value reported by Aernouts *et al.* [59] who found p to be between 1.55 and 2.02, depending on wavelength. The value of p as determined in this work would give the volume fraction of maximum attenuation at f_v=0.28, which is higher than the volume fraction of 0.227 of soy oil in pure Intralipid 20%. A measurement of denser Intralipid samples would improve the estimate of p.

This value of p gives an indication of the shape of the scatterers or the size polydispersity. Since the shape of the soy oil globules is not expected to deviate much from a spherical shape[59], it is also possible to attribute the difference in packing dimension to a difference in particle size distribution of the Intralipid sample. This may be caused by differences in particle size between Intralipid batches or due to a different shelf time.

2.5.3. SPECTRAL INTERFEROMETRIC SENSING

For sensing applications, measurement of the mixing ratio of the glycerol and Intralipid dilutions through the group index or GVD is straightforward as both are monotonously increasing functions. The mixing ratio of ethanol-water mixtures is more difficult to determine because the group refractive index has a maximum at 75 vol.% and therefore cannot be uniquely determined in the range of 50 to 100 vol.%. The GVD is both measured and predicted to monotonically increase with the mixing ratio at 800 nm. Measuring the GVD at this wavelength provides an opportunity to overcome the ambiguity in the group index measurement.

The attenuation coefficient, group index, and GVD were extracted from a single measured interference signal. This makes this method particularly suitable for the use in an on-chip implementation where the spectrum of the sample arm and the reference arm cannot be measured separately. A similar approach is also used in an on-chip application by Zhou *et al.* [30]. Alternatively, when higher accuracy is required, both the sample arm and the reference arm intensities can be measured separately. This can avoid the spatial domain filtering, which decreases the spectral resolution and leads to artifacts that result from the filtering. For the phase measurement the independent measurement of the background intensities decreases the prominence of the fringe patterns at the edges of the spectrum. However, for the attenuation coefficient measurements, the heterodyne detection as used in this work, offers increased sensitivity for opaque samples.

2.6. CONCLUSION

In this paper, a method is presented to simultaneously measure the group index, GVD, and attenuation coefficient over a broad wavelength range between 400 nm and 920 nm for glycerol and ethanol and from 500 nm for undiluted Intralipid. All three quantities are obtained from a single calibrated interference spectrum. All quantities are found to be similar to what is reported in literature.

DATA AVAILABILITY

Data underlying the results presented in this chapter and the relevant analysis routines are available in Ref. [65].

REFERENCES

[1] P. N. A. Speets and J. Kalkman, Measuring optical properties of clear and turbid media with broadband spectral interferometry, *Applied Optics*, 62(16):4349–4358, 2023.

[2] P. Bouguer, *Essai D'Optique, Sur La Gradation De La Lumiere*, Claude Jombert, 1729.

[3] C. Veenstra, A. Lenferink, W. Petersen, W. Steenbergen, and N. Bosschaart, Optical properties of human milk, *Biomedical Optics Express*, 10(8):4059–4074, 2019.

[4] N. Bosschaart, G. J. Edelman, and M. C. G. Aalders, A literature review and novel theoretical approach on the optical properties of whole blood, *Lasers in Medical Science*, 29:453–479, 2014.

[5] J. Trevathan, W. Read, and S. Schmidtke, Towards the development of an affordable and practical light attenuation turbidity sensor for remote near real-time aquatic monitoring, *Sensors*, 20(7), 2020.

[6] A. Postelmans, B. Aernouts, J. Jordens, T. van Gerven, and W. Saeys, Milk homogenization monitoring: Fat globule size estimation from scattering spectra of milk, *Innovative Food Science and Emerging Technologies*, 60:102311–102320, 2020.

[7] R. H. Sagor, M. F. Hassan, A. A. Yaseer, E. Surid, and M. I. Ahmed, Highly sensitive refractive index sensor optimized for blood group sensing utilizing the Fano resonance, *Applied Nanoscience*, 11(2):521–534, 2021.

[8] S. K. Chamoli, S. C. Singh, and C. Guo, Design of extremely sensitive refractive index sensors in infrared for blood glucose detection, *IEEE Sensors Journal*, 20(9):4628–4634, 2020.

[9] J. Chen, W. Guo, M. Xia, W. Li, and K. Yang, In situ measurement of seawater salinity with an optical refractometer based on total internal reflection method, *Optics Express*, 26(20): 25510–25523, 2018.

[10] S. M. Bagherzadeh, B. Grajciar, C. K. Hitzenberger, M. Pircher, and A. F. Fercher, Dispersion-based optical coherence tomography OCT measurement of mixture concentrations, *Optics Letters*, 32(20):2924–2926, 2007.

[11] A. K. Trull, J. van der Horst, J. G. Bijster, and J. Kalkman, Transmission optical coherence tomography based measurement of optical material properties, *Optics Express*, 23(26):33550–33563, 2015.

[12] Y. Park, T. Yamauchi, W. Choi, R. Dasari, and M. S. Feld, Spectroscopic phase microscopy for quantifying hemoglobin concentrations in intact red blood cells, *Optics Letters*, 34(23): 3668–3670, 2009.

[13] B. Aernouts, E. Zamora-Rojas, R. V. Beers, R. Watté, L. Wang, M. Tsuta, J. Lammertyn, and W. Saeys, Supercontinuum laser based optical characterization of Intralipid® phantoms in the 500-2250 nm range, *Optics Express*, 21(26):32450–32467, 2013.

[14] S. Korposh, S. W. James, S.-W. Lee, and R. P. Tatam, Tapered optical fibre sensors: Current trends and future perspectives, *Sensors*, 19(10):2294, 2019.

[15] I. Brice, K. Grundsteins, K. Draguns, A. Atvars, and J. Alnis, Whispering gallery mode resonator temperature compensation and refractive index sensing in glucose droplets, *Sensors*, 21(21):7184, 2021.

[16] A. Ksendzov and Y. Lin, Integrated optics ring-resonator sensors for protein detection, *Optics Letters*, 30(24):3344–3346, 2005.

[17] H.-Y. Lin, C.-H. Huang, G.-L. Cheng, N.-K. Chen, and H.-C. Chui, Tapered optical fiber sensor based on localized surface plasmon resonance, *Optics Express*, 20(19):21693–21701, 2012.

[18] W. R. Calhoun, H. Maeta, S. Roy, L. M. Bali, and S. Bali, Sensitive real-time measurement of the refractive index and attenuation coefficient of milk and milk-cream mixtures, *Journal of Dairy Science*, 93(8):3497–3504, 2010.

[19] M. K. Dong, K. G. Goyal, B. Worth, S. Makkar, W. R. Calhoun III, L. M. Bali, and S. Bali, Accurate in situ measurement of complex refractive index and particle size in Intralipid emulsions, *Journal of Biomedical Optics*, 18(8):087003, 2013.

[20] H. Contreras-Tello and A. García-Valenzuela, Refractive index measurement of turbid media by transmission of backscattered light near the critical angle, *Applied Optics*, 53(21):4768–4778, 2014.

[21] E. Gutiérrez-Reyes, A. García-Valenzuela, and R. G. Barrera, Extension of Fresnel's formulas for turbid colloidal suspensions: A rigorous treatment, *Journal of Physical Chemistry B*, 118 (22):6015–6031, 2014.

[22] G. H. Meeten, Refractive index errors in the critical-angle and the brewster-angle methods applied to absorbing and heterogeneous materials, *Measurement Science and Technology*, 8 (7):728–733, 1997.

[23] H. Liu, J. Ye, K. Yang, M. Xia, W. Guo, and W. Li, Real part of refractive index measurement approach for absorbing liquid, *Applied Optics*, 54(19):6046–6052, 2015.

[24] N. Bosschaart, M. C. G. Aalders, D. J. Faber, J. J. A. Weda, M. J. C. van Gemert, and T. G. van Leeuwen, Quantitative measurements of absorption spectra in scattering media by low-coherence spectroscopy, *Optics Letters*, 34(23):233746–233748, 2009.

[25] V. M. Kodach, D. J. Faber, J. van Marle, T. G. van Leeuwen, and J. Kalkman, Determination of the scattering anisotropy with optical coherence tomography, *Optics Express*, 19(7):6131–6140, 2011.

[26] V. D. Nguyen, D. J. Faber, E. van der Pol, T. G. van Leeuwen, and J. Kalkman, Dependent and multiple scattering in transmission and backscattering optical coherence tomography, *Optics Express*, 21(24):29145–29156, 2013.

[27] B. Ghafaryasl, K. A. Vermeer, J. Kalkman, T. Callewaert, J. F. de Boer, and L. J. van Vliet, Attenuation coefficient estimation in Fourier-domain OCT of multi-layered phantoms, *Biomedical Optics Express*, 12(5):2744–2758, 2021.

[28] C. Photiou and C. Pitris, Comparison of tissue dispersion measurement techniques based on optical coherence tomography, *Journal of Biomedical Optics*, 24(4):046003, 2019.

[29] S. M. Kolenderska, B. Bräuer, and F. Vanholsbeeck, Dispersion mapping as a simple postprocessing step for fourier domain optical coherence tomography data, *Scientific Reports*, 8(1): 9244, 2018.

[30] C. Zhou, M. K. Hedayati, and A. Kristensen, Multifunctional waveguide interferometer sensor: simultaneous detection of refraction and absorption with size-exclusion function, *Optics Express*, 26(19):24372–24383, 2018.

[31] D. Reolon, M. Jacquot, I. Verrier, G. Brun, and C. Veillas, High resolution group refractive index measurement by broadband supercontinuum interferometry and wavelet-transform analysis, *Optics Express*, 14(26):12744–12750, 2006.

[32] J. van der Horst, A. K. Trull, and J. Kalkman, Deep-tissue label-free quantitative optical tomography, *Optica*, 7(12):1682–1689, 2020.

[33] A. L. B. Cauchy, *Mémoire sur la dispersion de la lumière*, J. G. Calve, 1836.

[34] J. B. Biot and D. F. Arago, Sur les affinités des corps pour la lumière, et particulièrement sur les forces réfringentes des différens gaz, *Mémoires de l'Académie des sciences de l'Institut de France*, 6:301–387, 1806.

[35] L. Lorenz, Experimentale og theoretiske undersøgelser over legemernes brydningsforhold, *Det Kongelige Danske Videnskabernes Selskabs Skrifter*, 5(10):483–518, 1875.

[36] H. A. Lorentz, Over het verband tusschen de voortplantingssnelheid van het licht en de dichtheid en samenstelling der middenstoffen, *Verhandelingen der Koninklijke Academie van Wetenschappen*, 18, 1879.

[37] M. I. Mishchenko, L. D. Travis, and A. A. Lacis, *Multiple Scattering of Light by Particles: Radiative Transfer and Coherent Backscattering*, Multiple Scattering of Light by Particles: Radiative Transfer and Coherent Backscattering. Cambridge University Press, 2006, ISBN 9780521834902.

[38] A. Parola, R. Piazza, and V. Degiorgio, Optical extinction, refractive index, and multiple scattering for suspensions of interacting colloidal particles, *Journal of Chemical Physics*, 141(12): 124902, 2014.

[39] W. Sellmeier, Zur Erklärung der abnormen Farbenfolge im Spectrum einiger Substanzen, *Annalen der Physik*, 219(6):272–282, 1871.

[40] P. Drude, Eine Methode zur Messung der Dielectricitätsconstanten und electrischen Absorption kleiner Substanzmengen vermittelst electrischer Drahtwellen, *Annalen der Physik*, 297 (7):466–510, 1897.

[41] I. Newton, *Opticks: Or, A Treatise of the Reflections, Refractions, Inflections and Colours of Light*, William Innys at the West-End of St. Paul's, 4 edition, 1730.

[42] A. E. Shapiro, Skating on the edge: Newton's investigation of chromatic dispersion and achromatic prisms and lenses, In *Wrong for the right reasons*, pages 99–125. Springer, 2005.

[43] J. C. R. Reis, I. M. Lampreia, Â. F. Santos, M. L. C. Moita, and G. Douhéret, Refractive index of liquid mixtures: theory and experiment, *ChemPhysChem*, 11(17):3722–3733, 2010.

[44] D. Aspnes, Local-field effects and effective-medium theory: A microscopic perspective, *American Journal of Physics*, 50(8):704–709, 1982.

[45] A. Aubret, *Nanoparticules semi-conductrices et plasmoniques comme sondes locales de l'environnement diélectrique*, PhD thesis, Université Claude Bernard - Lyon I, 2015.

[46] A. Aubret, M. Orrit, and F. Kulzer, Understanding local-field correction factors in the framework of the Onsager- Böttcher model, *ChemPhysChem*, 20(3):345–355, 2019.

[47] H. J. van Staveren, C. J. M. Moes, J. van Marie, S. A. Prahl, and M. J. C. van Gemert, Light scattering in lntralipid-10% in the wavelength range of 400–1100 nm, *Applied Optics*, 30(31): 4507–4514, 1991.

[48] V. Twersky, Transparency of pair-correlated, random distributions of small scatterers, with applications to the cornea, *Journal of the Optical Society of America*, 65(5):524–530, 1975.

[49] P. A. J. Bascom and R. S. C. Cobbold, On a fractal packing approach for understanding ultrasonic backscattering from blood, *Journal of the Acoustical Society of America*, 98(6):3040–3049, 1995.

[50] P. Virtanen *et al.*, SciPy 1.0: Fundamental Algorithms for Scientific Computing in Python, *Nature Methods*, 17:261–272, 2020.

[51] M. Daimon and A. Masumura, Measurement of the refractive index of distilled water from the near-infrared region to the ultraviolet region, *Applied Optics*, 46(18):3811–3820, 2007.

[52] J. Rheims, J. Köser, and T. Wriedt, Refractive-index measurements in the near-IR using an abbe refractometer, *Measurement Science and Technology*, 8(6):601–605, 1997.

[53] S. Kedenburg, M. Vieweg, T. Gissibl, and H. Giessen, Linear refractive index and absorption measurements of nonlinear optical liquids in the visible and near-infrared spectral region, *Optical Materials Express*, 2(11):1588–1611, 2012.

[54] A. Volk and C. J. Kähler, Density model for aqueous glycerol solutions, *Experiments in Fluids*, 59(75), 2018.

[55] B. B. Danahy, D. L. Minnick, and M. B. Shiflett, Computing the composition of ethanol-water mixtures based on experimental density and temperature measurements, *Fermentation*, 4 (3):72, 2018.

[56] V. Gupta, O. Aftenieva, P. T. Probst, S. Sarkar, A. M. Steiner, N. Vogel, A. Fery, and T. A. F. König, Advanced colloidal sensors enabled by an out-of-plane lattice resonance, *Advanced Photonics Research*, 3(11):2200152, 2022.

[57] K. Mizuno, Y. Miyashita, Y. Shindo, and H. Ogawa, NMR and FT-IR studies of hydrogen bonds in ethanol-water mixtures, *Journal of Physical Chemistry*, 99(10):3225–3228, 1995.

[58] H. Ren, S. Xu, Y. Liu, and S.-T. Wu, Liquid-based infrared optical switch, *Applied Physics Letters*, 101(4):041104, 2012.

[59] B. Aernouts, R. Watté, R. V. Beers, F. Delport, M. Merchiers, J. D. Block, J. Lammertyn, and W. Saeys, Flexible tool for simulating the bulk optical properties of polydisperse spherical particles in an absorbing host: experimental validation, *Optics Express*, 22(17):20223–20238, 2014.

[60] V. Kodach, N. Bosschaart, J. Kalkman, T. G. van Leeuwen, and D. J. Faber, Concentration dependent scattering coefficients of Intralipid measured with OCT, In *Biomedical Optics and 3-D Imaging*, page BSuD11. Optica Publishing Group, 2010.

[61] M. Raju and S. N. Unni, Concentration-dependent correlated scattering properties of Intralipid 20% dilutions, *Applied Optics*, 56(4):1157–1166, 2017.

[62] P. R. Cooper, Refractive-index measurements of liquids used in conjunction with optical fibers, *Applied Optics*, 22(19):3070–3072, 1983.

[63] P. Kozma, F. Kehl, E. Ehrentreich-Förster, C. Stamm, and F. F. Bier, Integrated planar optical waveguide interferometer biosensors: A comparative review, *Biosensors and Bioelectronics*, 58:287–307, 2014.

[64] R. Michels, F. Foschum, and A. Kienle, Optical properties of fat emulsions, *Optics Express*, 16 (8):5907–5925, 2008.

[65] P. N. A. Speets and J. Kalkman, *Measuring optical properties of clear and turbid media with broadband spectral interferometry — data and analysis*, https://doi.org/10.5281/zenodo.7838373, 2023.

3

EXPERIMENT AND THEORY OF THE COMPLEX REFRACTIVE INDEX OF DENSE COLLOIDAL MEDIA

The complex refractive index is analyzed by measuring its scattering attenuation μ_{sca}, group index n_g and group velocity dispersion (GVD) for 100 *nm diameter silica nanoparticles dispersed in water. The experiments were performed for wavelengths between* 410 *and* 930 *nm. The experimental results were compared with different mixing models for the complex refractive index of colloidal suspensions. The group index linearly scaled with the volume fraction both in experiment and for all tested models. It was found that the GVD has a nonlinear dependence on volume fraction in agreement with the coupled dipole model of Parola et al. [2] The scattering attenuation is in good agreement with both the coupled dipole model and the low-frequency quasi-crystalline approximation [3] that take particle correlations into account. With an iterative fitting procedure of all the data based on both the coupled dipole model and the quasi-crystalline approximation, the refractive index, porosity, and size of the nanoparticles were determined. We determined that the coupled dipole model is in best agreement with the data.*

Parts of this chapter have been published in P.N.A. Speets and J. Kalkman, *Experiment and theory of the complex refractive index of dense colloidal media*, Journal of the Optical Society of America A, 41, 214-228 (2024) [1]

3.1. INTRODUCTION

An important parameter describing electromagnetic wave propagation in optical materials is the complex refractive index. The real part of the refractive index is related to refraction, phase delay, and phase velocity of the wave. The imaginary part of the refractive index is related to the optical attenuation of the wave caused by scattering and absorption.

For optical materials composed of atomic or molecular mixtures the real part of the refractive index is well described by the Lorentz-Lorenz equation [4, 5], which is based on the intrinsic polarizability of the atoms or molecules in the mixture. Colloidal media are composed of liquid or solid particles with a size range of 1-1000 nm in a molecular solvent. In a dilute colloidal suspension the real part of the refractive index is well approximated by the simple Arago-Biot mixing formula [6, 7]. This describes the refractive index as the average refractive index of the host medium and the suspended particles, weighted by their volume fraction.

The first theoretical description of the effect of small particles on the real part of the effective refractive index was given by Garnett who used the Clausius–Mossotti relation to incorporate the effect of embedded gold and silver particles to describe the optical properties of colored glass [8]. Since then, various mixing models [2, 3, 9–26] have been derived for the effective refractive index of particulate media. With some exceptions [9, 10, 15], these models predict both the real part and the imaginary part of the effective refractive index. In many cases, scattering models were developed to describe the attenuation, caused by absorption or scattering, but some obtained the refractive properties from the electric permittivity [9, 15, 22].

The full complex refractive index of a dilute particle suspension is well approximated with the simple and widely used mixing formula given by van de Hulst [17]. This model predicts both the real and imaginary part of the effective refractive index from a given complex scattering amplitude, for example from Mie theory. A disadvantage of the van de Hulst refractive index model is that it does not incorporate volume fraction dependent scattering. In other words, it does not take into account the correlations between the particle positions and predicts a linear relationship between the effective refractive index and the volume fraction. The van de Hulst refractive index is applicable for volume fractions lower than 1% [23], but for higher volume fractions leads to erroneous results as the relationship between the imaginary refractive index and the number of particles becomes nonlinear [27–31]. For volume fractions up to 5%, it is possible to derive a simple and nonlinear expression [23, 26, 32] for the effective refractive index. For higher particle volume fractions the effective complex refractive index can be obtained by taking into account the positional correlations between the scattering particles. In this way, the imaginary part depends explicitly on the radial distribution function $g(r)$, that describes the statistics of the distribution of the particles, and its spherical Fourier transform, the structure factor $S(q)$ describing the light scattering of the particles. Here, r is the distance from the center of a particle and q the scattering wavenumber [28, 30, 33, 34]. These correlations have a prominent effect at high volume fractions [2, 3, 14, 20]. However, it was observed that the volume fraction dependence of the real part deviates only slightly from linearity [23, 32, 35–40]. It is therefore difficult to compare different models of the real refractive index to experimental results. Indeed, some authors noted the

scarcity of experimental work on the effective refractive index [2, 23, 26, 41, 42]. Experimental evidence is particularly absent for high-volume fractions of particles where colloidal suspensions easily become unstable [23].

A second complication is that measuring the real part of the refractive index of colloidal suspensions is challenging. For example, when measuring a colloidal suspension with an Abbe refractometer, the critical angle becomes ambiguous [37, 43]. In this case, the Fresnel equations need to be modified to take into account the particulate nature of the medium [25, 31, 44, 45]. When measured in transmission, for example through strongly forward scattering media such as tissue [46], the partially coherent diffusive light makes a quantitative determination of the real part of the refractive index ambiguous. In that case, coherence gating may be applied to filter the diffusive light from the ballistic light [28, 46, 47].

The work presented in this chapter consists of experimental results and theoretical analysis of the complex refractive index of dense suspensions of 100 nm silica particles in water. Experimentally, we determine the group index, group velocity dispersion (GVD), and scattering attenuation with a spectral domain Mach-Zehnder interferometer over a broad wavelength range.

The experimental data is compared to two volume fraction dependent models for the complex effective refractive index of dense colloidal suspensions. The first model is the quasi crystalline approximation (QCA) of the Foldy-Lax equations in the low frequency limit described by Ding and Tsang [3]. The second is the coupled dipole model (CDM) by Parola *et al.* [2]. CDM is conceptually similar to the coupled dipole method to computationally obtain the scattering properties [48], or thermal radiation [49, 50] of an arbitrarily shaped particle.

We observe that the nonlinear response of the GVD to the particle size and concentration is much larger than that of the group index of the suspension. From a fit of the CDM model to the full complex refractive index over a large size parameter and concentration range we obtain the mean particle size, size polydispersity and refractive index. We show that the obtained size distribution is in good agreement with a reference measurement.

3.2. THEORY

3.2.1. THE REFRACTIVE INDEX OF DILUTE SUSPENSIONS

The complex refractive index is defined as

$$\tilde{n}(k) = n(k) + i\frac{\mu(k)}{2k} \tag{3.1}$$

with the real part $n(k)$ related to the phase velocity of a wave propagating through a medium and the imaginary part related to the attenuation of the wave in the medium. Here, k is the wavenumber in vacuum, and μ the attenuation coefficient, both due to absorption and scattering. In a non-absorbing medium and with non-absorbing particles, the attenuation coefficient is given only by the scattering attenuation coefficient μ_{sca}.

In a dilute suspension of particles, the effect of spatial correlations of particle positions can be neglected. In that case, the real part of the refractive index of a mixture of two components is, for many mixtures, well approximated with the Arago-Biot mixing

formula. This equation expresses the refractive index as the average refractive index of both components weighted by their volume fraction [6]

$$\mathrm{Re}\{\tilde{n}_{\mathrm{eff}}\} = f_v \,\mathrm{Re}\{\tilde{n}_p\} + (1 - f_v)\,\mathrm{Re}\{\tilde{n}_m\}\,. \tag{3.2}$$

Here, f_v is the volume fraction of suspended particles, $\mathrm{Re}\{\tilde{n}_{\mathrm{eff}}\}$ is the real part of the complex effective refractive index of the suspension and $\mathrm{Re}\{\tilde{n}_m\}$ and $\mathrm{Re}\{\tilde{n}_p\}$ are the real refractive indices of the embedding medium and of the suspended particles.

In dilute suspensions, μ_{sca} is equal to the concentration times the scattering cross section. Therefore, it scales linearly with volume fraction. The full refractive index of a dilute suspension of a mixture of particles with different sizes can be calculated from the Mie scattering amplitude S_{Mie} through the van de Hulst refractive index [16, 17, 51]

$$\tilde{n}_{\mathrm{eff}}(k) = n_m(k) - \sum_i^N \frac{3i\, n_p(k) f_{v,i}}{2x_i^3} S_{\mathrm{Mie},i}(\theta = 0)\,. \tag{3.3}$$

Here, the refractive index of the suspension $\tilde{n}_{\mathrm{eff}}(k)$ is given by the refractive index of the embedding medium $n_m(k)$ minus a sum over all particle size bins with volume fraction $f_{v,i}$ per size bin. The sum consists of the refractive index of the particle $n_p(k)$, the size parameter $x_i = k_m a_i$, k_m the wavenumber in the embedding medium $n_m k$, a_i the particle radius, and the complex Mie angular scattering amplitude in the forward direction $S_{\mathrm{Mie}}(\theta = 0)$. For unpolarized light $S_{\mathrm{Mie}}(\theta = 0)$ is the average of both angular scattering amplitudes S_1 and S_2. The angular scattering function is normalized such that $\mathrm{Re}\{S(\theta = 0)\} = \frac{k^2 \sigma_s}{4\pi n_m}$, where the scattering cross section of the particle σ_s is given according to Mie theory [52, 53]. Both the van de Hulst model and the Arago-Biot formula predict a linear scaling of the refractive index with volume fraction of colloids.

3.2.2. THE ELECTRIC FIELD IN DENSE SUSPENSIONS

To describe the complex refractive index for dense media the effect of the particle positions has to be taken into account in the electromagnetic field $\boldsymbol{E}(\boldsymbol{r})$ propagation through the medium. The starting point here is the Foldy-Lax equation [11, 54, 55]:

$$\boldsymbol{E}(\boldsymbol{r}) = \boldsymbol{E}_{\mathrm{inc}}(\boldsymbol{r}) + \sum_i \int_V \overleftrightarrow{G}_m(\boldsymbol{r} - \boldsymbol{r}') U_i(\boldsymbol{r}') \boldsymbol{E}(\boldsymbol{r}')\, \mathrm{d}\boldsymbol{r}' \tag{3.4}$$

with the field at every particle location $\boldsymbol{r}_i$ given by

$$\boldsymbol{E}(\boldsymbol{r_i}) = \boldsymbol{E}_{\mathrm{inc}}(\boldsymbol{r}_i) + \sum_{j \neq i} \int_V \overleftrightarrow{G}_m(\boldsymbol{r}_i - \boldsymbol{r}') U_j(\boldsymbol{r}') \boldsymbol{E}(\boldsymbol{r}')\, \mathrm{d}\boldsymbol{r}' \tag{3.5}$$

with $\boldsymbol{E}$ the total field, and $\boldsymbol{E}_{\mathrm{inc}}$ the external excitation field. The Green's dyadic operator of the embedding medium $\overleftrightarrow{G}_m$ is given by [55]:

$$\overleftrightarrow{G}_m(\boldsymbol{r}) = \left(\overleftrightarrow{I} + \frac{1}{k_m^2} \boldsymbol{\nabla} \otimes \boldsymbol{\nabla} \right) \frac{e^{i k_m |\boldsymbol{r}|}}{4\pi |\boldsymbol{r}|}. \tag{3.6}$$

Here, $\overleftrightarrow{I}$ is the identity matrix and $U_i(\boldsymbol{r})$ is the scattering potential given by the refrac-

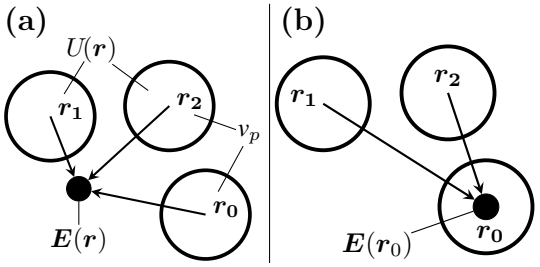

Figure 3.1: Sketch of the Foldy-Lax equations (a) The field at position $\boldsymbol{r}$ is the sum of the field radiated by all particles. (b) The field at the particle at position $\boldsymbol{r}_0$ depends on the radiated field from surrounding particles.

tive index contrast from the particle at position $\boldsymbol{r}_i$ and is given by $U_i(\boldsymbol{r}) = (m^2-1)k_m^2$ inside a particle volume v_i and is 0 within the embedding medium, and m the refractive index contrast of the particle n_p/n_m. The electromagnetic propagation is sketched in Fig. 3.1. Here, the Foldy-Lax equations are sketched for three particles at positions $\boldsymbol{r}_{0-2}$. In Fig. 3.1(a) the interactions as described in Eq. 3.4 are shown. The electric field at position $\boldsymbol{r}$ is given by the scattered field of all other particles and the external field $\boldsymbol{E}_{\text{inc}}(\boldsymbol{r})$. For this, the field of all particles must be known. The field for the particle at position $\boldsymbol{r}_0$ is given by the external field $\boldsymbol{E}_{\text{inc}}(\boldsymbol{r})$, and the field scattered by all other particles as given by Eq. 3.5, which is sketched in Fig. 3.1(b).

The total field $\boldsymbol{E}$ appears on both sides of the equation Eq. (3.5). In the Born approximation the electric field in the right hand side is set to $\boldsymbol{E}(\boldsymbol{r}) = \boldsymbol{E}_{\text{inc}}(\boldsymbol{r})$. The exact solution of the Foldy-Lax equations can then be obtained by taking the Born approximation as a first approximation for the electric field and iteratively solving for the total field for a system with a known spatial refractive index distribution $U(\boldsymbol{r}) = \sum_i U_i(\boldsymbol{r})$. For a correlated particulate medium in Brownian motion solving the Foldy-Lax equations would require averaging over all known particle positions. These can be obtained from a Monte Carlo simulation. However, since the number of particles that is needed for such a simulation is very high, a better solution is to look for an averaging method for the particle positions to obtain an average local field **E** for a particle located at position $\boldsymbol{r}_i$. In the next few sections, the description of the bulk optical properties by effective medium theories is explored.

3.2.3. FAR-FIELD INTERFERENCE

The dominant mechanism for concentration dependent scattering in the imaginary part of the complex refractive index is far-field interference. In this section the scattering attenuation is calculated by first calculating the scattering loss due to a collection of Mie scatterers, and then a positional averaging is applied to obtain the scattering of an effective medium.

In the Born approximation, the driving field is given by the incoming field E_0. Furthermore, Eq. 3.4 is valid for an arbitrary particle shape with scattering potential $U(\boldsymbol{r})$, however, often the scattering potential is known as the amplitude $f(\theta)$, with θ the scattering angle. In that case, Eq. 3.4 can be further simplified to include the known factor $f(\theta)$.

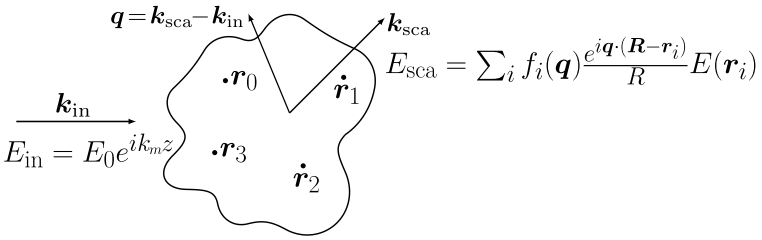

Figure 3.2: Example of the scattering of a field E_{in} with wavevector $\boldsymbol{k}_{\text{in}}$ to a collection of scatterers at positions $\boldsymbol{r}_i$. The scattered field E_{sca} given by Eq. 3.7 has wavevector $\boldsymbol{k}_{\text{sca}}$.

The scattering of an incoming plane wave in the axial direction $\hat{\boldsymbol{z}}$ on a collection of particles at positions $\boldsymbol{r}_i$ is sketched in Fig. 3.2. The incoming plane wave with wave vector $\boldsymbol{k}$ is given by $E_{\text{in}} = E_0 e^{ik_m z}$, with k_m the wavenumber in the embedding medium $k_m = n_m k$. Using the Born approximation, the scattered field E_{sca} at position $\boldsymbol{R}$ is

$$E_{\text{sca}}(\boldsymbol{R}, \boldsymbol{q}) = \sum_i^N f_i(\boldsymbol{q}) \frac{e^{i\boldsymbol{q}\cdot(\boldsymbol{R}-\boldsymbol{r}_i)}}{|\boldsymbol{R}-\boldsymbol{r}_i|} E_0(\boldsymbol{r}_i)\,. \tag{3.7}$$

Here $\boldsymbol{q} = \boldsymbol{k}_{\text{sca}} - \boldsymbol{k}_{\text{in}}$ is the scattering wavevector with length $q = 2k_m \sin(\theta/2)$, and $\boldsymbol{k}_{\text{in}}$ and $\boldsymbol{k}_{\text{sca}}$ the wavevectors of the incoming and the scattered waves. f_i is the scattering amplitude or form factor of the particle at position $\boldsymbol{r}_i$. It is proportional to the field scattered in direction $\boldsymbol{q}$, and is normalized such that $2\pi \int_0^\pi f_i(\theta)\,\mathrm{d}\theta = \sqrt{\sigma_i}$ where σ_i is the cross section of particle i. In the far field, the distance between the individual scatterers is much smaller than the distance to the observation point, and the distances between each scatterer and observation position $\boldsymbol{R}$ can be approximated with $R \approx \sqrt{|\boldsymbol{R}-\boldsymbol{r}_i|^2}$. Also, when the total volume of the collection of scatterers is small with respect to the wavelength, the external field $E_0(z)$ is the same for each particle. For identical particles, the scattering intensity at position $\boldsymbol{R}$ is then given by

$$I_{\text{sca}}(\boldsymbol{R}, \boldsymbol{q}) = E_{\text{sca}} E^*_{\text{sca}} = \sum_{i,j}^N f^2(\boldsymbol{q}) \frac{e^{i\boldsymbol{q}\cdot(\boldsymbol{r}_i-\boldsymbol{r}_j)}}{R^2} I_0. \tag{3.8}$$

In other words, the scattering intensity is the sum of the phase differences between each particle pair i, j multiplied with the phase function $f^2(\boldsymbol{q})$, and the intensity of the incoming wave I_0.

In a homogeneous and isotropic fluid, the scattered intensity is averaged over all possible particle positions $\boldsymbol{r}_i$, or rather all pairs $\boldsymbol{r}_i$ and $\boldsymbol{r}_j$. After averaging the average scattered intensity can be written as

$$\left\langle I_{\text{sca}}(\boldsymbol{R}, \boldsymbol{q}) \right\rangle_{i,j} = \frac{I_0 f^2(\boldsymbol{q})}{R^2} \left(N + \left\langle \sum_{i \neq j} e^{i\boldsymbol{q}\cdot(\boldsymbol{r}_i-\boldsymbol{r}_j)} \right\rangle_{i,j} \right). \tag{3.9}$$

This equation shows that the scattering intensity is given by the sum of all individual scattering contributions (term with N) and the sum of all constructive and destructive interfering phase differences of each particle pair (term with exponential function). This

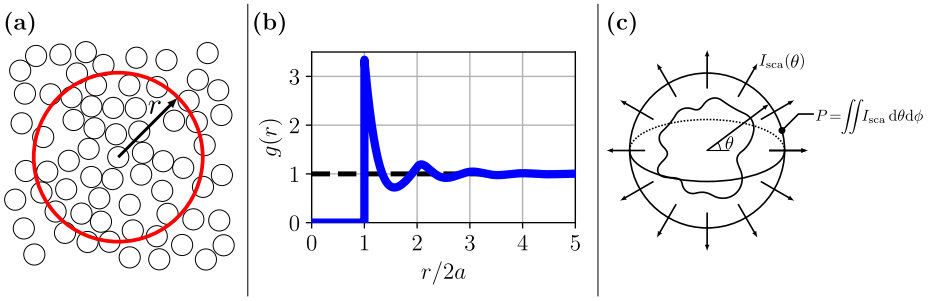

Figure 3.3: (**a**) A distance r, as seen from a random particle. (**b**) Radial distribution function, which is the probability relative to the bulk to find a center of mass of a particle at distance r, for $f_v = 0.4$. (**c**) Integration of the radiated intensity over all directions as done in Eq. 3.14 to obtain the radiated power.

is very similar to the well known Bragg's law, but derived for a small volume element of a correlated particle fluid.

Equation 3.9 is averaged over all particle positions $\boldsymbol{r}_i$ and then for $\boldsymbol{r}_j$ which includes higher-order correlations in the averaging. However, for an isotropic and homogeneous medium, the correlated particle positions should look the same in each direction. This means that the position $\boldsymbol{r}_i$ can be fixed at $\boldsymbol{r}_0 = \boldsymbol{0}$ without loss of generality. Equation 3.9 then only depends on averaging over all particle positions $\boldsymbol{r}_j$ and is given by

$$\left\langle I_{\mathrm{sca}}(\boldsymbol{R},\boldsymbol{q})\right\rangle_j = \frac{I_0 f^2(\boldsymbol{q})N + I_0 f^2(\boldsymbol{q})(N-1)\left\langle \sum_j e^{i\boldsymbol{q}\cdot\boldsymbol{r}_j}\right\rangle_j}{R^2}. \tag{3.10}$$

This approximation is called the quasi-crystalline approximation (QCA) [54]. It has its name, because it is only strictly true for periodic lattices. This approximation eliminates higher order correlations that are otherwise rather cumbersome [56].

Since in a typical physical system the number of particles is very high, it can be assumed that $N \approx N-1$ for which Eq. 3.10 can then be written in a part linear in N, or independent scattering, and a part that contains the averaging over all interference contributions between each particle pair under the QCA. It is this last term that describes the volume fraction-dependent scattering.

$$\langle I_{\mathrm{sca}}(\boldsymbol{R},\boldsymbol{q})\rangle = \overbrace{\frac{I_0 f^2(\boldsymbol{q})N}{R^2}}^{\text{Independent}}\left(1 + \overbrace{\left\langle \sum_j e^{i\boldsymbol{q}\cdot\boldsymbol{r}_j}\right\rangle_j}^{\text{Dependent scattering}}\right) \tag{3.11}$$

The dependent scattering term in Eq. 3.11 contains the particle positions $\boldsymbol{r}_j$ relative to the center of mass of a randomly chosen particle. In Fig. 3.3(a) a dense fluid of hard sphere particles is sketched. The probability relative to bulk of finding a center of mass from a distance r from the particle is given by the radial distribution function $g(r)$ and is shown in Fig. 3.3(b). Since the particles cannot overlap, there is zero probability of finding another particle at distances smaller than twice the particle radius a. In a dense medium, the particles are squeezed together. This means that there is a peak in probability when two particles directly border each other at $r = 2a$ with a the particle radius.

This radial distribution function $g(r)$ indicates the probability of finding a particle at distance r from a given particle and therefore is the weight for each exponential in Eq. 3.11. In other words, the sum in Eq. 3.11 is replaced with an integral

$$\left\langle \sum_j e^{i\boldsymbol{q}\cdot\boldsymbol{r}_j} \right\rangle \rightarrow \int_V g(r) e^{i\boldsymbol{q}\cdot\boldsymbol{r}} \, \mathrm{d}^3\boldsymbol{r} \,. \tag{3.12}$$

Here, V is the volume of the scattering element. Since $g(r)$ is spherically symmetric, and only depends on the distance from the origin r, the integral over the entire volume of the suspension V is a spherical Fourier transform of $g(r)$. This is given by

$$\int_V g(r) e^{i\boldsymbol{q}\cdot\boldsymbol{r}} \, \mathrm{d}^3\boldsymbol{r} = 4\pi \int_0^\infty g(r) \frac{r \sin(qr)}{q} \, \mathrm{d}r = S(q) - 1 \,, \tag{3.13}$$

where $S(q)$ is the structure factor of the suspension. The total power radiated by the small volume element can be obtained by integration over all scattering angles as sketched in Fig. 3.3(c). This can be written as an integral over all angles θ, since the length of the wavevector is given by $q = 2k_m \sin(\theta/2)$, and the number of scatterers replaced by the number of scatterers per unit volume ρ. This integral of Eq. 3.11 gives the radiated power P per unit of volume as

$$P = 2\pi\rho I_0 \int_0^\pi f^2\big(q(\theta)\big) \, S\big(q(\theta)\big) \sin(\theta) \, \mathrm{d}\theta \,. \tag{3.14}$$

The above equation is the volume equivalent of Eq. 3.11. The total radiated power from the volume element is removed from the system. This means that the intensity of the wave in the axial direction after the volume element is given by $I_1 = I_0 - I_{\mathrm{sca}}$. Since, in turn, I_1 is attenuated again by the next scattering layer, this gives rise to a scattering attenuation coefficient μ_{sca} given by

$$\mu_{\mathrm{sca}} = 2\pi\rho \int_0^\pi f^2(\theta) S(\theta) \sin\theta \, \mathrm{d}\theta \,. \tag{3.15}$$

This equation summarizes the effect of far-field interference due to the structure of the scattering medium. This equation is ubiquitous in X-ray scattering [33, 57–62], neutron scattering [60, 63–65] and optical scattering [28, 30, 66].

3.2.4. QCA IN THE SMALL SCATTERING ANGLE LIMIT

Not only for the imaginary part of the effective refractive index, but also for the real part of the complex refractive index the spatial correlations between scatterers can be taken into account with the QCA. The field equations Eq. 3.4 and 3.5 describe the field scattered on a sample with fixed particle positions. The particle positions can be averaged to get the field equations for an effective medium. To get the field at the particle $\boldsymbol{E}(\boldsymbol{r}_0)$, QCA replaces the contribution of all other particles $\boldsymbol{r}_{i\neq 0}$ to the electric field at particle position $\boldsymbol{r}_i$ with the scattered field of an average particle at position $\boldsymbol{r}_j$ weighted by the radial distribution function $g(|\boldsymbol{r}_i - \boldsymbol{r}_j|)$. The Foldy-Lax equations under the QCA are

$$\langle \boldsymbol{E}(\boldsymbol{r}) \rangle = \boldsymbol{E}_{\mathrm{inc}}(\boldsymbol{r}) + N \int_V \overleftrightarrow{G}_m(\boldsymbol{r} - \boldsymbol{r}') U_0(\boldsymbol{r}') \langle \boldsymbol{E}_0(\boldsymbol{r}') \rangle \, \mathrm{d}\boldsymbol{r}' \tag{3.16}$$

and

$$\langle \boldsymbol{E}_0(\boldsymbol{r})\rangle = \boldsymbol{E}_{\text{inc}}(\boldsymbol{r}) + (N-1)\times \int_V \overleftrightarrow{G}_m(\boldsymbol{r}-\boldsymbol{r}')U_0(\boldsymbol{r}')\, g(|\boldsymbol{r}-\boldsymbol{r}'|)\langle \boldsymbol{E}_0(\boldsymbol{r}')\rangle \,\mathrm{d}\boldsymbol{r}'. \tag{3.17}$$

Here, N is the number of particles, $\langle \boldsymbol{E}_0(\boldsymbol{r})\rangle$ the average electric field of a particle and $U_0(\boldsymbol{r})$ the potential of a single particle at position $\boldsymbol{r}$.

When propagating waves are considered, it is useful to express the radial distribution function $g(r)$ as its spherical Fourier transform: the structure factor $S(q)$. Here, $q = 2k_m \sin(\theta/2)$ is the scattering wavenumber and θ the scattering angle. The spatial correlations between particles of different species or in different size bins are encoded in the partial structure factor $S_{i,j}(q)$. A general expression for the partial structure factor of polydisperse hard sphere particles in the Percus-Yevick approximation [67] is given by Tsang *et al.* [68] (Appendix A).

Equations (3.16) and (3.17) can be solved for small size parameters in the small scattering angle limit ($\theta \to 0$), also called the low frequency limit ($q \to 0$) [69]. For a polydisperse particle size distribution, the solution for the complex refractive index $\tilde{n}_{\text{eff}}$ is presented by Ding and Tsang [3] as

$$\tilde{n}_{\text{eff}}^2 = n_m^2 + \frac{3n_m}{D}\sum_i^{N_s} f_{v,i}\, y_i \left\{ 1 + \frac{2i\, n_m^2 k^3}{3D}\left[a_i^3 y + \sum_j^{N_s} 8\pi^3 a_j^3 \rho_j y \left(1 - S_{i,j}(q=0)\right)\right]\right\}. \tag{3.18}$$

Here N_s is the number of size bins and the indices i, j denote the size bins. The concentration of particles of size bin j is ρ_j, $f_{v,i}$ is the volume fraction of particles with radius a_i, and the parameters y and D are given by

$$y = \frac{n_p^2 - n_m^2}{n_p^2 + 2n_m^2} \quad \text{and} \quad D = 1 - \sum_i^N f_{v,i}\, y. \tag{3.19}$$

The expression Eq. (3.18) is henceforth referred to as the low-frequency QCA (LF-QCA) model.

3.2.5. THE COUPLED DIPOLE MODEL

A different approach to obtain the effective refractive index in a scattering medium is to consider the individual molecules that make up a particle as discrete dipole scatterers. The field at the discrete dipole at position $\boldsymbol{r}_i$ is given by:

$$\boldsymbol{E}(\boldsymbol{r}_i) = \boldsymbol{E}_{\text{inc}}(\boldsymbol{r}_i) + \alpha \sum_{j\neq i} \overleftrightarrow{G}_d(\boldsymbol{r}_i - \boldsymbol{r}_j)\boldsymbol{E}(\boldsymbol{r}_j). \tag{3.20}$$

Here α is the polarizability of a dipole and G_d is given by

$$\overleftrightarrow{G}_d(\boldsymbol{r}) = \left[\left(3\hat{\boldsymbol{r}}\otimes\hat{\boldsymbol{r}} - \overleftrightarrow{I}\right)\left(\frac{1}{k^3r^3} - \frac{i}{k^2r^2}\right) \times \frac{1}{kr}(\hat{\boldsymbol{r}}\otimes\hat{\boldsymbol{r}} - \overleftrightarrow{I})\right]\exp(ikr). \tag{3.21}$$

If the particles are considered to be a continuum of dipoles, and the quasi-crystalline approximation is applied, the sum in Eq. 3.20 is replaced with an integral similar to

Eq. (3.17). This is given by

$$\boldsymbol{E}(\boldsymbol{r}_i) = \boldsymbol{E}_{\text{inc}}(\boldsymbol{r}_i) + \alpha\rho k^3 \int_V g_d(|\boldsymbol{r}_i - \boldsymbol{r}'|) \overleftrightarrow{G}_d(\boldsymbol{r}_i - \boldsymbol{r}')\boldsymbol{E}(\boldsymbol{r}')\,\mathrm{d}\boldsymbol{r}'. \tag{3.22}$$

Here, $g_d(r)$ is the dipole radial distribution function.

A solution to Eq. (3.22) was obtained by Parola *et al.* [2]. The field of two counterpropagating waves was chosen as an ansatz for the field $\boldsymbol{E}(\boldsymbol{r}_i)$, and the external field $\boldsymbol{E}_{\text{inc}}$. The complex refractive index was obtained from the consistency conditions required to solve Eq. (3.22) for a correlated dipole fluid.

The refractive index can be obtained from Eq. 3.22 with a similar procedure as is used in Section 2.2.3 for the Lorentz-Lorenz equation. In a molecular dipole fluid, $g_d(r) = 1$ in all space. In that case, the solution to Eq. 3.22 is given by Eq. 2.19. The deviation of the radial distribution function from the mean for an uncorrelated fluid can be written as $h_d(r) = g_d(r) - 1$ where $h(r)$ is zero in the bulk fluid. When the field is assumed to be only varying in the axial direction, that is, it only depends on z, Eq. 3.22 becomes

$$\begin{aligned} E(z_i) =& E_{\text{inc}}(z_i) + E_{\text{LL}}(z_i) + E_{LC}(z_i) + \\ & \alpha\rho k^3 \int_V h_d(|\boldsymbol{r} - \boldsymbol{r}'|) G_d(\boldsymbol{r} - \boldsymbol{r}') \left(A^+ e^{ik_m z'} + A^- e^{-ik_m z'}\right) \mathrm{d}\boldsymbol{r}'. \end{aligned} \tag{3.23}$$

Here E_{LL} is given by the left hand side of Eq. 2.19, and E_{LC} is the field excluded by the Lorentz cavity, given by Eq. 2.22. The field inside the medium is given by the two counterpropagating waves $A^{\pm}e^{\pm ik_m z}$, where the amplitudes $A^{\pm}$ are the same as those obtained in Section 2.2.3. This leads to the Lorentz-Lorenz equation with a correlation factor C resulting from the correlation term in Eq. 3.23,

$$\alpha\rho = \frac{3(n^2-1)}{4\pi\left(C(n^2-1) + (n^2+2)\right)} \tag{3.24}$$

and the correlation integral C given by

$$C = \frac{k^3\alpha\rho}{4\pi} \int G_d(r') h_d(r') \left(A^+ e^{ik_m z'} + A^- e^{-ik_m z'}\right) \mathrm{d}\boldsymbol{r}'. \tag{3.25}$$

Here, z' is the z component of $\boldsymbol{r}'$. For a fully uncorrelated medium, $C = 0$, which reduces Eq. 3.24 to the Lorentz-Lorenz equation given by Eq. 2.24.

In this model, the dipoles are embedded in a particle, as shown in Fig. 3.4. Therefore, the radial distribution function of the dipoles $g_d(r)$ depends on correlations within the same particle, and correlations with dipoles in nearby particles. The intra-particle correlation function $g_{\text{intra}}(r)$ between two dipoles within a particle is given by convolution of the particle shape by itself, i.e.,

$$g_{\text{intra}}(r) = s(r) * s(r) \tag{3.26}$$

with the particle shape function $s(r)$ for a spherical particle with volume v_p given by:

$$s(\boldsymbol{r}) = \frac{1}{v_p}(1 - \Theta(|\boldsymbol{r} - a|)). \tag{3.27}$$

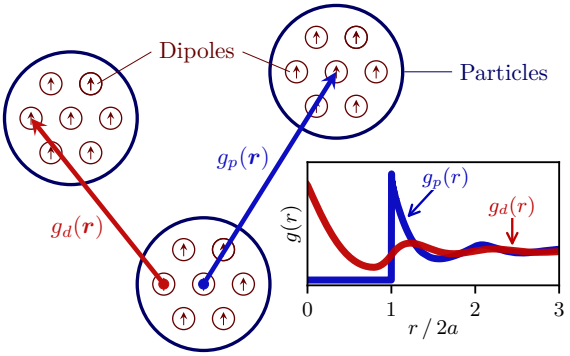

Figure 3.4: Sketch of the coupled dipoles, the scattering particles, and the radial distribution function of the particles $g_p(r)$ (blue) and the discrete dipoles $g_d(r)$ (red).

The inter-particle contribution $g_{\text{inter}}(r)$ is given by:

$$g_{\text{inter}}(r) = s(r) * s(r) * g_p(r) \tag{3.28}$$

The dipole radial distribution function $g_p(\boldsymbol{r})$ is the sum of both the inter-particle and the intra-particle contributions, i.e.,

$$g_d(r) = g_{\text{inter}}(r) + g_{\text{intra}}(r) = s(r) * s(r) * g_p(r) + s(r) * s(r)\,. \tag{3.29}$$

In the Fourier domain, this convolution can be written as a multiplication of the particle structure factor $S_p(q)$ and the spherical Fourier transform of the particle volume squared. The dipole structure factor $S_d(q)$ is then given by:

$$S_d(q) = F^2(q)\left(H(q)+1\right)+1 = F^2(q)S_p(q)+1\,. \tag{3.30}$$

Here, $F(q)$ is the form factor of the particle, which is the Fourier transform of the particle shape, and $H(q) = S(q) - 1$ is the spherical Fourier transform of $g(r) - 1$. Note that the delta peak in the forward direction ($q = 0$) is removed, since this would lead to unphysical results. For a spherical particle the form factor of the particle is given by:

$$F(q) = \frac{4\pi}{v_p}\int \frac{r\sin(qr)}{qr}\left(1-\Theta(r-a)\right)\mathrm{d}r = 3\frac{\sin(qa)-qa\cos(qa)}{(qa)^3}\,. \tag{3.31}$$

For a particle size distribution with size bins i with radius a_i, the partial form factor $F_i(q)$ and partial structure factor $S(q)$ can be geometrically averaged over the particle density per size bin with number density ρ_i as [34]

$$\left\langle a^3F^2(q)S_p(q)\right\rangle_{\text{PSD}} = \frac{\sum_{ij}(a_ia_j)^{3/2}F_i(q)F_j(q)S_{i,j}(q)\sqrt{\rho_i\rho_j}}{\sum_i\rho_i}\,, \tag{3.32}$$

with $S_{i,j}(q)$ the structure factor of size bin i,j. The real part of the effective refractive index n_{eff} of the suspension is then given by [2]

$$\mathrm{Re}\{\tilde{n}_{\mathrm{eff}}\} = n_m + f_v n_m (n_p - n_m) + \frac{f_v n_m}{2}\left(\frac{f_v - 1}{3} + \frac{C_r}{\pi}\right)\left(\frac{n_p - n_m}{n_m}\right)^2, \tag{3.33}$$

with

$$C_r = \frac{1}{3k_m^3}\int_0^\infty \left\langle a^3 F^2(q) S(q)\right\rangle_{\mathrm{PSD}} \left[\frac{8}{3}k_m^3 q - k_m q^3\left(2k_m^4 - k_m^2 q^2 + \frac{q^4}{4}\right)\ln\left(\frac{q+2k_m}{|q-2k_m|}\right)\right] q\,\mathrm{d}q. \tag{3.34}$$

The correlation integral C_r encodes nonlinear scattering effects on the real part of the refractive index. It is dependent on the particle volume fraction through the structure factor $S(q)$.

The imaginary part of the effective refractive index is an integral over the product of the scattering amplitude $f(q)$ and the structure factor over all scattering angles ($q \leq 2k_m$). For a particle size distribution, this is given by Vrij [30, 34] as

$$\mu_{\mathrm{sca}} = 2k\,\mathrm{Im}\{n_{\mathrm{eff}}\} = 2\pi\int_0^\pi \sum_{i,j}^{N} \sqrt{\rho_i \rho_j}\, f_i(\theta) f_j(\theta) S_{i,j}(\theta)\sin(\theta)\,\mathrm{d}\theta. \tag{3.35}$$

The scattering amplitude $f_i(q)$ for a particle in size bin i can be calculated with the particle form factor $F_i(q)$ through [2]

$$f^2(q) = \frac{\alpha_p^2 v_p^2 F^2(q)\left(8k_m^4 - 4k_m^2 q^2 + q^4\right)}{8n_m^2}. \tag{3.36}$$

Here, v_p is the particle volume and α_p is the dimensionless particle polarizability relative to the embedding medium, which is given by

$$\alpha_p = \frac{3}{4\pi}\left(\frac{(n_p - n_m + 1)^2 - 1}{(n_p - n_m + 1)^2 + 2}\right). \tag{3.37}$$

The aim of this work is to experimentally test the predictions given by Eqns. (3.3), (3.18), (3.33), and (3.35) for the concentration dependence of both parts of the complex refractive index. Here the latter two (Eqns. 3.33 and 3.35) are used together to provide the real and imaginary part of the CDM.

3.3. METHODS

3.3.1. EXPERIMENTAL SETUP

Optical properties of colloidal suspensions were measured with an optical setup based on a Mach-Zehnder interferometer. This setup is described in detail in chapter 2. In summary, the visible part of the spectrum with wavelengths between 400 nm and 950 nm emitted by a supercontinuum laser (EVO EUL-10, NKT) is split into the sample arm and the reference arm of the interferometer by a 10-90 beamsplitter (BS025, Thorlabs) and recombined with a 50-50 beamsplitter (BS013, Thorlabs). The spectrum is measured with a spectrometer (FX VIS-NIR, Ocean Optics). The intensity in each arm was measured separately, indicated as $I_{\mathrm{sam}}(k)$ and $I_{\mathrm{ref}}(k)$ for the sample arm and reference arm, respectively. The spectrum measured with both the arms open is given by $I_{\mathrm{tot}}(k)$.

The volume fractions of the prepared silica samples varied between 0.05 and 0.36. The samples were prepared from a stock sample of 0.5 volume fraction 100 nm silica particles (Levasil, Nouryon). This was diluted with demineralized water (Milli-Q 15 MΩcm) to 8 samples with volume fractions ranging from 0.05 to 0.4. In order to make sure the particles behave as hard spheres, 0.2 ml salt solution was added to each sample to lower the zeta potential. The salt solution was prepared with 400 ml demineralized water and 0.95 g NaCl.

The sample was measured in a 1000 µm flow cell (45/Q/1, Starna). The mixture was introduced to the flow cell by a BD10 luer lock syringe. Before each measurement the previous sample was flushed out by water and air. Between each two measurements a calibration measurement with demineralized water was performed. In addition to the interference spectrum, the transmission spectra of the sample arm and the reference arm were measured.

The spectra were obtained with an exposure time that was varied between 200 µs and 1000 µs, depending on the transmittance of the sample. The number of spectra acquired was 1000, except for the measurement at $f_v = 0.36$ where it was set to 10 000.

The variance of the attenuation measurements was determined with Intralipid 20% dilutions with similar attenuation coefficients as the samples of silica particles. These were 11 to 13 measurements of Intralipid for the volume fractions of 0.5 vol.%, 1 vol.% and 2 vol.% of Intralipid 20% in water. The standard deviation was determined as function of wavenumber k and attenuation μ. The standard deviation for a particular silica particle solution measurement was determined with the weighted average of the nearest two measured Intralipid attenuations. Since the transmission spectra of Intralipid differs from those for silica, this was done per wavenumber. The combined results of the Intralipid measurement is the wavelength and attenuation dependent standard deviation of the attenuation of the silica samples $\sigma_\mu(\mu_{\text{sca}}(k), k)$.

3.3.2. TEM PARTICLE ANALYSIS

The PSD of the particles that were used in this experiment was determined with transmission electron microscopy (TEM) analysis. The TEM images were imaged with a Talos

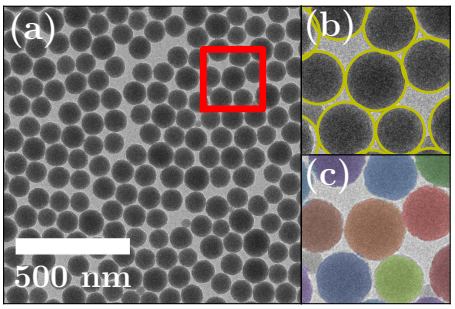

Figure 3.5: (a) TEM image of the silica particles. (b) The yellow circles show the particle circumference obtained with a Hough transform (c) Segmented particles. Pixels with the same color are associated with the same particle.

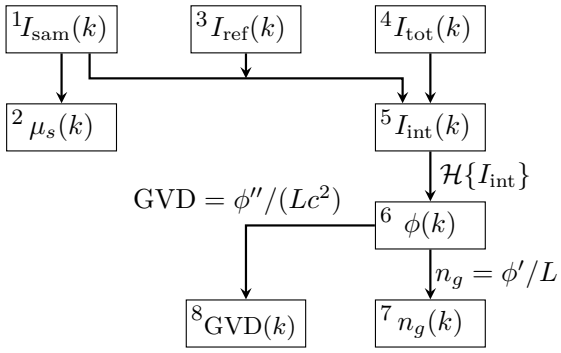

Figure 3.6: Flow chart of the analysis of a single interference spectrum measurement. $\mu_s(k)$, $n_g(k)$ and GVD(k) (steps 2,7,8) are obtained from $I_{\mathrm{sam}}(k)$, $I_{\mathrm{ref}}(k)$ and $I_{\mathrm{tot}}(k)$ as indicated in the main text.

L120C microscope operated at 120 kV. The TEM samples were prepared by drop-casting of the particle solution onto a carbon-formvar coated Cu TEM grid. An example of an acquired TEM image is shown in Fig. 3.5(a). First, the noise in the images was reduced with a convolution with a small square kernel of 5 pixels. Second, local outlying intensity peaks were removed by morphologically opening and subsequently closing the negative image with the same kernel. Third, the particles were selected from the image with a circular Hough transform from the OpenCV package [70], as is shown in Fig. 3.5(b). In total 7730 particles were analyzed in 4 micrographs. The particle diameter was determined from the area of the particles in pixels on the micrograph. This area was determined from the binarized TEM image, which is overlaid on top of the micrograph in Fig. 3.5(c). The cutoff pixel value was determined using Otsu's method [71]. A pixel is counted towards the area of a particle if it is within the Hough radius with a margin of 3 pixels and the pixel is in the binarized image.

3.3.3. PHASE AND AMPLITUDE ANALYSIS

The analysis of a single measurement is summarized in the flow chart shown in Fig. 3.6. The analysis is similar to our previous work [72].

The spectra I_{tot}, I_{sam} and I_{ref} are obtained in the wavelength domain. The wavelengths that are used in the analysis are between 410 nm and 930 nm. The spectra were interpolated to the wavenumber domain to an array size of 8192.

The scattering attenuation $\mu_{\mathrm{sca}}(k)$ is determined in step 1 and 2 of the flow chart from the measured optical transmittance divided by the transmission spectrum with demineralized water. The transmission spectrum of a sample with 5 vol.% particles and its calibration with water are shown in Fig. 3.7(a). The source spectrum $I_{\mathrm{source}}(k)$, the splitting ratio, and the losses of the setup itself are divided out with a calibration measurement of the transmission spectrum of water, where $\mu_{\mathrm{sca}}(k) = 0$. The transmittance, obtained from the ratio between the spectra in Fig. 3.7(a), is shown in Fig. 3.7(c). In step 5, the interference spectrum $I_{\mathrm{int}}(k)$ is calculated from the total spectrum I_{tot} with

$$I_{\mathrm{int}}(k) = I_{\mathrm{tot}}(k) - (I_{\mathrm{sam}}(k) + I_{\mathrm{ref}}(k)) \,. \tag{3.38}$$

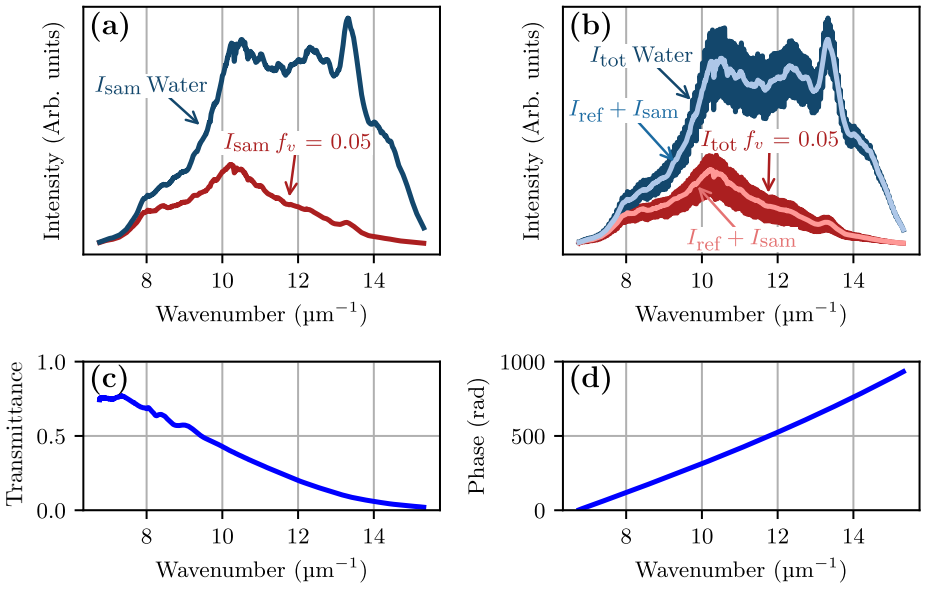

Figure 3.7: Analysis steps of a sample with 5 vol.% silica particles and its calibration measurement. The sample arm intensity $I_{\text{sam}(k)}$ is shown in (a). The interference when both arms are open is shown in (b). The transmittance of the same sample (c) and the spectral phase (d).

The measured spectrum of the same sample with blocked reference arm is shown in Fig. 3.7(b). The phase spectrum $\phi(k)$ is obtained from the Hilbert transform of $I_{\text{int}}(k)$ and fit to a third order polynomial (step 6). In the last steps, the group index and GVD are calculated from the fitted phase $\phi(k)$ with

$$n_g = n + k\frac{dn}{dk} = \frac{1}{L}\frac{d\phi}{dk} \tag{3.39}$$

and

$$\text{GVD} = \frac{2}{c^2}\frac{dn(k)}{dk} + \frac{k}{c^2}\frac{d^2n(k)}{dk^2} = \frac{1}{Lc^2}\frac{d^2\phi(k)}{dk^2}, \tag{3.40}$$

respectively. The group index $n_g(k)$ is related to the frequency of the calibrated interference signal $I_{\text{int}}(k)$. The GVD is related to the chirp of the same signal $I_{\text{int}}(k)$.

3.3.4. MODEL-BASED ANALYSIS

The model-based analysis is based on two independent fitting routines: one for the refractive index and one for the attenuation coefficient. A flowchart of the forward fitting algorithm is shown in Fig. 3.8. The fitting routine is executed for every volume fraction together.

In the refractive index routine the effective group refractive index as a function of wavenumber is calculated with either the LF-QCA and CDM scattering models. This loop uses a mean particle radius $\langle a \rangle$ and a phase index as initial input. The phase index

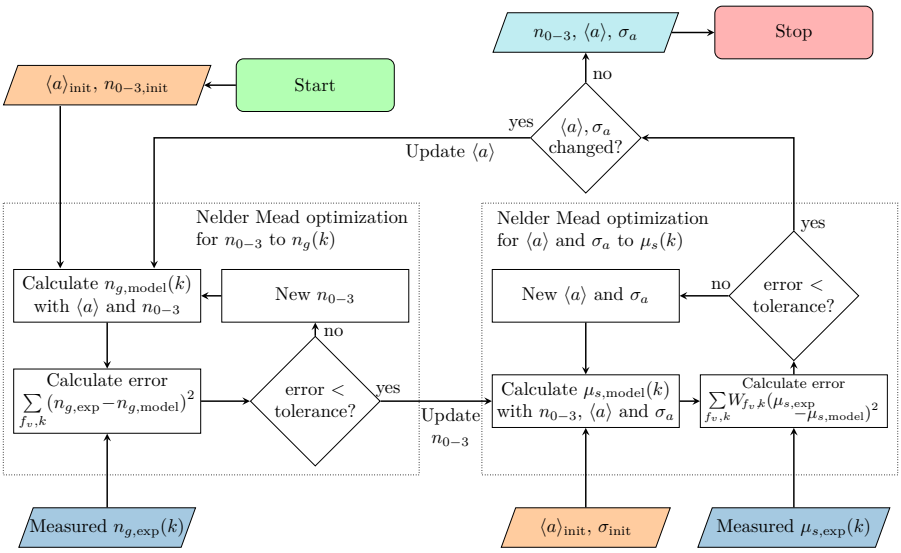

Figure 3.8: Flow chart of the fitting procedure with the forward model. The parallelograms indicate the in and output. The measured data are shown in blue, initial values are shown in beige and the fit parameters are shown in cyan.

of the particle is described by a polynomial expansion as

$$n_p(k) = n_0 + n_1 k + n_2 k^2 + n_3 k^3 . \tag{3.41}$$

The initial polynomial parameters n_{0-3} of the phase index were chosen for silica particles with a porosity of 15% based on Daimon [73] and Malitson [74] for water and silica, respectively.

The initial radius $\langle a \rangle$ was set to 50 nm. For particles that are small compared to the wavelength, the polydispersity has a small effect on the effective refractive index. Therefore, to speed up the calculation, the effective refractive index is calculated for a monodisperse suspension with radius $\langle a \rangle$.

For the LF-QCA model, the phase index of the suspension $\text{Re}\{\tilde{n}_{\text{eff}}(k)\}$ was calculated from Eq. 3.18. The phase index for the CDM was calculated with Eq. 3.33. From the estimated phase index, the effective group index of the suspension was calculated from Eq. 3.39 and was compared to the measured group index.

An estimate of the phase index of the particles was obtained by minimizing the sum of the square difference for all volume fractions between the measured effective group index and the fitted effective group index, as predicted from the refractive index model with volume fraction f_v and radius $\langle a \rangle$ as input. In successive iterations the square error was minimized with Scipy's [75] Nelder-Mead algorithm [76] using the default precision.

After obtaining sufficiently close agreement between the modeled group index and the measured group index the algorithm switches to estimate the attenuation coefficient, indicated with the loop shown on the right in the flow chart. Here, the particle size distribution is obtained from a fit of $\mu_s(k)$ from the LF-QCA and CDM models to the

attenuation with the estimated fit of the phase index from the previous loop. The particle size distribution was parameterized with a normal distribution with mean radius $\langle a \rangle$ and standard deviation σ_a. For the LF-QCA model, $\mu_{\text{sca}}(k)$ was calculated from Eq. (3.18). For the CDM, $\mu_{\text{sca}}(k)$ was calculated from Eq. (3.35). The error that was minimized is the square difference between the measured attenuation and the modeled attenuation with relative weights $W_{f_v,k} = 1/\sigma^2_{f_v,k}$ with $\sigma^2_{f_v,k}$ the variance in μ_{sca} obtained from the Intralipid measurements. Similar to the case for the refractive index loop, the error was minimized using the Nelder-Mead algorithm. The initial polydispersity was set at 5% of the mean radius of $\langle a \rangle_{\text{init}}$.

The forward models for both $n(k)$ and $\mu_{\text{sca}}(k)$ were computed on the wavelength range of 410 nm to 930 nm for 256 wavelengths. To compare with the measured scattering attenuation and group index, the measured data is interpolated to match the wavelengths of the forward fit. The scattering attenuation is calculated for 64 particle size bins within four standard deviations of the mean. This was done to make the quality of the sampling independent of the standard deviation of the particle radius σ_a.

The obtained mean particle radius $\langle a \rangle$ is transferred from the attenuation loop to the refractive index loop to calculate the polynomial parameters of the phase index n_{0-3} of the particles with the refractive index models. This phase index is then used to update the PSD in the attenuation loop. This procedure is repeated until no further improvement in the estimated mean diameter and polydispersity could be achieved. In practice, the diameter and polydispersity often do not significantly change after the first two iterations, and do not change within machine precision after approximately the sixth iteration, depending on the used model.

After completion of the full optimization routine, the porosity $f_{v,\text{pores}}$ is calculated from the fitted phase index of the silica particles with the assumption that the pores fully consist of water. The porosity is then calculated with

$$f_{v,\text{pores}} = \left\langle \frac{n_{\text{fit}}(k) - n_{\text{bulk}}(k)}{n_{\text{water}}(k) - n_{\text{bulk}}(k)} \right\rangle_k , \tag{3.42}$$

where $n_{\text{bulk}}(k)$ is taken from Malitson *et al.* [74] and $n_{\text{water}}(k)$ is taken from Daimon *et al.* [73].

3.3.5. ESTIMATION OF THE CONFIDENCE INTERVAL

The confidence interval of the mean diameter $\langle a \rangle$ and polydispersity σ_a is estimated from the weighted residual R

$$R(\langle a \rangle, \sigma_a) = \sum_{f_v,k} W_{f_v,k} (\mu_{s,\text{exp},k,f_v} - \mu_{s,\text{fit},k,f_v}(\langle a \rangle, \sigma_a))^2 . \tag{3.43}$$

Here μ_{exp} is the measured attenuation, μ_{fit} the fitted attenuation and W the weights given by the Intralipid measurements. The region of confidence can be estimated as the region $R(\langle a \rangle, \sigma_a)$ that lies below a threshold R_{cutoff} [77, 78]

$$R(\langle a \rangle, \sigma_a) \leq R_{\text{cutoff}} . \tag{3.44}$$

To heuristically find a reasonable R_{cutoff}, we fit $\langle a \rangle$ and σ_a to an attenuation spectrum with one standard deviation offset given by

$$\mu_{\text{var}}(f_v, k) = \mu_{\text{exp}}(f_v, k) + \sigma_\mu(f_v, k)/\sqrt{N}. \tag{3.45}$$

Here, μ_{var} is the attenuation spectrum perturbed with the measured standard deviation, N is the number of different measured volume fractions, which is 8, and $\sigma_\mu(f_v, k)$ is the standard deviation as determined from the Intralipid measurements. The $\langle a \rangle_{\text{var}}$ and $\sigma_{a,\text{var}}$ are the mean radius and polydispersity fitted to μ_{var}. The cutoff residual R_{cutoff} is then given by

$$R_{\text{cutoff}} = R(\langle a \rangle_{\text{var}}, \sigma_{a,\text{var}}). \tag{3.46}$$

The region of confidence for $\langle a \rangle$ and σ_a is then given by Eq. (3.44).

3.4. RESULTS

3.4.1. REAL PART OF THE EFFECTIVE REFRACTIVE INDEX

The measured group index and GVD for a volume fraction of $f_v = 0.36$ colloidal silica particles are shown in blue in Fig. 3.9. The result of the model-based analysis with the CDM model that best matches the data is shown in red. Because this is a result of a fit to all wavelength and volume fraction data, not just to the measurement at $f_v = 0.36$, a small offset from the group index data is present.

The volume fraction dependence of the model-based analysis of the group index is shown in Fig. 3.10 for the wavelengths 450 nm and 800 nm. Both n_g and GVD are linearly dependent on volume fraction with no discernible nonlinearity in the group index data. The prediction from the CDM model is shown in red. The group index obtained with

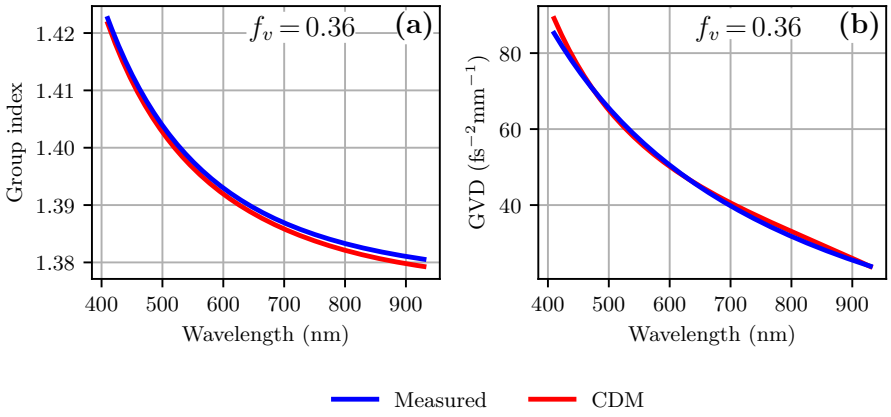

Figure 3.9: Measured group index (a) and GVD (b) at different wavelengths compared to the Parola model for a volume fraction of $f_v = 0.36$ of silica particles in water.

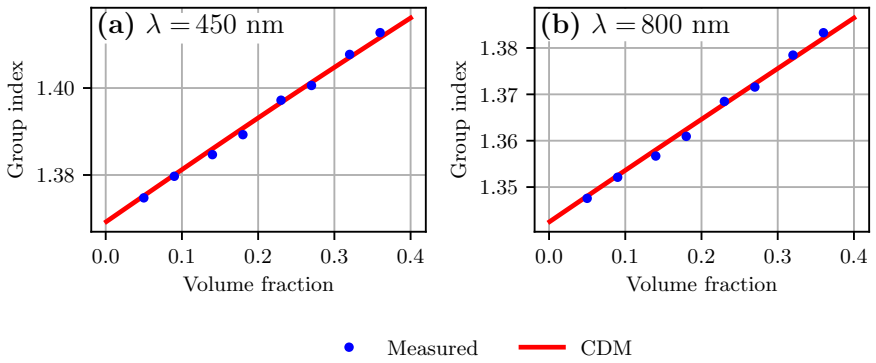

Figure 3.10: Measured and modeled group index at λ = 450 nm (a) and λ = 800 nm (b) for different volume fractions of silica particles in water.

LF-QCA is not appreciatively different from CDM and is not plotted in Figs. 3.9 and 3.10. The measurement uncertainty is of similar size as the plot markers.

For the real part of the effective refractive index, the most significant discriminator between the CDM and LF-QCA effective refractive index models is the volume fraction dependence of the GVD. In Fig. 3.11 the measured GVD and the fitted GVD are shown for various wavelengths. For all wavelengths, with the exception of the GVD measured at wavelengths longer than 700 nm, the GVD is nonlinear with increasing particle volume fraction, particularly for lower wavelengths. It is remarkable that all models quantitatively match the data so well, despite the fact that the group index shown in Fig. 3.10 shows an almost perfect linear behavior. The volume fraction dependence of the GVD at a single wavelength is small compared to the difference in GVD between the lowest and highest measured wavelength.

The CDM describes the measured GVD reasonably well for all wavelengths. It does have a constant offset at some wavelengths, but CDM clearly predicts a non-linear behavior of the GVD with volume fraction. The GVD, as calculated with the LF-QCA and van de Hulst model, is indicated with the dotted lines in green and purple. The LF-QCA and van de Hulst models always predict a linear increase of the GVD with volume fraction, which is clearly not in good agreement with the data. Note that the phase index used for the van de Hulst model was taken to be the same as for the CDM. The uncertainty in the measurements is smaller than the plot markers.

The phase index of the silica particles that is obtained with the CDM and LF-QCA model are shown in Fig. 3.12. Both models lead to a similar phase index. For comparison, the phase index of pure, nonporous silica is shown in black. The porosity, as obtained from the phase index of the particle obtained with the CDM, is 12.5%.

3.4.2. IMAGINARY PART OF THE EFFECTIVE REFRACTIVE INDEX

The measured scattering attenuation $\mu_{sca}(k)$ for the volume fractions of 0.05 and 0.36 as a function of wavelength is shown in Fig. 3.13, together with the CDM and LF-QCA

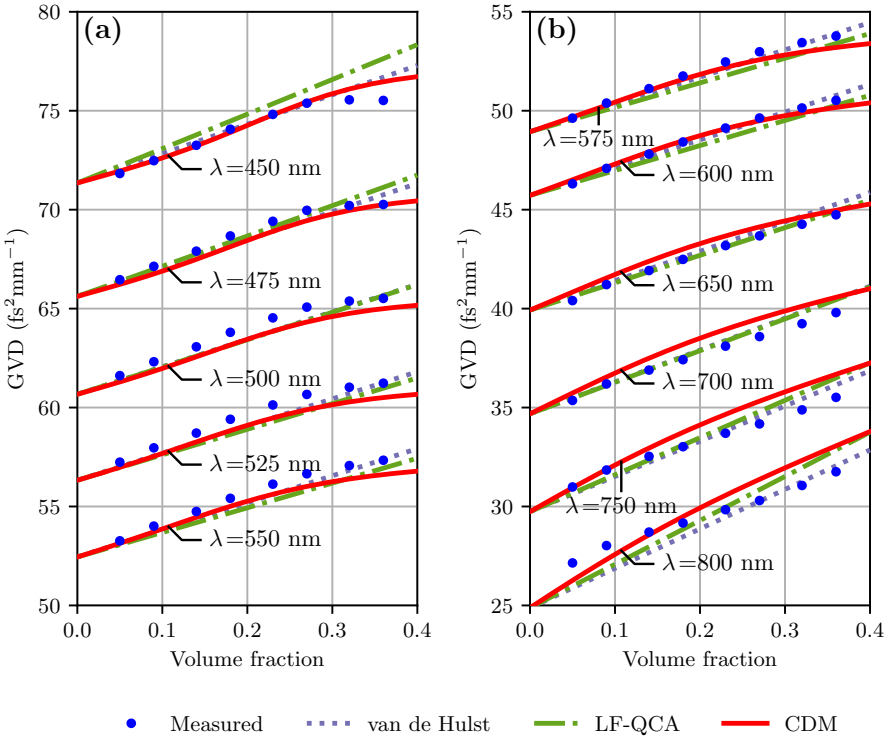

Figure 3.11: GVD for various wavelengths and models. The CDM model describes the shape of the volume fraction dependence reasonably well. For low volume fractions the van de Hulst formula gives adequate results. At high wavelengths, the size of the particle becomes small compared to the wavelengths, thus leading to a more linear increase of GVD with volume fraction.

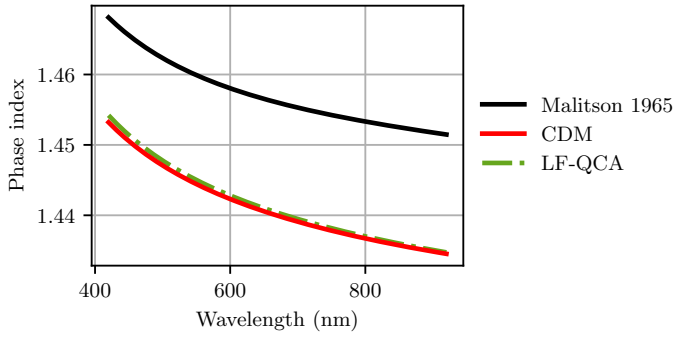

Figure 3.12: Phase index of silica particles as determined with the various models from the model-based analysis compared to the phase index of nonporous silica (black).

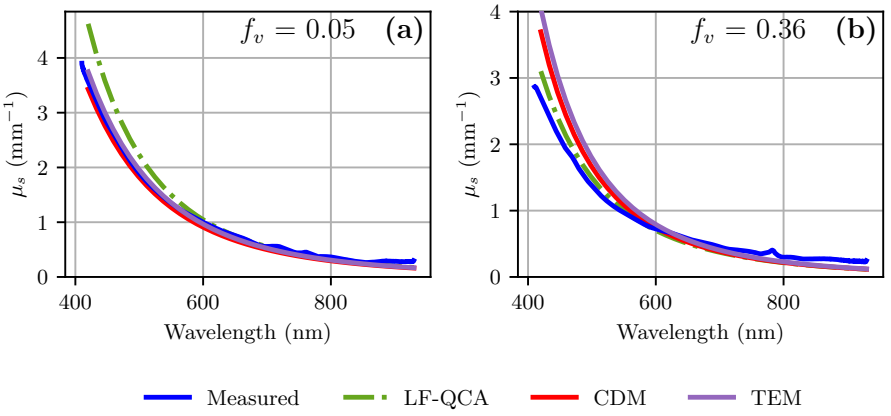

Figure 3.13: Measured scattering attenuation $\mu_{sca}(\lambda)$ compared with the fits with the various models. The CDM prediction of $\mu_{sca}(\lambda)$ for the PSD obtained with TEM is shown in purple

model predictions. For comparison, the CDM prediction with the PSD obtained from the TEM analysis is also shown in Figs. 3.13 and 3.14. For the volume fraction of 0.05, the CDM closely matches the measured attenuation, whereas the LF-QCA model overestimates the attenuation coefficient for shorter wavelengths. For higher volume fractions, it is the CDM that has an overestimation at lower wavelengths.

The differences for the various scattering models is more clearly visible when the scattering attenuation is visualized as a function of volume fraction, as shown in Fig. 3.14. For short wavelengths the higher attenuation results in a more precise attenuation measurement (smaller error bars). For the wavelengths 450 nm and 500 nm the CDM model is very close to the measured attenuation. However, for longer wavelengths both the LF-QCA and the CDM underestimate the measured attenuation at high volume fractions. The volume fraction of maximum attenuation for the CDM is 17.0% at $\lambda = 450$ nm and 14.5% at $\lambda = 700$ nm. For the LF-QCA model this is 13.2%. The peak of the CDM is closer to the measured maximum.

The particle size distribution as obtained from the TEM analysis and the model-based analysis for $\langle a \rangle$ and σ_a is shown in Fig. 3.15. The mean particle diameter as obtained with the CDM is 102.2 nm with a confidence interval of (97.5 nm, 105.5 nm) with a polydispersity of 6.6% (1.7%, 13.4%). For the LF-QCA model this is 89.7 nm (79.7 nm, 96.9 nm. The polydispersity obtained with the LF-QCA model is 19.6% (15.4%, 25.4%). The mean size and polydispersity obtained from the TEM images is 99.7 nm and 9.4%.

3.5. DISCUSSION

3.5.1. COMPARISON OF COMPLEX REFRACTIVE INDEX MODELS

To the best of our knowledge we are the first to compare experimental results with the CDM model. This is in contrast to the LF-QCA in the small scattering angle limit that is widely used to model the dependent scattering effect on both the imaginary part [79, 80]

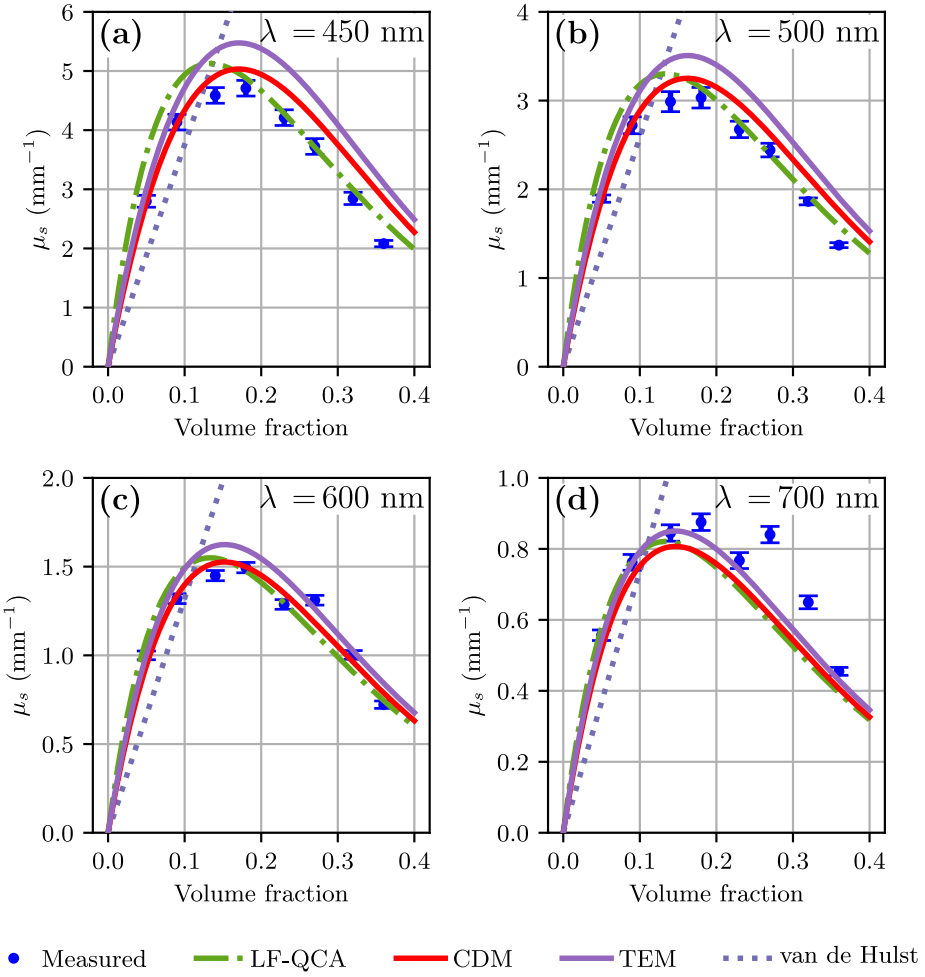

Figure 3.14: Scattering attenuation as function of the volume fraction for four wavelengths.

and the real part of the effective refractive index [23, 39]. The CDM and LF-QCA have in common that for both models the effective complex refractive index scales nonlinearly with the volume fraction of the suspended particles.

The CDM accurately describes both the imaginary and the real part of the effective refractive index. It is particularly noteworthy that this model is able to predict reasonably well the nonlinear shape of the measured GVD curves. The LF-QCA model describes the real refractive index reasonably well, but does not predict a nonlinear volume fraction dependence of the GVD. Instead, it predicts a linear behavior, which is clearly not in agreement with the measurements. The possible reason for this difference in behavior in the GVD is that the full q dependence of the structure factor is not used for the LF-QCA model, whereas for the CDM the full structure factor from 0 to $2k_m$ is taken into

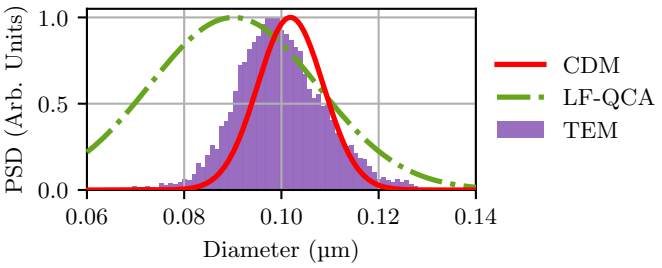

Figure 3.15: Particle size distribution as determined with the model-based analysis compared with the distribution as obtained from TEM.

account.

The LF-QCA model performs poorly on inverting the measured attenuation spectra to a PSD, since for the LF-QCA model an increase of polydispersity and an increase of mean particle radius have a similar effect on the attenuation spectrum. For longer wavelengths, the LF-QCA model and the CDM provide similar results for the imaginary part of the refractive index. However, for shorter wavelengths, the prediction for the attenuation coefficient of the LF-QCA model is shifted upwards compared to the low volume fraction experimental data and the CDM. For high volume fractions and at low wavelengths, the LF-QCA model deviates less from the measured attenuation than the CDM.

The shape of the volume fraction dependence of the scattering attenuation as calculated with the LF-QCA model does not change with the size parameter. For example, the maximum attenuation is at $f_v = 0.13$ for all wavelengths. However, the experimental data show that the volume fraction of maximum attenuation does depend on wavelength. This is visible in the CDM fit, where the peak of maximum attenuation varies with wavelength. The difference between the model predictions is due to the low frequency solution of the LF-QCA that assumes a small particle size parameter x, which at $\lambda = 450$ nm with $x = 0.94$ is clearly violated.

The small particle assumption of the LF-QCA also complicates the retrieval of the PSD through the iterative model-based fit. Moreover, the mean diameter and the polydispersity are strongly correlated. Increasing the mean particle size or increasing the polydispersity has similar effects on the scattering attenuation and therefore cannot independently be determined. This effect is visible in the obtained PSD parameters where both the mean particle radius $\langle a \rangle$ and polydispersity σ_a do not closely match the ground truth obtained with TEM. The CDM model yields reasonable estimates for both the mean particle size and the polydispersity, as it encodes the effect of polydispersity on the attenuation better.

In addition to the low-frequency QCA and CDM models, we have tested the low-frequency QCA with coherent potential (QCA-CP) [3] and Keller [14] models for the complex refractive index. The refractive index and attenuation predicted by QCA-CP is very similar to that as predicted by LF-QCA. The Keller model did not perform well for the attenuation, since the particles used in this work have a too low size parameter. Better results with the Keller model can be obtained with larger particles [81]. Interestingly, the

Keller model predicts a strong volume fraction dependence on the GVD, which, however, does not match data well. The comparison with these models can be found in Appendix B.

3.5.2. STRUCTURAL CORRELATION EFFECTS ON THE REFRACTIVE INDEX

We have shown how dependent scattering encoded in the partial structure factor $S_{i,j}(q)$ affects the refractive properties of a colloidal medium. Both the real and imaginary part of the effective refractive index are dependent on concentration through the structure factor. We believe we are the first to measure a nonlinear dependence of the real part of the effective refractive index on the particle volume fraction. Previous work was limited to the liquid-crystal phase transition of a colloidal crystal. For example, Okubo [41] measured an increase in the refractive index due to a phase transition in a dense colloidal medium. However, no comparison with a refractive index model was made, and no nonlinear concentration dependence in the liquid phase, other than the phase transition, was observed.

The experiments presented in this work were performed with to a high degree hard sphere particles. This has the advantage that a clear comparison with the theory can be made through the Percus-Yevick approximation of the structure factor. Hence, other structures, such as non-spherical particles, may give rise to different optical properties [82, 83], but can be described using the same formalism as long as the structure factor is known. Furthermore, the ionicity of the fluid strongly influences the interactions. For example, a lower salt concentration can give rise to an artificially high volume fraction [41, 84], since the particles occupy a higher effective volume due to the repellent inter-particle force. At a given particle volume fraction, this would lead to a stronger effective non-linear effect on the GVD. In this case, the hard sphere potential would need to be replaced by a potential based on the zeta potential of the particle for obtaining an accurate structure factor.

3.5.3. SCATTERING FORM FACTOR

Parola *et al.* provided a concentration dependent scattering amplitude $f_{\mathrm{CDM}}(q)$ given by Eq. (3.36) that is approximately equal to the Mie scattering amplitude $f_{\mathrm{Mie}}(q)$, shown in Fig. 3.16(a). In the Rayleigh regime, the differences between these scattering amplitudes are negligible. However, for larger particles, evaluation of Eq. (3.35) with the approximate $f_{\mathrm{CDM}}(q)$, gives a slightly lower attenuation than expected from the Mie solution, as can be seen in Fig. 3.16(b). When the Mie scattering amplitude is used, the estimated PSD is only slightly closer to the PSD as obtained with TEM: the Mie-based PSD has a mean diameter of 100.7 nm and a polydispersity of 6.4%. However, this result does not significantly differ from the PSD as obtained with the scattering amplitude of Eq. (3.36). Therefore, the particles used in this work were small enough to be well described with the CDM scattering amplitude.

To use the CDM for larger particles, the Mie scattering amplitude is more accurate. However, incorporation of the Mie phase function in CDM as used in Eq. (3.34) is not possible due to the integration boundaries spanning infinite q range. An ad-hoc solution would be to split the form factor such that for $q < 2k_m$ the Mie scattering amplitude f_{Mie} is used and for $q \geq 2k_m$ the CDM scattering amplitude f_{CDM}. However, in contrast to the

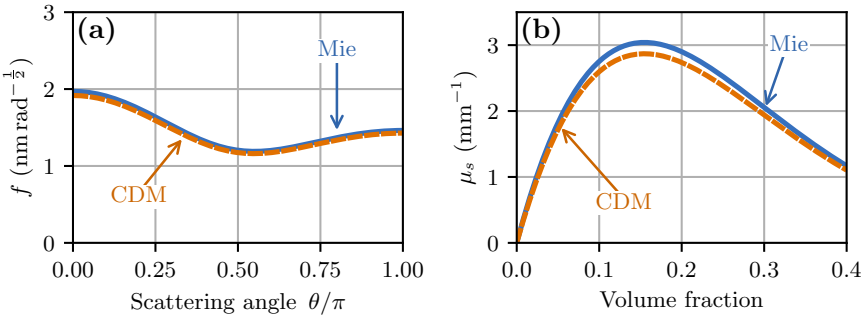

Figure 3.16: **(a)** The CDM scattering amplitude $f_{\mathrm{CDM}}(\theta)$ compared with the Mie form factor $f_{\mathrm{Mie}}(\theta)$ for monodisperse 100 nm particles at $\lambda = 500$ nm with a refractive index as measured in this work. In **(b)** the corresponding attenuation is shown.

calculation of the scattering attenuation, this would not make a measurable difference to the real part of the refractive index.

3.5.4. EFFECTS OF POLYDISPERSITY

The group index calculations were performed for a monodisperse particle size distribution and not by the polydisperse PSD used in the attenuation loop. This choice is substantiated by the fact that calculations showed that any realistic polydispersity of the particle suspension has only limited effect on the group index and the GVD, as can be seen in Fig. 3.17. Figure 3.17 shows that the GVD at the wavelengths of 500 nm and 600 nm is plotted for a monodisperse particle size distribution and a normal particle size distribution with a strong polydispersity of 20% for particles with an average diameter of 50 nm, 100 nm and 200 nm and the same refractive index as measured for the silica particles as used in this work. Even for a polydispersity of 20%, the effect of the size distribution on the GVD is very low for diameters smaller than 100 nm. It also shows that for smaller particles the particle correlations encoded in $g(r)$ have a negligible effect on the GVD, as would be expected for a molecular mixture [72].

Although the concentration effect on the group index and GVD was rather small for 100 nm particles, it was large enough to fit the phase index and distinguish the behavior of the different models. For larger particles Parola *et al.* predicted a more prominent concentration dependence of the refractive index for size parameters x between 1.5 and 2.0, particularly for a volume fraction higher than 0.3. This would correspond to particles with a diameter of 200 nm in Fig. 3.17. Therefore, it would be of interest to investigate the concentration dependence of larger particles.

3.5.5. MEASUREMENT OF PARTICLE PROPERTIES

The refractive index, PSD, and porosity of a sample of silica nanoparticles was determined through a fit of the refractive index and particle properties. The mean particle size and polydispersity obtained with the LF-QCA model deviates significantly from that

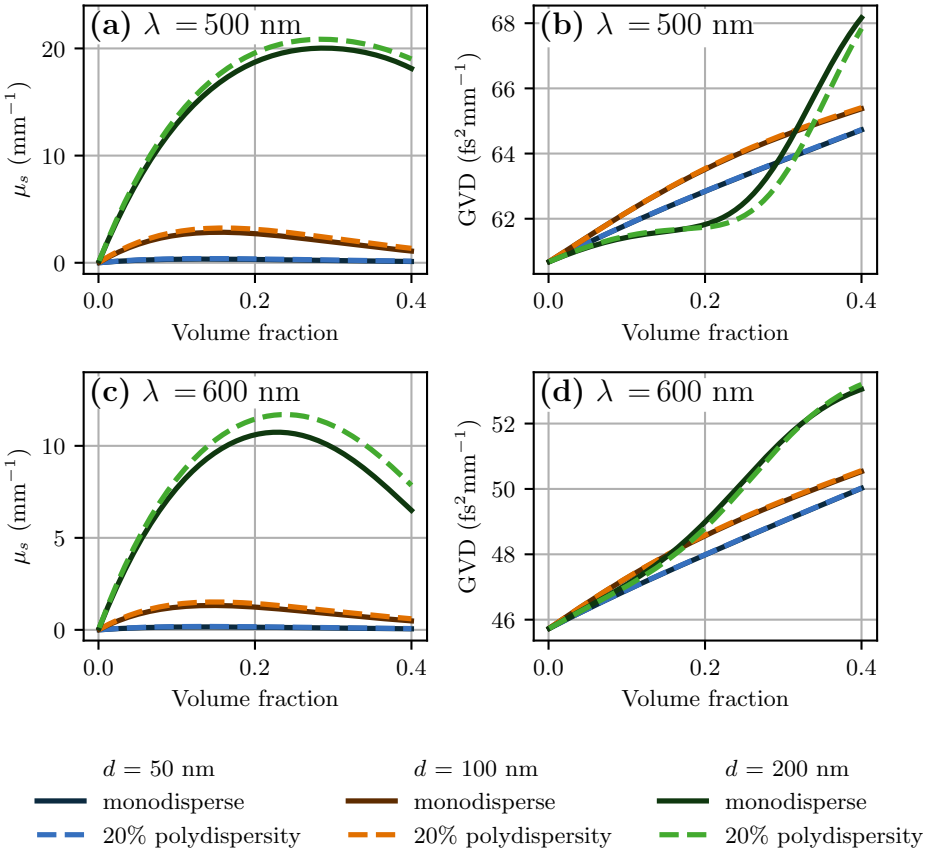

Figure 3.17: CDM calculations of the concentration dependence of the scattering attenuation μ_s and the GVD for particles with a diameter of 50 nm, 100 nm and 200 nm at the wavelengths of 500 nm and 600 nm.

obtained with TEM. Better results are obtained with the CDM, where the PSD has a mean radius very close to that obtained with TEM. However, the estimated polydispersity is lower compared to the TEM images, albeit comparable. A main contributor to the size of the confidence intervals of the diameter and polydispersity, is the strong correlation between them. Therefore, the confidence interval would be smaller for larger size parameters where the effects of the mean size and polydispersity on the scattering attenuation spectrum $\mu_{\text{sca}}(k)$ can be better separated. The porosity obtained from the CDM is 12.5%, which is similar to reported in literature for silica particles grown with the Stöber method, where this varied between 9% and 13% [85–87].

The phase index of the suspended particles themselves is determined by means of comparing forward modeling with measurements. Therefore, we present here an unintrusive method to determine the refractive index of the colloidal particles within a suspension. This can be beneficial in the case of porous particles, where the phase index

of the particles cannot be retrieved with an index matching experiment. Moreover, this provides an opportunity for particle sizing methods based on light scattering, since the CDM for the scattering attenuation is dependent on knowledge of the refractive index of the particles. In fact, uncertainty of the refractive index of the particle can be a limiting factor in the accuracy of particle sizing with Mie inversion [28, 88]. Furthermore, the effective refractive index itself has been used for particle sizing for a few decades [36]. Therefore, understanding of the concentration dependence of the effective refractive index is important, at least to give an upper bound for the volume fraction under which the regularly used van de Hulst or Arago-Biot equations are valid.

In this work, the inversion required measurements at different a priori known volume fractions. Obviously, this is not possible when measuring at a single volume fraction. However, when the refractive index of the particle is known a priori, measurement of the group index could be used for direct measurement of the volume fraction [72]. This could eliminate the need for measurements at different volume fractions for determining the particle size.

Although the wavelength range of 410 nm to 930 nm is broad, for distinguishing the effect of the mean diameter from the polydispersity, it is best to use wavelength such that $x > 1$, i.e., using smaller wavelengths than used here for 100 nm particles. This will allow for a better PSD reconstruction due to the Mie resonances, even without parametrization of the PSD [89]. For the particles used in this work, this would mean measurements of fewer volume fractions would be required when the transmittance would be measured at lower wavelengths.

3.6. CONCLUSION

In this work, the concentration dependence of the effective complex refractive index of a colloidal suspension of 100 nm silica nanoparticles was investigated with spectral interferometry. For the real part of the effective refractive index, it was found that the group index scaled linearly with the volume fraction but that the concentration dependence of the GVD was nonlinear.

The data were compared to two models: the coupled dipole model proposed by Parola *et al.* provided both quantitatively and qualitatively a good description for both the group index and the GVD. The LF-QCA model did not predict the nonlinear behavior of the GVD.

The models were used in an iterative loop to estimate the mean particle radius, polydispersity, and porosity. For the CDM, the porosity of the particles was 12.5%. The particle size was found to be 102.2 nm with a polydispersity of 6.6%. The size distribution obtained with the small angle LF-QCA model had a mean diameter of 89.7 nm and a polydispersity of 19.8%. The results obtained with the CDM were in good agreement with electron microscopy measurements.

DATA AVAILABILITY

Data underlying the results presented in this chapter and the relevant analysis routines are available in Ref. [90].

ACKNOWLEDGMENT

We would like to thank Kelly J.H. Brouwer in collaboration with the Electron Microscopy Centre at Utrecht University for the TEM images she provided.

REFERENCES

[1] P. N. A. Speets and J. Kalkman, Experiment and theory of the complex refractive index of dense colloidal media, *Journal of the Optical Society of America A*, 41(2):214–228, 2024.

[2] A. Parola, R. Piazza, and V. Degiorgio, Optical extinction, refractive index, and multiple scattering for suspensions of interacting colloidal particles, *Journal of Chemical Physics*, 141(12): 124902, 2014.

[3] K. H. Ding and L. Tsang, Effective propagation constants of dense nontenuous media with multi-species of particles, *Journal of Electromagnetic Waves and Applications*, 2(8):757–777, 1988.

[4] L. Lorenz, Experimentale og theoretiske undersøgelser over legemernes brydningsforhold, *Det Kongelige Danske Videnskabernes Selskabs Skrifter*, 5(10):483–518, 1875.

[5] H. A. Lorentz, Over het verband tusschen de voortplantingssnelheid van het licht en de dichtheid en samenstelling der middenstoffen, *Verhandelingen der Koninklijke Academie van Wetenschappen*, 18, 1879.

[6] J. B. Biot and D. F. Arago, Sur les affinités des corps pour la lumière, et particulièrement sur les forces réfringentes des différens gaz, *Mémoires de l'Académie des sciences de l'Institut de France*, 6:301–387, 1806.

[7] J. P. McClymer, Precise determination of the refractive index of suspended particles: light transmission as a function of refractive index mismatch, *American Journal of Physics*, 84(8): 602–605, 2016.

[8] J. C. M. Garnett, XII. Colours in metal glasses and in metallic films, *Philosophical Transactions of the Royal Society of London. Series A, Containing Papers of a Mathematical or Physical Character*, 203:385–420, 1904.

[9] D. A. G. Bruggeman, Berechnung verschiedener physikalischer Konstanten von heterogenen Substanzen. I. Dielektrizitätskonstanten und Leitfähigkeiten der Mischkörper aus isotropen Substanzen, *Annalen der Physik*, 416(7):636–664, 1935.

[10] W. Heller, The determination of refractive indices of colloidal particles by means of a new mixture rule or from measurements of light scattering, *Physical Review*, 68:5–10, 1945.

[11] L. L. Foldy, The multiple scattering of waves. I. general theory of isotropic scattering by randomly distributed scatterers, *Physical Review*, 67:107–119, 1945.

[12] M. Lax, Multiple scattering of waves, *Reviews of Modern Physics*, 23:287–310, 1951.

[13] B. H. Zimm and W. B. Dandliker, *Theory of Light Scattering and Refractive Index of Solutions of Large Colloidal Particles*, American Chemical Society, 1954.

[14] J. B. Keller, Stochastic equations and wave propagation in random media, *Proceedings of Symposia in Applied Mathematics*, 16:145–170, 1964.

[15] H. Looyenga, Dielectric constants of heterogeneous mixtures, *Physica*, 31(3):401–406, 1965.

[16] J. V. Champion, F. H. Meeten, and M. Senior, Refraction by spherical colloid particles, *Journal of Colloid and Interface Science*, 72(3):471–482, 1979.

[17] H. C. van de Hulst, *Light Scattering by Small Particles*, Dover Books on Physics. Dover Publications, 1981, ISBN 9780486642284.

[18] L. Tsang, J. A. Kong, and R. T. Shin, *Theory of Microwave Remote Sensing*, Wiley Series in Remote Sensing and Image Processing. Wiley, 1985, ISBN 9780471888604.

[19] W. T. Doyle, Optical properties of a suspension of metal spheres, *Physical Review B*, 39:9852–9858, 1989.

[20] L. Hespel, S. Mainguy, and J. Greffet, Theoretical and experimental investigation of the extinction in a dense distribution of particles: nonlocal effects, *Journal of the Optical Society of America A*, 18(12):3072–3076, 2001.

[21] S. Durant, O. Calvo-Perez, N. Vukadinovic, and J. Greffet, Light scattering by a random distribution of particles embedded in absorbing media: diagrammatic expansion of the extinction coefficient, *Journal of the Optical Society of America A*, 24(9):2943–2952, 2007.

[22] Y. Battie, A. Resano-Garcia, N. Chaoui, Y. Zhang, and A. En Naciri, Extended Maxwell-Garnett-Mie formulation applied to size dispersion of metallic nanoparticles embedded in host liquid matrix, *Journal of Chemical Physics*, 140(4):044705, 2014.

[23] A. Acevedo-Barrera and A. Garcia-Valenzuela, Analytical approximation to the complex refractive index of nanofluids with extended applicability, *Optics Express*, 27(20):28048–28061, 2019.

[24] A. Doicu and M. I. Mishchenko, Electromagnetic scattering by discrete random media. I: The dispersion equation and the configuration-averaged exciting field, *Journal of Quantitative Spectroscopy and Radiative Transfer*, 230:282–303, 2019.

[25] A. García-Valenzuela, A. Acevedo-Barrera, O. Vázquez-Estrada, A. Nahmad-Rohen, and R. G. Barrera, Full dynamic corrections to the Maxwell Garnett mixing formula and corresponding extensions beyond the dipolar approximation, *Journal of Quantitative Spectroscopy and Radiative Transfer*, 302:108578, 2023.

[26] A. Nahmad-Rohen and A. García-Valenzuela, Multiple-scattering model for the effective refractive index of dense suspensions of forward-scattering particles, *Journal of the Optical Society of America A*, 40(8):1552–1562, 2023.

[27] A. Ishiniaru and Y. Kuga, Attenuation constant of a coherent field in a dense distribution of particles, *Journal of the Optical Society of America*, 72(10):1317–1320, 1982.

[28] V. D. Nguyen, D. J. Faber, E. van der Pol, T. G. van Leeuwen, and J. Kalkman, Dependent and multiple scattering in transmission and backscattering optical coherence tomography, *Optics Express*, 21(24):29145–29156, 2013.

[29] B. Aernouts, R. Watté, R. V. Beers, F. Delport, M. Merchiers, J. D. Block, J. Lammertyn, and W. Saeys, Flexible tool for simulating the bulk optical properties of polydisperse spherical particles in an absorbing host: experimental validation, *Optics Express*, 22(17):20223–20238, 2014.

[30] M. Raju and S. N. Unni, Concentration-dependent correlated scattering properties of Intralipid 20% dilutions, *Applied Optics*, 56(4):1157–1166, 2017.

[31] G. Morales-Luna and A. García-Valenzuela, Viability and fundamental limits of critical-angle refractometry of turbid colloids, *Measurement Science and Technology*, 28(12):125203, 2017.

[32] H. Contreras-Tello and A. García-Valenzuela, Refractive index measurement of turbid media by transmission of backscattered light near the critical angle, *Applied Optics*, 53(21):4768–4778, 2014.

[33] F. Zernike and J. A. Prins, Die Beugung von Röntgenstrahlen in Flüssigkeiten als Effekt der Molekülanordnung, *Zeitschrift für Physik*, 41(2-3):184–194, 1927.

[34] A. Vrij, Mixtures of hard spheres in the Percus–Yevick approximation. light scattering at finite angles, *Journal of Chemical Physics*, 71(8):3267–3270, 1979.

[35] G. H. Meeten and A. N. North, Refractive index measurement of turbid colloidal fluids by transmission near the critical angle, *Measurement Science and Technology*, 2(5):441, 1991.

[36] M. Mohammadi, Colloidal refractometry: meaning and measurement of refractive index for dispersions; the science that time forgot, *Advances in Colloid and Interface Science*, 62(1): 17–29, 1995.

[37] A. Reyes-Coronado, A. García-Valenzuela, C. Sánchez-Pérez, and R. G. Barrera, Measurement

of the effective refractive index of a turbid colloidal suspension using light refraction, *New Journal of Physics*, 7(1):89, 2005.

[38] C. Sánchez-Pérez, A. García-Valenzuela, R. Sato-Berrú, J. Flores-Flores, and R. Barrera, Sizing colloidal particles from their contribution to the effective refractive index: Experimental results, *Journal of Physics: Conference Series*, 274(1):012064, 2011.

[39] R. Márquez-Islas and A. García-Valenzuela, On the extinction coefficient of light in nonabsorbing nanoparticle suspensions, *Applied Optics*, 57(13):3390–3394, 2018.

[40] F. Morales-Luna and A. García-Valenzuela, Optical sizing of nanoparticles in thin films of nonabsorbing nanocolloids, *Applied Optics*, 58(22):5989–5996, 2019.

[41] T. Okubo, Refractometric studies of "liquid-like" and "crystal-like" colloids in deionized solution, *Journal of Colloid and Interface Science*, 135(1):294–296, 1990.

[42] A. Nahmad-Rohen and A. García-Valenzuela, Detailed comparison of recent — and dissimilar — effective-medium models incorporating dependent scattering, *Journal of the Optical Society of America A*, 41(10):1994–2003, 2024.

[43] G. H. Meeten, Refractive index errors in the critical-angle and the brewster-angle methods applied to absorbing and heterogeneous materials, *Measurement Science and Technology*, 8 (7):728–733, 1997.

[44] E. Gutiérrez-Reyes, A. García-Valenzuela, and R. G. Barrera, Extension of Fresnel's formulas for turbid colloidal suspensions: A rigorous treatment, *Journal of Physical Chemistry B*, 118 (22):6015–6031, 2014.

[45] G. Morales-Luna, H. Contreras-Tello, A. García-Valenzuela, and R. G. Barrera, Experimental test of reflectivity formulas for turbid colloids: Beyond the Fresnel reflection amplitudes, *Journal of Physical Chemistry B*, 120(3):583–595, 2016, PMID: 26727494.

[46] J. van der Horst, A. K. Trull, and J. Kalkman, Deep-tissue label-free quantitative optical tomography, *Optica*, 7(12):1682–1689, 2020.

[47] A. K. Trull, J. van der Horst, J. G. Bijster, and J. Kalkman, Transmission optical coherence tomography based measurement of optical material properties, *Optics Express*, 23(26):33550–33563, 2015.

[48] E. M. Purcell and C. R. Pennypacker, Scattering and absorption of light by nonspherical dielectric grains, *Astrophysical Journal*, 186:705–714, 1973.

[49] S. Edalatpour, M. Čuma, T. Trueax, R. Backman, and M. Francoeur, Convergence analysis of the thermal discrete dipole approximation, *Physical Review E*, 91:063307, 2015.

[50] F. Herz and S. Biehs, Generalized coupled dipole method for thermal far-field radiation, *Physical Review B*, 105:205422, 2022.

[51] R. G. Barrera and A. García-Valenzuela, Coherent reflectance in a system of random Mie scatterers and its relation to the effective-medium approach, *Journal of the Optical Society of America A*, 20(2):296–311, 2003.

[52] G. Mie, Beiträge zur Optik trüber Medien, speziell kolloidaler Metallösungen, *Annalen der Physik*, 330(3):377–445, 1908.

[53] D. R. H. C. F. Bohren, *Absorption and Scattering by a Sphere*, chapter 4, pages 82–129, John Wiley & Sons, Ltd, 1998, ISBN 9783527618156, doi: https://doi.org/10.1002/9783527618156.ch4.

[54] M. Lax, Multiple scattering of waves. II. the effective field in dense systems, *Physical Review*, 85:621–629, 1952.

[55] M. I. Mishchenko, L. D. Travis, and A. A. Lacis, *Multiple Scattering of Light by Particles: Radiative Transfer and Coherent Backscattering*, Multiple Scattering of Light by Particles: Radiative Transfer and Coherent Backscattering. Cambridge University Press, 2006, ISBN 9780521834902.

[56] F. H. Ree, R. N. Keeler, and S. L. McCarthy, Radial distribution function of hard spheres, *The Journal of Chemical Physics*, 44(9):3407–3425, 1966.
[57] A. Guinier, G. Fournet, C. B. Walker, and K. L. Yudowitch, *Small-angle Scattering of X-rays*, Wiley New York, 1955.
[58] H. Matsuoka, H. Murai, and N. Ise, "Ordered" structure in colloidal silica particle suspensions as studied by small-angle X-ray scattering, *Physical Review B*, 37(3):1368, 1988.
[59] J. Moonen and A. Vrij, Determination of the structure factor for concentrated silica dispersions using small angle X-ray scattering. II. experiment, *Colloid and Polymer Science*, 266: 1140–1149, 1988.
[60] M. Ballauff, SAXS and SANS studies of polymer colloids, *Current Opinion in Colloid & Interface Science*, 6(2):132–139, 2001.
[61] T. Li, A. J. Senesi, and B. Lee, Small angle X-ray scattering for nanoparticle research, *Chemical Reviews*, 116(18):11128–11180, 2016.
[62] M. Hildebrandt, S. Lazarev, J. Pérez, I. A. Vartanyants, J.-M. Meijer, and M. Karg, SAXS investigation of core–shell microgels with high scattering contrast cores: Access to structure factor and volume fraction, *Macromolecules*, 55(7):2959–2969, 2022.
[63] M. Kotlarchyk and S.-H. Chen, Analysis of small angle neutron scattering spectra from polydisperse interacting colloids, *The Journal of Chemical Physics*, 79(5):2461–2469, 1983.
[64] C. G. De Kruif, W. J. Briels, R. P. May, and A. Vrij, Hard-sphere colloidal silica dispersions. the structure factor determined with SANS, *Langmuir*, 4(3):668–676, 1988.
[65] A. Huang, H. Yao, and B. D. Olsen, SANS partial structure factor analysis for determining protein–polymer interactions in semidilute solution, *Soft Matter*, 15(37):7350–7359, 2019.
[66] R. Shinde, G. Balgi, S. Richter, S. Banerjee, J. Reynolds, J. Pierce, and E. Sevick-Muraca, Investigation of static structure factor in dense suspensions by use of multiply scattered light, *Applied Optics*, 38(1):197–204, 1999.
[67] J. K. Percus and G. J. Yevick, Analysis of classical statistical mechanics by means of collective coordinates, *Physical Review*, 110:1–13, 1958.
[68] J. A. Kong, L. Tsang, K. H. Ding, and C. Ao, *Scattering of Electromagnetic Waves: Numerical Simulations*, Wiley Series in Remote Sensing. Wiley, 2001, ISBN 0-471-38800-9.
[69] L. Tsang, J. A. Kong, and T. Habashy, Multiple scattering of acoustic waves by random distribution of discrete spherical scatterers with the quasicrystalline and Percus–Yevick approximation, *The Journal of the Acoustical Society of America*, 71(3):552–558, 1982.
[70] G. Bradski, The OpenCV Library, *Dr. Dobb's Journal of Software Tools*, 2000.
[71] N. Otsu, A threshold selection method from gray-level histograms, *IEEE Transactions on Systems, Man, and Cybernetics*, 9(1):62–66, 1979.
[72] P. N. A. Speets and J. Kalkman, Measuring optical properties of clear and turbid media with broadband spectral interferometry, *Applied Optics*, 62(16):4349–4358, 2023.
[73] M. Daimon and A. Masumura, Measurement of the refractive index of distilled water from the near-infrared region to the ultraviolet region, *Applied Optics*, 46(18):3811–3820, 2007.
[74] I. H. Malitson, Interspecimen comparison of the refractive index of fused silica∗,†, *Journal of the Optical Society of America*, 55(10):1205–1209, 1965.
[75] P. Virtanen *et al.*, SciPy 1.0: Fundamental Algorithms for Scientific Computing in Python, *Nature Methods*, 17:261–272, 2020.
[76] J. A. Nelder and R. Mead, A simplex method for function minimization, *The Computer Journal*, 7(4):308–313, 1965.
[77] E. M. L. Beale, Confidence regions in non-linear estimation, *Journal of the Royal Statistical Society: Series B (Methodological)*, 22(1):41–76, 1960.

[78] K. W. Vugrin, L. P. Swiler, R. M. Roberts, N. J. Stucky-Mack, and S. P. Sullivan, Confidence region estimation techniques for nonlinear regression in groundwater flow: Three case studies, *Water Resources Research*, 43(3), 2007.

[79] R. West, D. Gibbs, L. Tsang, and A. K. Fung, Comparison of optical scattering experiments and the quasi-crystalline approximation for dense media, *Journal of the Optical Society of America A*, 11(6):1854–1858, 1994.

[80] A. García-Valenzuela, R. Márquez-Islas, and R. G. Barrera, Reducing light-scattering losses in nanocolloids by increasing average inter-particle distance, *Applied Physics A*, 123(84):1432–0630, 2017.

[81] A. García-Valenzuela, H. Contreras-Tello, J. A. Olivares, and F. L. S. Cuppo, Insights into the dependent-scattering contributions to the extinction coefficient in highly scattering suspensions, *Journal of the Optical Society of America A*, 30(7):1328–1334, 2013.

[82] P. Bertsch, A. Sánchez-Ferrer, M. Bagnani, S. Isabettini, J. Kohlbrecher, R. Mezzenga, and P. Fischer, Ion-induced formation of nanocrystalline cellulose colloidal glasses containing nematic domains, *Langmuir*, 35(11):4117–4124, 2019.

[83] F. Dekker, B. W. M. Kuipers, Á. G. García, R. Tuinier, and A. P. Philipse, Scattering from colloidal cubic silica shells: Part II, static structure factors and osmotic equation of state, *Journal of Colloid and Interface Science*, 571:267–274, 2020.

[84] K. van Gruijthuijsen, M. Obiols-Rabasa, M. Heinen, G. Nägele, and A. Stradner, Sterically stabilized colloids with tunable repulsions, *Langmuir*, 29(36):11199–11207, 2013.

[85] G. H. Bogush, M. A. Tracy, and C. F. Zukoski, Preparation of monodisperse silica particles: Control of size and mass fraction, *Journal of Non-Crystalline Solids*, 104(1):95–106, 1988.

[86] S. R. Parnell, A. L. Washington, A. J. Parnell, A. Walsh, R. M. Dalgliesh, F. Li, W. A. Hamilton, S. Prevost, J. P. A. Fairclough, and R. Pynn, Porosity of silica stöber particles determined by spin-echo small angle neutron scattering, *Soft Matter*, 12:4709–4714, 2016.

[87] Y. Zheng, L. Zhou, Y. Dong, C. Qiu, X. Chen, G. Guo, and F. Sun, Robust optical-levitation-based metrology of nanoparticle's position and mass, *Physical Review Letters*, 124:223603, 2020.

[88] P. Eneren, Y. T. Aksoy, Y. Zhu, E. Koos, and M. R. Vetrano, Light extinction spectroscopy applied to polystyrene colloids: Sensitivity to complex refractive index uncertainties and to noise, *Journal of Quantitative Spectroscopy and Radiative Transfer*, 261:107494, 2021.

[89] F. Ferri, A. Bassini, and E. Paganini, Modified version of the chahine algorithm to invert spectral extinction data for particle sizing, *Applied Optics*, 34(25):5829–5839, 1995.

[90] P. N. A. Speets and J. Kalkman, *Experiment and theory of the complex refractive index of dense colloidal media - data and analysis*, https://doi.org/10.5281/zenodo.10247006, 2024.

4

OPTICAL INTERFEROMETRIC SPECTRAL AND DYNAMIC MULTI-PARAMETER FLOW SENSING

In this work, a Mach-Zehnder spectral interferometer in transmission with a wavelength range of 450 nm-950 nm was combined with a monochromatic (λ = 637 nm) Michelson interferometer in reflection. With transmission spectral interferometry, the optical transmittance, and the refractive properties of a medium can be measured. With the reflection signal, the heterodyne DLS signal was measured. This allows for the real-time measurement of the mean particle size, polydispersity, volume fraction and flow rate. These parameters were measured for various flow conditions and four volume fractions of a monodisperse sample of 100 nm sodium silicate particles. In addition, the response of Intralipid in an acidic environment was monitored real-time in-flow over several hours. Changes in the mean particle size and the increase in polydispersity due to simultaneous dissolution and aggregation of the Intralipid sample were measured.

4.1. INTRODUCTION

In-line flow sensors that are able to sense multiple parameters in turbid media find a wide range of applications. Among the quantities of interest are flow rate [1, 2], pressure [2, 3], viscosity, volume or mass fraction [2] and composition [4]. Examples of real-time monitoring of these quantities include the chemical industry [5, 6], the food industry [4, 7], the pharmaceutical industry [8, 9] and environmental science [10, 11]. The applicability of flow sensing methods does not need to be confined to a tube or flow cell. Flow speed and particle size are routinely measured *in vivo*, as well [1, 12]. Furthermore, real-time flow sensing has many applications for organs-on-chips [2].

For particle suspensions, the particle size distribution is often one of the key parameters of interest [8, 13]. Around the turn of the millennium, real-time in-flow characterization of the particle size distribution was considered as one of the key challenges in the development of new particle sizing techniques [14]. Decades later, this is still considered a technical challenge [6].

The particle size distribution of a suspension can be measured non-optically using a Coulter counter [15] or with ultrasound [16]. A Coulter counter can be used for particle sizing for dilute particle suspensions. With ultrasound spectroscopy, the particle size distribution can be accurately measured in-flow, and for a very broad size range, potentially spanning from 10 nm to 1 mm. However, proper particle sizing with ultrasound requires substantial prior knowledge about wave propagation through the sample [17].

Optical methods to measure the particle size have the advantage that they are non-invasive. Furthermore, changes in composition can be detected with a measurement of the absorption spectrum [4, 18]. On-chip [19] and fiber-based [20] optical sensors are ubiquitous and therefore economical. Optical methods to determine the particle size are, among others, focused beam reflection measurements (FBRM) [21], or particle tracking analysis (PTA), also called nanoparticle tracking analysis (NTA) [22–24]. The particle size can also be derived from the angle dependence of the scattering, which can be measured with laser diffraction analysis or static light scattering. The angle dependence of the scattered light on a particle is often used for cell sizing in-flow cytometry [25]. FBRM is commonly applied in industrial settings [5], but is only applicable for larger particles (> 100 nm), and the chord length distribution needs to be mapped to a size distribution [26]. NTA is only applicable for dilute samples and for very low flow rates.

Dynamic light scattering (DLS) is a well-established technique for particle sizing [27, 28]. While mainly used for off-line particle sizing, it can also be applied to real-time size control for the laser fabrication of nanoparticles [29]. The DLS signal is often measured with a homodyne detection scheme [30, 31]. However, heterodyne detection leads to increased sensitivity, higher temporal correlation, and sensitivity to the Doppler shift caused by the axial flow component.

The DLS signal can also be measured with optical coherence tomography (OCT) and is called DLS-OCT. This technique is already commercialized and widely applied [32], for example for size monitoring during liposome production [33]. With OCT, a reflection tomogram is made with spectral interferometry [34–36]. Therefore, the intensity fluctuations that are measured with DLS-OCT can be resolved in depth. With Doppler OCT, the phase in the interference spectrum is used to measure the flow speed in the

axial direction [35, 37]. In fact, DLS and Doppler OCT can be combined [38–40] to give all components of the velocity vector in 2D. However, for a full 3D characterization of the flow, a scanning beam is required. Furthermore, OCT needs a spectrometer, which typically is slower than a photodiode. This limits the lowest particle size that can be measured with DLS. For high flow speeds, the decay of the autocorrelation is fully dominated by the flow, the diffusion coefficient cannot be extracted. This can be mitigated with the use of scanning DLS-OCT, where a B-scan is made in the direction of the flow, thereby reducing the flow decorrelation. However, for non-scanning DLS-OCT measurements, the diffusion contribution to the autocorrelation can only be measured close to the edges, where the flow is lowest [39].

Whereas DLS(-OCT) is sensitive to the flow speed, the transmittance of the sample is not. The transmittance can be used for real-time in-flow particle sizing using a fit with Mie theory to the measured attenuation spectrum [41]. For example, the Mie attenuation spectrum is used to measure particle aggregation during a latex agglutination antigen test [42]. For smaller particles, the polydispersity and the mean diameter of a particle size distribution have a similar effect on the Mie scattering spectrum. This leads to ambiguity when Mie scattering is used for particle sizing, as is discussed in Chapter 3. This ambiguity can be broken with a transmission measurement for different concentrations, but this would make real-time sensing impossible.

More importantly, for small particles or for polydisperse particle size distributions, the inversion of the Mie spectrum requires the concentration or volume fraction of the dispersed particles. With optical methods, the volume fraction can be obtained with a measurement of the refractive index, or chromatic dispersion [43]. Conveniently, the attenuation and the group index n_g can be measured simultaneously.

In sum, an interferometric transmission experiment will allow for the measurement of the volume fraction and of the Mie scattering spectrum, whereas in reflection the particle dynamics caused by flow and Brownian motion can be used to determine the mean particle size. Simultaneous measurement in both reflection and transmission will allow for both. The Mie scattering spectrum and the DLS signal will complement each other to obtain a better estimate of the particle size distribution.

This work combines broadband interferometric transmission measurements with reflection heterodyne DLS. The simultaneous measurement of the transmittance and DLS autocorrelation allows for a real-time measurement of the flow speed, volume fraction and particle size distribution. These parameters are measured for a sample of 100 nm sodium silicate particles for varying flow speeds and volume fractions. In addition, the response of a diluted Intralipid 20% solution to HCl is measured in a time-lapse measurement to show the feasibility for real-time applications.

4.2. THEORY

4.2.1. TRANSMISSION INTERFEROMETRY

The interference spectrum of a Mach-Zehnder interferometer is described in Chapter 2, concluding with Eq. 2.4:

$$I_{\text{int}}(k) \propto S(k)\, e^{\frac{1}{2}\mu(k)L} \cos(k\delta - n(k)kL)\,. \tag{4.1}$$

Here, $S(k)$ is the source spectrum, $\mu(k)$ is the attenuation of the sample, L the width of the sample, and δ the length difference between the reference and the sample arm, and $n(k)$ the refractive index of the medium.

The group index at the center wavenumber k_c can be calculated from the difference in position of the maximum of the Fourier transform of I_{int}, z_{COM}, and a calibration measurement [44]. The group index can be obtained from an optical path length (OPL) shift of the center of mass of the peak $\Delta z = z_{\text{COM}} - z_{\text{COM, cal}}$. Here z_{COM} and $z_{\text{COM, cal}}$ are the center of masses of the peak in the depth domain, and the calibration measurement, respectively. The group index calculated from this shift is given by

$$n_g(k_c) = n_{g,\text{cal}}(k_c) + \frac{\Delta z}{L}. \tag{4.2}$$

4

With a known phase index of the particle $n_p(k)$, and of the embedding medium, $n_m(k)$, the group index can be used to measure the volume fraction with

$$f_v = \frac{n_g(k_c) - n_{g,m}(k_c)}{n_{g,p}(k_c) - n_{g,m}(k_c)}. \tag{4.3}$$

Here, $n_{g,p}$ and $n_{g,m}$ are the group indices of the particle and the embedding medium calculated from the phase index, respectively. The attenuation spectrum $\mu(k)$ can be found from a Lambert-Beer relation

$$\mu(k)L = \ln\left(I_{\text{cal}}(k)\right) - \ln\left(I_{\text{sam}}(k)\right). \tag{4.4}$$

The dependent scattering attenuation μ for a polydisperse system can be calculated with the same scattering model used in Chapter 4, Eq. 3.35 [45, 46],

$$\mu_{\text{sca}} = 2\pi \int_0^{\pi} \sum_{i,j}^{N} \sqrt{\rho_i \rho_j} f_i(\theta) f_j(\theta) S_{i,j}(\theta) \sin(\theta)\, \mathrm{d}\theta. \tag{4.5}$$

Here, θ is the scattering angle, ρ_i the number density and f_i the scattering amplitude per size bin i. The partial structure factor $S_{i,j}$ in the Percus-Yevick approximation is taken from [47], and is also given in Appendix A.

4.2.2. HETERODYNE DLS IN FLOW

The intensity on the detector of an interferometric DLS setup as shown in Fig. 4.1(a) is given by

$$I_{\text{det}} = E_r E_r^* + E_s E_s^* + E_r E_s^* + E_s E_r^*, \tag{4.6}$$

with E_r the field of the reference arm and E_s the field of the sample arm. When the source light is highly stable ($E_r(t) = E_r$) and the amplitude of the reference field is much larger than the amplitude of the sample field ($E_r \gg E_s$), the autocorrelation of the intensity on the detector $g_{\text{det}}(\tau)$ after subtraction of the DC component $E_r^* E_r$, is given only by the cross terms of Eq. 4.6,

$$g_{\text{det}}(\tau) = \frac{\langle E_r E_s^*(t) E_r^* E_s(t+\tau)\rangle}{\langle E_r^* E_s E_r E_s^* + E_r^* E_s E_r E_s^*\rangle} + \frac{\langle E_r^* E_s(t) E_r E_s^*(t+\tau)\rangle}{\langle E_r^* E_s E_r E_s^* + E_r^* E_s E_r E_s^*\rangle} = \text{Re}\left\{g_1(\tau)\right\}. \tag{4.7}$$

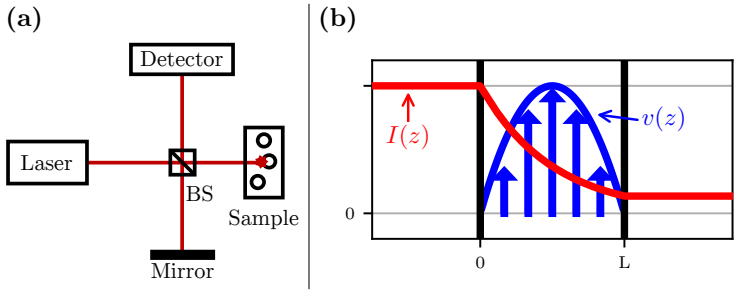

Figure 4.1: **(a)** A Michelson interferometer. BS stands for beam splitter. **(b)** The flow profile $v(z)$ and the intensity decay $I(z)$ in a flow cell.

Since the left fraction equals the complex conjugate of the right fraction, the autocorrelation of the detector intensity equals the real part of the autocorrelation of the sample field E_s, which is given by g_1. In the single scattering approximation, the autocorrelation g_1 for a field originating from depth z and for monodisperse diffusive particles in constant flow is given by [48]

$$g_1(\tau, z) = \frac{\langle E_s(t) E_s^*(t+\tau)\rangle}{\langle E_s E_s^*\rangle} = A e^{-Dq^2\tau} e^{iqv_z(z)\tau} e^{-v(z)^2\tau^2/w_0^2}. \tag{4.8}$$

Here, q is the scattering wavenumber, which is for backscattered light given by $q = 2n_{\text{eff}}(k)k$. A is a fit parameter related to uncorrelated measurement noise in the signal, which can depend on depth [39], but is assumed to be constant. The flow profile $v(z)$ has an axial component $v_z(z) = v(z)\sin\alpha$, with α the angle between the direction of the flow and the lateral plane. That is, $\alpha = 0$, when the flow is perpendicular to the optical axis.

In Eq. 4.8, w_0 is the lateral beam waist for a Gaussian beam shape and D is the diffusion constant of the particles given by the Stokes-Einstein equation

$$D = \frac{k_B T}{6\pi a \eta}, \tag{4.9}$$

with k_B the Boltzmann constant, T the absolute temperature, a the particle radius, and η the viscosity [49–51].

A sketch of the flow profile $v(z)$ and the intensity $I(z)$ is shown in Fig. 4.1(b). The autocorrelation g_1 from the field is given by Eq. 4.8. Fields originating from depths are uncorrelated, except for very short time scales. Therefore, the autocorrelation of the field at the detector, which is the sum of all fields originating from all depths, is the average autocorrelation $g(\tau, z)$ weighted by the amplitude of the electric field at depth z. The amplitude of the field in the sample is given by the Lambert-Beer's law, $e^{-\mu z}$. Therefore, the measured autocorrelation is assumed to be given by the average of the autocorrelation over the length of the channel with spatially varying flow weighted by the intensity decay $e^{-\mu z}$, i.e.,

$$g_1(\tau) = \frac{1}{L} e^{-Dq^2\tau} \int_0^L e^{iqv_z\tau} e^{-v^2(z)\tau^2/w_0^2} e^{-\mu z}\, \mathrm{d}z. \tag{4.10}$$

If v_z is small, the effects of the diffusion and flow on $g_1(\tau)$ can be separated by the ratio of $g_1(\tau)$ and its time derivative $g_1'(\tau)$. Since the diffusion part $e^{-Dq^2\tau}$ does not depend on z, it can be written outside the integral of Eq. 4.10. Here we define the flow autocorrelation $g_{\text{flow}}(\tau)$ to be

$$g_{\text{flow}}(\tau) = \frac{1}{L}\int_0^L e^{iqv_z\tau} e^{-v^2(z)\tau^2/w_0^2} e^{-\mu z}\,\mathrm{d}z, \tag{4.11}$$

where z being the physical depth. Hence, Eq. 4.10 can be simplified to

$$g_1(\tau) = g_{\text{flow}}(\tau) e^{-Dq^2\tau}. \tag{4.12}$$

Assuming v_z is small, the logarithmic derivative $g_1'(\tau)/g_1(\tau)$ is given by:

$$\frac{g_1'(\tau)}{g_1(\tau)} = \frac{g_{\text{flow}}'(\tau)}{g_{\text{flow}}(\tau)} - Dq^2. \tag{4.13}$$

The fraction $g_{\text{flow}}'(\tau)/g_{\text{flow}}(\tau)$ is only sensitive to the nonlinear exponents of Eq. 4.10.

4.3. MATERIALS AND METHODS

4.3.1. EXPERIMENTAL SETUP

The experimental setup is shown in Fig. 4.2. The setup combines a spectral Mach-Zehnder interferometer as described in Chapter 2, with a single wavelength Michelson interferometer for reflection. This setup was used for two experiments. First, the flow rate, mean diameter, volume fraction and polydispersity were measured with the autocorrelation g_1, group index n_g and transmittance for a sample of a sample of moderately monodisperse 100 nm sodium silicate particles (Köstrosol 10050, CBK).

These quantities were determined for various volume fractions and flow rates. The second experiment is a long-term measurement of the change of the particle size distribution of an Intralipid sample with a gradually decreasing pH value in-flow.

The transmission beam path is shown in green. The source is a supercontinuum laser (EVO EUL-10, NKT). The part of the spectrum with a wavelength larger than 950 nm is filtered with a dichroic mirror (DMLP950, Thorlabs) and sent to a beam dump. The beam is split into a reference arm and a sample arm with a plate beam splitter with a splitting ratio of 50/50 (BSW26R, Thorlabs). In the sample arm, the light is focused on the flow cell by an $f = 50$ mm lens (AC254-050-AB-ML, Thorlabs), and collimated with a similar lens. In the reference arm, there is a second beam splitter to split the reference beam for the Mach-Zehnder interferometer from the reference of the Michelson interferometer (BSW26R, Thorlabs). The length of the Mach-Zehnder reference arm can be adjusted with a translation stage. In the reference path, two lenses (AC254-050-AB-ML, Thorlabs) are placed to compensate for the dispersion for the lenses in the sample arm. The intensity of the reference signal is adjusted with a neutral density filter wheel (NDC-100C-4M, Thorlabs).

The beams are recombined with a plate beam splitter (BSW26R, Thorlabs). After recombination, the light passes two neutral density filters (ND4A and ND10A, Thorlabs) to attenuate the signal and an iris (SM1D12D, Thorlabs) to filter out stray light. The beam is coupled into a fiber (M23L01, Thorlabs) with a reflective collimator (RC08FC-P10, Thorlabs) and analyzed with a spectrometer (FX VIS-NIR, Ocean Optics).

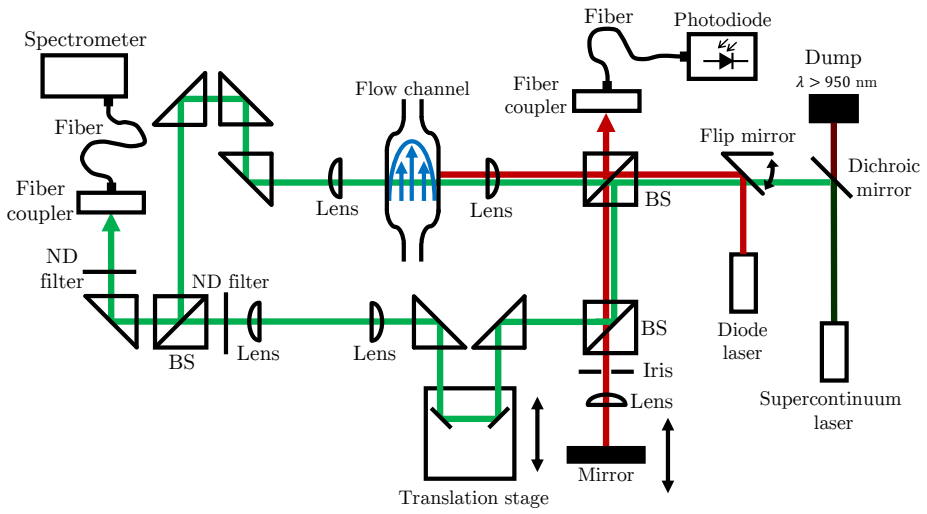

Figure 4.2: Schematic of the combined spectral interferometry/DLS setup. BS and ND stand for beam splitter and neutral density, respectively.

The beam path of the Michelson interferometer for the reflection mode is shown in red in Fig. 4.2. The light source is a diode laser that emits at 637 nm (CPS635R, Thorlabs). The beam path shares the same plate beam splitter and the same lens as the Mach-Zehnder interferometer. The strength of the reference path is set with an iris (SM1D12D, Thorlabs). The intensity of the reference signal is approximately 10× to 20× as strong as the sample signal, varying from experiment to experiment. When the intensity of the reference signal is approximately 100× larger than the sample signal, the interferometer signal can be approximated as being fully heterodyne [31]. Therefore, the detection and signal analysis are from here on approximated as fully heterodyne. The reference beam passes through the same lens as the sample arm. The length of the reference arm is changed with a translation stage to match the optical path length of the sample arm.

The combined sample and reference signals are coupled into an optical fiber (M23L01, Thorlabs) using the same type of reflective collimator (RC08FC-P10, Thorlabs) as in the Mach-Zehnder part of the setup. The beams are detected with a photodiode (PDA100A2, Thorlabs) with 50 dB gain. In front of the photodiode a 10 nm wide bandpass filter with a center wavelength of 635 nm is placed (FLH635-10, Thorlabs). The signal is detected with an oscilloscope (DS1102E, Rigol). A single oscilloscope measurement has 1048572 points. During experiments, the setup can be switched from transmission mode to reflection mode with a flip mirror (MFF101/M, Thorlabs).

4.3.2. SAMPLE MOUNTING AND CALIBRATION

For the experiment, a 1 mm flow cell (45/Q/1, Starna) was used. To reduce reflections from the surface of the flow cell, a tilt angle β was introduced. This angle was set to about 4°, as indicated in Fig. 4.3(a). This angle was perpendicular to the flow. This did not fully prevent that a small additional Doppler angle was introduced. The flow is created with a

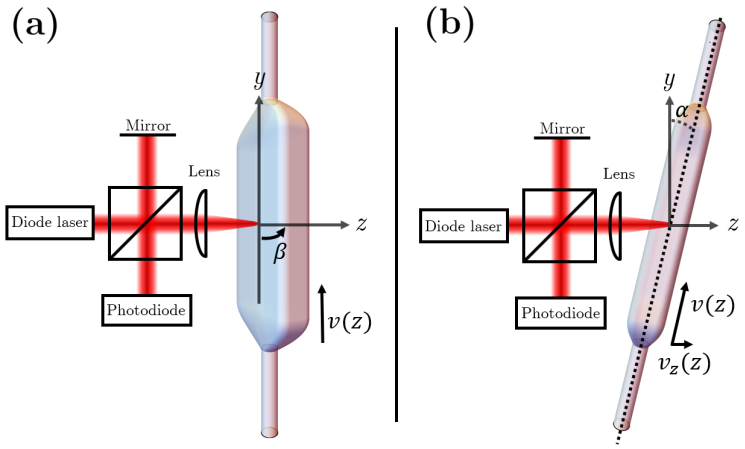

Figure 4.3: (**a**) Sketch of the tilt angle β (**b**) and the Doppler angle α with respect to the cuvette and interferometer.

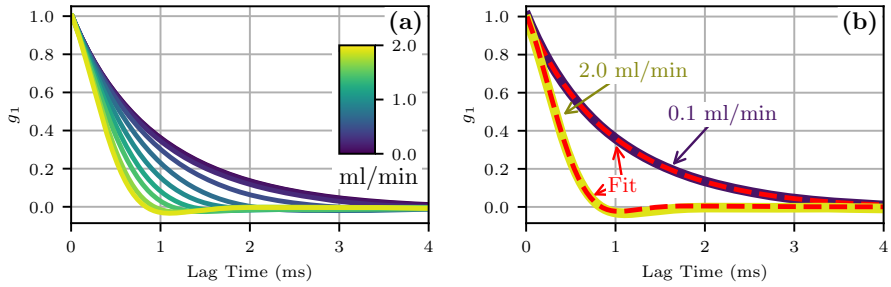

Figure 4.4: (**a**) The autocorrelation functions measured for a dilute Intralipid sample used for flow calibration. (**b**) Fit with Eq. 4.10 of the highest and lowest discharges.

syringe pump (Fusion 100, Chemyx) and a 5 ml syringe (Plastipak, BD).

The angle α and beam waist w_0 of Eq. 4.11 were calibrated with an Intralipid flow measurement with 5 vol.% Intralipid 20% dilution (1.1 vol.% particles). The autocorrelation functions from the calibration measurements are shown in Fig. 4.4(a). Each flow rate is calibrated with 6 measurements of each 1048572 points in length. The beam waist is measured to be 5.5 µm, and the angle α 1.37°. This angle is too small to cause prominent Doppler fringes in the autocorrelation. The angles α and β together make a total angle with the z-axis of 4.2°. This increases the path length in the channel to 1001.5 µm. Calibration was performed using a dilute sample of large particles, in this case Intralipid, to minimize the effect of diffusion on the autocorrelation. The fit to the autocorrelation is shown for two flow rates in Fig. 4.4(b).

The volume fraction of the particles was determined by measuring the density of the bulk particle suspension, which has a mass fraction of 0.5. The mass density of the

particles is measured to be 1.85 g/cm^3. This corresponds to a bulk volume fraction of 0.35. The refractive index of the sodium silicate particles is determined with a calibration measurement of the group index with the 11.7 vol.% Köstrosol sample. The dispersion is assumed to be the same as for the silica particles used in Chapter 3. The calibration yields a refractive index $n_g(k)$ that is 0.992 times the refractive index of the silica particles used in Chapter 3.

For the monodisperse sample, the attenuation, group index and autocorrelations were measured for 4 different volume fractions for flow rates up to 2 ml/min. This flow rate corresponds to a maximum flow speed in the center of the channel of 5.3 mm/s. For each flow rate, two transmittance measurements for the attenuation and group index were made and four measurements of the autocorrelation. The flow rates were measured in the order 0 ml/min, 0.5 ml/min, 1.0 ml/min, 1.5 ml/min, 2 ml/min, 1.75 ml/min, 1.25 ml/min, 0.75 ml/min, 0.25 ml/min and 0.1 ml/min. This order was chosen to detect drift in the measurements, possibly as a result of sample heating. The oscilloscope time scale was set to 1 s. The time resolution of the autocorrelation measurement is 11.4 µs. An example of the photodiode potential $V(t)$ for both sodium silicate particles and Intralipid is shown in Fig. 4.5. The optical transmittance measurements are calibrated with demineralized water at the start and end of the flow rate sweep.

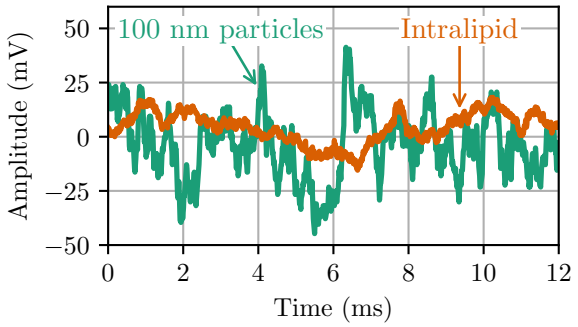

Figure 4.5: Example of the measured photodiode potential for the two particle species and used for dynamic light scattering measurements.

The supercontinuum laser has pulse-to-pulse variations in the spectrum. Furthermore, the laser has a power drift when operated for a long time, that is, more than an hour. To compensate for the power drift, the water spectrum used for calibration is based on the reference power of a measurement, since this is independent of the sample. The calibration spectrum at the start of the measurement series is given by $I_{\text{sam,water1}}(k)$, and at the end by $I_{\text{sam,water2}}(k)$. The calibration spectrum that is used for a measurement taken between these two calibrations is the average of these two spectra, weighted by the total power in the reference arm for that specific measurement compared to the total power in the reference arm in the calibration measurements. In short, the calibration for a measurement is then given by:

$$I_{\text{water}}(k) = a_{\text{cal}} I_{\text{sam,water1}}(k) + (1 - a_{\text{cal}}) I_{\text{sam,water2}}(k) \tag{4.14}$$

with a_{cal} given by

$$a_{\text{cal}} = \frac{\int I_{\text{ref,sample}}(k)\,\mathrm{d}k - \int I_{\text{ref,water1}}(k)\,\mathrm{d}k}{\int I_{\text{ref,water2}}(k)\,\mathrm{d}k - \int I_{\text{ref,water1}}(k)\,\mathrm{d}k}. \tag{4.15}$$

Since the group index measurements are not affected by power fluctuations, the position of the center of mass in the OPL distribution $z_{\text{COM,water}}$ is the average of both calibration measurements. Each time the syringe ran out, the same suspension was pulled again into the syringe, and reused for the next measurement.

The time-lapse flow sensing measurement was done with the same flow cell and with the same angle and as for the monodisperse sample. The sample was 3 ml of 5 vol.% Intralipid 20% with a particle volume fraction of 1.1 vol.%. For each time step, there was one attenuation and group index measurement, four autocorrelation measurements with a flow rate of 0.5 ml/s and two autocorrelation measurements of the suspension without flow. The time between each combined measurement was about five minutes. During the time-lapse, 10 µl of a solution of 0.37 wt.% HCl (258148, Sigma-Aldrich) and demineralized water was added to the Intralipid. The estimated lower bound of the pH at the end of the time-lapse experiment at $t = 5.2$ h, is 0.57, based on the amount of added HCl and approximating the sample as demineralized water. However, this ignores the buffering capacity of the Intralipid and dissolution of the soy oil particles would remove H^+ ions from the bulk solution, thereby increasing the pH.

4.3.3. SIGNAL ANALYSIS

The analysis steps for the small angle configuration are summarized in the flowchart in Fig. 4.6. In step 1, the attenuation of the sample is determined from the transmission spectrum. An example of the measured intensity on the spectrometer is shown in Fig. 4.7(a). The spectra between 450 nm and 950 nm are resampled over 8192 bins to ensure linear spacing in wavenumber. For the time-lapse experiment, the minimum wavelength is 550 nm, since the transmittance is less for this more turbid sample.

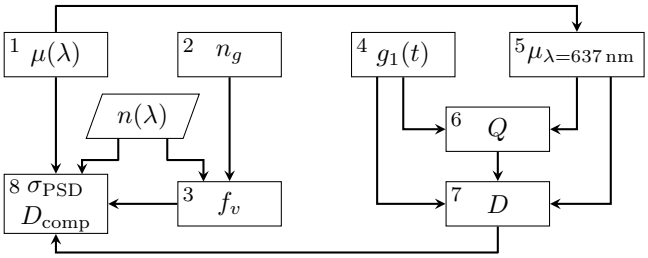

Figure 4.6: Flow chart for the analysis of the monodisperse sample and time-lapse experiment.

In Fig. 4.7(a), the red spectrum is the measured intensity of the sample, and in blue is the spectrum of the water calibration measurement. The transmission spectrum is obtained by dividing the sample intensity with the water calibration intensity. This transmittance is shown in Fig. 4.7(b). The fringes of the self-interference and transmission spectra of beam splitters are the same in the water and divide out. In addition, the spec-

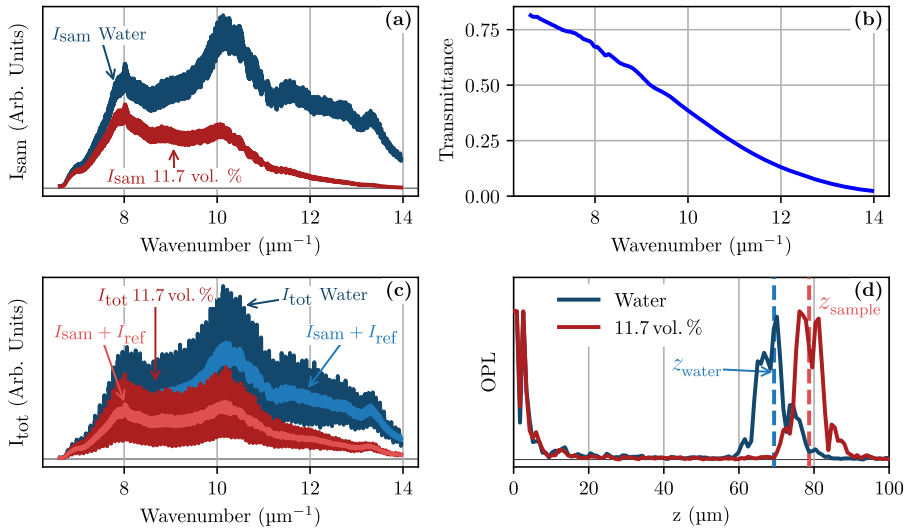

Figure 4.7: Transmission measurement of the 11.7 vol.% sample without flow. **(a)** Spectra as measured. **(b)** the interference spectra. **(c)** the transmittance as calculated from the spectra shown in **(a)**. **(d)** Shift in the peak of the OPL distribution.

trum is smoothened with a Savitzky-Golay filter as provided by Scipy [52] with 101 bins and order 3.

In step 2, the group index is determined from the interference spectrum. As an example, the measured sample and reference interference spectra are shown in Fig. 4.7(c). The measured transmission spectra of the sample arm and reference arm are subtracted from the interference spectrum. The spectrum is divided by the envelope of the interference signal, where the envelope is obtained from the absolute value of its Hilbert transform. The envelope is filtered by a Savitzky-Golay filter with 201 bins and order 3. The OPL distribution, as shown in Fig. 4.7(d) is the square of the Fourier transform of the apodized interference spectrum. The group index at the center wavenumber $k_c = 10.3\,\mu\text{m}^{-1}$ is determined from the center of mass of the peak in the optical path length distribution according to Eq. 4.2. The peak width is 34 µm around the position of the maximum.

In step 3, the volume fraction is calculated based on the measured group index and the calibrated phase index according to Eq. 4.3.

In step 4, in the flowchart of Fig. 4.6, the autocorrelation of the potential fluctuations $V(t)$ of the photodiode is calculated according to

$$g_1(\tau) = \mathscr{F}^{-1}\left\{\mathscr{F}\left\{\left(V(t) - V_{\text{avg}}\right)\right\}\mathscr{F}^*\left\{\left(V(t) - V_{\text{avg}}\right)\right\}\right\}. \tag{4.16}$$

Here, V_{avg} is the average potential of a measurement. The amplitude term A of Eq. 4.8 is normalized, and the average of g_1 between 5 ms and 10 ms is subtracted. The latter is done to remove the effect of long-timescale drift or fluctuations over time in $V(t)$ on g_1 that is present in some measurements. For the Intralipid time-lapse experiment, the

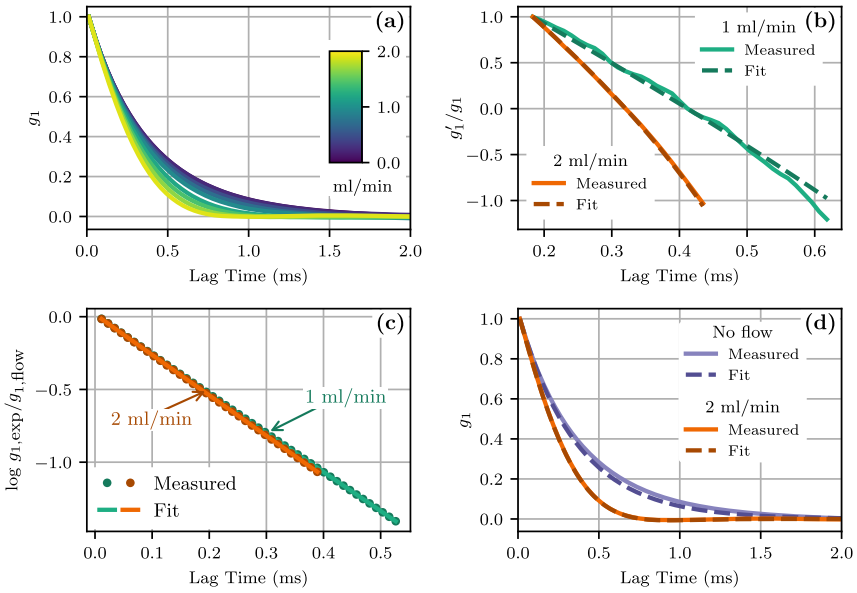

Figure 4.8: **(a)** autocorrelation for each measured flow rate for the 11.7 vol.% particles. **(b)** Fraction g_1'/g_1 for the flow rates 1 ml/min and 2 ml/min. **(c)** the logarithm of the flow corrected autocorrelation. **(d)** Measured and fit autocorrelation for a flow rate of 2 ml/min compared to the autocorrelation without flow.

average of g_1 between 16 ms and 20 ms was subtracted. The average autocorrelation g_1 for the $f_v = 11.7$ sample is shown in Fig. 4.8(a) for all measured flow rates.

In step 5, the attenuation at the wavelength of the diode laser is taken from the attenuation measurement of step 1. This is used for the fit of the flow rate, as calculated from Eq. 4.11 to the first term of Eq. 4.13 in step 6. The depth-dependent flow rate $v(z)$ for a laminar flow for a rectangular channel was calculated using an analytical expression [53], for a profile at the center of the channel, as is also given in Appendix C. The autocorrelation fit domain was $\tau > 172$ µs and $g_1(\tau) \geq 0.15$. Therefore, the autocorrelation for the stationary sample was fit with 45 points and the autocorrelation for $Q = 2.0$ ml/min with 21 points. These fits are shown in Fig. 4.8(b).

In step 7, the diffusion coefficient D is obtained by a third order polynomial fit to the logarithm of the autocorrelation

$$\ln(g_1) - \ln(g_{1,\mathrm{flow}}) = a_0\tau^3 + a_1\tau^2 + a_2\tau + a_3\,. \tag{4.17}$$

Here, $\ln(g_{1,\mathrm{flow}})$ is the theoretical flow component calculated with Eq. 4.11 for Q as obtained in step 5, and α and w_0 as calibrated. The cubic term is to incorporate the small, but nonzero, axial velocity component v_z. The diffusion is $D = a_2 q^{-2}$. The particle diameter is then obtained from Eq. 4.9. The viscosity is assumed to be that of water at 22° C, the value taken from [54]. The resulting fit to the flow compensated autocorrelation $g_{\mathrm{exp}}/g_{\mathrm{flow}}$ is shown in Fig. 4.8(c), and in Fig. 4.8(d) to the full autocorrelation.

In step 8, the polydispersity σ_{PSD} is determined from the attenuation spectrum $\mu(k)$ and the measured volume fraction. The dependent scattering attenuation is calculated

according to Eq. 3.35, with the Mie scattering amplitude $f_i(\theta)$ calculated with the Miepython package [55]. For the monodisperse sample, the attenuation spectrum is divided in 45 linearly spaced wavenumbers. The particle size distribution ρ_i is assumed to have a normal distribution. The distribution is discretized with 33 bins between $\pm 1.5\sigma_{\text{PSD}}$. The forward calculated dependent scattering attenuation spectrum is fit to the experimental attenuation with the Scipy implementation of the Nelder-Mead optimization algorithm [52, 56], by minimizing

$$\left| a_m - \frac{\sum_i a_i \sigma_{\text{back},i}\, e^{-(a_i - a_{\text{comp}})^2/(2\sigma_{\text{PSD}}^2)}}{\sum_i \sigma_{\text{back},i}\, e^{-(a_i - a_{\text{comp}})^2/(2\sigma_{\text{PSD}}^2)}} \right|^2 . \tag{4.18}$$

Here, a_m is the measured uncompensated particle radius, $\sigma_{\text{back},i}$, the backscattering cross section of a particle with radius a_i, and a_{comp} the polydispersity compensated radius. Note that this compensated particle radius is incorporated into the error function used for minimizing the attenuation spectrum fit, resulting in two nested optimization loops.

The process in step 8 is similar for the time-lapse experiment. In this case, because of the lower particle concentration, the volume fraction dependent scattering is not taken into account, which significantly reduces the computation time. This allows for a larger number of size bins and wavenumber subdivisions, which are both set to 257. The particle size distribution is assumed to have a log-normal distribution, with a polydispersity range $\pm 2.5\sigma_{\text{PSD}}$. Furthermore, the mean diameter is not compensated for the polydispersity. The refractive index of soy oil particles, used for the attenuation spectrum fit, is taken from [57].

The uncertainty in the attenuation and group index measurements of the sodium silicate sample is assumed to be two times the standard deviation for each volume fraction. The uncertainty in the flow rate is two times the standard deviation for each flow rate.

4.4. RESULTS

4.4.1. IN-FLOW SENSING OF SILICA PARTICLE SUSPENSIONS

The measured and fitted scattering spectra of the monodisperse sample of sodium silicate particles are shown in Fig. 4.9. Since the relative uncertainty of the high volume fractions is lower, the fit to the data of the 11.7 vol.% sample (pink) is better than the fit to the spectrum of the 2.9 vol.% sample (green). The increase in turbidity is clearly smaller at larger volume fractions, indicating the need to incorporate volume fraction dependent scattering in the fit model. The attenuation spectra for $Q > 0$ is similar to those shown in Fig. 4.9.

The mean particle diameter obtained from DLS measurements of sodium silicate particles in water fitted with Eq. 4.10 is shown in Fig. 4.10. The obtained mean particle diameters have not been corrected for polydispersity. The diameter standard deviation is quite low for measurements at different flow rates for the same volume fraction. However, the measured diameter for the highest volume fraction of 11.7 vol.% is about 5% higher than that for the lower volume fractions.

An overview for all results of the sodium silicate samples is shown in Fig. 4.11 for the four volume fractions, different flow rates, and for the case without flow. In Fig. 4.11(a),

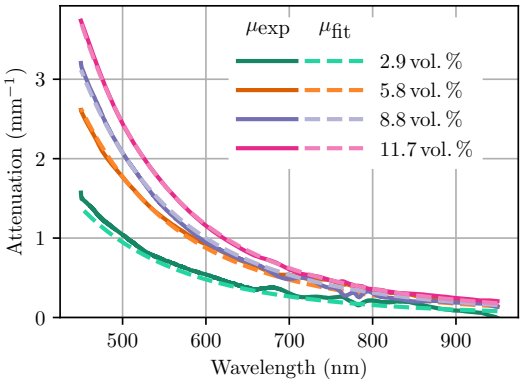

Figure 4.9: Measured attenuation of monodisperse sodium silicate particles in water from transmitted intensity.

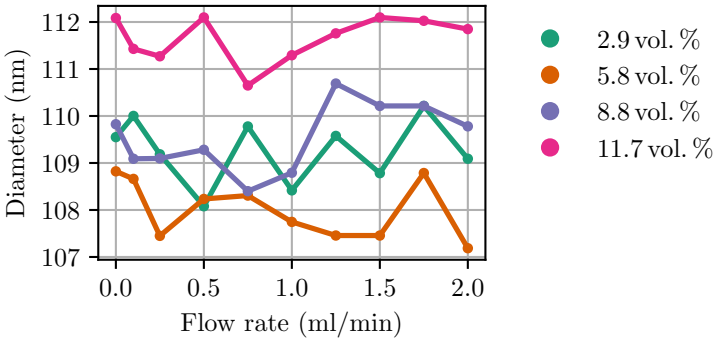

Figure 4.10: Mean particle diameter obtained from dynamic light scattering measurements without performing polydispersity compensation

the attenuation at the wavelength of 637 nm is shown, and in Fig. 4.11(b) the group index at center wavenumber $k_c = 10.3\ \mu\text{m}^{-1}$ ($\lambda = 611$ nm). The flow rate does not have an influence on the transmittance nor the group index. The flow rate Q, as determined from Eq. 4.13, is shown in Fig. 4.11(c). The flow rate can be accurately measured between $Q = 0.75$ ml/min and $Q = 1.75$ ml/min. Flow rates below or equal to $Q = 0.5$ ml/min have a high variance, and are generally lower than the expected value.

The measured diameter after polydispersity compensation is shown in Fig. 4.11(d). The systematic error is reduced compared to the uncompensated diameter. However, this comes at the cost of a higher variance. The standard deviation is 7.4 nm for 2.9 vol.% and 0.6 nm for 11.7 vol.%. The measured volume fraction is shown in Fig. 4.11(e). The volume fraction is a rescaling of the group index according to Eq. 4.3. There is no dependence on the flow rate and good agreement with the expected value is observed. Particle number polydispersity is shown in Fig. 4.11(f). For the two larger volume fractions,

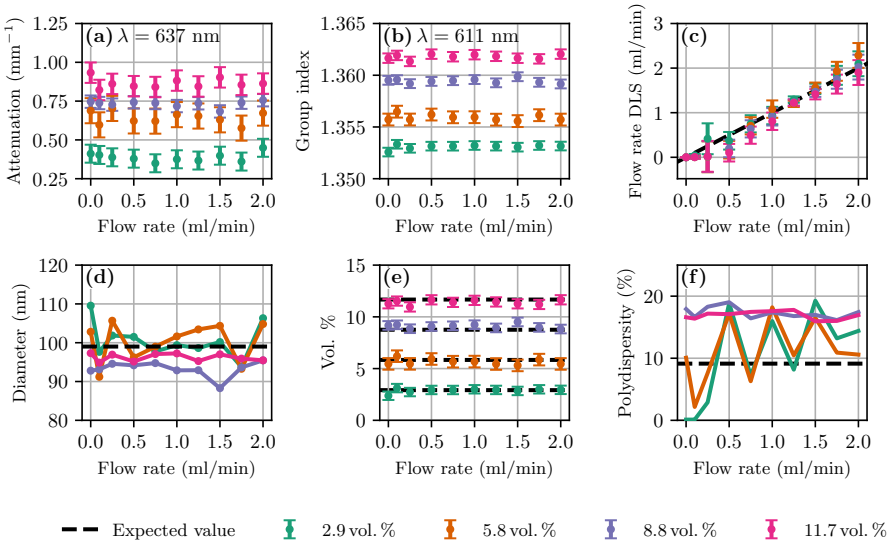

Figure 4.11: Summary of all quantities measured for the flow sensing experiment of the monodisperse sample for all four volume fractions and for all measured flow speeds. **(a)** The measured attenuation. **(b)** The measured group index at 611 nm. **(c)** The flow rate. **(d)** The diameter corrected for the polydispersity. **(e)** The volume fraction as determined from the group index. **(f)** The polydispersity.

the polydispersity shows small variance but has a systematic error towards larger values compared to our expected polydispersity. For the lower two volume fractions the variance in the volume fraction is quite high, and for some flow rates the measured polydispersity is 0%. This large error for the measured polydispersity of these two volume fractions is caused by the uncertainty in the measured group index, and consequently the volume fraction. Although the variance in the volume fraction, as shown in Fig. 4.11(e), is low compared to the measured polydispersity, a small error in the volume fraction has a large effect on the fitted polydispersity, particularly for small polydispersities (< 10%). The attenuation is only slightly higher for samples with a polydispersity of 10%, compared to ideal monodisperse samples.

4.4.2. TIME-LAPSE IN-FLOW INTRALIPID SENSING

The results of the time-lapse Intralipid flow experiment are shown in Fig. 4.12. The weight fraction ($\cdot 10^{-5}$) of HCl dissolved in the sample is indicated with the numbers at the top of each panel. The HCl was added to the sample at the start of each beige or white colored time interval with the exception of the first interval. The development of the attenuation at $\lambda = 637\,\text{nm}$ is shown in Fig. 4.12(a). The expected value for the attenuation taken from the measurement shown in Chapter 2 is indicated with the dashed black line. The attenuation increases with increasing HCl concentration. After the addition of additional HCl to the sample at 1 h and 2.3 h, the attenuation peaks before it slowly decays. After 2.7 h the attenuation remains flat, until the 4.2 h time mark, after

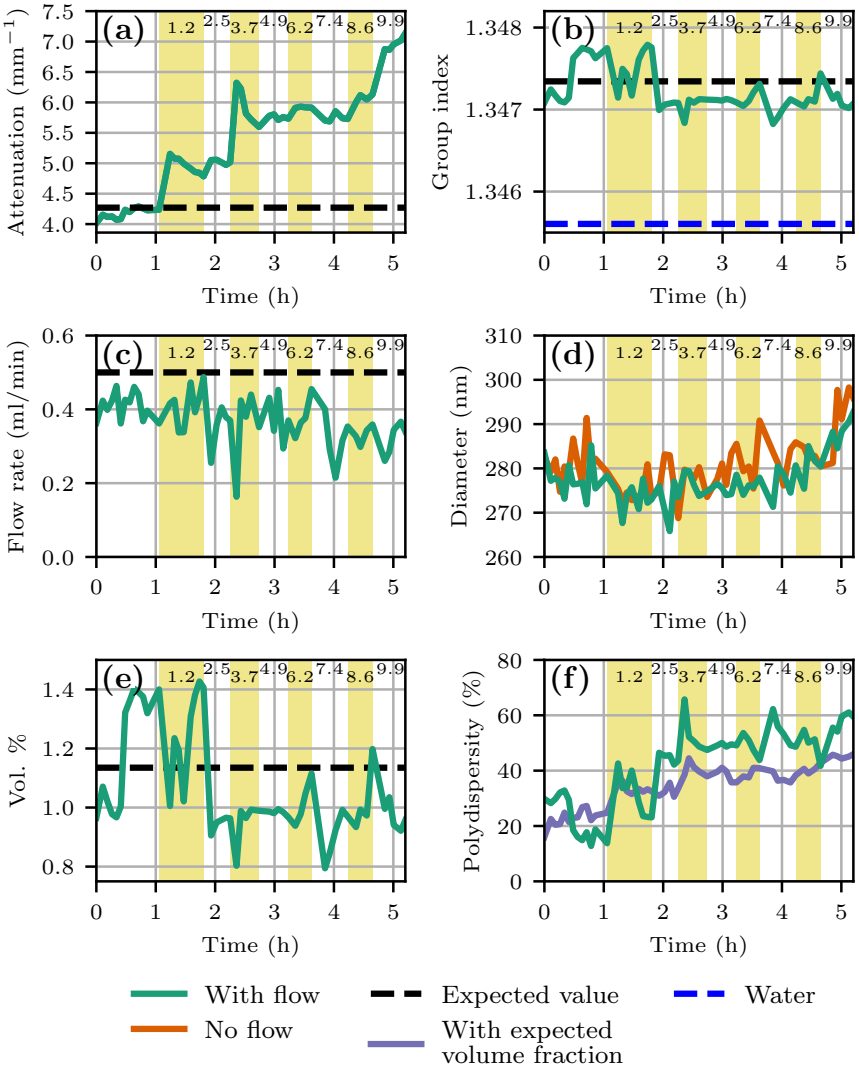

Figure 4.12: Summary of the results of the time-lapse flow sensing experiment, with the measured value shown in green. Dashed black lines represent expected values. The numbers at the top of each graph indicate the HCl weight fraction in units of 10^{-5}.**(a)** The measured attenuation at 637 nm over time. The expected attenuation is 4.27 µm^{-1}. **(b)** The measured group index. The expected group index is $n_g = 1.3473$, taken from [57], and the group index of water, shown in blue, is $n_g = 1.3456$, taken from [58]. **(c)** Measured flow rate. The flow rate is set to be 0.5 ml/min during the experiment. **(d)** The measured diameter in flow (green), and without flow (red). **(e)** The measured volume fraction. The expected volume fraction is 1.1 vol.%. **(f)** The measured polydispersity in flow, using the measured volume fraction (green), and using the expected volume fraction (purple).

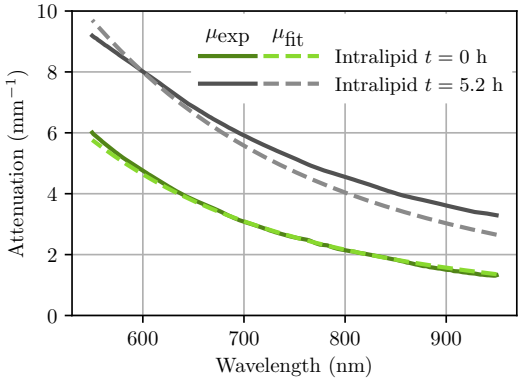

Figure 4.13: Measured and fitted attenuation as a function of wavelength at two times of the time-lapse flow sensing experiment.

which the attenuation increases but becomes too high to reliably measure the optical properties.

The measured group index of the suspension is shown in Fig. 4.12(b). Overall, the measured group index is slightly underestimated compared to the literature value, with the exception of the region around $t = 1$ h. The flow rate is shown in Fig. 4.12(c). After adding HCl, the variance of the flow rate measurements increases significantly. For all measurements the flow rate is underestimated and the estimate of the flow rate slowly decreases over time. The development of the diameter over time is shown in Fig. 4.12(d). The diameter measured without flow is shown in orange and with a flow of $Q = 0.5$ ml/min is shown in green. The diameter decreases with about 10 nm after adding HCl. The diameter slowly increases again after the $t = 2$ h mark. The diameters obtained with and without flow are very similar. The volume fraction as obtained from the group index is shown in Fig. 4.12(e). The measured volume fraction is lower than the expected value, with the exception of the region around $t = 1$ h.

Particle polydispersity over time is shown in Fig. 4.12(f). The polydispersity as obtained from the fit with the measured diameter, measured volume fraction and attenuation is shown in green. The polydispersity as obtained with the expected volume fraction, instead of the measured volume fraction, is shown in purple. The polydispersity increases steadily over time. When the expected volume fraction is used to fit the polydispersity, the increase in polydispersity over time is much more gradual.

The attenuation spectra of the first ($t = 0$ h) and last ($t = 5.2$ h) measurement of the time-lapse series are shown in Fig. 4.13. The log-normal size distribution is a good fit for the first measured spectrum. This is no longer the case for the last spectrum. It was observed that during the time-lapse experiment the sample visibly changed, switching from white to gray. The transmitted beam shape at $t = 0$ h did not seem to be affected by the Intralipid suspension other than having a lower intensity due to the attenuating sample. The transmitted beam for $t = 5.2$ h had a more pronounced and moving speckle pattern compared to the beam at $t = 0$ h.

4.5. DISCUSSION

In this work, the combination of a transmission spectral interferometer with heterodyne DLS allows for real-time sensing of the mean particle size, polydispersity, volume fraction and flow speed of a turbid medium. The combination of transmission and reflection potentially allows for access to more properties of colloidal media than the sum of both would, as we have access to the flow rate and realize a reduction of the ambiguity between the mean size and polydispersity in the Mie inversion of the transmission spectrum.

4.5.1. SILICATE PARTICLE SUSPENSION SENSING

The polynomial fit of the logarithm of the autocorrelation according to Eq. 4.17 enabled the removal of the effect of the flow rate on the fitted diameter. This permits simultaneous measurement of both flow speed and particle diameter. However, a polydisperse sample gives rise to higher-order exponents in the autocorrelation function [59]. This has a similar effect on the autocorrelation as flow, which may lead to flow rate estimation errors. The resulting autocorrelation would retain the effect of the polydispersity. Potentially, and without flow, a polydispersity index can be obtained with a fit to the autocorrelation, with a cumulant expansion[59], or the CONTIN algorithm[60, 61].

The variance in the measured polydispersity is quite large. This is caused by the fact that the measurement uncertainty in the attenuation, group index and diameter, as well as the choice of the particle size distribution, all affect the uncertainty of the polydispersity. Furthermore, a low polydispersity (around 10%) has only a small effect on the attenuation coefficient, as can also be seen in Chapter 3. Therefore, the polydispersity of these narrow distributions is difficult to measure with the Mie scattering spectrum. The spikes in the polydispersity as shown in Fig. 4.11(f) correlate with the order, and hence the sample drift, in which the measurements were made. Since this drift affects the refraction measurements, and also correlates with a slight increase in the measured volume fraction, this is likely caused by heating of the components of the experiment. Since the sample is flowing, heating should not be significant in the sample. The sodium silicate particles used for this work have a moderate size polydispersity of 9%. In addition, in the independent scattering regime, an increase in the particle diameter or in the polydispersity has a similar effect on the scattering attenuation, which causes an ambiguity when relying on the attenuation alone to obtain the particle size distribution.

The ambiguity between the diameter and polydispersity in the attenuation spectrum results in amplification of measurement errors when the diameter as measured with DLS is compensated for the polydispersity as obtained with the attenuation spectrum. An overestimate of the diameter would create an underestimate of the polydispersity and vice versa. This, in turn, would result in an undercompensation, leaving the estimated diameter still too large. There is less ambiguity between the polydispersity and diameter in the dependent scattering regime.

In summary, the fitted polydispersity serves as a good indicator of particle size distribution changes over time, or to compare two otherwise similar samples, but the method needs to be improved upon for the sensing of absolute polydispersities. A lower flow rate or higher particle diameter will increase the reliability of the measurement of absolute values. Furthermore, the reference power may be increased such that the homodyne

component of the autocorrelation is even lower compared to the heterodyne component. However, for sensing changes in the size distribution, instead of the measurement of the absolute size and polydispersity, this method can still work well.

4.5.2. TIME-LAPSE INTRALIPID SENSING

There are two mechanisms behind the increase in polydispersity upon addition of HCl. First, the screening effect of the hydrochloric acid ions decreases the zeta potential. This, in turn, leads to aggregation from the decrease in repellent electrostatic forces. Both the polydispersity and the mean particle size would increase. A similar screening effect can be achieved with other ions, such as NaCl.

The second mechanism is the dissolution of the lipid particles. In this case, the apolar molecules in the soy oil particles react with the H^+ ions to form polar, soluble molecules. This mechanism would decrease the particle size, and increase the polydispersity, since larger particles have a lower outer surface to volume ratio than small particles.

The mean particle size decreases from t = 1 h onward, and then increases from the t = 2 h mark. This indicates that both mechanisms play a role. For comparison, Ife *et al.* [62] found that for similar lipid particles the mean diameter decreases for pH levels between 4 and 2.5, and they observed a small increase for a pH lower than 2.5. They found that the substitution of HCl with NaCl with similar molarities only led to an increase in particle size. This means that both mechanisms apply to the dissolution of Intralipid with HCl.

The particle size distribution of Intralipid is assumed to be log-normal. A log-normal distribution has a similar shape as the skewed distribution as reported in [63]. This distribution fits the measured attenuation spectrum of Intralipid well, which can be seen in Fig. 4.13. However, for the Intralipid sample with HCl, the underlying particle size distribution seems to have deviated from log-normal. The change in attenuation between the sample at t = 0 h and t = 5.2 h is not only visible in the attenuation spectrum, but is also noticeable in the appearance of the sample. The change of color, and the appearance of the speckle pattern indicates the presence of larger particles in the sample. The small change in mean diameter suggests that the significant change in the attenuation spectrum is due to a broadening of the particle size distribution.

For the sodium silicate particle suspension, the volume fraction measurement is a limiting factor to an accurate polydispersity fit. In Fig. 4.12(f) the polydispersity, as determined with the expected volume fraction, does not have the dip in polydispersity around the 1 h mark. This time range corresponds to a time when there is an increased measured volume fraction, as can be seen in Fig. 4.12(e). The precision of the refractive index measurement is limited to setup stability and channel height. The group index can be measured more accurately in wider channels. However, this would limit the maximum volume fraction that can be accurately measured for strongly scattering materials. The stability of the setup is less of a concern for on-chip optics, where there is less room for movement, or uneven temperature changes.

4.5.3. DLS AUTOCORRELATION FUNCTION IN FLOWING SUSPENSIONS

The separation of the effect of diffusion and flow on the measured autocorrelation in Eq. 4.13 assumes that any nonlinearity in the decorrelation rate is due to flow. This assumption holds for the higher flow rates observed in the sodium silicate measurements, but for a high polydispersity and a low flow rate this is no longer the case. The high polydispersity and low flow rates in Intralipid measurements make the change in polydispersity a likely cause for the decrease in flow rate visible in Fig. 4.12(c). The autocorrelation for a moderately polydisperse sample may be written with a cumulant expansion [64]

$$g_1(\tau) = Ae^{-D_0 q^2 \tau + \frac{1}{2}\mu_2 \tau^2}. \tag{4.19}$$

Here the parameter μ_2 increases with increasing polydispersity, and is positive. Therefore, g_1 decays slower with higher polydispersity, and a lower flow rate may be obtained using the procedure outlined here.

The model used in this chapter also neglects hydrodynamic interactions between the particles [65, 66]. The hydrodynamic interactions increase the apparent diameter for large volume fractions. Therefore, the slightly higher diameter for the 11.7 vol.% in Fig. 4.10 may be caused by hydrodynamic interaction between the particles. The differences in diameter for different volume fractions appear to be smaller in Fig. 4.11(d) compared to Fig. 4.10, however this cannot be concluded due to the larger standard deviation in the polydispersity compensated measurements. Other improvements that could be made to the DLS model include the sub-diffusion part of the autocorrelation, which must be considered for very low volume fractions [35].

The accuracy of DLS flow measurements can be improved by increasing the Doppler angle α. In that case, the flow rate can be easily determined by the complex Doppler part of the heterodyne autocorrelation in Eq. 4.10, which is very similar to LDF. A disadvantage of LDF is that the correlation time is much shorter. This limits its applicability for accurate particle sizing. An LDF experiment for both flow measurement and particle sizing is described in Appendix D.

Another factor that is not accounted for, is the effect of shear on diffusion [67–70]. For a maximum flow speed of 5.3 mm/s in a 1 mm wide channel, the shear effects are not expected to be significant with respect to the diffusion and Doppler terms [71]. This means that a simple integration over the depth dependent flow speeds in Eq. 4.10 is justified.

The averaging in Eq. 4.10 only weights the electric fields based on the amplitude of the field, which is proportional to $e^{-\mu_s z}$, with μ_s the scattering attenuation and z the depth into the channel. This can be improved upon by considering the effect of the depth dependence of the signal to noise ratio (SNR) on the autocorrelation. Because the SNR is governed by shot noise, which scales with the square root of the detected signal, it decreases with increasing depth z, where the signal is attenuated according to the Lambert-Beer law.

4.5.4. SENSING APPLICATIONS

In this work, the interferometric transmission spectrum and the heterodyne DLS signal in reflection were measured. The particle size can potentially be measured more accurately with the incorporation of more scattering angles. This is often used in flow cy-

tometers and commercial particle sizers. The method presented in this work can also be used to detect changes in the scattering anisotropy. The standard deviation in the intensity of the photodiode is proportional to the anisotropy factor. The standard deviation for the time-lapse measurement is shown in Fig. 4.14. Since the decrease in backreflected signal is related to both the cross section of the particles, the anisotropy factor and the volume fraction of the dispersed particles, proper modeling of the scattering is required to obtain the anisotropy factor [72–74]. For dilute samples, the anisotropy factor is simply given by the ratio of forward and backscattered light [75]. For strongly scattering media, multiple scattering needs to be taken into account, with, for example, the adding-doubling method [76, 77].

For industrial sensing applications, the measurement of absolute values is often less important than detecting changes in relevant quantities, or to monitor whether the measured values are nominal [5]. Therefore, the sensor read-out, in this case the attenuation, group index and the decay rate of the autocorrelation, is often sufficient. This diminishes the need for a model for the sample parameters, such as particle diameter, volume fraction and polydispersity. In this case, the diffusion coefficient is sensitive to changes in the particle size, the group index to changes in volume, and the attenuation to the polydispersity.

The techniques presented here, can potentially be integrated into a sensing platform. Besides integration of the optical path and spectrometer, a main issue is the broadband light source, While supercontinuum lasers have a high output power, they are bulky and expensive. It is possible to generate a supercontinuum spectrum on a chip, but this would still require a high power external pump laser [78, 79]. In this case, SLDs could provide a suitable alternative. SLDs have a narrower spectrum, but they are more stable and have less noise in the spectrum, which would make it possible to do DLS and transmission measurements with the same source. Furthermore, with on-chip integration, the optical sensors can be combined with mechanical sensors, such as MEMS and Coriolis sensors, to include measurement of pressure and viscosity [80].

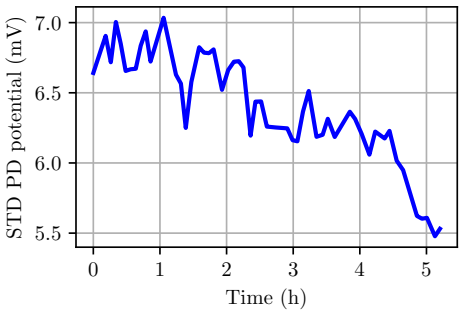

Figure 4.14: Standard deviation of the measured photodiode (PD) potential in the time-lapse experiment.

4.6. CONCLUSION

The experiments and analysis in this work provide a method for real-time, in-flow simultaneous measurement of flow, volume fraction, particle size and polydispersity. This is achieved with the combination of a spectral Mach-Zehnder interferometer combined with a heterodyne DLS setup. These parameters were tested for a monodisperse sample of 100 nm particles for volume fractions between 2.9 vol.% and 11.7 vol.% and flow speeds up to 5.3 mm/s. The same method was applied for a real-time in-flow measurement of a sample of Intralipid 20% and water in which the pH steadily decreased to an estimated lower bound of 0.57 over the duration of 5.2 h.

DATA AVAILABILITY

Data underlying the results presented in this chapter and the relevant analysis routines are available in Ref. [81].

REFERENCES

[1] V. Rajan, B. Varghese, T. G. van Leeuwen, and W. Steenbergen, Review of methodological developments in laser Doppler flowmetry, *Lasers in Medical Science*, 24:269–283, 2009.

[2] P. de Haan, J.-P. S. Mulder, J. C. Lötters, and E. Verpoorte, A highly stable, pressure-driven, flow control system based on Coriolis mass flow sensors for organs-on-chips, *Flow Measurement and Instrumentation*, 97:102576, 2024.

[3] G. Gervinskas, D. J. Day, and S. Juodkazis, Optofluidic Fabry-Pérot sensor for water solutions at high flow rates, *Optical Materials Express*, 2(3):279–286, 2012.

[4] M. I. Veríssimo, J. A. Gamelas, A. J. Fernandes, D. V. Evtuguin, and M. T. S. Gomes, A new formaldehyde optical sensor: Detecting milk adulteration, *Food Chemistry*, 318:126461, 2020.

[5] L. L. Simon, H. Pataki, G. Marosi, F. Meemken, K. Hungerbühler, A. Baiker, S. Tummala, B. Glennon, M. Kuentz, G. Steele, *et al.*, Assessment of recent process analytical technology (PAT) trends: A multiauthor review, *Organic Process Research & Development*, 19(1):3–62, 2015.

[6] J. Emmerich, Q. Tang, Y. Wang, P. Neubauer, S. Junne, and S. Maaß, Optical inline analysis and monitoring of particle size and shape distributions for multiple applications: Scientific and industrial relevance, *Chinese Journal of Chemical Engineering*, 27(2):257–277, 2019.

[7] B. Aernouts, E. Polshin, J. Lammertyn, and W. Saeys, Visible and near-infrared spectroscopic analysis of raw milk for cow health monitoring: reflectance or transmittance?, *Journal of Dairy Science*, 94(11):5315–5329, 2011.

[8] B. Y. Shekunov, P. Chattopadhyay, H. H. Y. Tong, and A. H. L. Chow, Particle size analysis in pharmaceutics: principles, methods and applications, *Pharmaceutical Research*, 24:203–227, 2007.

[9] A. F. T. Silva, A. Burggraeve, Q. Denon, P. Van der Meeren, N. Sandler, T. Van Den Kerkhof, M. Hellings, C. Vervaet, J. P. Remon, J. A. Lopes, *et al.*, Particle sizing measurements in pharmaceutical applications: Comparison of in-process methods versus off-line methods, *European Journal of Pharmaceutics and Biopharmaceutics*, 85(3):1006–1018, 2013.

[10] F. Caputo, R. Vogel, J. Savage, G. Vella, A. Law, G. Della Camera, G. Hannon, B. Peacock, D. Mehn, J. Ponti, *et al.*, Measuring particle size distribution and mass concentration of nanoplastics and microplastics: addressing some analytical challenges in the sub-micron size range, *Journal of Colloid and Interface Science*, 588:401–417, 2021.

[11] J. Droujko and P. Molnar, Open-source, low-cost, in-situ turbidity sensor for river network monitoring, *Scientific Reports*, 12(1):10341, 2022.
[12] A. Sdobnov, G. Piavchenko, A. Bykov, and I. Meglinski, Advances in dynamic light scattering imaging of blood flow, *Laser & Photonics Reviews*, 18(2):2300494, 2024.
[13] R. Xalter and R. Mülhaupt, Online monitoring of polyolefin particle growth in catalytic olefin slurry polymerization by means of lasentec focused beam reflectance measurement (FBRM) and video microscopy (PVM) probes, *Macromolecular Reaction Engineering*, 4(1): 25–39, 2010.
[14] T. Provder, Challenges in particle size distribution measurement past, present and for the 21st century, *Progress in Organic Coatings*, 32(1-4):143–153, 1997.
[15] W. Zhang, Y. Hu, G. Choi, S. Liang, M. Liu, and W. Guan, Microfluidic multiple cross-correlated Coulter counter for improved particle size analysis, *Sensors and Actuators B: Chemical*, 296:126615, 2019.
[16] M. J. W. Povey, Ultrasound particle sizing: A review, *Particuology*, 11(2):135–147, 2013.
[17] K. Kitao, M. Tani, M. Yamane, S. Inui, M. Yamada, and T. Norisuye, Nano and submicron particle sizing in concentrated suspension by dynamic ultrasound scattering method, *Colloids and Surfaces A: Physicochemical and Engineering Aspects*, page 133807, 2024.
[18] W. Wang, L. Xia, X. Xiao, and G. Li, Recent progress on microfluidics integrated with fiber-optic sensors for on-site detection, *Sensors*, 24(7):2067, 2024.
[19] C. Chen and J. Wang, Optical biosensors: An exhaustive and comprehensive review, *Analyst*, 145(5):1605–1628, 2020.
[20] Y. Zhao, X.-g. Hu, S. Hu, and Y. Peng, Applications of fiber-optic biochemical sensor in microfluidic chips: A review, *Biosensors and Bioelectronics*, 166:112447, 2020.
[21] A. R. Heath, P. D. Fawell, P. A. Bahri, and J. D. Swift, Estimating average particle size by focused beam reflectance measurement (FBRM), *Particle & Particle Systems Characterization: Measurement and Description of Particle Properties and Behavior in Powders and Other Disperse Systems*, 19(2):84–95, 2002.
[22] K. P. McComiskey and L. Tajber, Comparison of particle size methodology and assessment of nanoparticle tracking analysis (NTA) as a tool for live monitoring of crystallisation pathways, *European Journal of Pharmaceutics and Biopharmaceutics*, 130:314–326, 2018.
[23] M. A. Al-Khafaji, A. Gaál, A. Wacha, A. Bóta, and Z. Varga, Particle size distribution of bimodal silica nanoparticles: A comparison of different measurement techniques, *Materials*, 13(14): 3101, 2020.
[24] J. Gross-Rother, M. Blech, E. Preis, U. Bakowsky, and P. Garidel, Particle detection and characterization for biopharmaceutical applications: Current principles of established and alternative techniques, *Pharmaceutics*, 12(11):1112, 2020.
[25] J. Agagliate, R. Röttgers, M. S. Twardowski, and D. McKee, Evaluation of a flow cytometry method to determine size and real refractive index distributions in natural marine particle populations, *Applied Optics*, 57(7):1705–1716, 2018.
[26] A. Cameirão, H. Le Ba, M. Darbouret, J.-M. Herri, J.-L. Peytavy, and P. Glénat, Chord length distributions interpretation using a polydispersed population: Modeling and experiments, *Journal of Crystal Growth*, 342(1):65–71, 2012.
[27] R. Pecora, Doppler shifts in light scattering from pure liquids and polymer solutions, *The Journal of Chemical Physics*, 40(6):1604–1614, 1964.
[28] R. Foord, E. Jakeman, C. Oliver, E. R. Pike, R. J. Blagrove, E. Wood, and A. R. Peacocke, Determination of diffusion coefficients of haemocyanin at low concentration by intensity fluctuation spectroscopy of scattered laser light, *Nature*, 227(5255):242–245, 1970.
[29] B. Freeland, R. McCann, P. O'Neill, S. Sreenilayam, M. Tiefenthaler, M. Dabros, M. Juillerat, G. Foley, and D. Brabazon, Real-time monitoring and control for high-efficiency autonomous

laser fabrication of silicon nanoparticle colloids, *The International Journal of Advanced Manufacturing Technology*, 114:291–304, 2021.

[30] R. Pecora, Dynamic light scattering measurement of nanometer particles in liquids, *Journal of Nanoparticle Research*, 2:123–131, 2000.

[31] W. Wu, M. S. G. Knoll, C. Giraudet, M. H. Rausch, and A. P. Fröba, Heterodyne dynamic light scattering for the characterization of particle dispersions, *Applied Optics*, 62(30):8007–8017, 2023.

[32] R. Besseling, M. Damen, J. Wijgergangs, M. Hermes, G. Wynia, and A. Gerich, New unique PAT method and instrument for real-time inline size characterization of concentrated, flowing nanosuspensions, *European Journal of Pharmaceutical Sciences*, 133:205–213, 2019.

[33] M. Sheybanifard, L. P. Guerzoni, A. Omidinia-Anarkoli, L. De Laporte, J. Buyel, R. Besseling, M. Damen, A. Gerich, T. Lammers, and J. M. Metselaar, Liposome manufacturing under continuous flow conditions: towards a fully integrated set-up with in-line control of critical quality attributes, *Lab on a Chip*, 23(1):182–194, 2023.

[34] J. Lee, W. Wu, J. Y. Jiang, B. Zhu, and D. A. Boas, Dynamic light scattering optical coherence tomography, *Optics Express*, 20(20):22262–22277, 2012.

[35] K. Cheishvili and J. Kalkman, Sub-diffusion flow velocimetry with number fluctuation optical coherence tomography, *Optics Express*, 31(3):3755–3773, 2023.

[36] K. Cheishvili, R. Besseling, M. Hermes, and J. Kalkman, Wavenumber-dependent dynamic light scattering optical coherence tomography measurements of collective and self-diffusion, *Optics Express*, 32(11):19963–19983, 2024.

[37] J. Kalkman, A. V. Bykov, D. J. Faber, and T. G. van Leeuwen, Multiple and dependent scattering effects in Doppler optical coherence tomography, *Optics Express*, 18(4):3883–3892, 2010.

[38] B. K. Huang and M. A. Choma, Resolving directional ambiguity in dynamic light scattering-based transverse motion velocimetry in optical coherence tomography, *Optics Letters*, 39(3): 521–524, 2014.

[39] K. Cheishvili and J. Kalkman, Scanning dynamic light scattering optical coherence tomography for measurement of high omnidirectional flow velocities, *Optics Express*, 30(13):23382–23397, 2022.

[40] N. Uribe-Patarroyo and B. E. Bouma, Velocity gradients in spatially resolved laser Doppler flowmetry and dynamic light scattering with confocal and coherence gating, *Physical Review E*, 94(2):022604, 2016.

[41] F. R. A. Onofri, I. Rodriguez-Ruiz, and F. Lamadie, Microfluidic lab-on-a-chip characterization of nano-to microparticles suspensions by light extinction spectrometry, *Optics Express*, 30(2): 2981–2990, 2022.

[42] B. C. Heinze, J. R. Gamboa, K. Kim, J.-Y. Song, and J.-Y. Yoon, Microfluidic immunosensor with integrated liquid core waveguides for sensitive Mie scattering detection of avian influenza antigens in a real biological matrix, *Analytical and Bioanalytical Chemistry*, 398:2693–2700, 2010.

[43] A. K. Trull, J. van der Horst, J. G. Bijster, and J. Kalkman, Transmission optical coherence tomography based measurement of optical material properties, *Optics Express*, 23(26):33550–33563, 2015.

[44] J. de Wit, S. Tonn, G. V. den Ackerveken, and J. Kalkman, Quantification of plant morphology and leaf thickness with opticalcoherence tomography, *Applied Optics*, 59(33):10304–10311, 2020.

[45] A. Vrij, Mixtures of hard spheres in the Percus–Yevick approximation. light scattering at finite angles, *Journal of Chemical Physics*, 71(8):3267–3270, 1979.

[46] P. N. A. Speets and J. Kalkman, Experiment and theory of the complex refractive index of dense colloidal media, *Journal of the Optical Society of America A*, 41(2):214–228, 2024.

[47] L. Tsang, J. A. Kong, and R. T. Shin, *Theory of Microwave Remote Sensing*, Wiley Series in Remote Sensing and Image Processing. Wiley, 1985, ISBN 9780471888604.

[48] N. Weiss, T. G. van Leeuwen, and J. Kalkman, Localized measurement of longitudinal and transverse flow velocities in colloidal suspensions using optical coherence tomography, *Physical Review E*, 88:042312, 2013.

[49] G. G. Stokes, On the effect of the internal friction of fluids on the motion of pendulums, *Transactions of the Cambridge Philosophical Society*, 9:8, 1851.

[50] W. Sutherland, A dynamical theory of diffusion for non-electrolytes and the molecular mass of albumin, *The London, Edinburgh, and Dublin Philosophical Magazine and Journal of Science*, 9(54):781–785, 1905.

[51] A. Einstein, Über die von der molekularkinetischen Theorie der Wärme geforderte Bewegung von in ruhenden Flüssigkeiten suspendierten Teilchen, *Annalen der Physik*, 4:549–560, 1905.

[52] P. Virtanen *et al.*, SciPy 1.0: Fundamental Algorithms for Scientific Computing in Python, *Nature Methods*, 17:261–272, 2020.

[53] J. V. Boussinesq, Mémoire sur l'influence desfrottements dans les mouvements réguliers des fluides, *Journal de Mathématiques pures et Appliquées*, 13(2):377–424, 1868.

[54] N.-S. Cheng, Formula for the viscosity of a glycerol- water mixture, *Industrial & Engineering Chemistry Research*, 47(9):3285–3288, 2008.

[55] S. Prahl, *Miepython*, 2024.

[56] J. A. Nelder and R. Mead, A simplex method for function minimization, *The Computer Journal*, 7(4):308–313, 1965.

[57] H. J. van Staveren, C. J. M. Moes, J. van Marie, S. A. Prahl, and M. J. C. van Gemert, Light scattering in lntralipid-10% in the wavelength range of 400–1100 nm, *Applied Optics*, 30(31): 4507–4514, 1991.

[58] M. Daimon and A. Masumura, Measurement of the refractive index of distilled water from the near-infrared region to the ultraviolet region, *Applied Optics*, 46(18):3811–3820, 2007.

[59] B. J. Frisken, Revisiting the method of cumulants for the analysis of dynamic light-scattering data, *Applied Optics*, 40(24):4087–4091, 2001.

[60] S. W. Provencher, A constrained regularization method for inverting data represented by linear algebraic or integral equations, *Computer Physics Communications*, 27(3):213–227, 1982.

[61] R. T. C. Ju, C. W. Frank, and A. P. Gast, Contin analysis of colloidal aggregates, *Langmuir*, 8(9): 2165–2171, 1992.

[62] A. F. Ife, I. H. Harding, R. M. Shah, E. A. Palombo, and D. S. Eldridge, Effect of pH and electrolytes on the colloidal stability of stearic acid–based lipid nanoparticles, *Journal of Nanoparticle Research*, 20:1–8, 2018.

[63] M. Raju and S. N. Unni, Concentration-dependent correlated scattering properties of Intralipid 20% dilutions, *Applied Optics*, 56(4):1157–1166, 2017.

[64] A. G. Mailer, P. S. Clegg, and P. N. Pusey, Particle sizing by dynamic light scattering: non-linear cumulant analysis, *Journal of Physics: Condensed Matter*, 27(14):145102, 2015.

[65] C. Beenakker and P. Mazur, Self-diffusion of spheres in a concentrated suspension, *Physica A: Statistical Mechanics and its Applications*, 120(3):388–410, 1983.

[66] U. Genz and R. Klein, Collective diffusion of charged spheres in the presence of hydrodynamic interaction, *Physica A: Statistical Mechanics and its Applications*, 171(1):26–42, 1991.

[67] B. Ackerson and N. Clark, Dynamic light scattering at low rates of shear, *Journal de Physique*, 42(7):929–936, 1981.

[68] A. Acrivos, G. K. Batchelor, E. J. Hinch, D. L. Koch, and R. Mauri, Longitudinal shear-induced diffusion of spheres in a dilute suspension, *Journal of Fluid Mechanics*, 240:651–657, 1992.

[69] Y. D. Yan and J. K. G. Dhont, Shear-induced structure distortion in nonaqueous dispersions of charged colloidal spheres via light scattering, *Physica A: Statistical Mechanics and its Applications*, 198(1-2):78–107, 1993.

[70] F. Destremaut, J.-B. Salmon, L. Qi, and J.-P. Chapel, Microfluidics with on-line dynamic light scattering for size measurements, *Lab on a Chip*, 9(22):3289–3296, 2009.

[71] L. M. Torquato, N. Hélaine, Y. Cui, R. O'Connell, J. Gummel, E. S. Robles, D. Jacob, and J. T. Cabral, Microfluidic in-line dynamic light scattering with a commercial fibre optic system, *Lab on a Chip*, 23(11):2540–2552, 2023.

[72] A. Kienle, M. S. Patterson, L. Ott, and R. Steiner, Determination of the scattering coefficient and the anisotropy factor from laser Doppler spectra of liquids including blood, *Applied Optics*, 35(19):3404–3412, 1996.

[73] V. M. Kodach, D. J. Faber, J. van Marle, T. G. van Leeuwen, and J. Kalkman, Determination of the scattering anisotropy with optical coherence tomography, *Optics Express*, 19(7):6131–6140, 2011.

[74] M. Almasian, N. Bosschaart, T. G. van Leeuwen, and D. J. Faber, Validation of quantitative attenuation and backscattering coefficient measurements by optical coherence tomography in the concentration-dependent and multiple scattering regime, *Journal of Biomedical Optics*, 20(12):121314, 2015.

[75] I. Niskanen, V. Forsberg, D. Zakrisson, S. Reza, M. Hummelgård, B. Andres, I. Fedorov, T. Suopajärvi, H. Liimatainen, and G. Thungström, Determination of nanoparticle size using Rayleigh approximation and Mie theory, *Chemical Engineering Science*, 201:222–229, 2019.

[76] S. A. Prahl, M. J. C. van Gemert, and A. J. Welch, Determining the optical properties of turbid media by using the adding–doubling method, *Applied Optics*, 32(4):559–568, 1993.

[77] B. Aernouts, R. Watté, R. V. Beers, F. Delport, M. Merchiers, J. D. Block, J. Lammertyn, and W. Saeys, Flexible tool for simulating the bulk optical properties of polydisperse spherical particles in an absorbing host: experimental validation, *Optics Express*, 22(17):20223–20238, 2014.

[78] J. P. Epping, T. Hellwig, M. Hoekman, R. Mateman, A. Leinse, R. G. Heideman, A. van Rees, P. J. M. van der Slot, C. J. Lee, C. Fallnich, and K. Boller, On-chip visible-to-infrared supercontinuum generation with more than 495 thz spectral bandwidth, *Optics Express*, 23(15):19596–19604, 2015.

[79] H. Zia, K. Ye, Y. Klaver, D. Marpaung, and K. Boller, Ultraefficient on-chip supercontinuum generation from sign-alternating-dispersion waveguides, *Advanced Photonics Research*, 4(5):2200296, 2023.

[80] E. Van der Wouden, J. Groenesteijn, R. Wiegerink, and J. Lötters, Multi parameter flow meter for on-line measurement of gas mixture composition, *Micromachines*, 6(4):452–461, 2015.

[81] P. N. A. Speets and J. Kalkman, *Optical interferometric spectral and dynamic multi-parameter flow sensing - data and analysis*, https://zenodo.org/uploads/14911557, 2025.

5

CONCLUSION AND OUTLOOK

5.1. CONCLUSION

In this work, the bulk optical properties of turbid and transparent media were measured with visible light transmission spectral interferometry. The light source is a supercontinuum laser, which allows the measurement of the optical properties for a broad spectrum of 400 nm to 930 nm. The interferometer and its performance are described in Chapter 2. With Fourier filtering, amplitude, and phase analysis, the transmission spectrum, group refractive index and group velocity dispersion (GVD) are determined from a single measurement of the spectral interferogram. These properties are extracted from a single-shot measurement, which makes this approach suitable for optical sensing. The GVD is obtained from a single broad-spectrum measurement, instead of a fit through multiple measurements at a single wavelength. This greatly increases the precision of the GVD, since the GVD is dependent on the first and second derivative of the phase index with the wavenumber.

In Chapter 2, the transmission spectra of turbid media were described with a semi-empirical light scattering model, where there was no direct relationship between the optical properties to physical fluid properties, such as the volume fraction and particle size distribution. Therefore, fluid properties could only be obtained through calibration. Hence, in Chapter 3, the attenuation coefficient and refractive index of a suspension were calculated from the fluid properties through more complete effective refractive index models that incorporate dependent scattering effects. Volume fraction dependent scattering in the imaginary part of the effective refractive index is well known. However, the effect of the volume fraction on the real part of the refractive index is smaller, and there is little experimental research in the literature. Therefore, the physics of the dependent scattering effect of the effective complex-valued refractive index was further investigated. The complex refractive indices of various volume fractions of silica nanoparticles with a diameter of 100 nm were measured, and related to a dipole model and the low-frequency QCA model [1]. In this work, a nonlinear relationship between the volume fraction and the GVD was found and compared to theory. The dipole model given by Parola *et al.* [2] described the nonlinear relationship of the GVD both qualitatively and quantitatively.

Both the dipole and QCA model were used to fit the particle phase index and size distribution to the measured group index and attenuation coefficient. The size distribution as calculated with the dipole model was close to the particle size distribution as obtained with transmission electron microscopy. Moreover, the fit with the dipole model allows for a simultaneous measurement of both the phase index and the particle size distribution of suspended particles. This is particularly useful for characterizing porous particles, since the refractive index of porous particles depends on the embedding medium.

For particles that are too small to have Mie resonances and for polydisperse particle size distributions, where the Mie resonances are washed out, there is ambiguity between the mean particle size and the polydispersity. That is, both have a similar effect on the scattering attenuation spectrum. Therefore, the method presented in Chapter 3 only works when there are multiple dilutions of the same particle sample, which makes it less applicable for in-line sensing. A solution for in-line sensing is presented in Chapter 4. Here, the transmission interferometer described in Chapter 2 was expanded with a Michelson interferometer in backreflection. With the second interferometer, the het-

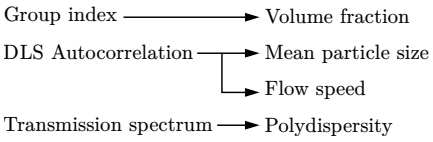

Figure 5.1: Measured physical properties and obtained flow parameters.

erodyne DLS signal was measured at a single wavelength. The use of the additional DLS information broke the ambiguity between the mean particle size and the polydispersity that arises when the particle size is determined from the Mie spectrum alone. For this experiment, all measured parameters are summarized in Fig. 5.1. The volume fraction is determined with the group index, and the mean particle size and the flow speed are determined with DLS. Together with the mean particle size obtained with DLS, the Mie spectrum was used to obtain the polydispersity. The DLS extension enables sensing of smaller particles, though its signal must be corrected for flow effects. The method described in this thesis allows DLS not only to be used in flow, but also to be used to measure the flow rate.

5

5.2. OUTLOOK

5.2.1. IMPROVED PHASE ESTIMATION

Throughout this thesis, the instantaneous spectral phase is obtained from a Hilbert transform of the interferometric signal. The Hilbert transform is relatively fast and easy to implement. A disadvantage of the Hilbert transform is that it creates fringes near the edges of the spectrum, see Fig. 2.6, that cause the first derivative of the reconstructed phase to the wavenumber k to have limited useful spectral range. These fringes can be reduced by means of a continuous wavelet transform (CWT). With this method, a signal is convolved with a range of wavelets with different frequencies, or chirplets with different frequencies and chirps [3, 4].

An example of how the CWT can improve the calculation of the spectral phase is shown in Fig. 5.2. Here, the interference spectrum of a water sample of 200 µm and a

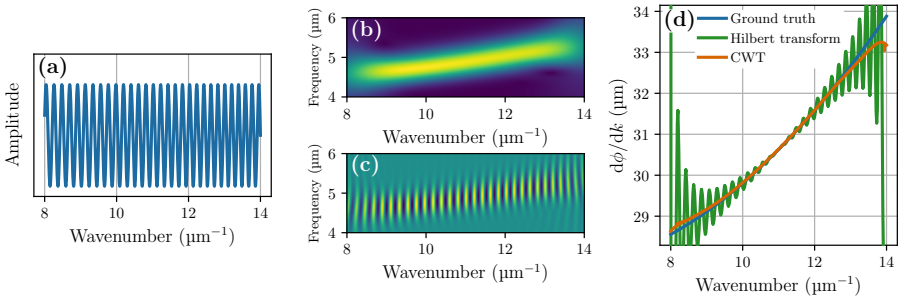

Figure 5.2: **(a)** Interference spectrum of a water sample. **(b)** The absolute value of the CWT and **(c)** the real value of the CWT. **(d)** The phase of the signal as obtained with the Hilbert transform and the CWT.

240 µm distance between the sample arm and the reference arm. The frequency with the highest overlap with the wavelet kernel function has the highest amplitude when the signal is convolved with the kernel. Therefore, the interference spectrum shown in Fig. 5.2(a) is convolved with Morlet wavelets with a range of center frequencies. The absolute value shown in Fig. 5.2(b) represents how much of each frequency is present at each wavenumber k. The real part of the CWT is shown in Fig. 5.2(c). The y-axes of Fig. 5.2(b) and Fig. 5.2(c) indicate the center frequencies of the wavelets. The phase obtained from the complex angle of the average CWT spectrum weighted by the absolute value given in Fig. 5.2(b) is less sensitive to the edge fringes than the Hilbert transform. As an example, the derivative of the phase to k is shown in Fig. 5.2(d), and compared to the result of the Hilbert transform. The CWT is very close to the ground truth, but a polynomial fit to the phase obtained with a Hilbert transform gives a similar result and the CWT is much slower. The main advantage of a CWT over a Hilbert transform is that it does not require a fit with, for example, a polynomial, to obtain the refractive properties of the sample. In addition, it may no longer be necessary to remove the lowest and highest wavenumbers, as shown in Fig. 2.6(e), where the spurious fringes are the strongest, from the data.

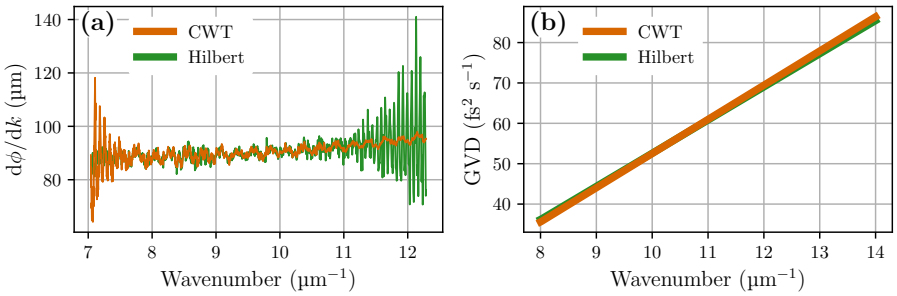

Figure 5.3: **(a)** Derivative of the spectral phase ϕ to the wavenumber k of an Intralipid sample with a Hilbert transform and the CWT. **(b)** The GVD obtained from a polynomial fit to the phase obtained with both methods.

An example of the phase estimated with CWT for an Intralipid 20% sample in a 200 µm cuvette is shown in Fig. 5.3(a). The fringes in the derivative of the phase for CWT are slightly lower than the fringes obtained with the Hilbert transform. Furthermore, the region where the phase is undisturbed by the edge effects is larger for the phase as obtained with CWT. Since the GVD depends on the second derivative of the phase, smoothening the data or fitting the phase is still necessary to obtain the GVD accurately. The GVD calculated from a polynomial fit to the phase, as obtained for both methods, is shown in Fig. 5.3(b). Both methods give very similar results for the type of interference signals used in this work. However, for signals that are not as clean as those measured in this thesis, for example when there are more frequencies present in the signal, the inherent frequency filtering of the CWT may yield better results. The CWT is also useful to analyze spectra with more frequencies, e.g. when there are multiple pathlengths in the signal. In that case, the CWT wavelength can be tuned to a single frequency such that the phase is estimated only for the frequency of interest. The main advantage over Fourier filtering

is that this frequency can be wavenumber dependent, which is useful for signals with a strong chirp.

5.2.2. PHASE REFRACTIVE INDEX ESTIMATION

An advantage of spectral interferometry is that both the phase (spectral dispersion) and amplitude (spectral attenuation) are directly measured. An example of this advantage is the measurement of the GVD. The GVD is often obtained from a fit through a few individual data points, e.g., measured with an Abbe refractometer at a few distinct wavelengths. Since the GVD depends on the first and second derivative of the phase index to the wavenumber, this fit induces a large error in the measured GVD. When measured spectrally, the interferometric signal is close to a continuum, with as many data points as there are pixels in the spectrometer. This enables much more accurate dispersion measurements, though it introduces a 2π ambiguity in the relationship between the phase index and the group index given by Eqns. 2.8 and 2.9. However, there are some cases where a phase-index measurement is required. For example, in Chapter 4, the calculation of the particle size polydispersity required the phase index of the particle, where the phase index was obtained from literature. This requires prior knowledge of the sample, and is difficult to apply to porous particles, where the refractive index of the particle is lower than that of bulk.

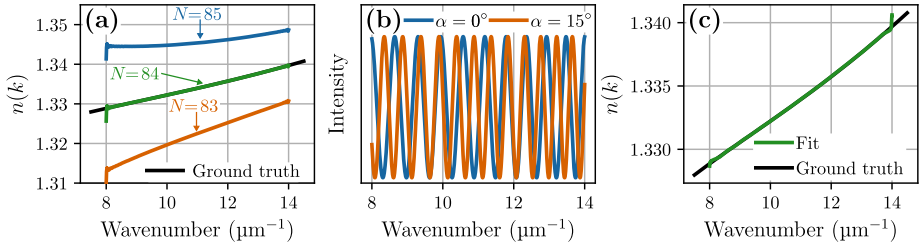

Figure 5.4: **(a)** Refractive index as obtained for $N = 83$ to $N = 85$. **(b)** Interference spectrum as obtained with no angle and an angle of $\alpha = 15°$. **(c)** The phase refractive index as obtained from the interference in Figure **(b)**.

The setup described in this thesis can be modified to measure the phase index together with the group index. For example, when the channel is sufficiently small, the phase index can be obtained with relatively little prior knowledge of the dispersion curve [5]. The phase index $n(k)$ can be obtained directly from the unwrapped spectral phase $\phi(k)$ with

$$n(k) = \frac{\phi(k) + 2\pi N}{kL}. \tag{5.1}$$

Where N is the integer number of full wavelengths that fit within the channel size L from the starting point of the phase wrapping. This is typically the lowest measured wavenumber.

An example of the phase index obtained from various values of N is shown in Fig. 5.4(a). Here, the refractive index $n(k)$ of water is shown as obtained from the interferometric signal and its Hilbert transform of a hypothetical $L = 50$ µm wide channel. The phase ambiguity $2\pi N$ can be determined with prior knowledge and the use of Eq. 5.1,

since the refractive index curve for $N = 83$ is unrealistically low, and the curve for $N = 85$ exhibits negative dispersion, which is not impossible, but uncommon. Therefore it is found that $N = 84$.

The phase index can also be obtained from a spectral phase measurement with two or more distinct and known path lengths through the sample [6]. An example is shown in Fig. 5.4(b). Here, two interference signals are shown for a 100 µm wide cuvette with water and a distance between the sample arm and reference arm of 125 µm. The blue signal is for a cuvette placed normal to the incident beam, $\alpha = 0$, therefore the path length through the sample is $L_1 = 100$ µm. The orange signal is for a cuvette placed with an angle $\alpha = 15°$. This angle increases the path length L_2 to 100.97 µm. The number of phase wraps for both angles, N_1 and N_2, can be found by solving

$$n(k) = \frac{\phi_1(k) + 2\pi N_1}{kL_1} = \frac{\phi_2(k) + 2\pi N_2}{kL_2}. \tag{5.2}$$

This can be done with a range of reasonable trials for values of N_1. The value for N_2 can be obtained from the ratio L_2/L_1 as

$$N_2 = \text{round}\left[\frac{1}{2\pi}\left\langle \frac{L_2}{L_1}\left(2\pi N_1 + \phi_1(k)\right) - \phi_2(k)\right\rangle_k\right]. \tag{5.3}$$

The correct value for N_1 is then found when the equation for N_2 gives the same refractive index spectrum $n(k)$ as obtained for one of the values for N_1. This gives $N_1 = 10$ and $N_2 = 13$. The number of phase wraps is low, compared the previous example due to the longer distance between the sample arm and the reference arm. Note that Eq. 5.2 can only be solved when L_1/L_2 is not a natural number. Furthermore, the best fit results are obtained when the difference between L_1 and L_2 is not too large. Therefore, the small difference in sample distance induced by the small angle of the cuvette works well compared to an additional path through the sample.

5.2.3. BULK OPTICAL PROPERTIES OF STRONGLY SCATTERING MEDIA

One application of the measurement and theoretical modeling of dependent scattering effects is the measurement of both the particle size distribution and the phase index of the particles. The theory used in this work was implemented to moderately sized particles with a size parameter slightly larger than unity. In this case, the nonlinear volume fraction dependence of the refractive index is small and only noticeably nonlinear in the volume fraction dependence of the GVD. When applied to larger size parameters, the nonlinear effects are expected to be larger and to change the volume fraction dependence of the imaginary part of the effective refractive index [2]. When the size parameter $x = k_m a$ becomes significantly larger than 1, the scattering efficiency of the scatterers may even increase for high volume fractions, as opposed to the more typical decrease of the attenuation for high volume fractions [7–9]. For even larger particles, the coupled dipole model may no longer be sufficient. An example of an alternative model that has been applied for larger particles is the Keller multiple scattering model [8, 10, 11].

For propagation through dense media composed of particles with a high scattering anisotropy, the diffusive component of the transmitted light is non-negligible, or even sizable. Therefore, the transmitted light is partially spatially coherent and the electric

field in the medium is no longer a plane wave. Hence, the assumptions behind the models used in this thesis are no longer valid. In that case, the electric field consists of a coherent plane wave, and a diffuse part [12].

Ballistic light can still be described with an effective refractive index, but the diffusive component no longer has a well-defined optical path length. The diffusive part can be filtered out with coherence gating, filtering based on optical path length [13–15]. The ballistic light has a relatively thin peak at low path lengths in the optical path length distribution, whereas the diffusive part has a long tail at higher path lengths. Diffusive light and multiple scattering also affect the DLS signal, but for this case also coherence gating can be applied to DLS by means of DLS-OCT. For DLS-OCT, the diode laser must be replaced by the supercontinuum laser, and the photodiode by a high speed spectrometer. By selecting only low penetration depths, the effect of multiple scattering and diffuse light can be avoided.

For strongly scattering media with fully diffusive transmitted light, the optical properties can be calculated with the diffusive wave approximation to the radiative transfer equation. This approximation is often used to model wave propagation in tissue [16–19]. For very complex media it may be impossible to calculate the attenuation spectrum and refractive index analytically and need to be simulated, e.g. with Monte Carlo methods. However, this is slow, and requires much prior knowledge of the sample.

5.2.4. IMPROVEMENTS FOR DLS DIFFUSION ESTIMATION

In this work, the diffusion part of the DLS signal is assumed to be fully governed by the Stokes-Einstein equation, which describes free diffusing particles. However, a high volume fraction of scatterers influences the DLS signal. The presence of other neighboring particles, which is prominent for concentrated samples, influences the mean square displacement caused by hydrodynamic interactions that are mediated through the embedding medium, electrostatic and excluded volume interactions, and multiple scattering [20]. These effects are not included in the Stokes-Einstein equation, which assumes independent diffusion only. A model that is often used to describe hydrodynamic effect is given by Beenakker [21] and has been applied to DLS-OCT [20]. This model was tested on the polydispersity corrected mean size, as shown in Fig. 4.11(d) in Chapter 4. However, in this case the standard deviation of the measured mean particle size increased, and an unwanted volume fraction dependence of the measured diameter was found. Therefore, a compensation of the hydrodynamic interactions, as well as for the electrostatic and excluded volume interactions were omitted in this thesis. Potentially, the q dependence of DLS-OCT can be used for improved particle sizing in dense media [20].

In this work, the first-order autocorrelation $g_1(\tau)$ was measured with a heterodyne DLS setup. However, for dilute samples, the number-fluctuation term in the second-order autocorrelation term $g_2(\tau)$ can also be used for particle concentration measurements and flow characterization [22]. To measure the number-fluctuation term, the DLS setup as described in Chapter 4, needs to be modified to a DLS-OCT system to ensure a small coherence-gated measurement volume. This can be done by changing the diode laser with a broadband light source, and the photodiode with a high-speed spectrometer. The number-fluctuation term is present in the homodyne signal, i.e., the sample intensity without the reference signal. In this case the coherence gating of OCT and the

improved sensitivity make this method better suitable for DLS-OCT. Coherence gating creates a high axial resolution to reduce the total number of particles in the focal volume, while the improved sensitivity is required since dilute samples have low backscattering. Number-fluctuation DLS-OCT creates an opportunity for particle concentration and flow speed measurement in very dilute suspensions, where measuring other parameters, such as the group index, are challenging. However, since the number-fluctuation term requires very low particle concentrations, detecting a signal that is strong enough can be challenging.

The DLS signal analysis used in this work assumes single scattering. However, for dense colloidal media, multiple scattered light cannot be neglected in the autocorrelation function. In that case diffusive wave spectroscopy (DWS) multiple scattering may be used to provide a better particle size estimate in dense media [23, 24]. Multiple scattering has two advantages over single scattering DLS. First, multiple scattering potentially allows the measurement of more scattering wavenumbers q. Second, this method is more sensitive to small movements on short time scales. The autocorrelation of DWS depends on the phase shift due the Brownian motion at each scattering event, but also on the optical path length distribution, which depends on the sample geometry.

Alternatively, the q dependence of the diffusion can be measured with differential dynamic microscopy [25]. Here, the intensity autocorrelation of a pixel in a microscope video is measured over time. The q dependence is obtained by a spatial Fourier transform of the image. With this technique, the autocorrelation for very low scattering wavenumbers q can be measured, which allows for the use of slower detectors compared to DLS in a back-scattering configuration.

5.2.5. FUTURE IMPROVEMENTS OF MULTI-PARAMETER FLOW SENSING

The spectral interferometric method described in this thesis can be applied for sensing in both transparent and turbid media. Applications for spectral interferometry alone include, for transparent media, glucose content monitoring and salinity measurements [14, 26]. For turbid media, both the transmission spectrum and the refraction can be used for particle sizing [27, 28]. Chapter 4 describes how spectral interferometry augmented with DLS can be used to measure the particle size and flow rate in real-time. Similarly, the addition of more sensing modes will allow the extraction of more information about the sample.

For example, to make better use of the autocorrelation function for particle sizing of polydisperse samples, the dependence on the flow rate can be eliminated by measuring the flow with a reference method, for example, the measurement of the pressure difference [29], using MEMS [30, 31] or Coriolis sensors [32, 33]. The autocorrelation function can then be corrected for the effect of the flow rate, and subsequently be used for particle sizing. The particle size distribution can then be obtained from the autocorrelation with the methods of cumulants [34], or the CONTIN algorithm [35].

Alternatively, flow or pressure sensors can be used to measure the viscosity to remove uncertainty about this from the fitting routine. The viscosity depends on the composition of the medium and is used to calculate the particle diameter from the measured diffusion constant. Therefore, continuous measurement of the viscosity makes it a useful addition for in-flow DLS applications. In addition, similar to the group index, the

viscosity can be used to estimate the relative volume fractions [36, 37]. Since the refractive index of the medium depends on the volume fraction, the combination of the group index and viscosity measurement can be used for a simultaneous measurement of the volume fraction and the refractive index of the suspended particles. Also, for large-scale sensors, where interferometry over the entire flow channel is impractical, viscosity measurements would be a good alternative to group index measurements to determine the volume fraction. Interestingly, DLS can also be used to measure the viscosity of the embedding medium, but this requires prior knowledge of the particle size [38].

In this work, only the autocorrelation of the backscattered light is used for DLS particle sizing. There is an opportunity to also use the intensity of the backscattered light for the measurement of the scattering anisotropy. An example is the addition of the measurement of the transmission attenuation coefficient with the adding-doubling method. However, this requires proper calibration [39]. Since scattering anisotropy is strongly correlated with mean particle size, this provides additional data on the particle size distribution, which can be used in a forward fitting algorithm [40, 41]. When the backreflected signal is measured with OCT, the attenuation coefficient can be measured with a fit to the intensity decay in depth [42, 43]. For this, the intensity decay needs to be calibrated for the detection roll-off and confocal sensitivity. The optical properties can be localized in depth using a local fit to the OCT attenuation. However, when the optical properties can be assumed to be homogeneous over the sample, depth localization is not necessary.

In our application of DLS, we assumed Newtonian fluid and laminar flow, with a Reynolds number of about 6 for the highest flow speed and the largest channel width. However, for many industrial applications, the flow profile cannot be assumed *a priori*. For example, in the continuous production of some pharmaceutical ingredients, the fluid can be non-Newtonian and the flow profile can be, for example, given by a plug flow [44]. The flow profile can be obtained by DLS-OCT or Doppler OCT, where the flow profile can be spatially resolved [20, 45]. DLS-OCT can be readily used with the same experimental setup, since it can use the same light source and spectrometer. The back-reflected spectrum can be measured with the setup as described in Chapter 4, if the photodiode is replaced with a spectrometer. When a high-speed spectrometer is used, the DLS signal can still be measured. However, a spectrometer, as required for DLS-OCT is typically slower than a photodiode, so the smallest measurable particle sizes are larger. The depth-resolved flow profile then can be used for improved particle size estimation in combination with the other measured parameters.

To obtain additional sample information, also the polarimetric properties of the sample can be measured. For example, glucose rotates the polarization state of light, and the amount of polarization rotation can be used to determine the glucose concentration. Also, polarimetry can be applied to turbid media. In transmission, the depolarization of the light through the sample relates to the size and concentration of suspended particles [46]. To measure the polarization with the optical setup as described in Chapter 2, linear polarizers can be placed before the first beam splitter and directly after the sample. The polarization can be measured by rotating one of the polarizers. For polarizers mounted at 90 degrees with respect to each other, there is no transmitted light when the sample does not change the polarization of the light. Hence, it is sensitive to small

amounts of depolarization. An advantage of the use of polarizers in combination of the interferometer is that a small signal, corresponding to low depolarization, can be amplified with the heterodyne detection geometry.

The angular dependence of Mie scattering is another method to improve particle-size estimation [47, 48]. The particle size can then be obtained with a fit with the Mie-calculated phase function. The scattering in the forward direction is not polarization sensitive. However, light that is scattered at an angle with respect to the forward direction has an elliptical polarization. Since the angle dependence of the polarization ratio of the scattered light can be measured, the size distribution can be obtained with a forward fit with Mie theory to the polarization of the scattered light [49–51]. The measurement of the angle dependence of the scattering is not as straightforward as measuring the polarization of the transmitted light. It is possible to add an additional arm to collect the scattered light on a fixed angle, but a simpler solution is to build a fiber-based interferometer and to mount both the sample, and the collecting fiber coupler, on a rotation stage.

One of the advantages of the methods described in this thesis, is that they are applicable in the infrared. The only fundamental change is the use of an infrared light source for the DLS experiment, and the use of InGaAs instead of silicon detectors. Many molecular absorption peaks, which are often used as a fingerprint for various substances, are outside of the visible wavelength range and located in the infrared region. For example, infrared detection allows the measurement of the fat and protein content of milk [52]. Therefore, near-infrared is routinely applied for in-line sensing [53]. While the scattering attenuation is lower in the infrared, allowing transmittance measurements in more strongly scattering media, the high absorption of water is a limiting factor for the use of infrared light in transmission spectroscopy [52].

5.2.6. ON-CHIP INTEGRATION

The methods presented in this thesis can potentially be integrated on-chip to reduce sensor size and cost. The free space interferometer, as presented in this thesis, is sensitive to vibrations, bulky, and expensive. Since an on-chip interferometer is smaller and fully fixed on a chip, interferometric measurements are possibly easier to use in an industrial setting. On-chip, the reference and sample arm intensities of Mach-Zehnder interferometers are difficult to control individually, but in principle the transmission spectrum and the phase can be sensed with a single shot measurement using spatial filtering. Therefore, interferometric sensing in combination with Fourier filtering, as was done in Chapter 2, has good potential for on-chip implementation.

A main advantage of on-chip integration is the possibility to include MEMS sensors on the same chip for pressure and flow sensing [54–57]. However, MEMS sensors are often made from materials, for example silicon-rich nitride, that only allow sensing in the infrared region [58]. Lowering silicon content and implementing other fabrication processes may lower the absorption in the visible spectrum [59].

Next to material absorption, the available spectral width also depends on the light source. A supercontinuum laser allows for a large spectral bandwidth, but is expensive. For sensing applications, superluminescent diodes (SLDs) are often used, but they have a limited spectral bandwidth. This does not necessarily hamper their use, but the wave-

length needs to be carefully selected in advance for the specific sensing application. For narrow-bandwidth sources, the volume fraction can be measured easily with the group index. However, the measurement of the GVD will be more challenging as estimating the second-order derivative of the spectral phase is challenging with a narrow spectral bandwidth. Although a full characterization of the sample may not be possible, it can be used to determine whether the process operates under the right conditions. When needed, multiple SLDs with different spectra may be coupled together to broaden the spectrum. Alternatively, when a broad spectrum is required, it is possible to generate a supercontinuum spectrum in the visible wavelength range on a silicon nitride chip, but this would still require an expensive pump laser [60–62].

It is possible to integrate the detection on a chip as well, for example, with an on-chip spectrometer. The main parameters to assess the quality of a on-chip spectrometer are the spectral width $\Delta\lambda$, the spectral resolution $\delta\lambda$, and the feasibility for on-chip implementation. With a larger bandwidth it is possible to gather more data on a sample. In the case of scattering media and Mie inversion of the transmission spectrum, a broad-range device could measure a broader range of particle sizes. The second requirement for an on-chip spectrometer is sufficient spectral resolution. Since the Mie spectrum for small particles varies only slowly with wavelength, the main need for a high resolution is to obtain a high maximum measurable optical path length $z_{\max} = \frac{\lambda_0}{2\delta\lambda}$, with λ_0 the central wavelength. In this work, the spectral resolution is approximately 1.3 nm. Therefore, the maximum optical path length is given by 164 µm, which is enough to measure the difference in optical path length between various samples, which is typically not larger than 50 µm for a 1 mm wide flow channel.

The spectrometer can be etched on the chip itself with many variations on the traditional grating spectrometer with the grating part of the chip design [63]. Light can also be split into different wavelength bands with an arrayed waveguide grating (AWG) [64–66], which already has been applied to OCT [65]. The spectrum can also be obtained using Fourier transform spectroscopy. Although this is usually applied for narrowband spectrometers, it can be used for broadband spectrometers as well [67]. All three methods, the grating-based spectrometer, AWG, and Fourier transform spectrometer, have bandwidths of a few hundred nanometers and resolutions of around 6 nm, which corresponds to a maximum depth of $z_{\max} = 36$ µm, depending on the design [66–68]. Light detection still requires a linescan camera that needs to be fixed on the chip. For a simpler chip design, it is possible is to fix a MEMS spectrometer on the flow cell, instead of using an etched spectrometer. Small-scale MEMS spectrometers are already commercially available and are able to provide similar performance with a resolution of 10 nm to 15 nm [69, 70].

In the experiment described in Chapter 4 a bandpass filter around the diode laser wavelength was placed just in front of the photodiode to filter out background light. This bandpass filter can also be used to allow the supercontinuum (SC) laser to be used directly for the DLS measurement, thereby removing the need for the flip mirror and the additional diode laser. However, for our SC source, the pulse-to-pulse variance was too large for proper particle sizing, and better results were obtained using a single wavelength diode laser and high-speed photodiode.

To combine DLS with interferometric transmission measurements, both the detector

and the light source can be shared between both modalities. When a low-noise source, such as a superluminescent diode (SLD), or multiple coupled SLDs, the same source can be used both for the measurement of the transmission spectrum and the DLS signal in reflection. Combination of the detectors is less straightforward, but a cost-effective solution for detection is using self-mixing interferometry. Here, the photodiode, which is present in many laser packages to regulate the output power, is used to measure the temporal self-mixing due to the time-varying reflected field. The diffusion constant can be related to the frequency distribution of the photodiode signal [71].

5.2.7. DATA-DRIVEN SENSING

This work uses physics-based models to relate the measured optical parameters to sample properties such as volume fraction and particle size. However, it may also be used for industrial applications where absolute quantities are not necessary, but rather the measurement of a change relative to a reference value is of importance. In those cases, a data-driven approach might often be sufficient on the directly measured signals such as the transmission spectrum. A data-driven approach is an empirical method where any sensor output is related to desired and undesired production outcomes. The measured sample properties are no longer given as a physical parameter, such as particle size, but as a quality parameter, or a pass-fail test [72]. For these use-cases, a semi-empirical model, for example as used in Chapter 2, or even a calibration only, is sufficient. With a data-driven approach, the relationship between sensor output and quality parameter will then depend on the application.

However, there are still benefits of relating the sensor output to physical quantities. Many process analytical technology (PAT) applications rely on careful characterization of the production process, where the actual composition is important for certification and product efficacy and safety. An example is the characterization of Intralipid, as used in this work. Intralipid is mostly known as an intravenous nutrient. Since intravenous administration of Intralipid, or commercially available lipid emulsions, can potentially have fatal results when the emulsified particles are too large, the mean and maximum particle size is subject to regulation [73, 74]. Another example of the need for quantitative data, is when exceeding a parameter is too unsafe for calibration. An example is the concentration of Grignard reagent used in the production of Tamoxifen, a breast cancer drug [75, 76]. Since the production of the reagent is an exothermic reaction, too high concentrations may cause a runaway reaction, damaging equipment. Lastly, sensing of absolute physical quantities are necessary as an input for system models, such as for digital twin or soft-sensing applications [77].

REFERENCES

[1] K. H. Ding and L. Tsang, Effective propagation constants of dense nontenuous media with multi-species of particles, *Journal of Electromagnetic Waves and Applications*, 2(8):757–777, 1988.

[2] A. Parola, R. Piazza, and V. Degiorgio, Optical extinction, refractive index, and multiple scattering for suspensions of interacting colloidal particles, *Journal of Chemical Physics*, 141(12): 124902, 2014.

[3] S. Mann and S. Haykin, The chirplet transform: Physical considerations, *IEEE Transactions on Signal Processing*, 43(11):2745–2761, 1995.

[4] I. Daubechies, J. Lu, and H.-T. Wu, Synchrosqueezed wavelet transforms: An empirical mode decomposition-like tool, *Applied and Computational Harmonic Analysis*, 30(2):243–261, 2011.

[5] J. R. Rogers and M. D. Hopler, Conversion of group refractive index to phase refractive index, *Journal of the Optical Society of America A*, 5(10):1595–1600, 1988.

[6] S. H. Kim, S. H. Lee, J. I. Lim, and K. H. Kim, Absolute refractive index measurement method over a broad wavelength region based on white-light interferometry, *Applied Optics*, 49(5): 910–914, 2010.

[7] A. Ishiniaru and Y. Kuga, Attenuation constant of a coherent field in a dense distribution of particles, *Journal of the Optical Society of America*, 72(10):1317–1320, 1982.

[8] A. García-Valenzuela, H. Contreras-Tello, J. A. Olivares, and F. L. S. Cuppo, Insights into the dependent-scattering contributions to the extinction coefficient in highly scattering suspensions, *Journal of the Optical Society of America A*, 30(7):1328–1334, 2013.

[9] A. Nahmad-Rohen and A. García-Valenzuela, Multiple-scattering model for the effective refractive index of dense suspensions of forward-scattering particles, *Journal of the Optical Society of America A*, 40(8):1552–1562, 2023.

[10] J. B. Keller, Stochastic equations and wave propagation in random media, *Proceedings of Symposia in Applied Mathematics*, 16:145–170, 1964.

[11] H. Contreras-Tello and A. García-Valenzuela, Refractive index measurement of turbid media by transmission of backscattered light near the critical angle, *Applied Optics*, 53(21):4768–4778, 2014.

[12] D. W. Mackowski and M. I. Mishchenko, Direct simulation of extinction in a slab of spherical particles, *Journal of Quantitative Spectroscopy and Radiative Transfer*, 123:103–112, 2013.

[13] V. D. Nguyen, D. J. Faber, E. van der Pol, T. G. van Leeuwen, and J. Kalkman, Dependent and multiple scattering in transmission and backscattering optical coherence tomography, *Optics Express*, 21(24):29145–29156, 2013.

[14] A. K. Trull, J. van der Horst, J. G. Bijster, and J. Kalkman, Transmission optical coherence tomography based measurement of optical material properties, *Optics Express*, 23(26):33550–33563, 2015.

[15] J. van der Horst, A. K. Trull, and J. Kalkman, Deep-tissue label-free quantitative optical tomography, *Optica*, 7(12):1682–1689, 2020.

[16] V. P. Tishkovets, E. V. Petrova, and M. I. Mishchenko, Scattering of electromagnetic waves by ensembles of particles and discrete random media, *Journal of Quantitative Spectroscopy and Radiative Transfer*, 112(13):2095–2127, 2011.

[17] L. A. Dombrovsky, The use of the transport approximation and diffusion-based models in radiative transfer calculations, *Computational Thermal Sciences*, 4(4):297–315, 2012.

[18] H. Fujii, Y. Hoshi, S. Okawa, T. Kosuge, and S. Kohno, Numerical modeling of photon propagation in biological tissue based on the radiative transfer equation, *AIP Conference Proceedings*, 1518(1):579–585, 2013.

[19] W. Zhou, O. Kholiqov, S. P. Chong, and V. J. Srinivasan, Highly parallel, interferometric diffusing wave spectroscopy for monitoring cerebral blood flow dynamics, *Optica*, 5(5):518–527, 2018.

[20] K. Cheishvili, R. Besseling, M. Hermes, and J. Kalkman, Wavenumber-dependent dynamic light scattering optical coherence tomography measurements of collective and self-diffusion, *Optics Express*, 32(11):19963–19983, 2024.

[21] C. W. J. Beenakker and P. Mazur, Diffusion of spheres in a concentrated suspension II, *Physica A: Statistical Mechanics and its Applications*, 126(3):349–370, 1984.

[22] K. Cheishvili and J. Kalkman, Sub-diffusion flow velocimetry with number fluctuation optical coherence tomography, *Optics Express*, 31(3):3755–3773, 2023.

[23] G. Maret, Diffusing-wave spectroscopy, *Current Opinion in Colloid & Interface Science*, 2(3): 251–257, 1997.

[24] K. A. Dennis, Q. Li, N. Sbalbi, S. C. Brown, and E. M. Furst, Diffusing wave spectroscopy measurements of colloidal suspension dynamics, *Langmuir*, 40(12):6129–6137, 2024.

[25] R. Cerbino and V. Trappe, Differential dynamic microscopy: probing wave vector dependent dynamics with a microscope, *Physical Review Letters*, 100(18):188102, 2008.

[26] S. M. Bagherzadeh, B. Grajciar, C. K. Hitzenberger, M. Pircher, and A. F. Fercher, Dispersion-based optical coherence tomography OCT measurement of mixture concentrations, *Optics Letters*, 32(20):2924–2926, 2007.

[27] F. R. A. Onofri, I. Rodriguez-Ruiz, and F. Lamadie, Microfluidic lab-on-a-chip characterization of nano-to microparticles suspensions by light extinction spectrometry, *Optics Express*, 30(2): 2981–2990, 2022.

[28] M. Mohammadi, Colloidal refractometry: meaning and measurement of refractive index for dispersions; the science that time forgot, *Advances in Colloid and Interface Science*, 62(1): 17–29, 1995.

[29] R. E. Oosterbroek, T. S. J. Lammerink, J. W. Berenschot, G. J. M. Krijnen, M. C. Elwenspoek, and A. van den Berg, A micromachined pressure/flow-sensor, *Sensors and Actuators A: Physical*, 77(3):167–177, 1999.

[30] R. Philip-Chandy, P. J. Scully, and R. Morgan, The design, development and performance characteristics of a fibre optic drag-force flow sensor, *Measurement Science and Technology*, 11(3):N31, 2000.

[31] M. Dijkstra, J. J. Van Baar, R. J. Wiegerink, T. S. J. Lammerink, J. H. De Boer, and G. J. M. Krijnen, Artificial sensory hairs based on the flow sensitive receptor hairs of crickets, *Journal of Micromechanics and Microengineering*, 15(7):S132, 2005.

[32] D. Alveringh, R. J. Wiegerink, and J. C. Lötters, Integrated pressure sensing using capacitive Coriolis mass flow sensors, *Journal of Microelectromechanical Systems*, 26(3):653–661, 2017.

[33] A. C. De Oliveira, T. V. P. Schut, J. Groenesteijn, Q. Fan, R. J. Wiegerink, and K. A. A. Makinwa, A MEMS Coriolis mass flow sensing system with combined drive and sense interface, In *2019 IEEE SENSORS*, pages 1–4. IEEE, 2019.

[34] B. J. Frisken, Revisiting the method of cumulants for the analysis of dynamic light-scattering data, *Applied Optics*, 40(24):4087–4091, 2001.

[35] S. W. Provencher, A constrained regularization method for inverting data represented by linear algebraic or integral equations, *Computer Physics Communications*, 27(3):213–227, 1982.

[36] N.-S. Cheng, Formula for the viscosity of a glycerol- water mixture, *Industrial & Engineering Chemistry Research*, 47(9):3285–3288, 2008.

[37] P. C. Mishra, S. Mukherjee, S. K. Nayak, and A. Panda, A brief review on viscosity of nanofluids, *International Nano Letters*, 4:109–120, 2014.

[38] S. Deguchi, S. K. Ghosh, R. G. Alargova, and K. Tsujii, Viscosity measurements of water at high temperatures and pressures using dynamic light scattering, *The Journal of Physical Chemistry B*, 110(37):18358–18362, 2006.

[39] B. Aernouts, R. Watté, R. V. Beers, F. Delport, M. Merchiers, J. D. Block, J. Lammertyn, and W. Saeys, Flexible tool for simulating the bulk optical properties of polydisperse spherical particles in an absorbing host: experimental validation, *Optics Express*, 22(17):20223–20238, 2014.

[40] A. Postelmans, B. Aernouts, and W. Saeys, Estimation of particle size distribution from bulk scattering spectra: validation on monomodal suspensions, *Analytical Chemistry*, 91(15): 10040–10048, 2019.

[41] A. Postelmans, B. Aernouts, J. Jordens, T. van Gerven, and W. Saeys, Milk homogenization monitoring: Fat globule size estimation from scattering spectra of milk, *Innovative Food Science and Emerging Technologies*, 60:102311–102320, 2020.

[42] N. Bosschaart, M. C. G. Aalders, D. J. Faber, J. J. A. Weda, M. J. C. van Gemert, and T. G. van Leeuwen, Quantitative measurements of absorption spectra in scattering media by low-coherence spectroscopy, *Optics Letters*, 34(23):233746–233748, 2009.

[43] N. Bosschaart, M. C. G. Aalders, T. G. van Leeuwen, and D. J. Faber, Spectral domain detection in low-coherence spectroscopy, *Biomedical Optics Express*, 3(9):2263–2272, 2012.

[44] S. Ferguson, G. Morris, H. Hao, M. Barrett, and B. Glennon, In-situ monitoring and characterization of plug flow crystallizers, *Chemical Engineering Science*, 77:105–111, 2012, 18th International Symposium on Industrial Crystallization.

[45] K. Cheishvili and J. Kalkman, Scanning dynamic light scattering optical coherence tomography for measurement of high omnidirectional flow velocities, *Optics Express*, 30(13):23382–23397, 2022.

[46] L. F. Rojas-Ochoa, D. Lacoste, R. Lenke, P. Schurtenberger, and F. Scheffold, Depolarization of backscattered linearly polarized light, *Journal of the Optical Society of America A*, 21(9): 1799–1804, 2004.

[47] A. Wax, C. Yang, V. Backman, M. Kalashnikov, R. R. Dasari, and M. S. Feld, Determination of particle size by using the anglular distribution of backscattered light as measured with low-coherence interferometry, *Journal of the Optical Society of America A*, 19(4):737–742, 2002.

[48] J. T. Butement, P. M. Holloway, J. A. Welsh, J. A. Holloway, N. A. Englyst, P. Horak, J. West, and J. S. Wilkinson, Monolithically-integrated cytometer for measuring particle diameter in the extracellular vesicle size range using multi-angle scattering, *Lab on a Chip*, 20:1267–1280, 2020.

[49] P. Massoli, F. Beretta, and A. D'Alessio, Single droplet size, velocity, and optical characteristics by the polarization properties of scattered light, *Applied Optics*, 28(6):1200–1205, 1989.

[50] D. L. Hofeldt, Full-field measurements of particle size distributions: I. theoretical limitations of the polarization ratio method, *Applied Optics*, 32(36):7551–7558, 1993.

[51] X. Q. Huang, J. Y. Yuan, and P. Hervé', Determination of particle size distribution by polarization analysis of the scattered light, *Optik*, 251:168454, 2022.

[52] B. Aernouts, E. Polshin, J. Lammertyn, and W. Saeys, Visible and near-infrared spectroscopic analysis of raw milk for cow health monitoring: reflectance or transmittance?, *Journal of Dairy Science*, 94(11):5315–5329, 2011.

[53] J. U. Porep, D. R. Kammerer, and R. Carle, On-line application of near infrared (NIR) spectroscopy in food production, *Trends in Food Science & Technology*, 46(2):211–230, 2015.

[54] J. Haneveld, T. S. J. Lammerink, M. J. de Boer, R. G. P. Sanders, A. Mehendale, J. C. Lötters, M. Dijkstra, and R. J. Wiegerink, Modeling, design, fabrication and characterization of a micro coriolis mass flow sensor, *Journal of Micromechanics and Microengineering*, 20(12):125001, 2010.

[55] J. C. Lötters, T. S. Lammerink, J. Groenesteijn, J. Haneveld, and R. J. Wiegerink, Integrated thermal and microcoriolis flow sensing system with a dynamic flow range of more than five decades, *Micromachines*, 3(1):194–203, 2012.

[56] W. Sparreboom, J. Van de Geest, M. Katerberg, R. Postma, J. Haneveld, J. Groenesteijn, T. Lammerink, R. Wiegerink, and J. Lötters, Compact mass flow meter based on a micro coriolis flow sensor, *Micromachines*, 4(1):22–33, 2013.

[57] T. V. P. Schut, D. Alveringh, W. Sparreboom, J. Groenesteijn, R. J. Wiegerink, and J. C. Lötters, Fully integrated mass flow, pressure, density and viscosity sensor for both liquids and gases, In *2018 IEEE Micro Electro Mechanical Systems (MEMS)*, pages 218–221. IEEE, 2018.

[58] A. Sundararajan, P. C. Pericas, R. J. Wiegerink, and J. C. Lötters, Silicon rich silicon nitride microchannels to determine fluid composition by near infrared absorbance, In *2022 IEEE 35th International Conference on Micro Electro Mechanical Systems Conference (MEMS)*, pages 676–679. IEEE, 2022.

[59] M. Corato-Zanarella, X. Ji, A. Mohanty, and M. Lipson, Absorption and scattering limits of silicon nitride integrated photonics in the visible spectrum, *Optics Express*, 32(4):5718–5728, 2024.

[60] C. Lafforgue, S. Guerber, J. M. Ramirez, G. Marcaud, C. Alonso-Ramos, X. L. Roux, D. Marris-Morini, E. Cassan, C. Baudot, F. Boeuf, S. Cremer, S. Monfray, and L. Vivien, Broadband supercontinuum generation in nitrogen-rich silicon nitride waveguides using a 300 mm industrial platform, *Photonics Research*, 8(3):352–358, 2020.

[61] A. Ishizawa, K. Kawashima, R. Kou, X. Xu, T. Tsuchizawa, T. Aihara, K. Yoshida, T. Nishikawa, K. Hitachi, G. Cong, N. Yamamoto, K. Yamada, and K. Oguri, Direct f-3f self-referencing using an integrated silicon-nitride waveguide, *Optics Express*, 30(4):5265–5273, 2022.

[62] K. Ren, Y. Guo, Y. Zhai, and L. Zhang, On-chip octave-spanning flat supercontinuum in all-normal-dispersion silicon nitride waveguides, *Optics Express*, 32(6):8527–8536, 2024.

[63] D. Sander and J. Müller, Selffocussing phase transmission grating for an integrated optical microspectrometer, *Sensors and Actuators A: Physical*, 88(1):1–9, 2001.

[64] P. Cheben, J. H. Schmid, A. Delâge, A. Densmore, S. Janz, B. Lamontagne, J. Lapointe, E. Post, P. Waldron, and D.-X. Xu, A high-resolution silicon-on-insulator arrayed waveguide grating microspectrometer with sub-micrometer aperture waveguides, *Optics Express*, 15(5):2299–2306, 2007.

[65] V. D. Nguyen, B. I. Akca, K. Wörhoff, R. M. de Ridder, M. Pollnau, T. G. van Leeuwen, and J. Kalkman, Spectral domain optical coherence tomography imaging with an integrated optics spectrometer, *Optics Letters*, 36(7):1293–1295, 2011.

[66] D. Geuzebroek, A. van Rees, E. Klein, and K. Lawniczuk, Ultra-wide band (400-1700nm) integrated spectrometer based on arrayed waveguide gratings for spectral tissue sensing, In *2017 IEEE 14th International Conference on Group IV Photonics (GFP)*, pages 83–84. IEEE, 2017.

[67] D. Pohl, M. Reig Escalé, M. Madi, F. Kaufmann, P. Brotzer, A. Sergeyev, B. Guldimann, P. Giaccari, E. Alberti, U. Meier, *et al.*, An integrated broadband spectrometer on thin-film lithium niobate, *Nature Photonics*, 14(1):24–29, 2020.

[68] R. Cheng, C.-L. Zou, X. Guo, S. Wang, X. Han, and H. X. Tang, Broadband on-chip single-photon spectrometer, *Nature Communications*, 10(1):4104, 2019.

[69] K. Laganovska, A. Zolotarjovs, M. Vázquez, K. Mc Donnell, J. Liepins, H. Ben-Yoav, V. Karitans, and K. Smits, Portable low-cost open-source wireless spectrophotometer for fast and reliable measurements, *HardwareX*, 7:e00108, 2020.

[70] C. Zhu, X. Fu, J. Zhang, K. Qin, and C. Wu, Review of portable near infrared spectrometers: Current status and new techniques, *Journal of Near Infrared Spectroscopy*, 30(2):51–66, 2022.

[71] C. Zakian, M. Dickinson, and T. King, Particle sizing and flow measurement using self-mixing interferometry with a laser diode, *Journal of Optics A: Pure and Applied Optics*, 7(6):S445, 2005.

[72] L. L. Simon, H. Pataki, G. Marosi, F. Meemken, K. Hungerbühler, A. Baiker, S. Tummala, B. Glennon, M. Kuentz, G. Steele, *et al.*, Assessment of recent process analytical technology (PAT) trends: A multiauthor review, *Organic Process Research & Development*, 19(1):3–62, 2015.

[73] D. F. Driscoll, The pharmacopeial evolution of intralipid injectable emulsion in plastic containers: From a coarse to a fine dispersion, *International Journal of Pharmaceutics*, 368(1): 193–198, 2009.

[74] T. Rooimans, M. Damen, C. M. A. Markesteijn, C. C. L. Schuurmans, N. H. C. De Zoete, P. M. Van Hasselt, W. E. Hennink, C. F. van Nostrum, M. Hermes, R. Besseling, and H. Vromans, Development of a compounded propofol nanoemulsion using multiple non-invasive process analytical technologies, *International Journal of Pharmaceutics*, 640:122960, 2023.

[75] J. Wiss, M. Länzlinger, and M. Wermuth, Safety improvement of a grignard reaction using on-line NIR monitoring, *Organic Process Research & Development*, 9(3):365–371, 2005.

[76] P. R. Murray, D. L. Browne, J. C. Pastre, C. Butters, D. Guthrie, and S. V. Ley, Continuous flow-processing of organometallic reagents using an advanced peristaltic pumping system and the telescoped flow synthesis of (E/Z)-tamoxifen, *Organic Process Research & Development*, 17(9):1192–1208, 2013.

[77] Y. Jiang, S. Yin, J. Dong, and O. Kaynak, A review on soft sensors for monitoring, control, and optimization of industrial processes, *IEEE Sensors Journal*, 21(11):12868–12881, 2020.

APPENDIX

A. PARTIAL STRUCTURE FACTOR

The partial structure factor for size bins i and j, $S_{ij} = H_{ij} + \delta_{ij}$, as given by Tsang *et al.*[1] is

$$H_{ij} = C_{ij} + \sum_k C_{ik} H_{kj} \,. \tag{4}$$

Which requires a matrix inversion to solve. In the same notation of [1], C_{ij} is given by

$$\begin{aligned} C_{ij}(q) = \frac{-\pi}{6} \frac{\sqrt{n_i n_j}}{1-\xi_3} \Bigg\{ & M_j \left[\cos X_i + X_i \sin X_i + \frac{3\xi_2 R_i \cos X_i}{1-\xi_3} + \frac{3\xi_1 N_i}{1-\xi_3} + \frac{3\xi_1 N_i}{1-\xi_3} + \frac{9\xi_2^2 N_i}{(1-\xi_3)^2} \right] \\ & + M_i \left[\cos X_j + X_j \cos X_j + \frac{3\xi_2 R_j \cos X_j}{1-\xi_3} + \frac{3\xi_1 N_j}{1-\xi_3} + \frac{9\xi_2^2 N_j}{(1-\xi_3)^2} \right] \\ & + M_i M_j \left[\frac{\xi_0}{1-\xi_3} + \frac{q^2 \xi_2}{4(1-\xi_3)} + \frac{6\xi_1 \xi_2}{(1-\xi_3)^2} + \frac{9\xi_2^3}{(1-\xi_3)^3} \right] \\ & + 3 N_i R_j \cos X_j + 3 N_j R_i \cos X_i + \frac{9\xi_2 N_i N_j}{(1-\xi_3)} \Bigg\} \end{aligned} \tag{5}$$

with ξ_α M_i, N_i and X_i given by

$$\xi_\alpha = \frac{\pi}{6} \sum_{j=1}^{L} n_j (2a_j)^\alpha \tag{6}$$

$$M_i = 3R_i^3 \left[\frac{\sin X_i}{X_i^3} - \frac{\cos X_i}{X_i^2} \right] \tag{7}$$

$$N_i = R_i^2 \frac{\sin X_i}{X_i} \tag{8}$$

$$X_i = \frac{q R_i}{2} \,. \tag{9}$$

Here, L is the number of bins, R_i is the particle diameter, a_i the particle radius, and n_i the number density.

B. COMPARISON OF VARIOUS MODELS FOR THE COMPLEX REFRACTIVE INDEX

B.1. THE QCA-CP MODEL

For small particles, the complex refractive index given by the low-frequency quasi-crystalline approximation with coherent potential (QCA-CP). This is given by[3]:

$$\tilde{n}_{\text{eff}}^2 k^2 = n_m^2 k^2 + \frac{3\tilde{n}_{\text{eff}} k^2}{D'} \sum_i^N f_{v,i} y_i \left\{ 1 + \frac{2i\,\tilde{n}_{\text{eff}}^2 k^3}{3D'} \left[\tfrac{1}{8} d_i^3 y + \sum_j^N \pi^3 d_j^3 \rho_j y \left(1 - S_{i,j}(q=0)\right) \right] \right\}. \tag{10}$$

y' and D' are given by

$$y' = \frac{k^2 n_p^2 - k^2 n_m^2}{3k^2 n_{\text{eff}}^2 + n_p^2 k^2 - n_m^2 k^2} \quad \text{and} \quad D' = 1 - \sum_i^N f_{v,i} y'. \tag{11}$$

This model is very similar to the QCA model. However, the refractive index on the right hand side of Eq. 10 no longer only depends on the refractive index of the embedding medium n_m, but also on the effective refractive index of the suspension n_{eff}. This equation is solved iteratively in 10 iterations. For the first iteration, the refractive index of the right hand side is given by[4]:

$$\tilde{n}_{\text{eff}}^2 = n_m^2 + 3 v_f n_m^2 \Gamma \left(1 + \frac{2i}{3} x \Gamma \left(1 + 4\pi\rho \int_0^\infty r^2 (g(r) - 1)\, \mathrm{d}r \right) \right) \tag{12}$$

Here the factor Γ is given by:

$$\Gamma = \frac{\chi}{1 - v_f \chi} \quad \text{and} \quad \chi = \frac{\frac{n_p^2}{n_m^2} - 1}{\frac{n_p^2}{n_m^2} + 2}$$

B.2. THE KELLER MODEL

For $x > 1$, a suitable model for the effective refractive index is given by Keller[5]. The effective refractive index for the Keller model is given by[6, 7]:

$$k^2 \tilde{n}_{\text{eff}}^2 = k^2 + \frac{4\pi i \rho}{k} f_{\text{Mie}}(0) - \frac{16\pi^2 \rho^2 f_{\text{Mie}}^2(0)}{k^2} \int_0^\infty \left(g(r) - 1\right) \frac{\sin(k\,\tilde{n}_{\text{eff}} r)}{k\,\tilde{n}_{\text{eff}}} e^{ikr}\, \mathrm{d}r \tag{13}$$

Here ρ is the number density of particles. Note that the effective refractive index $\tilde{n}_{\text{eff}}$ appears on both sides of the equation. This integral can be iteratively solved by calculating new values for the refractive index based on $\tilde{n}_{\text{eff}}$ of the previous iteration. The initial effective index is given by the second order expansion of Eq. 13[8]:

This section has been published as supplementary materials to P.N.A. Speets and J. Kalkman, *Experiment and theory of the complex refractive index of dense colloidal media,* Journal of the Optical Society America A, 41, 214-228 (2024)[2]

$$k\tilde{n}_{\text{eff}} = k\left(1 + \frac{2\pi\rho i}{k^3} f_{\text{Mie}}(0) + \frac{4\rho^2\pi^2}{k^6} S_{\text{Mie}}(0)\,(1 + G(k_m))\right) \tag{14}$$

Where $G(k)$ is given by:

$$G(k_m) = 2k_m^2 \int_0^\infty (g(r) - 1) \frac{\sin(k_m r)}{k_m} e^{ik_m r}\,\mathrm{d}r\,. \tag{15}$$

The refractive index of the particle does not appear explicitly in Eq. 13, but enters the model through the Mie scattering amplitude $f_{\text{Mie}}(0)$.

B.3. COMPARISON WITH EXPERIMENTAL RESULTS

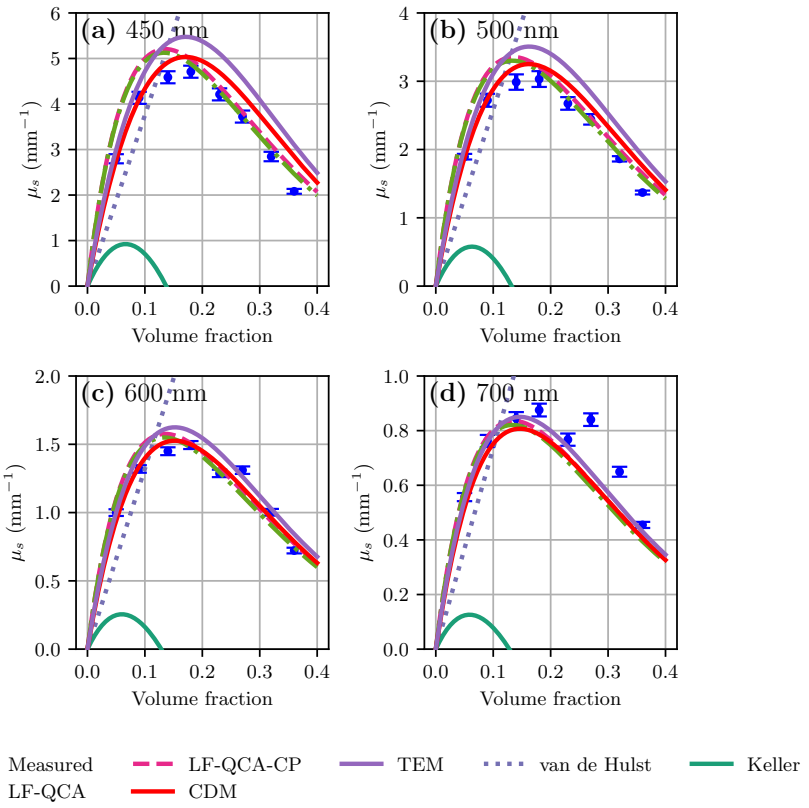

Figure 5: Attenuation given by all tested models. For the van de Hulst and Keller models, the particle size distribution to calculate the attenuation is given by Eq 17 with the Mie scattering amplitude.

Figure. 5 shows the measured attenuation compared to fits with all tested models to all data (incorporated in the iterative loop Fig. 6). For the QCA(-CP) and the CDM models, both the real and imaginary part of the refractive index is fit with the same model.

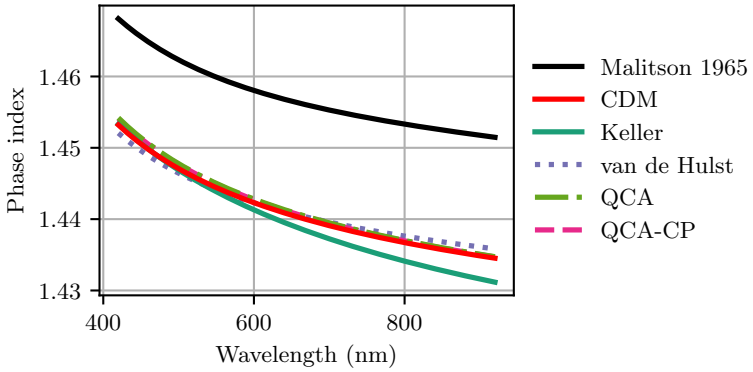

Figure 6: Refractive index of the particles as obtained by all tested models.

The imaginary part of the Keller and van de Hulst refractive index does not match well to the measured dependent scattering. Therefore, for these two models, the particle size distribution is determined with Eq. 17 and the Mie scattering amplitude f_{Mie}. Thus, the refractive index is fit with the real part of the refractive index only. The QCA and QCA-CP models yield very similar results. However, the Keller model fails to give results that get close to the measured data. This is similar to reported by Garcia-Valenzuela *et al.*[8] for a similar particle size. For comparison the CDM result for the TEM PSD is shown in purple.

In Fig. 6 the phase index of the silica particles as calculated with all models is shown and compared with the phase index of bulk silica. The TEM PSD was used for the van de Hulst and Keller models. All models, with the exception of the Keller model, give similar results.

The GVD of the suspension as calculated with all tested refractive index models is shown in Fig. 7. The QCA and QCA-CP models yield very similar. results with both giving a linear dependence on volume fraction The GVD determined with the Keller model is very nonlinear and does not match the measured GVD.

In Fig. 8 the PSD as determined with the various models is shown. In Fig. 8(a), the PSD is shown for all tested models where the phase index of the particle is determined with the indicated model, and the PSD is fit to imaginary part of the effective index with the Mie scattering amplitude in Eq. 17. In Fig. 8(b) both the real and imaginary part of the effective refractive index is fully determined with the indicated model. The results of the QCA and CDM models are discussed in the paper whereas the QCA-CP model is only slightly closer to the TEM PSD compared to the QCA model. The PSD fit results of Fig. 8 are summarized in Table 1. The refractive index is always calculated with the indicated model. The attenuation μ is fit with the model (μ_{model}), or with the Mie scattering amplitude f_{Mie} in Eq. 17, (μ_{Mie}).

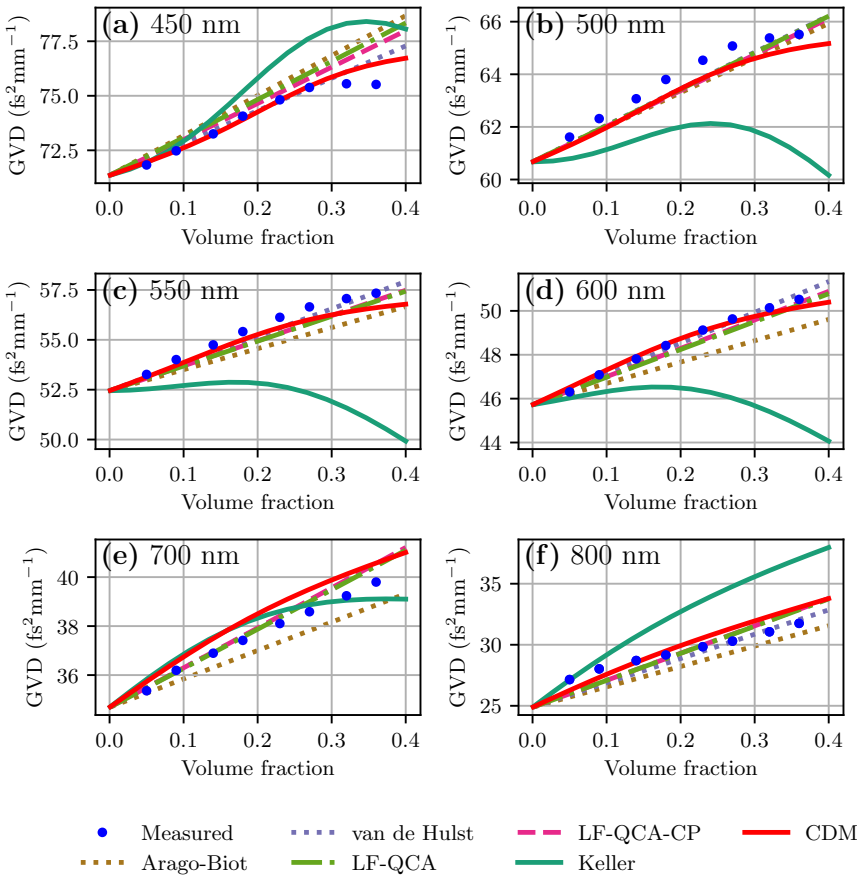

Figure 7: The GVD of the suspension calculated with all models.

Model	Diameter (nm)		Polydispersity	
	μ_{model}	μ_{Mie}	μ_{model}	μ_{Mie}
CDM	101.7	99.8	6.9 %	7.3 %
QCA	90.1	99.7	19.8 %	6.6 %
QCA-CP	91.1	99.7	17.1	6.6 %
Keller		110.3		6.3 %
van de Hulst		98.9		6.9 %
TEM	99.7		9.4 %	

Table 1: Obtained particle sizes for all tested models.

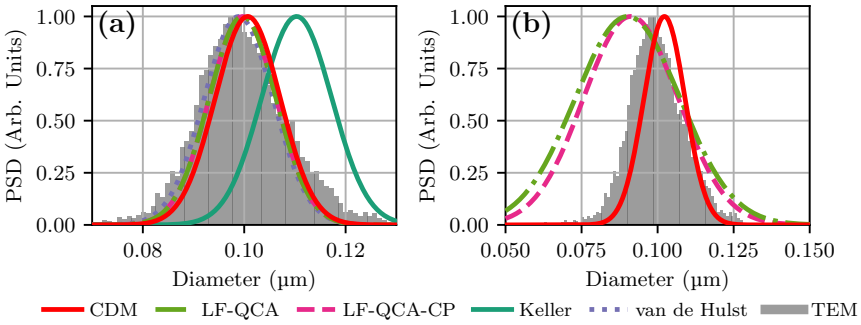

Figure 8: (a) The particle size distribution as obtained by fitting the real part of the effective refractive index with the indicated model, and the imaginary part with the Mie scattering amplitude in Eq. 17. (b) The PSD obtained with inverting both the real and imaginary part of the effective refractive index with the indicated model.

B.4. PHASE INDEX OF COLLOIDAL SILICA

We consider the CDM model to be best model to obtain the phase index of the silica particles used in this experiment. The refractive index as obtained from this model is given by:

$$n_p(k) = n_0 + n_1 k + n_2 k^2 + n_3 k^3 . \tag{16}$$

With n_{0-3} given by: 1.41517637, $3.37754432 \cdot 10^{-3}$ µm , $-1.33978325 \cdot 10^{-4}$ µm^2, and $5.08633502 \cdot 10^{-6}$ µm^3.

This is the same phase index as shown in red in Fig. 6 shown above, and Fig. 3.12 of the Chapter 3.

C. RECTANGULAR HAGEN–POISEUILLE FLOW

The laminar flow profile $v(z)$ in in the center of a rectangular channel is given by Eq 17. *bis.* on page 390 of [9]. The flow profile at the center of the channel is given by

$$v(z, x = \tfrac{1}{2}W) = \frac{GL^2}{8\pi^3\eta}\left(\pi^3 - 32\sum_{n=1}^{\infty}\frac{\cos(\pi n)\left(\sinh\left(\beta_n(L-z)\right) + \sinh\left(\beta_n z\right)\right)}{\sinh\left(\beta_n L\right)(2n-1)^3}\right). \tag{17}$$

With the pressure gradient G given by

$$G = \frac{12\pi^5\eta Q}{L^3\left(\pi^5 W - 192L\sum_{n=1}^{\infty}\frac{(\cosh(W\beta_n)-1)}{\sinh(W\beta_n)(2n-1)^5}\right)} \tag{18}$$

and β_n given by $\pi(2n-1)/L$, and all other quantities as defined in Chapter 4.

D. LASER DOPPLER VELOCIMETRY

Chapter 4 described a method to use the DLS signal to measure the flow speed. With this method, both the flow speed and the mean particle size can be measured. The mean

particle size can be measured relatively well compared to the the flow speed, which has a relatively large error. A better measurement of the flow speed can be obtained with laser Doppler velocimetry. For this, the Doppler component of Eq. 4.10 is used to obtain the flow speed. Since the Doppler component decreases the correlation time, this comes a the cost of a poorer mean size measurement.

The Doppler angle α is determined with a similar method as described in Chapter 3. The Doppler component of the autocorrelation is used to determine the flow speed of a dilute Intralipid 20 % sample with a volume fraction of 10 vol %. The angle α, as can be seen in Fig. 4.3(b), was set such that there is a measurable axial component of the flow. This angle of α 4.8°was determined with a linear fit of the measured flow rates. The maximum flow rate was 0.3 ml/min, which corresponds to a maximum flow speed of 7.5 mm/s in the center of the channel. The time resolution of the oscilloscope was set to 22.9 µs.

The flow cell for the Doppler measurement is a 100 µm flow cell (45/Q/0.1, Starna). This smaller flow cell is used, to prevent fringe washout and low penetration depth for larger channels. For the laser Doppler flowmetry configuration, the angle is changed such that there is a larger flow component v_z in the axial direction, as indicated in Fig. 4.3(b).

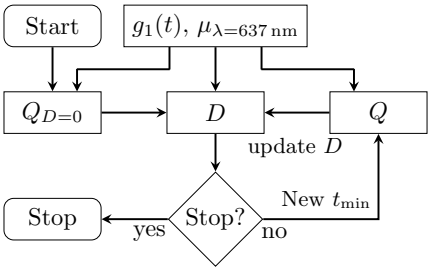

Figure 9: Flow chart for simultaneous size and flow measurement with LDF

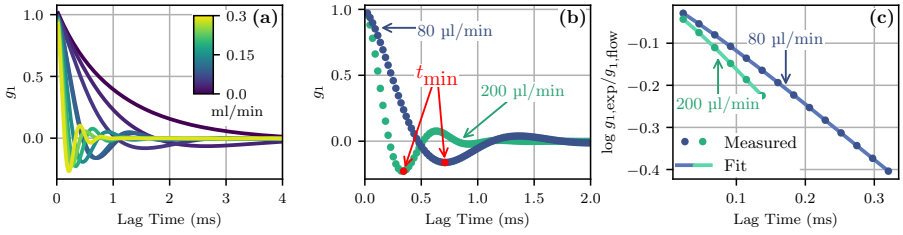

Figure 10: **(a)** Measured autocorrelation. **(b)** The found minima in the autocorrelations. **(c)** the natural logarithm of the autocorrelation.

The analysis steps for the laser Doppler flowmetry configuration are shown in the flowchart in Fig. 9, and the intermediate results are shown in Fig. 10. The measured autocorrelation is shown in Fig. 10(a). The flow rate is determined by the first minimum

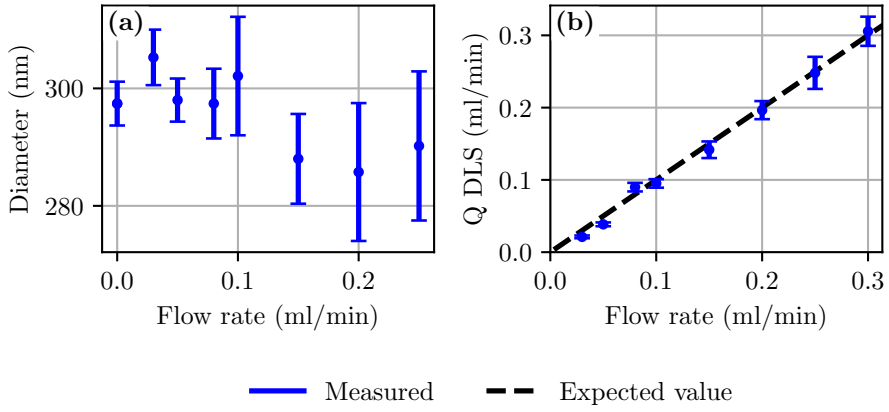

Figure 11: **(a)** Diameter as measured with the Doppler flowmetry configuration **(b)** Measured flow rates.

t_{min} in the measured autocorrelation function $g_1(t)$, as shown in Fig. 10(b). The attenuation at 637 nm is taken to be the same as determined with the wider channel. For the initial value of the the flow rate Q, a diffusion of $D = 0$ is assumed. This gives a slight overestimation of the flow rate. This flow rate is used to fit the diffusion constant D. The diffusion constant is fit using the same method as for the larger channel, but with a cutoff of $g_1(t) \leq 0.25$, and no minimum t. Fluctuations in the flow rate cause a lower amplitude of the autocorrelation around the minimum due to fringe washout. Therefore, the diffusion is only fit to the first few data points of the autocorrelation. The diffusion is used for a better estimate for Q. The optimization loop run for 20×, but converges quickly. The converged fit of the flow compensated autocorrelation is shown in Fig. 10(c).

The measured diameter and flow rates for the Doppler flowmetry configuration is shown in Fig. 11. The measured diameter in Fig. 11(a) is determined with reasonable precision, until the $Q = 10$ ml/min mark. The diameter measurements at the largest three flow rates are about 10 nm to 15 nm lower compared to the lower flow rates. The measured flow rate is shown in Fig. 11(b). The measured flow rate is close to the expected value. The precision decreases for larger flow rates.

With the Doppler flow measurement both the mean diameter and the flow speed were measured. The flow rate could be accurately measured with the position of the first minimum. The accuracy gained in the flow rate measurement comes at the cost of a poorer diameter measurement, compared to the low axial angle α, as shown in Fig. 4.3(a). A second disadvantage is that low diffusion constants more difficult to measure, since only a small part of the exponential decay can be measured. For method to obtain the flow rate through Eq. 4.13, there is no such upper measurable upper diameter. Since for most applications the flow rate is a more accessible quantity to measure, a low Doppler angle, as used in Chapter 4, is usually desirable.

REFERENCES

[1] L. Tsang, J. A. Kong, and R. T. Shin, *Theory of Microwave Remote Sensing*, Wiley Series in Remote Sensing and Image Processing. Wiley, 1985, ISBN 9780471888604.

[2] P. N. A. Speets and J. Kalkman, Experiment and theory of the complex refractive index of dense colloidal media, *Journal of the Optical Society of America A*, 41(2):214–228, 2024.

[3] K. H. Ding and L. Tsang, Effective propagation constants of dense nontenuous media with multi-species of particles, *Journal of Electromagnetic Waves and Applications*, 2(8):757–777, 1988.

[4] R. Márquez-Islas and A. García-Valenzuela, On the extinction coefficient of light in non-absorbing nanoparticle suspensions, *Applied Optics*, 57(13):3390–3394, 2018.

[5] J. B. Keller, Stochastic equations and wave propagation in random media, *Proceedings of Symposia in Applied Mathematics*, 16:145–170, 1964.

[6] L. Hespel, S. Mainguy, and J. Greffet, Theoretical and experimental investigation of the extinction in a dense distribution of particles: nonlocal effects, *Journal of the Optical Society of America A*, 18(12):3072–3076, 2001.

[7] S. Durant, O. Calvo-Perez, N. Vukadinovic, and J. Greffet, Light scattering by a random distribution of particles embedded in absorbing media: diagrammatic expansion of the extinction coefficient, *Journal of the Optical Society of America A*, 24(9):2943–2952, 2007.

[8] A. García-Valenzuela, H. Contreras-Tello, J. A. Olivares, and F. L. S. Cuppo, Insights into the dependent-scattering contributions to the extinction coefficient in highly scattering suspensions, *Journal of the Optical Society of America A*, 30(7):1328–1334, 2013.

[9] J. V. Boussinesq, Mémoire sur l'influence desfrottements dans les mouvements réguliers des fluides, *Journal de Mathématiques pures et Appliquées*, 13(2):377–424, 1868.

ACKNOWLEDGEMENTS

I would like to thank the many people who had a positive influence on both this PhD thesis and on its author. First, I would like to thank my promotor and advisor Jeroen for this opportunity. You are really approachable, which I think is a very important trait for an advisor: not everything in research goes smoothly. You gave me a lot of liberty in how I worked towards my thesis, and you managed to strike a good balance between optimism and realism. I also would like to thank my promotor Bernd. It really helped to discuss my project with a bird's-eye view: it is way too easy to get lost in all the small little details that are usually on my mind. Your quick and thorough reading of my last draft really made that there is now less room for discussion in my conclusion.

I would like to thank Valeria Garbin, Allard Mosk, Rut Besseling and Willem Vos for being on my committee and providing useful comments and suggestions that I believe made my thesis better. Professors might not know this, but we PhD candidates sometimes wonder how much the committee actually reads from the thesis. Your comments were such that I can now say that: yes, the committee actually reads the full thesis.

I would like to thank all the project members both from the University of Twente and Bronkhorst: Joost, Remco, Egbert, Cor, Pep and Anneirudh, for the helpful discussions, which really helped to shape my research direction. I would like to thank Pep and Anneirudh specifically for all the formal and informal on-line meetings we had, particularly in the first half of my project. It was always a good start of my Friday. Your optimism and enthusiasm worked contagiously. Our conversations were always rich in both humor and silicon-nitride.

I think I can count myself lucky with the colleagues I had at the TU Delft. First, of course, Jos, Kote, Huangcheng, Alim, Devrim, Vahid and Wei-Yun. Jos, you helped me not only with the science, but also helped me to find my way at the TU Delft. I really appreciated your mentoring, your strong sense of responsibility, and your optimism. Kote, particularly for my last project, I could really benefit from the knowledge you have as our DLS expert. Also, I can really learn from your, sometimes literally laser-focused, results-oriented attitude. Alim, I really appreciated our in-depth conversations. I hope we do not look like savages, now you work with civil engineers. Huangcheng and Vahid, I was never shy to ask you when I needed something, and you were never shy to help me. For example, Vahid, you prevented my last experiment to turn sour. You gave your full 37 wt.%, when I needed it most. Devrim, many people worked on your project, and you can be proud you really finished it.

I would like to thank all support staff, among others, Angela, Karin and Nicolette, but I would like to thank Ron, Annelies, Ronald and Henry in particular. I felt that you were always genuinely happy to help. There is a reason why the words 'Just ask Ron', 'Just ask Annelies', 'Just ask Ronald' and 'Just ask Henry' were uttered a lot by many people, since that is simply often the solution to many problems.

What I consider one of the best things of my time at the TU Delft, is the amount of great people I had the privilege to meet. Among many others, these are: Ahmed, Anna, Awoke, Boyd, Christiaan, Dion, Enya, Fabian, Gijs, Hamid, Hamed, Isabel, Koen, Leo, Linda, Loes, Mani, Maria, Mark, Martijn, Miriam, Myron, Qingru, Rasmus, Siamak, Sjoerd, Sobhan, Spozmai, Taylor, Valerii, Wenxiu, Xiufeng, Yi, Yidong, Yiming and Yutong. To my office mates Sobhan and Enya, thanks for your sincerity and good-natured sarcasm. I think you know which applies. Qingru, Isabel and Valerii, I think you really brought a sense of community to all the PhDs. Also, Mani, thanks for initiating the Codenames Fridays. Wenxiu, I could really enjoy your sense of humor. I like how you have your very own method to always generate a new topic to talk about. Comrades Yi and Yidong, also with you I really liked our conversations at the coffee machine. For that purpose (coffee that is), Yidong, thanks for lending me your green mug for about two years.

With all the new people that joined, let's not forget the 'old' people, which definitely does not include me: Christiaan, Hamid, Awoke, Leo, Siamak, Taylor and Rasmus. When I shared the office with Rasmus, it was really easy to ask a quick question. You saved me a few hundred euros by telling me about the Individueel Keuzemodel Arbeidsvoorwaarden. Speaking of arbeidsvoorwaarden: Leo, thanks for keeping me company when we both apparently incorrectly assumed that taking the night shift would give us a higher pay. It did not.

These are not the only people that made my time in Delft memorable. Many other colleagues from, for example, medical imaging in the next corridor, and the optics group and electron microscopy group downstairs, but also the people I met during during courses and project related events. With so many different research projects, hobbies and personalities, there was always something new to learn. Did you know that the matrix inversion in the RIAA algorithm can be sped up using Levinson-Durbin recursion? Well, these are the kinds of things you learn when you talk to PhDs.

Perhaps unconventional, but I also would like to thank Sanli, my former master thesis supervisor. Thanks to my positive experiences in Utrecht and due to his encouragement, I dared to take the big leap to pursue a PhD.

Mijn ouders Nico en Jeanette, en mijn broer Stijn: bedankt voor de tijd dat ik ook eens niet aan mijn proefschrift hoefde te denken. Soms is het prettig dat het dagelijks worden van een genie even het belangrijkste in de wereld is. Gelukkig kan dat geautomatiseerd worden. Ik wil ook graag mijn vrienden Bryan, Freek, Michał, Patrick, Stefan, Vincent, en de West-Friezen uit Schagen en omstreken bedanken. Stefan, bedankt dat je deze Nederlandse Delftse promovendus hebt uitgenodigd voor de on-line bordspellenavond van de internationale studentenvereniging Leiden, een welkome afleiding tijdens corona. Bryan, mijn kli-maat (ik kon het niet laten): ik ben blij met onze gedeelde interesse in geschiedenis en kijk op de wereld. Michał, je kwam vaak precies op het juiste moment even buurten, namelijk als ik eigenlijk dit proefschrift moest schrijven. Patrick, ik heb afgelopen vijf jaar veel onderzoek gedaan, en Percivals zijn toch echt de beste. Vincent, jouw opmerkingen zijn precies bot genoeg om scherp te zijn, dat helpt om te relativeren, en Freek, ik ben blij dat ik nu net zo'n grote nerd mag zijn als jij.

Zoals je hebt kunnen lezen, hebben veel mensen direct of indirect invloed gehad op dit proefschrift. Hoewel natuurkundige modellen het toch vaak aannemen, bestaat een proefschrift namelijk niet in een vacuüm. Het is trouwens ook niet bolvorming.

CURRICULUM VITÆ

Peter Nicolaas Adriaan SPEETS

12-03-1994 Geboren te Amsterdam, Nederland.

EDUCATION

2012–2016 Bachelor of Science in Natuur- en Sterrenkunde
Universiteit Utrecht

2016–2019 Master of Science in Experimentele Natuurkunde
Universiteit Utrecht

2020–2025 Promovendus in de Natuurkunde
Technische Universiteit Delft
Proefschrift: Optical interferometric multi-parameter flow sensing of particle suspensions with complex refractive index models
Promotoren: Dr. J. Kalkman and Prof. dr. B. Rieger

LIST OF PUBLICATIONS

4. D. Tugberk, K. Cheishvili, **P.N.A Speets**, W. Quirós-Solano, A. Ballal, N. Gaio and J. Kalkman, Multi modal optical coherence tomography flowmetry of organ on chip devices, *Scientific Reports* 15:26013, 2025.

3. **P.N.A. Speets** and J. Kalkman, Experiment and theory of the complex refractive index of dense colloidal media, *Journal of the Optical Society of America A* 41(2):214-228, 2024.

2. **P.N.A. Speets** and J. Kalkman, Measuring optical properties of clear and turbid media with broadband spectral interferometry, *Applied Optics* 62(16):4349-4358, 2023.

1. E.B. van der Wee, J. Fokkema, C.L. Kennedy, M. Del Pozo, M.D.A. de Winter, **P.N.A. Speets**, H.C. Gerritsen and A. van Blaaderen, 3D test sample for the calibration and quality control of stimulated emission depletion (STED) and confocal microscopes, *Communications Biology* 4(1):909, 2021.